THE JOURNAL OF
PHYSICAL CHEMISTRY

COMMUNICATIONS TO THE EDITOR

AUTHOR INDEX

Isotope Effects in the Hydrogen-Atom Addition to Olefins

at Low Temperatures

by Richard D. Kelley,* Ralph Klein, and Milton D. Scheer

National Bureau of Standards, Washington, D. C. 20234   *(Received July 17, 1970)*

The ratio of rates of addition of atomic hydrogen to the two possible sites of the double bond for several olefins has been measured over the temperature range 63–143°K. A pronounced isotope effect was found. In the comparison of addition ratios at a given temperature, the data show that the isotope effect is related to the value of the addition ratio, large ratios showing relatively large effects. The ratio of terminal to nonterminal addition of H to propylene at 90°K is 126, while for D it is 398. The ratio of H addition to carbon 2 relative to carbon 3 in cis-2-pentene at 90°K is 1.5 and that of D is the same. The results of these findings are discussed in terms of a one and two barrier model for the reaction of H with the olefinic bond. Both zero point energy effects and quantum tunneling of H through the reaction barriers are considered. It is concluded that a two barrier model with tunneling is most appropriate. The data generated from the H atom–olefin addition reactions in the low temperature region support the existence of chemical quantum tunneling. This is apart from the more equivocal arguments based on curvature of Arrhenius plots although indeed such curvature is found in the low-temperature H-atom additions.

Introduction

The addition of H atoms to condensed olefins at low temperatures was first reported about 12 years ago by Klein and Scheer.[1] Since then about 50 papers, from this as well as other laboratories, have appeared dealing with this reaction under cryogenic conditions. A number of generalizations, germane to the subject of this paper, can now be clearly stated. (1) The principal primary process is hydrogen-atom addition to the less substituted carbon of the double bond. (2) The temperature dependence for this process is small with only a fourfold increase in the rate between 77 and 90°K. (3) The secondary processes observed are alkyl–alkyl radical disproportionation and combination as well as hydrogen atom–alkyl radical combination and disproportionation. Addition of alkyl radicals to the olefin does not occur to any significant extent under these conditions since the activation energy is in excess of 5 kcal/mol.[2] (4) The alkyl–alkyl radical disproportionation and combination reactions predominate in matrices where diffusion is rapid, while H–alkyl radical disproportionation and combination are the major secondary reactions when high viscosity matrices are employed.

The relative rates of addition of a hydrogen atom to the two possible sites of an olefinic bond are considered here. In the case of propylene at 90°K, for example, addition to the terminal carbon to form an isopropyl radical is about 126 times as fast as n-propyl formation. It has been found that deuterium shows a significantly larger ratio of rates of addition to the two olefinic carbons. This unexpected isotope effect is not ascribed to zero point energy differences, but to quantum mechanical tunneling.

* To whom correspondence should be addressed.

(1) R. Klein and M. D. Scheer, *J. Amer. Chem. Soc.*, **80**, 1007 (1958).

(2) (a) J. A. Pinder and D. J. LeRoy, *Can. J. Chem.*, **35**, 588 (1957); (b) F. W. Lampe and F. H. Field, *ibid.*, **37**, 995 (1959); (c) J. A. Kerr and A. F. Trotman-Dickenson, *J. Chem. Soc.*, 1609 (1960).

The penetration of a one-dimensional barrier by light particles has been treated by many authors.[3-5] The application to chemical systems was discussed by Bell[6] and Johnston,[7] among others. Johnston[8] has made calculations with tunneling corrections for the $CH_3 + RH$ compared to the $CH_3 + RD$ reactions. The results depend strongly on the nature of the potential energy surface and the structure of the transition state assumed. It is clear that only those chemical systems involving hydrogen will exhibit measurable effects which can be attributed to tunneling. The unequivocal demonstration of such effects has been elusive. Studies of the low-temperature H-atom addition to olefins would appear to offer a reasonable possibility for the observation of tunneling in a chemical system.

Orientation Effects. It is well established that H atoms add predominantly to the terminal carbon atom of 1-alkenes at room temperature. However, little quantitative data have been available. It has been shown that H atoms add 5% nonterminally to 1-butene at room temperature.[9] Cvetanović and Falconer[10] have found addition to propylene to be about 6% nonterminal at room temperature. Recently, Falconer and Sunder[11] have studied the radical combination products from the H-atom addition to several olefins in the gas phase at 300°K. The H atoms were produced by the Hg-photosensitized decomposition of H_2. The ratio of terminal to nonterminal addition of H atoms to C_3H_6 is 21 with an identical result for D atoms.[12] Kelley, Klein, and Scheer[13] have measured the orientation of addition of H atoms to a number of olefins at 90°K. The low-temperature results for propylene showed even less nonterminal addition than found at room temperature, demonstrating a temperature coefficient of the orientation. Urch and Wolfgang[14] estimated the orientation of the addition of tritium atoms to 1-pentene as a function of their kinetic energy. They concluded that addition, though favored at the terminal carbon at low energies, becomes equal on both carbon positions at higher kinetic energies. The same results were obtained by Kushner and Rowland[15] for addition of tritium to 1-butene.

Addition of H atoms to asymmetrical olefins produces two alkyl radicals.

$$\text{(R}_1\text{)} \quad (1)$$
$$\text{(R}_2\text{)} \quad (2)$$
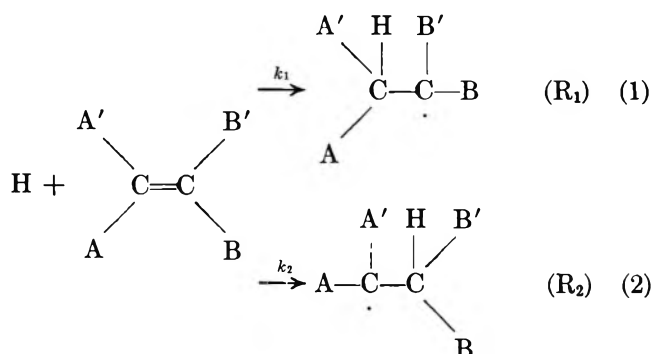
R_1 will designate that radical formed by the addition of

H to the less substituted carbon. The olefin is represented as $A'AC=CB'B$ where A', A, B', and B are alkyl groups or H atoms. The orientation of the addition can be defined as the rate constant ratio, k_1/k_2. Under certain conditions[16] all products arise from the disproportionation and combination reactions of the alkyl radicals, R_1 and R_2.

$$R_1 + R_1 \xrightarrow{k_3} \text{olefin}_1 + \text{alkane} \quad (3)$$
$$\xrightarrow{k_4} R_1\text{–}R_1 \quad (4)$$
$$R_1 + R_2 \xrightarrow{k_5} \text{olefin}_1 + \text{alkane} \quad (5)$$
$$\xrightarrow{k_6} \text{olefin}_2 + \text{alkane} \quad (6)$$
$$\xrightarrow{k_7} R_1\text{–}R_2 \quad (7)$$
$$R_2 + R_2 \xrightarrow{k_8} \text{olefin}_2 + \text{alkane} \quad (8)$$
$$\xrightarrow{k_9} R_2\text{–}R_2 \quad (9)$$
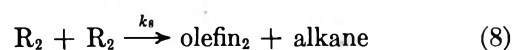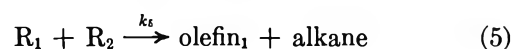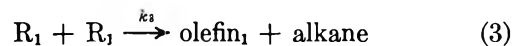
where R_1–R_1, R_1–R_2, and R_2–R_2 are the radical dimers and olefin$_1$ and olefin$_2$ represent all olefins produced by H-atom transfer from R_1 and R_2 in the disproportionation reactions. We have found that the auto disproportionation–combination ratios (Δ) at 90°K, for a number of alkyl radicals of interest are

$$\Delta_{\text{isopropyl}} = 6; \quad \Delta_{\text{sec-butyl}} = 11; \quad \Delta_{\text{tert-butyl}} \approx 500;$$
$$\Delta_{\text{tert-pentyl}} > 100$$

Thus, at low temperatures, the disproportionation reaction predominates. The orientation ratio k_1/k_2 can be derived from the measurement of the olefin products provided olefin$_1$ and olefin$_2$ are distinct from the parent olefin (case I). The measurement of the radical dimers provides an alternate derivation of the orientation ratio

(3) R. H. Fowler and L. Nordheim, *Proc. Roy. Soc., Ser. A*, 119, 173 (1928).

(4) C. Eckart, *Phys. Rev.*, 35, 1303 (1930).

(5) E. Wigner, *Z. Phys. Chem. Abt B*, 19, 203 (1932).

(6) (a) R. P. Bell, *Proc. Roy. Soc., Ser. A*, 139, 466 (1933); 148, 241 (1935); 158, 128 (1937). (b) R. P. Bell, *Trans. Faraday Soc.*, 55, 1 (1959).

(7) H. S. Johnston, *Advan. Chem. Phys.*, 3, 131 (1961).

(8) H. S. Johnston and D. Rapp, *J. Amer. Chem. Soc.*, 83, 1 (1961).

(9) R. E. Harrington, B. S. Rabinovitch, and H. M. Frey, *J. Chem. Phys.*, 33, 1271 (1960).

(10) R. J. Cvetanović, *Advan. Photochem.*, 1, 158 (1963).

(11) W. E. Falconer and W. A. Sunder, Abstracts, 159th National Meeting of the American Chemical Society, Houston, Texas, Feb 1970.

(12) W. E. Falconer, private communication.

(13) R. D. Kelley, R. Klein, and M. D. Scheer, *J. Phys. Chem.*, 69, 905 (1965).

(14) D. S. Urch and R. L. Wolfgang, *J. Amer. Chem. Soc.*, 81, 2025 (1959).

(15) R. Kushner and F. S. Rowland, *ibid.*, 91, 1539 (1969).

(16) R. Klein, M. D. Scheer, and R. Kelley, *J. Phys. Chem.*, 68, 598 (1964).

if the disproportionation–combination ratios are known (case II).

Case I. The experimentally determined olefin product ratio can be related to the orientation ratio by assuming a steady state in the radical concentrations

$$\frac{k_1}{k_2} = \frac{2k_3[R_1]^2 + (k_5 + k_6)[R_1][R_2]}{2k_8[R_2]^2 + (k_5 + k_6)[R_1][R_2]} \quad (A)$$

and

$$\frac{olefin_1}{olefin_2} = \frac{k_3[R_1]^2 + k_5[R_1][R_2]}{k_8[R_2]^2 + k_6[R_1][R_2]} \quad (B)$$

There is evidence that the disproportionation rate constants (k_3, k_5, k_6, and k_8) are proportional to the number of H atoms on carbons bonded to the carbon with the unpaired electron. This is based on recent measurements of the disproportionation–combination ratio of a number of C_3, C_4, and C_5 radicals listed in Table I.

Table I: Disproportionation–Combination Ratios for Several Alkyl Radicals at 300°K

Radicals		$\Delta(R_1, R_2)^a$	Ref
R_1	R_2		
i-C_4H_9	i-C_4H_9	0.078	b,c
n-C_4H_9	n-C_4H_9	0.14	d
i-C_3H_7	i-C_3H_7	0.69	c
n-C_3H_7	i-C_3H_7	0.41	e
n-C_3H_7	n-C_3H_7	0.15	e
CH_3	i-C_3H_7	0.163	e
CH_3	n-C_3H_7	0.058	e
C_2H_5	i-C_3H_7	0.180	e
C_2H_5	n-C_3H_7	0.066	e
i-C_3H_7	i-C_5H_{11}	0.082	f
i-C_5H_{11}	i-C_3H_7	0.24	f

^{a} $\Delta(R_1,R_2)$ refers to the disproportionation–combination ratio in which R_2 becomes the olefin product. ^{b} J. O. Terry and J. H. Futrell, *Can. J. Chem.*, **46**, 664 (1968). ^{c} D. H. Slater, S. S. Collier, and J. G. Calvert, *J. Amer. Chem. Soc.*, **90**, 268 (1968). ^{d} W. E. Morganroth and J. G. Calvert, *ibid.*, **88**, 5387 (1966). ^{e} J. O. Terry and J. H. Futrell, *Can. J. Chem.*, **45**, 2327 (1967). ^{f} L. A. O'Deen and K. W. Watkins, *J. Phys. Chem.*, **73**, 4094 (1969).

It can be seen that the isopropyl radical (six available H atoms) disproportionates to the olefin, by reaction with both CH_3 and C_2H_5 radicals, at a rate three times that of the n-propyl radicals (two available H atoms). This pattern is also observed in the isopentyl–isopropyl disproportionation reactions. On this basis we assume that, for the C_3 and C_5 radicals encountered in this work, the rate constants for disproportionation per H atom available for transfer are equal. Thus

$$k_3 = k_5 = \alpha k_6 = \alpha k_8$$

where α is the ratio of the number of transferrable atoms in R_1 to that in R_2. Equations A and B then lead to

$$\frac{k_1}{k_2} = \frac{K(2K + \alpha + 1)}{2\alpha + K(\alpha + 1)} \quad (C)$$

where $K = olefin_1/olefin_2$.

Case II. The analysis of the radical dimers from reactions 4, 7, and 9 together with the required disproportionation–combination ratios establishes the orientation ratio. The two olefins investigated in this manner were propylene and isobutene. The addition is preponderantly at the terminal carbon so that $[R_1] \gg [R_2]$ and the reactions 8 and 9 may be neglected. The dimer ratio, $(R_1–R_1)/(R_1–R_2)$, is given by $k_4[R_1]/k_7[R_2]$.

Assuming a steady-state radical concentration

$$\frac{k_1}{k_2} = 2D\left(\frac{\Delta + 1}{\Delta' + 1}\right) + 1 \quad (D)$$

where $\Delta = k_3/k_4$, $\Delta' = k_5 + k_6/k_7$, and $D = (R_1–R_1)/(R_1–R_2)$.

Experimental Section

The experimental techniques have been described previously.[16] In most of this work the inert diluent was removed chromatographically, trapping all reactants and products. The trapped material was transferred and analyzed by glpc with flame ionization detection. The entire analytical procedure, including the trapping and gas handling of trace quantities of products, was evaluated with standardized mixtures.

The isotopic purity of the deuterium (and tritium) was monitored by mass analysis of samples of the gas phase following a reaction. Exchange processes producing HD were observed in the reaction vessel containing no hydrocarbon film. These were eliminated by conditioning the vessel at 77°K with a high D-atom partial pressure. HD was also found when the wire dissociator was heated in the presence of a low D_2 pressure and a film of pure propane. The source of the hydrogen was found to be the vapor propane ($<10^{-5}$ Torr at 90°K) decomposing on the hot filament. The use of C_3D_8 as the diluent eliminated the problem. In the tritium experiments only small quantities of T_2 were used. The reaction vessel could not be adequately conditioned, and the extraneous exchange processes produced some HT in all experiments with T_2.

The determination of the orientation of the H-atom addition from the product analysis is simplified by the exclusion of H-atom–radical reactions. The disproportionation of H atoms and alkyl radicals yields olefins in a ratio different from the alkyl radical + alkyl radical reaction.[16] Also, the D-atom–alkyl radical disproportionation reaction produces HD, introducing hydrogen contamination in the deuterium. The H-atom–radical reactions were excluded by the choice of diluent, H-atom, and olefin concentrations. The criteria used for determining their absence were (a) the constancy of the product ratios over at least a ten-

fold change in H-atom concentration; (b) the absence of HD production when D_2 was used; (c) the ratio of product olefins to alkane [(olefin$_1$ + olefin$_2$)/R–H from reactions 3, 5, 6, and 8] was equal to 1.0 when extrapolated to zero conversion. (The occurrence of H + radical reactions has been shown to alter this stoichiometric value.[16])

Results

Propylene. The H-atom addition to propylene produces the radicals isopropyl and *n*-propyl. The dimerization products are 2,3-dimethylbutane (R$_1$–R$_1$), 2-methylpentane (R$_1$–R$_2$), and *n*-hexane (R$_2$–R$_2$). In a previous paper we reported the distribution of the hexanes from H + C_3H_6 at 90°K. We have reexamined these results and extended the measurements to D + C_3H_6, T + C_3H_6, H + C_3D_6, and D + C_3D_6 at 90, 77, and 63°K. The reaction conditions were varied extensively, the conversion of propylene to alkane, from 0.1 to 30%; the film composition, from pure propylene to 1:200 in propane; the reaction rate (formation of products), by a factor of 100; the hydrogen pressure, from 10 to 500 mTorr; and the dissociator wire temperature, from 1200 to 2400°K. The results of T + C_3H_6 are low due to hydrogen contamination.

The hexane analysis and the orientation ratio k_1/k_2, calculated from eq D are presented in Table II. *n*-

Table II: Orientation of H-, D-, and T-Atom Addition to Propylene

	T, °K	2,3-DMB/2-MP[a]	k_1/k_2[b]
H + C_3H_6	90	34 ± 2	126
	77	40 ± 2	167
	63	40 ± 4	189
H + C_3D_6	90	34 ± 2	126
	77	40 ± 2	167
D + C_3H_6	90	108 ± 4	398
	77		
D + C_3D_6	90	108 ± 4	398
	77	138 ± 4	575
T + C_3H_6	90	(105)	(387)

[a] The hexane analysis was performed on glpc with a 12-m × 0.635 cm o.d. 40% 3,3′-oxydipropionitrile column. The error limits are one standard deviation: 2,3-DMB = 2,3-dimethylbutane; 2-MP = 2-methylpentane. [b] Derived from eq D. The values used for Δ and Δ′ were $\Delta_{90°K}$ = 6, $\Delta_{77°K}$ = 10, $\Delta_{63°K}$ = 22, $\Delta'_{90°K}$ = 2.8, $\Delta'_{77°K}$ = 4.3, $\Delta'_{63°K}$ = 8.8. In arriving at these figures it was assumed that the temperature dependence observed for Δ($\Delta_{300°K}$ = 0.69 and $\Delta_{90°K}$ = 6) results from an activation energy difference of 550 cal mol^{-1}, the combination reaction having the higher value. The value of $\Delta'_{90°K}$ has not been measured. However, if it is assumed that the rate constants for disproportionation per H atom available for transfer are equal, *i.e.*, $k_{disp}(i\text{-}C_3 + i\text{-}C_3) = {}^3/_2 k_{disp}(i\text{-}C_3 + n\text{-}C_3)$, then at 300°K (see Table I) $k_{comb}(i\text{-}C_3 + n\text{-}C_3) = 1.13 k_{comb}(i\text{-}C_3 + i\text{-}C_3)$. If this rate difference is attributed entirely to an activation energy difference (70 cal mol^{-1}), the activation energy for combination of an isopropyl and an *n*-propyl radical exceeds that of disproportionation by 480 cal mol^{-1}.

Hexane was not ordinarily measured, being in much smaller concentrations than the other hexanes. The data in Table II indicate that the orientation of H- and D-atom addition differ by a factor of 3. These orientation effects are not changed appreciably when deuterated propylene is used. Since Δ′ has not been measured at low temperatures, the values derived for k_1/k_2 are somewhat uncertain. However, the observed isotope effect is not subject to this uncertainty, being dependent on the measured dimer ratio only.

Isobutene. The addition of H atoms to i-C_4H_8 produces the two radicals, *tert*-butyl and isobutyl. We have attempted to measure the orientation of the addition at low temperatures through the analysis of the dimer products. The results were only partially successful giving a lower limit of about 1000 at 90°K for the ratio of terminal to nonterminal addition. The lack of accuracy is due to the interference of the 2,2,4-trimethylpentane produced from radical addition to the olefin. Terminal addition of *tert*-butyl radicals to isobutene produces a C_8 radical which may disproportionate to C_8 olefins and 2,2,4-trimethylpentane. We have detected the two C_8 olefins expected from this source (2,4,4-trimethyl-1-pentene and 2,4,4-trimethyl-2-pentene). The products from the radical addition to the olefin form only a small fraction (10^{-5}) of the products of the H-atom addition. We have found that the disproportionation to combination ratio for *tert*-butyl radicals at 90°K is approximately 500. This fact, together with the low concentration of isobutyl radicals, results in an uncertainty in the orientation measurements. However, it is clear from the analysis of all the C_8 products that the orientation ratio favors terminal addition at 90°K by more than a factor of 1000.

cis-2-Pentene. The H-atom addition to *cis*-2-pentene produces the 3-pentyl (R$_1$) and the 2-pentyl (R$_2$) radicals. The products observed are *trans*-2-pentene, 1-pentene, *n*-pentane, and a small quantity of C_{10} dimers. We have previously reported the product distribution for H + *cis*-C_5H_{10} at 90°K.[13] We have now extended these measurements to D + *cis*-C_5H_{10} and find the olefin product ratio to be identical with that from the H addition. Table III indicates the product distribution

Table III: Orientation of H- and D-Atom Addition to *cis*-2-Pentene at 90°K

C_3H_8/ *cis*-2-pentene	Addend atom	Product yield[a] in nanomoles			(olefin$_1$/ olefin$_2$)[b]	(k_1/k_2)[c]
		n-Pentane	*trans*-2-Pentene	1-Pentene		
10	H	494	374	110	1.63	1.48
	D	633	458	138	1.59	1.46
40	H	280	210	63	1.60	1.47
	D	76.6	55.5	16.8	1.58	1.45

[a] Analysis performed with glpc on a 4 m × 0.635 cm column with dimethylsulfolane as liquid phase at 300°K. [b] Calculated from eq E. [c] Calculated from eq C.

Table IV: Orientation of H and D Addition to 2-Methyl-2-butene

Temperature, °K	K^a		$(k_1/k_2)^b$		$(k_1/k_2)_D/(k_1/k_2)_H$
	H	D	H	D	
77	172 ± 2	351 ± 6	115 ± 1.3	234 ± 4	2.03 ± 0.06
90	173 ± 3	350 ± 1	115 ± 2	233 ± 1	2.03 ± 0.04
113	153 ± 3	232 ± 2	102 ± 2	155 ± 1.3	1.52 ± 0.04
143	81 ± 3	113 ± 6	53 ± 2	75 ± 4	1.42 ± 0.12

^{a} The confidence level is 95%; K = (2-methyl-1-butene)/(3-methyl-1-butene); product analysis was performed with glpc on a 4 m × 0.635 cm o.d. 20% squalane column at 300°K. ^{b} Calculated from eq C.

from several experiments in which the conversion was low. In the disproportionation reactions of 2-pentyl radicals, 1-pentene and 2-pentene should be formed in the ratio of 3:2.[13] The 2-pentene product is formed in the cis–trans equilibrium ratio, which at 90°K is largely the trans isomer.[13] The 2-pentene product is thus distinguishable from the cis-2-pentene reactant. Based on these considerations, the ratio K (olefin₁/olefin₂) from reactions 3, 5, 6, and 8 for the H-atom addition to cis-2-pentene is given by

$$K = (Y - {}^2/_3X)/{}^5/_3X \qquad (E)$$

where Y = trans-2-pentene and X = 1-pentene. The data in Table III give a value for K of 1.6. The orientation ratio from (C) is 1.5 for both H-atom and D-atom addition.

2-Methyl-2-butene. The addition of H atoms to 2-methyl-2-butene produces the radicals $\overset{C}{\underset{C}{C}}{>}\dot{C}\text{-C-C}$, R_1, and $\overset{C}{\underset{C}{C}}{>}\text{C-}\dot{C}\text{-C}$, R_2. The observed reaction products are 3-methyl-1-butene, 2-methyl-1-butene, 2-methylbutane, and trace amounts of C_{10} dimers. The disproportionation–combination ratio for R_1, the predominant radical, is >100 at 90°K.

The disproportionation of R_1 to the olefin should yield 2-methyl-1-butene and 2-methyl-2-butene in the ratio of 3:1. The disproportionation of R_2 to the olefin should produce 3-methyl-1-butene and 2-methyl-2-butene, also in a 3:1 ratio. On this basis, olefin₁ = $^4/_3$(2-methyl-1-butene) and olefin₂ = $^4/_3$(3-methyl-1-butene) and the measurement of the 2-methyl-1-butene/3-methyl-1-butene ratio when extrapolated to zero conversion (to avoid hydrogenation of the product olefins) gives K. The assumption that the product olefins are formed in a 3:1 ratio is supported by the observation that 2-methylbutane = $^4/_3$(2-methyl-1-butene + 3-methyl-1-butene) (at zero conversion). It was found that at a given temperature K is constant and independent of conversion in spite of extensive product reaction. Therefore, the rate constants for H atom addition to 2-methyl-1-butene and 3-methyl-1-butene are nearly identical. This fact facilitated the use of a wide range of reaction conditions since the extrapolation to zero conversion was not required. The

value of K was measured at 77, 90, 113, and 143°K for both H- and D-atom addition. The orientation ratio is then calculated from (C). The diluents used at 77, 90, and 113°K were C_3H_8 and C_3D_8. At 143°K, 2 methylpentane and 2,3-dimethylpentane, as well as the undiluted olefin, were used. At each temperature, the H atom concentration, olefin concentration, and conversion were varied widely. Table IV summarizes the data.

Relative Reactivities of Olefinic Bonds. We have investigated the relative rates of addition of H atoms to a terminal and an internal double bond. This was accomplished in two ways: by measuring the relative rates of H-atom addition (1) to the two double bonds in cis-1,4-hexadiene, and (2) to propylene and cis-2-butene. The addition of H atoms to cis-1,4-hexadiene yields radicals which disproportionate to the following products

I = (2-hexene, 2,4-hexadiene, and 1,4-hexadiene)

and

II = (1-hexene, 1,5-hexadiene,

1,3-hexadiene, and 1,4-hexadiene)
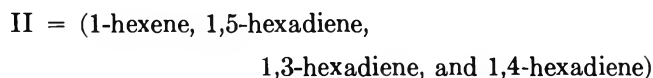
The olefin products referred to as I result exclusively from addition of H atoms at the terminal double bond, while those of II arise exclusively from addition at the internal double bond. The ratio of the rate of H-atom addition at the terminal to that of the internal bond is then I/II. This value must be extrapolated to zero conversion since the products are reactive to the H atoms. In both (I) and (II), 1,4-hexadiene is produced. This can be taken into account if, as before, it is assumed that the radicals disproportionate to the olefin with a rate constant proportional to the number of transferrable hydrogens. On that basis, the 1,4-hexadiene arising from the 2-hexenyl radical will equal $^3/_2$(2,4-hexadiene). Similar considerations for the other radicals involved give

$$\frac{I}{II} = \frac{[(2\text{-hexene}) + {}^5/_2(2,4\text{-hexadiene})]}{[(1\text{-hexene}) + {}^5/_3(1,5\text{-hexadiene}) + 2(1,3\text{-hexadiene})]}$$

Table V: Product Analysis and the Relative Rates of H- and D-Atom Addition to the Olefinic Bonds in *cis*-1,4-Hexadiene

		Product yield, nmol[a]				
	2-Hexene	2,4-Hexadiene	1-Hexene	1,5-Hexadiene	1,3-Hexadiene	I/II[b]
			90°K			
H	474	114	47	7	6	11.1
D	472	96	43	6	7	10.6
			143°K			
H	218	39	39	4	3	6.1
D	497	85	91	13	7	5.6

[a] Analysis performed by glc with a 4 m × 0.635 o.d., 20% 3,3'-oxydipropionitrile at 300°K. [b] I/II gives the relative rates of addition to the two double bonds (see text).

Table VI: Dimer Products from H and D Addition to Equimolar Mixtures of C_3H_6 + 2-C_4H_8 and of C_3H_6 + 1-C_4H_8 at 90°K

Addend atom	Dimer yield in nmol[a]			$(k_{C_3H_6}/k_{C_4H_8})$[b]
	C_6	C_7	C_8	
		C_3H_6 + 2-C_4H_8		
H	156.8	22.6	0.8	10.3
D	18.4	2.7	0.1	10.0
		C_3H_6 + 1-C_4H_8		
H	20.0	28.4	11.7	1.0
D	21.6	28.4	12.5	1.0

[a] C_6 = 2,3-dimethylbutane; C_7 = 2,3-dimethylpentane; C_8 = 3,4-dimethylhexane. [b] Calculated from eq F with Δ = 6.0, Δ' = 8.5, and Δ'' = 11.0.

The results of a number of experiments at 90°K Table V, indicate that for both H- and D-atom addition, the ratio I/II is about 11 when extrapolated to zero conversion. At 143°K this ratio is approximately 6.

Equal quantities of propylene and *trans*-2-butene, diluted to 1:50 in C_3H_8 (or C_3D_8) were deposited at 90°K. The relative rates of H- (or D-) atom addition to the two olefins were determined by measuring the C_6, C_7, and C_8 dimers. The rate ratio is given by

$$\frac{k_{C_3H_6}}{k_{2\text{-}C_4H_8}} = \frac{2C_6(\Delta + 1) + C_7(\Delta' + 1)}{2C_8(\Delta'' + 1) + C_7(\Delta' + 1)} \quad (F)$$

where Δ, Δ', and Δ'' are the disproportionation–combination ratios for (isopropyl–isopropyl), (isopropyl–*sec*-butyl), and (*sec*-butyl–*sec*-butyl), respectively. The values of Δ and Δ'' have been determined under the conditions of these experiments. At 90°K, Δ = 6 and Δ'' = 11, while Δ' is assigned the mean value 8.5. The results of several experiments are given in Table VI, along with similar measurements of the propylene-1-butene system. These relative rate measurements indicate that for both H- and D-atom addition at 90°K

$$k_{C_3H_6} = k_{1\text{-}C_4H_8} = 10k_{trans\text{-}2\text{-}C_4H_8}$$

The Zero Point Energy Model. A possible interpretation of the observed isotope effect is in terms of the zero point energy differences in the activated complexes associated with the two possible addition sites of the olefinic bond. Figure 1 is a schematic representation of the zero point energy levels of the transition states associated with each of the olefinic carbons for both H- and D-atom addition. Carbon 1 represents the less substituted one so that the energy barriers E_a and E_b are less than E_c and E_d. The ground-state vibrational level for the (Ol–D)* complex lies lower than for (Ol–H)*. The ratio of rate constant ratios (Q) is given by $\exp[(\Delta E_1 - \Delta E_2)/RT]$. The quantities ΔE_1 and ΔE_2 are the zero point energy differences between (Ol–H)* and (Ol–D)* at carbons 1 and 2. This model

requires that Q should monotonically decrease with increasing temperature, and the difference between the zero point energy differences ($\Delta E_1 - \Delta E_2$) should be constant. Table VII shows that the experimental results are not consistent with this hypothesis. Column 3 gives the uncertainties associated with the experimental values for $RT \ln Q$. It is seen that ($\Delta E_1 - \Delta E_2$) is *not constant*. In particular it should be noted that within the experimental uncertainty, Q shows no temperature dependence between 77 and 90°K.

Table VII: The "Zero Point Energy Difference" Model

T, °K	$Q(obsd)$ for 2-methyl-2-butene	$(\Delta E_1 - \Delta E_2) = RT \ln Q$, cal/mol
77	2.03 ± 0.06	108 ± 5
90	2.03 ± 0.04	127 ± 4
113	1.52 ± 0.04	94 ± 6
143	1.42 ± 0.12	100 ± 24

There is no isotope effect on the position 1 to position 4 addition ratio for 1,4 hexadiene at 90°K or higher (Table V). Mixtures of 1-butene and 2-butene are also characterized by the absence of any isotope effect (Table VI). The difference in zero point energies of the weak primary C–H bond of the transition complex on isotopic substitution compared to the weak secondary one fixes the ratio at a given temperature. The final free-radical products from 1-butene are C–C–C–C and C–C–C–C for primary and secondary addition, respectively. That from 2-butene is the C–C–C–C radical. In comparing terminal to nonterminal addition in 1-butene with addition to 1-butene and 2-butene, since one radical (C–C–C–C) and its corresponding transition precursor are identical for the two sets, we are, in effect, comparing the two transition states C–C–C(H)–C and C–C–C(H)–C, designated as A and B, respectively. The ratio of ratios, Q, in the

CARBON 1   CARBON 2

$$\left(\frac{k_H}{k_D}\right)_1 = \exp\left(\frac{E_b - E_a}{RT}\right) = \exp\left(-\frac{\Delta E_1}{RT}\right); \left(\frac{k_H}{k_D}\right)_2 = \exp\left(\frac{E_d - E_c}{RT}\right) = \exp\left(-\frac{\Delta E_2}{RT}\right)$$

$$Q = \left(\frac{k_H}{k_D}\right)_2 \Big/ \left(\frac{k_H}{k_D}\right)_1 ; \quad (\Delta E_1 - \Delta E_2) = RT \ln Q$$
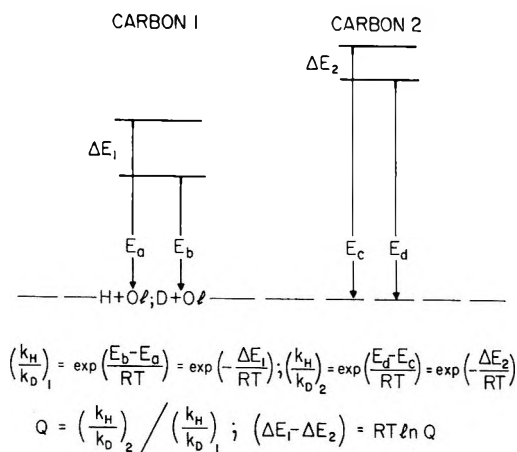
Figure 1. Zero point energy model.

terminal to nonterminal addition of 1-butene is 3 at 90°K. The isotope ratio is found to be 1 (no isotope effect) when H- and D-addition rates to 1-butene and 2-butene are compared. To maintain the zero point energy model, the *ad hoc* assumption would have to be made that the C–H bond in A is stronger than that in B. This is a consequence of the fact that the isotope effect increases with the bond strength, and in order to have an isotope ratio of 1 rather than 3, the isotope effect due to the secondary C–H transition state bond must be increased so that it is equal to that of the primary C–H transition state bond. The difference between the newly formed bonds in A and B cannot be very large, and it is most unlikely that there would be sufficient difference in the transition state precursors to account for the observed isotope effect. The implication is quite strong that the zero point energy model for the isotope effect is inadequate. The previous conclusion of the incorrectness of the model based on the temperature–isotope ratio relationship is reenforced.

Barrier Models for the Hydrogen-Atom Addition to the Olefinic Bond. A direct measure of the rate of formation of the two alkyl radicals would be preferable but is not feasible due to low concentrations. Several proposals need be considered to account for the experimental rate differences for addition to the two carbons. One is that the hydrogen atom reacts with the olefinic bond to form a single transition intermediate. The passage to R_1 or R_2 would then occur as a process fixed by the thermodynamic properties of the two radicals. The single barrier model is suggested by the fact that the rate of addition of H to propylene relative to 2-butene is ten although the terminal to nonterminal rate in propylene is 126 at 90°K. A two barrier model, with the assumption that barrier heights are dependent only on whether the newly formed CH bond is primary, secondary, or tertiary, cannot account for these results. For example, ethylene with respect to 2-butene should show the same ratio of H-atom addition as that in the two positions of propylene. Carbon 2 of propylene is

similar to the olefinic carbons of 2-butene, and carbon 1 to ethylene. It is of no consequence in the experiment that propylene instead of ethylene was compared with 2-butene because the addition to propylene is greater than 99% terminal.

The relative rates in the H-atom addition observed for mixtures of propylene and 2-butene were not affected by possible differences in the diffusion of these two species in the condensed phase. This was shown by the agreement with the 1,4-hexadiene results. Addition to the terminal relative to the internal double bond at 90°K was found to be 10:1 the same as for the propylene–2-butene ratio. A similar result in the comparison of rates of addition to the two sites of an olefinic bond *vis-à-vis* that of two different but corresponding olefins was noted for oxygen-atom addition.[10] In this case, 2-pentene was compared with the pair propylene and 2-butene. The conclusion was that the rate of addition to different olefins could not be related to the relative rates of addition to the two positions in the unsymmetrical double bond.

The single barrier model may be one in which the transition state is represented as a triangular configuration of H with the two olefinic carbons. The model, however, has consequences that are not in accord with the experimental results. These show that although the temperature effect on the ratio of rates at the two addition sites is not large, it is not negligible. The single barrier model requires the product distribution to be temperature independent. The model also implies that rearrangement to end states is either random or concerted. In the former case, the ratio of products could be determined by their relative energetics. Regardless of the auxiliary assumptions, the single barrier model is in accord with neither the temperature nor the isotope effects experimentally observed.

The two barrier model for addition is more reasonable in accounting for the experimental data. Clearly the two barriers are not mutually independent. If they were, the terminal to nonterminal addition ratio in propylene would be expected to be the same as that for the relative rate of addition to propylene compared with 2-butene. Alkyl substituents alter the charge density distribution at the two carbon sites of the double bond. The effect is that H atoms add at a faster rate to the terminal carbon of propylene than to either of the carbons of ethylene, but addition to the nonterminal carbon is slower than to one of the carbons of 2-butene. A significant difference between addition ratios for the two positions of the double bond as compared to the ratios for two separate olefins is the absence of an isotope effect in the latter. At 90°K, for example, the ratio of terminal to nonterminal addition to propylene of H with respect to D is 3. The ratio of propylene to 2-butene addition for H compared to D is 1. It is established that although a two barrier model is applicable to the H-atom addition, the relative barrier

heights are dictated by the nature of the attached groups and the resulting electronic configuration of the double bond.

To what extent the observed isotope effect may be ascribed to a preexponential factor can be determined. Since the temperature coefficient of the isotope ratio is small, let us suppose that it is due to symmetry factors. If this were true, the ratio $(k_1/k_2)_H/(k_1/k_2)_D$ should be equal to $(k_1/k_2)_D/(k_1/k_2)_H$ using C_3D_6. No such relationship was found. The results for H and D were independent of the deuteration of the propylene. Symmetry factors, therefore, play no role in accounting for the observed isotope effect.

Tunneling, the One-Dimensional Model. The isotope effect observed in the hydrogen-atom addition to the olefinic bond at low temperatures is attributed to tunneling through the potential barriers along the reaction path. The potential surface may, in principle, be calculated but practical considerations preclude such an exercise. One-dimensional models, though highly idealized, can be applied to gain some insights. Even for the one-dimensional case, analytical solutions are possible for only a few barriers such as the rectangular or Eckart types. As has been frequently noted, the tunneling correction in the calculation of reaction rates is very sensitive to the details of the barrier shape, its thickness and curvature. Since the concern here is not that of absolute rates, but only ratios, indeed the ratio of terminal to nonterminal addition for H as compared with D, the sensitivity to choice of barrier configuration is somewhat diminished.

The simplest representation of the one-dimensional barrier is that of the rectangular shape specified by three parameters as shown in Figure 2. The probabilities for transmission under and over the barrier are

$$T_u(E) =$$

$$\frac{4}{\left(\frac{\alpha}{\mu} + 1\right)\left(\frac{\mu}{\alpha} + 1\right) + \left(\frac{\alpha^2 + \beta^2 + \mu^2}{\mu\alpha} + \frac{\mu\alpha}{\beta^2}\right)\sinh^2\beta l}$$

and

$$T_0(E) = \frac{8}{\left(\frac{\alpha}{\mu} + 1\right)\left(\frac{\mu}{\alpha} + 1\right) + \left(\frac{\alpha}{\beta} + \frac{\beta}{\mu}\right)\left(\frac{\mu}{\beta} + \frac{\beta}{\alpha}\right) + \left[\frac{\alpha}{\mu} - \left(\frac{\beta^2}{\mu\alpha} + \frac{\alpha\mu}{\beta^2}\right) + \frac{\mu}{\alpha}\right]\cos 2\beta l}$$

respectively. The parameters are $\alpha = (1/h)\sqrt{2mE}$, $\beta = (1/h)\sqrt{2m(V - E)}$, and $\mu = (1/h)\sqrt{2m(E + A)}$. The exothermicity of the reaction is A and m is the mass of the tunneling particle. The rate k is calculated in the customary manner by integrating the product of the transmission probability with the supply function over all energy values. Thus

$$k = K\int_0^\infty T(E)e^{-SE}\, dE$$

where K is a constant, $S = 1/kT$, and the distribution is Boltzmann. k/K is recognized as the Laplace transform of the transmission function $T(E)$ and is designated as $T(S)$. Rectangular barriers, as in Figure 2, were chosen as models to simulate the H- and D-atom addition to the two positions of the olefinic bond. The experimental data for comparison with the model were most detailed and precise for 2-methyl-2-butene, as given in Table IV. The less substituted carbon, to which the atom addition is more rapid, will be represented by subscript 1, and that of the more substituted carbon by subscript 2. An attempt was made to generate the experimental values using a two rectangular barrier model with appropriate choices of parameters. These are circumscribed to V's of less than 5 kcal/mol, $A \simeq 35$ kcal/mol, and barrier thicknesses between 0.05 and 0.15 nm. The ratio of rates at the two positions is
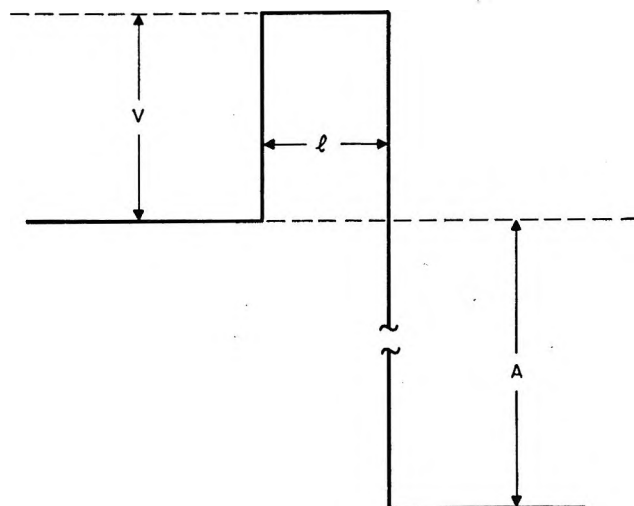

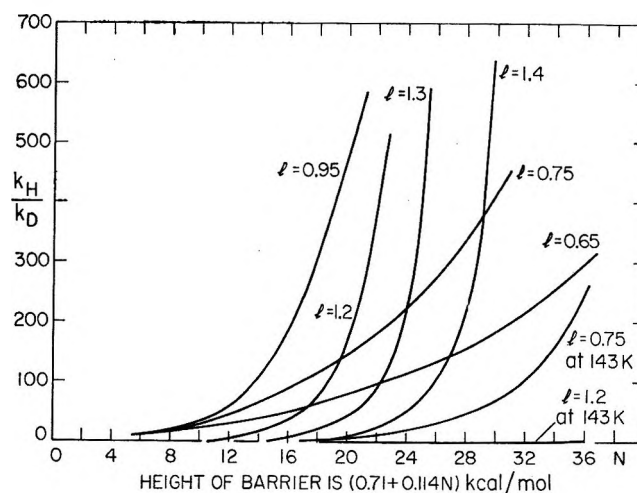Figure 2. Rectangular potential energy barrier.

Figure 3. Rate ratio of H- and D-atom transmission through rectangular barriers of varying thickness as a function of the barrier height. Except as noted, the temperature is 77°K.

$T_1(S)/T_2(S)$. Numerical calculations were made within the given range of variables on a computer in the time-sharing mode. The effect of variation of barrier thickness on the ratio of H- to D-addition rates over a range of barrier heights and at two temperatures is shown in Figure 3 (where l, the barrier thickness parameter, is in units of Ångstroms). The restrictions imposed by the data of Table IV on a model are very severe, indeed. The parameters chosen to supply the ratios of addition at the two positions for the two isotopes at one temperature must lead to the observed ratios at other temperatures. There is no combination of barrier thicknesses and heights of two rectangular barriers for which the experimental data of Table IV can be generated. For example, a choice of barriers with reasonable heights and widths leading to the experimental ratio of rates $(k_1/k_2)_H$ gives a value of $(k_1/k_2)_D/(k_1/k_2)_H$ which is too large. To lower the ratio of ratios at the lowest temperature to be more in accord with the experimental values, the barrier widths are chosen to be small. One is then able to obtain a reasonable fit for all experimental values at one temperature. However, it then becomes impossible to satisfy the temperature effects because the thin barriers emphasize the tunneling contributions excessively. Table VIII is an illustrative example of this behavior.

Table VIII: Some Results of Calculations with Rectangular Barriers

	—V, kcal mol⁻¹—		—l, nm—	
Barrier₁	1.17		0.095	
Barrier₂	2.31		0.085	
	77°K	90°K	113°K	143°K
$(k_1/k_2)_H{}^a$	129	180	276	226
Q	25	2.2	4.9	1.6
Barrier₁	1.28		0.055	
Barrier₂	3.67		0.045	
	77°K	90°K	113°K	143°K
$(k_1/k_2)_H{}^b$	96	93	100	113
Q	4.0	4.4	6.5	9.4

Transmission through potential barriers is particularly sensitive to their thickness. Use of a rectangular configuration ignores the thinning of the actual barrier in the vicinity of its maximum. To obtain a more realistic representation an Eckart barrier[4] was employed. Rates were calculated by machine computation for a range of parameter values. Table IX shows some of the results. As for the rectangular barriers, it was impossible to reproduce the experimental values. In fact, calculation of the ratio of ratios with the Eckart barriers gave results similar to those of the rectangular barriers. The supposition that the ratio of ratios is not very sensitive to the barrier model was confirmed. It can be

Table IX: Some Results of Calculations with Eckart Barriers[a]

	—V, kcal mol⁻¹—		—l, nm—	
Barrier₁	1.50		0.28	
Barrier₂	3.30		0.28	
	77°K	90°K	113°K	143°K
$(k_1/k_2)_H$	114	107	89	64
Q	6.4	5.6	4.1	2.7
Barrier₁	1.50		0.16	
Barrier₂	3.30		0.16	
	77°K	90°K	113°K	143°K
$(k_1/k_2)_H$	150	145	136	123
Q	3.1	3.1	2.9	2.6
Barrier₁	1.50		0.80	
Barrier₂	3.30		0.40	
	77°K	90°K	113°K	143°K
$(k_1/k_2)_H$	93	130	146	94
Q	21	11	4	2

[a] Reference 4; see also H. S. Johnston and J. Heicklen, *J. Phys. Chem.*, **66**, 532 (1962).

speculated that (1) a multidimensional barrier representation is required or (2) a mechanism in addition to penetration and surmounting of potential barriers must be invoked. Support for 2 on the basis of recognized models is lacking. There is an intuitive appeal for 1 because of its physical reality. In principle, the potential surface could be calculated. Unfortunately, even if this information were available, tunneling could be approximated only crudely. Completely rigorous proof that the addition of atomic hydrogen to an olefinic bond in the low-temperature region involves tunneling through, comparable in magnitude to thermal surmounting of, the potential barrier is of course not at hand. Tunneling appears to be the sole mechanism by which the isotope effect can be explained even though a physically reasonable model is lacking.

Radiolysis of Chloroform Vapor.   Effects of Phase on the Arrhenius

Parameters of the Hydrogen-Atom Abstraction Reaction of

Dichloromethyl Radicals with Chloroform

by Leland C. Dickey and Richard F. Firestone[1]

Department of Chemistry, The Ohio State University, Columbus, Ohio   43210   (Received August 17, 1970)

The products of the radiolytic decomposition of air-free $CHCl_3$ vapor are the same as those formed in the radiolysis of liquid $CHCl_3$, except that CCl_4 is not formed in the irradiated vapor under conditions of these experiments.   The effects of irradiation temperature on the rates of formation of major organic products are also the same as in the liquid phase.   An interpretation of data based upon assumption of the homogeneous liquid phase radiolysis mechanism provides values of $A/A_c^{1/2}$ and $E - E_c/2$ for the reaction, $CHCl_2 \cdot + CHCl_3 \rightarrow CH_2Cl_2 + CCl_3 \cdot$, equal to 8.1 $(\pm 0.4) \times 10^{-10}$ (cc molecule^{-1} sec^{-1})$^{1/2}$ and 6.4 $\pm$ 0.5 kcal mol^{-1}, respectively. The cross-combination ratio for $CHCl_2$ and CCl_3 radicals is equal to 2.1 $\pm$ 0.1 at 79–100°. Estimates of absolute values of the Arrhenius parameters indicate that the activation energy of the abstraction reaction is the same in both phases, but that the frequency factor is an order of magnitude smaller in the liquid phase.

Introduction

Although there is a considerable body of literature concerning reactions of fluoromethyl and fluorochloromethyl radicals,[2] information on the gaseous phase reaction kinetics of partially chlorinated methyl radicals is very limited and is currently confined to that presented in a report on the photochlorination of several partially chlorinated methanes.[3] This situation is understandable, because the direct photolysis of partially chlorinated analogs of convenient sources of methyl and fluoromethyl radicals does not produce partially chlorinated methyl radicals.[4-7] Similarly, empirical knowledge of the effects of phase on the Arrhenius parameters of elementary steps which have been shown to require thermal activation in the gaseous phase is almost nonexistent, although such effects have been a subject of interest for a half century.[8-12] This, too, is understandable, because although the apparently most promising techniques for study of such effects are those of the very active area of photochemistry, it has been difficult to identify photolytic systems in which the same primary processes and secondary reaction steps predominate in both liquid and gaseous phases. It appears that the photolysis of chloroform would satisfy this requirement, but there are, unfortunately, no reports on the photolysis of liquid chloroform, and only two cursory investigations of the direct photolysis of chloroform vapor have been reported, and these at a single temperature.[13,14] Results of earlier investigations[15,16] of the radiolytic decomposition of liquid chloroform suggested to the present authors that an examination of the radiolysis of chloroform vapor might provide estimates of the Arrhenius parameters of elementary reactions of $CHCl_2$ radicals in the gaseous phase and

thereby make possible a determination of the effects of phase on these parameters.

It has been shown that $CHCl_2$ and CCl_3 radicals are immediate precursors of all organic products of the radiolysis of liquid chloroform and that the observed dependence of their rates of formation upon temperature and dose rate is caused by competition between H-atom abstraction from chloroform by $CHCl_2$ radicals and radical combination steps.[15,16] Numerical solutions of the steady-state equations for the free radicals have led to estimates of the frequency factor and activation energy of the abstraction step in the liquid

(1) To whom all correspondence should be addressed.

(2) J. M. Tedder and J. C. Walton, *Progr. React. Kinet.*, **4**, 37 (1967).

(3) R. Eckling, P. Goldfinger, G. Huybrechts, G. Martens, L. Meyers, and S. Smoes, *Chem. Ber.*, **93**, 3014 (1960).

(4) A. N. Strachan and F. E. Blacet, *J. Amer. Chem. Soc.*, **77**, 5254 (1955).

(5) R. P. Taylor and F. E. Blacet, *ibid.*, **78**, 706 (1956).

(6) W. F. Yates and L. J. Hughes, *J. Phys. Chem.*, **64**, 672 (1960).

(7) G. A. Razuvaev and N. A. Osanova, *Zh. Obshch. Khim.*, **24**, 1771 (1954).

(8) E. Rabinowitch, *Trans. Faraday Soc.*, **33**, 1225 (1937);   E. Rabinowitch and W. C. Wood, *ibid.*, **32**, 1381 (1936).

(9) M. G. Evans and M. Polanyi, *ibid.*, **32**, 1333 (1936).

(10) R. P. Bell, *ibid.*, **33**, 496 (1937);   *Ann. Rep. Chem. Soc.*, **36**, 82 (1939).

(11) F. Daniels and E. H. Johnston, *J. Amer. Chem. Soc.*, **43**, 53 (1921);   H. Eyring and F. Daniels, *ibid.*, **52**, 1473 (1930).

(12) B. S. Khambata and A. Wassermann, *Nature*, **137**, 496 (1936); **138**, 368 (1936); A. Wassermann, *J. Chem. Soc.*, 1028 (1936); G. A. Benford, B. S. Khambata, and A. Wassermann, *Nature*, **139**, 669 (1937); A. Wassermann, *Trans. Faraday Soc.*, **34**, 128 (1938).

(13) J. P. Simons and A. J. Yarwood, *ibid.*, **57**, 2167 (1961).

(14) G. P. Semeluk and I. Unger, *Nature*, **198**, 853 (1963).

(15) H. R. Werner and R. F. Firestone, *J. Phys. Chem.*, **69**, 840 (1965).

(16) F. P. Abramson and R. F. Firestone, *ibid.*, **70**, 3596 (1966).

phase.[16] This article reports effects of temperature on the rates of formation of organic products in chloroform vapor exposed to 50-pkV X-rays. The results provide values of the radical cross-combination ratio and estimates of the Arrhenius parameters of the abstraction reaction in the gaseous phase and make possible a comparison of liquid and gaseous phase values of these parameters.

Experimental Section

Mallinckrodt AR grade chloroform was purified by means described previously.[16] Ohio Chemical and Surgical U.S.P. grade nitrous oxide was prepared for use as a dosimeter gas by successive trap-to-trap distillation at $-196°$ until mass spectrometric analysis indicated that oxygen had been reduced below the limit of detectability (ca. 0.1%). Pure, air-free samples of chloroform vapor were irradiated with X-rays from a Machlett OEG-60 X-ray tube operated at 35 mA and 50 kV. The irradiation vessel was a 500-ml spherical Pyrex flask; the X-rays were admitted through a thin dome shaped section blown in the wall of the flask. The temperature of the vessel and its contents was held constant within $\pm 0.5°$ during irradiations. Each vapor sample was irradiated for 1.00 hr. Yields of organic reaction products were determined quantitatively by gas chromatography, and the presence or absence of inorganic products was established as described previously.[16] Quantitative data reported below are averaged values of three or more replicate experiments.

The absorbed dose has been estimated from measured yields of N_2 from the X-ray induced decomposition of N_2O in the irradiation vessel at 25°. The yield of N_2 was observed to be directly proportional to the pressure of N_2O between 47.6 and 1270 Torr. $G(N_2)$ is equal to 10.0 molecules/100 eV under these conditions.[17] It has been assumed that the respective rates of energy dissipation per unit mass in $CHCl_3$ and N_2O vapors bear the same proportionality to their respective photoelectric mass absorption coefficients. Atomic mass absorption coefficients have been evaluated by interpolating those of Berger[18] to the mean energy of the distribution (30 keV), and molecular coefficients have been equated with the mass fraction weighted sums of atomic coefficients. The absorbed dose has thereby been estimated to have been approximately 5×10^{17} eV/cc of chloroform vapor in each experiment. This datum is not directly relevant to the interpretation of results, but simply indicates that the 100-eV yields of products were equal within a factor of approximately two to those from the radiolysis of liquid chloroform[15,16] and that the vapor phase mechanism was of nonchain character.

Results

Products observed were those which are formed in the radiolysis of liquid chloroform above room tem-

perature excepting CCl_4 which was absent from the irradiated vapor samples. Time average rates of product formation at 79, 90, and 100° are presented in Table I. All data were obtained by irradiating chloro-

Table I: Rates of Product Formation[a] in the Radiolysis of $CHCl_3$ Vapor

	Temp, °C		
	79	90	100
CH_2Cl_2	8.1 ± 0.6	9.7 ± 0.8	11.7 ± 1.1
$C_2H_2Cl_4$	3.5 ± 0.2	3.9 ± 0.2	2.7 ± 0.3
C_2HCl_5	16 ± 1	17 ± 1	16 ± 1
C_2Cl_6	15 ± 1	16 ± 1	20 ± 1
C_2Cl_4	1.3 ± 0.3	1.3 ± 0.4	1.1 ± 0.4

[a] Rates are expressed in units of molecules $cc^{-1} sec^{-1} \times 10^{-11}$. Experimental uncertainties are average deviations from the means of three or more replicate experiments.

form vapor at a concentration equal to 1.50×10^{19} molecules cc^{-1} for 1.00 hr. The fraction of chloroform converted to products in each experiment was less than 0.002. Measurements made in this laboratory by R. C. Bair have shown that the yield of each organic product was directly proportional to irradiation time at 0.50 and 1.00 hr, at this vapor concentration at temperatures up to 100°. It was observed that spontaneous thermal decomposition of pure, air-free chloroform vapor did not take place under conditions of experiments whose results are reported here. The presence of air was observed to greatly increase the variety of products and the rate of decomposition.

Discussion

The form of the effects of temperature is the same as that observed in the radiolysis of liquid chloroform at low dose rates.[15,16] These effects in the liquid phase have been shown to be quantitatively consistent with a homogeneous mechanism comprising the following steps.[16] There is no evidence for radical dispropor-

$$CHCl_3 \rightsquigarrow CHCl_2\cdot,\ Cl\cdot \qquad (1)$$

$$CHCl_2\cdot + CHCl_3 \longrightarrow CH_2Cl_2 + CCl_3\cdot \qquad (2)$$

$$Cl\cdot + CHCl_3 \longrightarrow HCl + CCl_3\cdot \qquad (3)$$

$$2CHCl_2\cdot \longrightarrow C_2H_2Cl_4 \qquad (4)$$

$$CCl_3\cdot + CHCl_2\cdot \longrightarrow C_2HCl_5 \qquad (5)$$

$$2CCl_3\cdot \longrightarrow C_2Cl_6 \qquad (6)$$

tionation steps in either phase. Reaction 3 consumes all Cl atoms at 0° and above in the liquid phase. It is certain that it also does so in the vapor phase under conditions of these experiments as may be readily demonstrated with relative rate constant values from
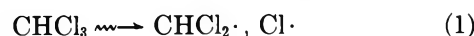
(17) F. T. Jones and T. J. Sworski, J. Phys. Chem., 70, 1546 (1966).
(18) R. T. Berger, Radiat. Res., 15, 1 (1961).

earlier work[3,19-22] from which k_3, e.g., has been estimated to be of the order $10^{-11}e^{-(3.3 \times 10^5)/RT}$ cc molecule^{-1} sec^{-1}.

Detailed investigations of effects of temperature, dose rate, and the presence of free halogens in the radiolysis of liquid chloroform[15,16] have suggested that dichlorocarbene is the precursor of C_2Cl_4 in the liquid phase via reactions 7 and 8, below

$$CCl_2 + CHCl_3 \longrightarrow C_2HCl_5* \qquad (7)$$

$$C_2HCl_5* \begin{cases} \nearrow C_2Cl_4 + HCl & (8 \text{ and } 9) \\ \searrow_M \\ \searrow C_2HCl_5 & (10) \end{cases}$$
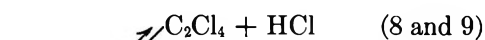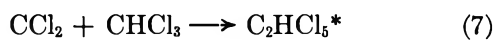
as appears to be the case, as well, in the pyrolysis of chloroform vapor.[23] It has been observed that the rate of C_2Cl_4 formation exhibits a pronounced positive temperature coefficient in the liquid phase[15,16] but is essentially independent of temperature in chloroform vapor. This difference might reasonably have been anticipated because reactions 9 and 10 must be much less effective in the vapor phase, in the absence of solvent cage effects and at a several hundredfold lesser chloroform concentration.

Measured rates of formation of CH_2Cl_2, C_2HCl_5, $C_2H_2Cl_4$, and C_2Cl_6 may be used variously to evaluate the cross-combination ratio for $CHCl_2$ and CCl_3 radicals and to estimate the activation energy of reaction 2 and the frequency factor of reaction 2 relative to that of reaction 4. Assuming time-independent rates of product formation the cross-combination ratio, $k_5/(k_4k_6)^{1/2}$, equals the ratio of the rate of pentachloroethane formation to the square root of the product of the rates of formation of tetrachloroethane and hexachloroethane and has been found to be equal to 2.1 ± 0.1 and to be independent of temperature at 79–100°. This value is consistent with measured values for halogenated methyl radical pairs[2] and for small alkyl radical pairs in the gaseous phase.[24,25] Values of $k_2(CHCl_3)/k_4^{1/2}$ are given by the ratio of the rates of formation of methylene chloride to the square root of the rates of formation of tetrachloroethane at 79, 90, and 100°. These values indicate that $E_2 - E_4/2$ equals 6.4 ± 0.5 kcal/mol. It follows that $A_2/A_4^{1/2}$ is equal to 8.1 (± 0.4) $\times 10^{-10}$ (cc molecule^{-1} sec^{-1})$^{1/2}$ and that $k_2/k_4^{1/2} = 8.1 \times 10^{-10}$ $e^{-(6.4 \times 10^5)/RT}$ (cc molecule^{-1} sec^{-1})$^{1/2}$ at 79–100°.

An estimate of the absolute value of k_2 must depend either upon the single published estimate of k_4 (4.2×10^{-12} cc molecule^{-1} sec^{-1})[3] or upon consideration of the probable value of k_4 relative to k_6 and the several quite different published estimates of k_6.[3,22,26] The best source of a reliable value of k_4 relative to k_6 appears to be data from the study of the direct photolysis of chloroform vapor reported by Semeluk and Unger.[14] These were measured under conditions which precluded occurrence of reaction 2 and which effected quantitative

removal of Cl atoms by reaction 3 in the absence of primary photolytic rupture of the CH bond of $CHCl_3$, thus causing formation of $CHCl_2$ and CCl_3 radicals at equal rates. Under these conditions the ratio of measured rates of tetrachloroethane and hexachloroethane was equal to k_4/k_6. These data indicate that k_4/k_6 is equal to 1.3, in close agreement with hard-sphere collision theory estimates.[27] Assuming the value of k_6 reported in ref 22 to be most nearly accurate and that k_4 like k_6 is independent of temperature,[22,26] k_2 is represented most reliably by the expression, $k_2 = 3 \times 10^{-15}e^{-(6.4 \times 10^3)/RT}$ cc molecule^{-1} sec^{-1}. The probable uncertainty in A_2 is a factor of two, up or down, based upon data of ref 26 or 3, respectively.

There are no other published estimates of the Arrhenius parameters of reaction 2 in the gaseous phase, and there are few estimated values for reactions of other halogenated methyl radicals with chloroform. Available information indicates that the frequency factor and activation energy of the reaction

$$CF_3\cdot + CHCl_3 \longrightarrow CHF_3 + CCl_3\cdot \qquad (11)$$

are approximately equal to A_2 and E_2, respectively.[28,29] A_{11} appears to lie between (0.6 and 5) $\times 10^{-14}$ cc molecule^{-1} sec^{-1}, and E_{11} lies near 6.3 to 6.6 kcal/mol.

It has been estimated[16] that in liquid chloroform, $k_2 = 2 \times 10^{-16}e^{-(6.7 \times 10^3)/RT}$ cc molecule^{-1} sec^{-1}, an absolute value which is subject to the same kinds of uncertainties as the gaseous phase value, but which can reasonably be expected to be better than an order of magnitude estimate. Pending future independent determinations, it may be tentatively concluded that E_2 is independent of phase, but that A_2 is an order of magnitude smaller in the liquid phase. For diffusion-limited reactions, such as radical combination steps, rate constants are, of course, markedly smaller in the liquid phase. For reactions which have significant activation energies in the gaseous phase, however, there is simply not sufficient experimental information to establish an empiri-

(19) J. H. Knox, Trans. Faraday Soc., 58, 275 (1962).

(20) P. G. Ashmore and M. S. Spencer, ibid., 60, 1608 (1964).

(21) P. Goldfinger, G. Huybrechts, and G. Martens, ibid., 57, 2210 (1961).

(22) G. R. DeMaré and G. Huybrechts, ibid., 64, 1311 (1968).

(23) A. I. Shilov and R. P. Sabirova, Russ. J. Phys. Chem., 34, 408 (1960).

(24) S. W. Benson and W. B. DeMore, Ann. Rev. Phys. Chem., 16, 413 (1965).

(25) J. A. Kerr and A. F. Trotman-Dickenson, Progr. React. Kinet., 1, 107 (1961).

(26) J. M. Tedder and J. C. Walton, Chem. Commun., 160 (1966).

(27) H. S. Johnston, "Gas Phase Reaction Rate Theory," Ronald Press, New York, N. Y., 1966, p 152 ff.

(28) H. Carmichael and H. S. Johnston, J. Chem. Phys., 41, 1975 (1964).

(29) W. G. Alcock and E. Whittle, Trans. Faraday Soc., 62, 134 (1966).

cal rule. Excepting the present instance and, possibly, the cases of dimerization and reverse dissociation of cyclopentadiene, for which the respective liquid and gaseous phase A and E values seem to be roughly equal,[12] there are no available data concerning effects of phase on the Arrhenius parameters of an elementary reaction which requires thermal activation in the gaseous phase.

Acknowledgment. The authors are grateful to the U. S. Atomic Energy Commission for partial support of this work under Contract No. AT(11-1)-1116.

Reactions of Electrons and Free Radicals in Glassy Ethanol[1]

by S. Fujii and J. E. Willard

Department of Chemistry, University of Wisconsin, Madison, Wisconsin 53706 (Received June 22, 1970)

Experiments designed to increase understanding of the mechanisms of trapping and reaction of electrons and free radicals in γ-irradiated glassy ethanol at 77°K are reported. They show that the concentration of electrons grows with increasing γ dose to a maximum at 6×10^{20} eV g^{-1} and then decreases, accompanied by a decrease in G(free radicals). Free radicals are produced during thermal decay of trapped electrons, as well as by photobleaching. There is a blue shift in the optical absorption spectrum (λ_{max} 535 nm) of trapped electrons during thermal decay and also during photobleaching with 650-nm radiation, but not with 540 nm. Prolonged annealing of C_2H_5OH glass at 90°K prior to γ irradiation alters the available trapping sites in such a manner that the trapped electron spectrum is shifted to the red, the yield is reduced, and the decay rate is increased. CH_3CHOH radicals produced in the radiolysis decay by second-order kinetics. Parallel growth and decay of the esr free-radical signal and absorption at 200 nm are consistent with the conclusion that the latter is in part attributable to free radicals.

Introduction

The concentration of trapped electrons produced in hydrocarbon glasses by γ irradiation increases to a maximum and then decreases to zero with increasing γ dose.[2] This phenomenon is attributed to competing reactions involving free radicals and trapped and mobile positive charge and electrons.[2b] It does not occur in solid alcohols[3] at the doses thus far reported.[4] This may be because the polarity of the matrices increases the trapping probability for electrons and positive charge in such a way as to allow a higher concentration to be achieved than in hydrocarbons before neutralization processes and reaction of electrons with radicals compete effectively. In the work of the present paper we have tested higher γ doses with ethanol and isobutyl alcohol glasses. Secondly, we have sought clarifying evidence as to whether the thermal decay of trapped electrons in ethanol glass generates free radicals as does photobleaching[5,6]—a question on which differing opinions have been advanced.[4a,5b,6] We have also obtained information on the correlation between the uv absorption of γ-irradiated ethanol glass and the CH_3CHOH esr signal, the kinetics of CH_3CHOH decay, and the effect of annealing at 90°K on the trapping capability of ethanol glass at 77°K.

Experimental Section

Absolute ethanol was further purified by refluxing with 2,4-dinitrophenylhydrazine to remove aldehydes and ketones and by distillation, following which it showed less than 0.25% impurity by gas chromatography. It was allowed to react with sodium and distilled before introduction to the vacuum line where it was degassed and stored over sodium prior to distillation into the reaction cell. Isobutyl alcohol was purified by preparative gas chromatography to >99.6% purity,

(1) This work has been supported in part by U. S. Atomic Energy Commission Contract AT(11-1)-1715 and by the W. F. Vilas Trust of the University of Wisconsin.

(2) (a) M. Shirom and J. E. Willard, *J. Amer. Chem. Soc.*, **90**, 2184 (1968); (b) A. Ekstrom, R. Suenram, and J. E. Willard, *J. Phys. Chem.*, **74**, 1888 (1970).

(3) (a) A. Ekstrom and J. E. Willard, *ibid.*, **72**, 4599 (1968); (b) F. S. Dainton, G. A. Salmon, and J. Teply, *Proc. Roy. Soc., Ser. A*, **286**, 27 (1965).

(4) (a) Reviews of the literature on the radiation chemistry of solid alcohols have been given by L. Kevan in "Actions Chimiques et Biologiques des Radiations," Vol. 13, M. Haissinsky, Ed., Masson, Paris, 1969; (b) Also, see J. Teply, *Radiat. Res. Rev.*, **1**, 361 (1969).

(5) (a) R. S. Alger, T. H. Anderson, and L. A. Webb, *J. Chem. Phys.*, **30**, 695 (1959); (b) C. Chachaty and E. Hayon, *J. Chim. Phys.*, **61**, 1115 (1964).

(6) J. E. Bennett, B. Mile, and A. Thomas, *J. Chem. Soc. A*, 1399 (1967).

treated with sodium, degassed, and distilled under vacuum into the reaction cells.

Reaction cells for spectrochemical analysis were made by drawing down a 15-mm i.d. Suprasil tube over a metal form to give cells *ca.* 5 mm wide, 35 mm high, and with a light path of 0.5 to 1 mm. Use of these thin cells greatly reduced the problems of cell cracking encountered when C_2H_5OH was frozen in larger cells, and also made it possible to measure optical densities at high doses. Esr measurements were usually made in 4 mm o.d., 3 mm i.d. Suprasil tubes. For optical and esr measurements on the same cell, rectangular cells with internal cross section of 3 mm × 4 mm were made by drawing down Suprasil over a mandrel.

γ irradiations were carried out under liquid nitrogen at 77°K with a dose rate of $(4 \pm 1) \times 10^{18}$ eV g^{-1} min^{-1}. Corrections were made for the optical density of the irradiated Suprasil cells which was about 0.17 at 540 nm and 0.10 at 700 nm for a dose of 1×10^{21} eV g^{-1}, and 0.28 and 0.23 at 540 and 700 nm, respectively, at a dose of 3×10^{21} eV g^{-1}. Measurements were made with a Varian 4500 esr spectrometer using 100-kHz modulation and a power level of 0.38 mW and with a Cary 14R spectrophotometer, using neutral density filters where necessary to extend the available optical density range.

Thermal decay studies of trapped electrons were made at 90°K using liquid oxygen as refrigerant, 87°K using liquid argon and 77°K using liquid nitrogen. For photobleaching the sample was exposed at the focus of the condensing lens of a Bausch and Lomb high intensity monochromator using an Osram 200-W high pressure mercury arc as the source, and a band width at half-height of 10 nm centered at 540 nm.

Results

Optical and Esr Spectra. We observe, as has been reported previously[4,5a] that γ-irradiated C_2H_5OH glass at 77°K has an absorption maximum at 535 nm attributable to trapped electrons and absorption increasing from 300 toward 200 nm which appears to be attributable in part to free radicals and possibly in part to charged species (Figure 1). Our experiments show that partial photobleaching of the spectrum with 540-nm light reduces the 535-nm band nearly uniformly, as does bleaching with 476[7] or 650-nm light. However, allowing the sample to stand for 4 hr in the dark at 90°K causes a blue shift (Figure 1). After removal of the trapped electrons by exhaustive photobleaching with 650-nm light, a long wavelength tail of the uv absorption, extending to at least 400 nm, remains. γ irradiation of ethanol glass does not produce any species which absorbs in the region of 900 to 2000 nm.

As previously observed,[4,5] γ-irradiated C_2H_5OH glass at 77°K gives a five-line esr spectrum attributable to CH_3CHOH with the intensity of the central line increased by the trapped electron signal (Figure 2a).
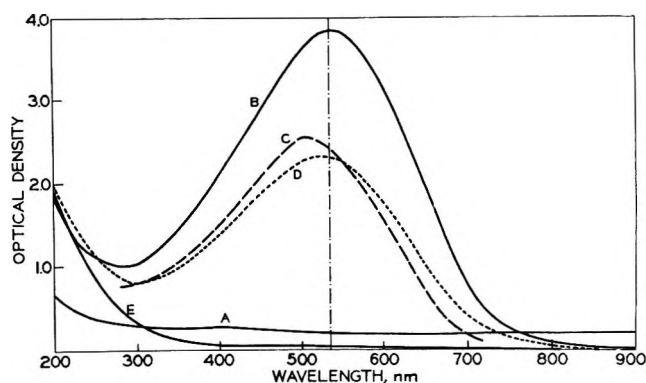
Figure 1. Uv-visible-ir spectra of C_2H_5OH glass at 77°K: (A), unirradiated; (B) γ-irradiated; (C) γ-irradiated sample after 4-hr decay in dark at 90°K; (D) γ-irradiated sample after partial photobleaching at 650 nm; (E) γ-irradiated sample after exhaustive photobleaching. γ doses from 0.95×10^{20} to 2×10^{20} eV g^{-1}. The data were normalized for dose, and the values of spectrum A for the unirradiated sample were subtracted from the observed spectra of the irradiated samples to give the spectra shown.
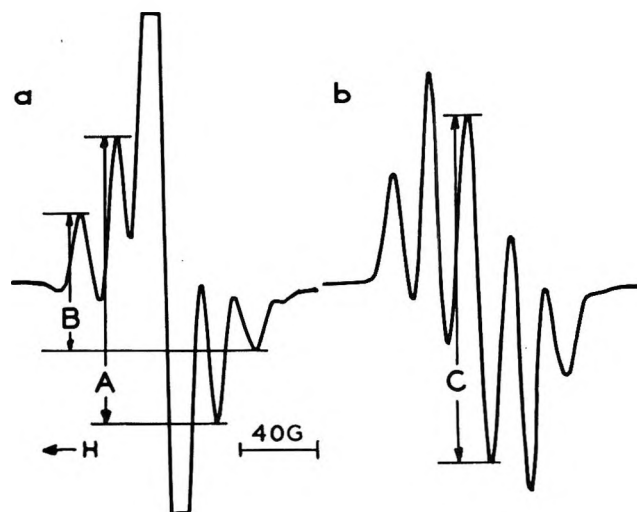
Figure 2. Esr spectra of γ-irradiated C_2H_5OH glass: (a) before photobleaching; (b) after photobleaching at 540 nm. Dose 1.7×10^{20} eV g^{-1}.

Photobleaching at 540 nm reduces the intensity of the central line and increases that of the outer lines (Figure 2b). In the discussion below, the vertical distance "A" from the maximum of peak 2 to the minimum of peak 4 (Figure 2) is used as a measure of the relative concentration of radicals. It remains in constant ratio to B through photobleaching or thermal decay at 77°K.

Electron and Radical Concentrations As a Function of Dose. Figures 3 and 4 show that in both ethanol and isobutyl alcohol glasses the trapped electron concentration passes through a maximum with increasing γ dose and then declines. The optical density at 220 nm grows nearly linearly with dose through the dose range of the maxima of $[e_{tr}^-]$ but less rapidly at higher doses.

(7) M. R. Ronayne, J. P. Guarino, and W. H. Hamill, *J. Amer. Chem. Soc.*, **84**, 4230 (1962).
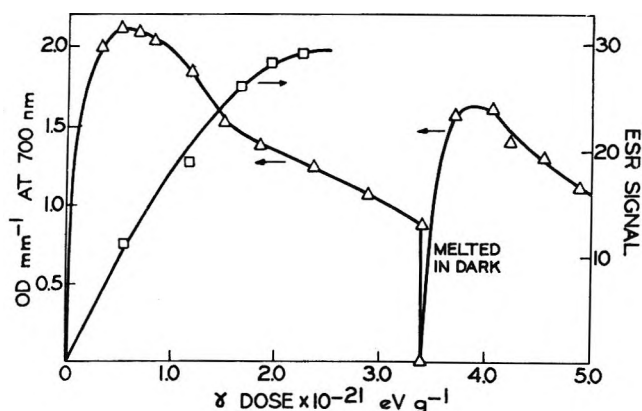
Figure 3. Concentrations of trapped electrons and radicals in C_2H_5OH glass as a function of γ dose at 77°K: $\triangle$, OD at 700 nm due to e_{tr}^-; $\square$, esr signal of CH_3CHOH radicals (measured as "A" of Figure 2).
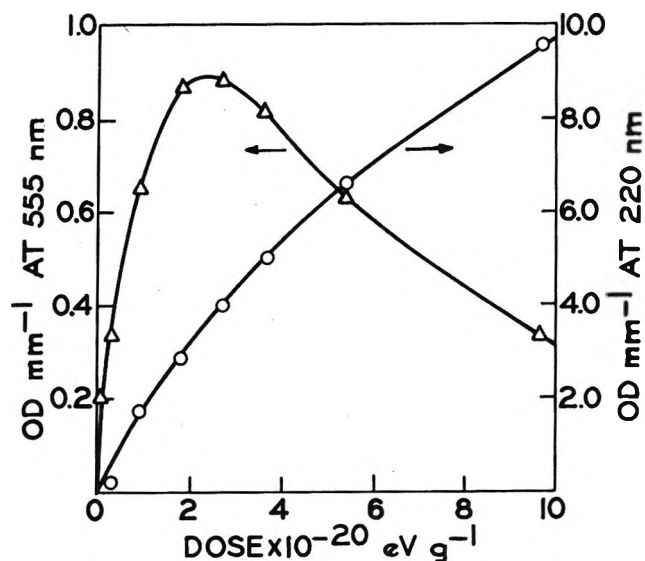
Figure 4. Concentrations of trapped electrons and radicals in i-C_4H_9OH glass as a function of γ dose at 77°K: $\triangle$, OD e_{tr}^- at 555 nm; $\bigcirc$, OD at 220 nm, ascribed in part to radicals (last point on curve estimated from OD at 235 nm).

Figure 5. Effect of thermal decay at 90°K, and of melting, on electron trapping ability of γ-irradiated C_2H_5OH glass at 77°K. The sample was melted and refrozen to 77°K after a dose of 3.3×10^{21} eV g^{-1}.
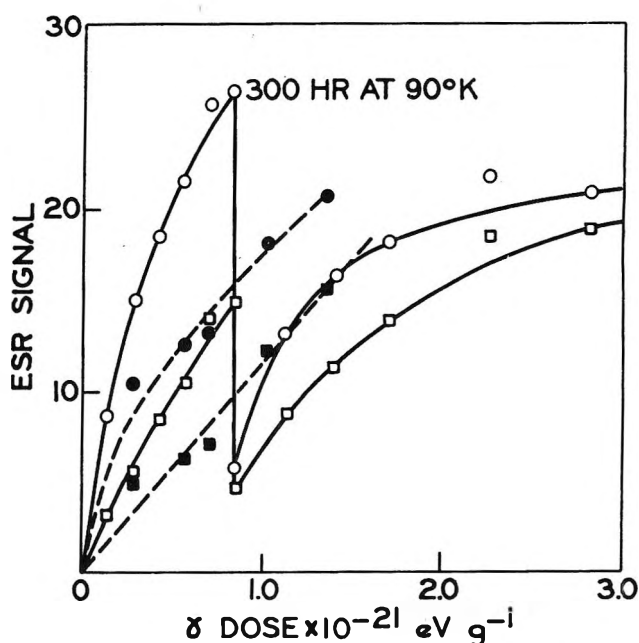
Figure 6. Effects of thermal decay at 90°K and of melting and refreezing to 77°K on growth of esr signals "A" and "C" (Figure 2) with continued γ irradiation: $\bigcirc$, signal C before melting; $\square$, signal A before melting; $\bullet$ and $\blacksquare$, signals C and A after melting following a dose of 3.4×10^{21} eV g^{-1} and recooling to 77°K.

To determine whether removal of e_{tr}^- by thermal decay regenerates the ability of the matrix to trap electrons in samples which have reached the maximum $[e_{tr}^-]$ illustrated in Figure 3, we have $\gamma$-irradiated such a sample following 300 hr at 90°K. Qualitatively the concentration of trapped electrons grows in the same manner after thermal bleaching as before, with a maximum at about the same dose, but the maximum is only about one-third as high (Figure 5).

The maximum electron concentration achieved during irradiation of a sample which has been melted and refrozen following previous irradiation is lower than for an unirradiated sample (curve C, Figure 5). This indicates that stable products of irradiation scavenge electrons, or reduce the electron-trapping ability of the matrix, but the effect is not sufficient to account for the low electron yield following thermal decay without

melting (curve B). Similar evidence from esr data is given in Figure 6. Because the central esr line (C of Figure 2) contains the growing radical signal as well as the electron signal, it does not pass through a maximum at the doses of Figure 6. The decrease in the central esr line during standing at 90°K includes the complete decay of the electron signal as well as a decrease in the esr free-radical signal.

Quantitative comparison of radical concentrations at 90 or 95°K with those at 77°K cannot be made by comparison of the esr signal heights because the esr spectra undergo rapid changes in shape and relative line heights at the higher temperatures. The esr spectrum at 77°K of a sample of γ-irradiated, photobleached ethanol
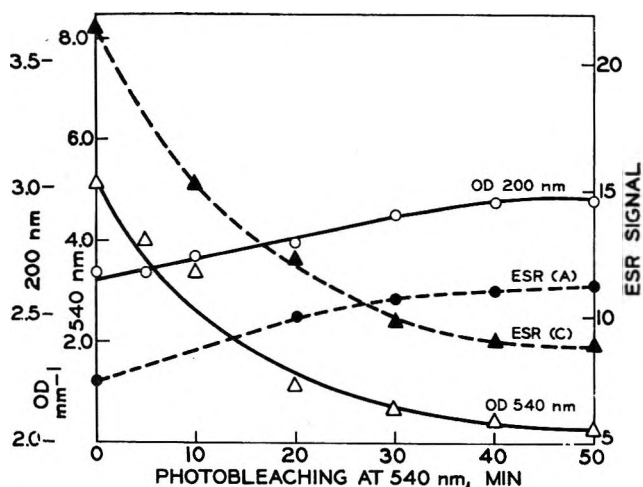
Figure 7. Effect of 540-nm photobleaching of γ-irradiated C_2H_5OH glass at 77°K on OD_{540nm}, OD_{200nm}, esr signal "A," and esr signal "C." Dose 1.7×10^{20} eV g^{-1} in each case.
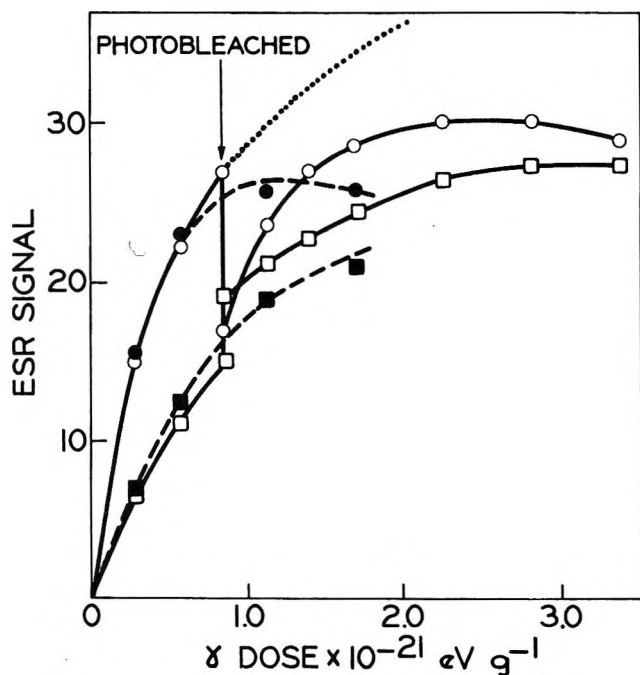
Figure 8. Effects of photobleaching and of melting and refreezing to 77°K on esr signals "A" and "C" of Figure 2: O and □, signals "C" and "A" before melting; ● and ■, signals "C" and "A" after sample which had received 3.4×10^{20} eV g^{-1} was melted and refrozen. Dotted line shows growth in "C" which would have occurred if initial irradiation had not been interrupted by photobleaching.

glass (Figure 2b) changed from a line ratio of ca. 1:3.1: 4.4:3.3:1.5 at 77°K to 1:5.7:15:5.7:1.4 after 16 min at 95°K, with an accompanying severalfold decay in intensity. During an additional 77 min at 95°K the signal decayed by a factor of 5 while the line ratios changed only slightly (1.6.3:17:6.2:1.3). When the sample was then cooled to 77°K, the line ratios changed to 1:3.8:8.5:3.1:1.2, suggesting that the coupling constants of the unpaired electron with the α- and β-hydro-
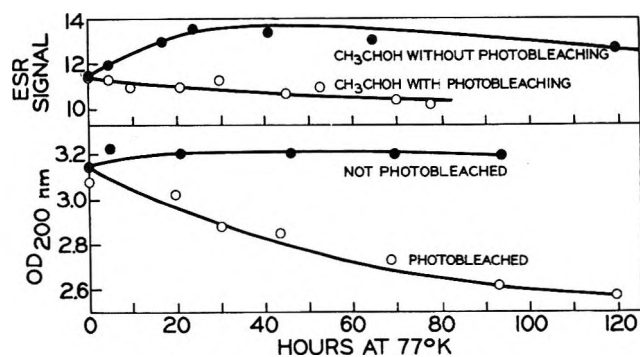
Figure 9. Radical concentration in γ-irradiated C_2H_5OH glass at 77°K as a function of time for samples containing trapped electrons as compared to samples from which the electrons were removed by photobleaching. Dose 1.7×10^{20} eV g^{-1}, except top curve 1.3×10^{20} eV g^{-1}.

gen atoms change as a result of changes in configuration of the radicals with changes in the temperature of the matrix. A similar change with increasing temperature from 77 to 100–105°K has been reported previously.[5b]

Radical Production during Photobleaching and Thermal Decay of Electrons. Consistent with previous investigations,[5,7] we find that the radical concentration in γ-irradiated ethanol at 77°K grows when the trapped electrons are photobleached at 77°K (Figure 7). Assuming that the initial $G(CH_3CHOH)$ is 5.6,[4] the increase in radical concentration as a result of photobleaching as shown by the esr data is $G = 3.1$, a value within experimental error of the reported values of $G(e_{tr}^-)$, which range from 2.3 to 2.9.[4] This confirms the conclusion that radical production by photobleached electrons is efficient. Further evidence on radical production during photobleaching and also on dose effects following photobleaching is given in Figure 8. The fractional increase in radical concentration as a result of the photobleaching illustrated in Figure 8 is less than that for Figure 7 because the γ dose was such that the ratio of e_{tr}^- to radicals was lower.

To evaluate the production of free radicals during thermal decay of trapped electrons, it is necessary to correct for radical decay during electron decay. The upper section of Figure 9 allows comparison of the free-radical esr signal (line A of Figure 2) as a function of time of standing at 77°K for two samples of ethanol glass which had received identical γ irradiation following which one was photobleached to remove all trapped electrons and the other was maintained in the dark. The higher radical concentration of the photobleached sample has been normalized to that of the unbleached sample at $t = 0$. Assuming that the differences in the esr plots for the two samples are experimentally significant, the measurements indicate radical production accompanying electron decay during standing at 77°K. The growth of the radical signal of the unbleached sample to the point of its maximum (35 hr) (corrected for second-order radical decay by reference to the

Figure 10. Comparison of trapped electron spectra in samples of ethanol glass γ-irradiated at 77°K with (B) and without (A) preannealing for 500 hr at 90°K. Dose 8×10^{19} eV g^{-1}.

Figure 11. OD at 540 and 200 nm as a function of time of standing in the dark of samples of ethanol glass γ-irradiated at 77°K with and without preannealing for 500 hr at 90°K. Open points are for annealed samples; closed points for nonannealed samples. Dose 8.1×10^{19} eV g^{-1}; sample thickness 1.17 mm in each case.

bleached sample) is *ca.* 20%. Assuming G(radicals) before bleaching to be 5.6 the increase in G at 35 hr is *ca.* 1 or equivalent to about 35% of the electrons if $G(e_{tr}^-) = 2.9$. The curve for the unbleached sample after 35 hr is consistent with a slower decay of electrons continuing to produce radicals which are also decaying. Experiments at 87, 90, and 95°K also indicat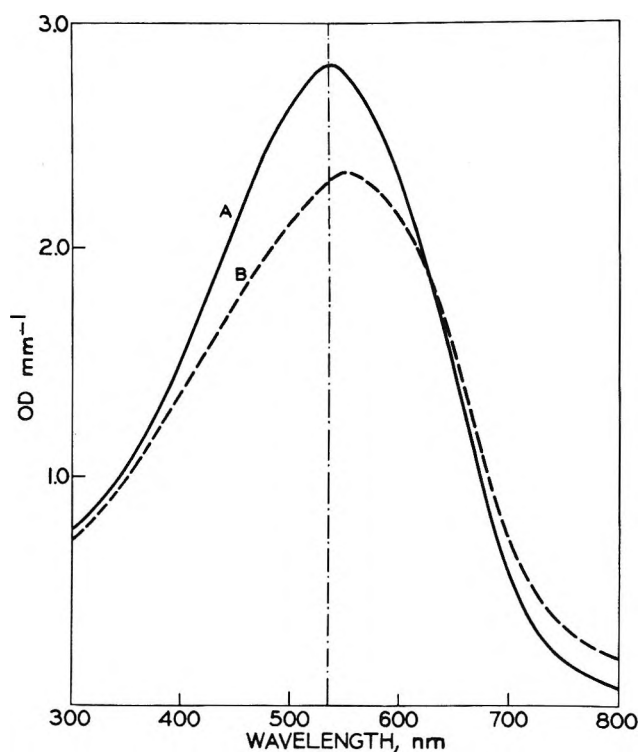e a growth in radical concentration accompanying an initially rapid electron decay followed by a net decrease in radical concentration as the electron decay becomes slower and the rate of radical production becomes less than the rate of decay. The lower portion of Figure 9 shows a significant difference in rate of change of absorption at 200 nm as a function of time for bleached and unbleached samples, but the absorption at 200 nm is clearly due to more than one species, and no quantitative correlations with G(radicals) and $G(e_{tr}^-)$ have been possible.

Effects of Annealing Matrix at 90°K. To determine whether the electron-trapping characteristics of ethanol glass which has been formed by rapid cooling of the liquid to 77°K can be changed by allowing opportunity for molecular relaxation at a higher temperature prior to γ irradiation, we have irradiated such a sample at 77°K after holding it at 90°K for 500 hr. Three differences in trapping properties relative to the unannealed sample were found. (1) The trapped electron spectrum is red-shifted (Figure 10). (2) The trapped electron yield is reduced (Figures 10 and 11). (3) The initial decay on warming the sample to 87°K and the

accompanying increase in absorption at 200 nm are increased (Figure 11).

Thermal Decay of CH_3CHOH Radicals at 95°K. The glassy C_2H_6OH which had been γ irradiated at 77°K to a dose of 1.7×10^{20} eV g^{-1} was photobleached at 77°K with a 200-W Mazda lamp, following which the concentration of radicals (line A of Figure 2) was followed by esr spectroscopy as a function of time at 95°K in the Varian variable temperature device. The decay, as shown in Figure 12, is second order.

Discussion

Spectral Shifts with Bleaching. Previous work has shown that bleaching of the trapped electrons in γ-irradiated ethanol at 77°K with 476-nm light[7] reduces the intensity of the spectrum uniformly, while bleaching at "wavelengths greater than the 540-nm maximum"[8] causes a blue shift. We find nearly uniform bleaching at 540 nm, while both 650-nm bleaching and decay in the dark at 90°K cause a blue shift. These facts imply the presence of traps of different depths which can be selectively depopulated.

Similar evidence for a broad population of traps in ethanol glass comes from pulse radiolysis studies which show an e_{tr}^- spectrum extending into the infrared immediately after the pulse. These weak traps are thermally depopulated within microseconds at 77°K with a

(8) A. K. Pikaev, private communication quoted in ref 2a.
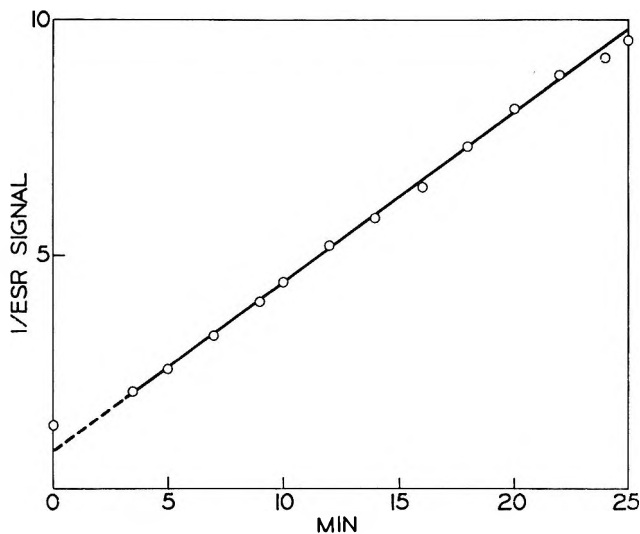
Figure 12. Second-order plot of radical concentration as a function of time at 95°K following γ irradiation of C_2H_5OH glass at 77°K (esr signal "A" of Figure 2). Dose 1.7×10^{20} eV g^{-1}.

concurrent growth in the 540-nm band.[9a] Still other evidence for the presence in the matrix of weaker traps than are normally populated is the irreversible increase in the width of the electron esr singlet when ethanol glass which has been irradiated at 4°K is raised to 77°K.[9b,c]

The results for photobleaching in ethanol are similar to those observed for various alcohol–water mixtures[10] but are in contrast to the uniform thermal decay of the electron spectrum in 3-methylpentane (3MP) observed in our laboratory[11a] and to literature reports of uniform decay in methyltetrahydrofuran (MTHF),[11b] and slight asymmetry of decay in 3MP[11b] and MTHF.[11c] However, other evidence (the change of esr line widths and shifts of λ_{max} with matrix polarity[3a]) indicates that there is not a discontinuous difference in the nature of trapping sites in polar compounds as compared to nonpolar compounds.[3] There is as yet no theory of electron trapping which satisfactorily correlates these and related properties of trapped electrons.[12]

Rise and Fall of $[e_{tr}^-]$ *with Dose.* The trapped electron concentrations in ethanol and isobutyl alcohol glasses pass through maxima at 6×10^{20} and 2×10^{20} eV g^{-1}, respectively (Figures 3 and 4), as compared to 1.4×10^{20}, 1.4×10^{20}, 6×10^{19}, and 1.4×10^{20} eV g^{-1} for 3MP, 3-methyloctane, 3-ethylpentane (3EP), and methylcyclohexane (MCHx), respectively.[2,3a] The optical densities per millimeter at the maxima are 2.1 at 700 nm and *ca.* 8.8 at 535 nm (assuming constant OD_{535}/OD_{700}) for ethanol; 0.9 at 555 nm for isobutyl alcohol; 0.3 at 1600 nm for 3EP; and 0.3 at 1600 nm for MCHx. In both ethanol and isobutyl alcohol the rate of growth of free radicals with dose is approximately linear up to the doses of the maximum of the electron concentration, but decreases thereafter. The pattern of growth and

decrease of the electron concentration and of growth of the radical concentration is consistent with the conclusion that the maximum in electron concentration is reached when the concentrations of trapped positive charge and trapped radicals in the matrix are high enough so that most newly formed electrons are neutralized without trapping, while a small fraction are captured by radicals. The decrease in $[e_{tr}^-]$ after reaching a maximum is then due to a small fraction of the freshly formed positive charges and radicals encountering trapped electrons and reacting with them. These phenomena are similar to those discussed earlier for nonpolar matrices.[2b] The fact that $[e_{tr}^-]_{max}$ occurs at higher doses in the polar than nonpolar matrices is consistent with the conclusion that both electrons and positive charge have a shorter range before trapping in the former than in the latter.

If it is assumed that the molar extinction coefficient of e_{tr}^- in ethanol at 77°K at 535 nm is 1×10^4, it may be estimated that the concentration of electrons at the maximum of the concentration *vs.* dose curve is *ca.* 4 $\times 10^{-4}$ mole fraction, while the concentration of radicals which grow linearly with a $G(R)$ of *ca.* 5.6 is 2.6×10^{-3} mole fraction. The distance between nearest-neighbor electrons if they were uniformly distributed would then be about 15 molecular diameters, and the average distance of a newly formed electron from a previously trapped electron would be about 7 molecular diameters. The average distance of an electron from a cation would be about 7 molecular diameters and from a radical 3 molecular diameters.

Radical Production As a Result of Trapped Electron Decay. The esr signal of CH_3CHOH radicals grows in C_2H_5OH at 77°K when trapped electrons produced by either radiolysis[5] (Figure 7) or deposition of alkali metal[6] are photobleached. Similar growth occurs when trapped electrons produced by deposition of alkali metals decay in the dark.[6] A recent review[4a] indicates that such reaction does not occur during the dark decay of electrons produced by radiolysis, but there is experimental evidence that growth is observed.[5b] The data of Figure 9, obtained in an attempt to resolve these inconsistencies, indicate that radical production does accompany thermal decay of electrons.

(9) (a) J. T. Richards and J. K. Thomas, *J. Chem. Phys.*, **53**, 218 (1970); (b) H. Yoshida and T. Higashimura, *Can. J. Chem.*, **48**, 504 (1970); (c) D. R. Smith and J. J. Pieroni, *ibid.*, **45**, 2724 (1967).

(10) B. G. Ershov, L. E. Makarov, and A. K. Pikaev, *Khim. Vysokikh Energii*, **1**, 472 (1967); *High Energy Chem.*, **1**, 355 (1967).

(11) (a) A. Ekstrom, R. Fass, and J. E. Willard, unpublished; (b) J. B. Gallivan and W. H. Hamill, *J. Chem. Phys.*, **44**, 1279 (1966); (c) P. J. Dyne and O. A. Miller, *Can. J. Chem.*, **43**, 2696 (1965).

(12) (a) Review articles with references dealing with this problem include J. E. Willard, in "Fundamental Processes in Radiation Chemistry," Peter Ausloos, Ed., Wiley, New York, N. Y., 1968, Chapter 9; (b) W. H. Hamill, in "Radical Ions," E. T. Kaiser and L. Kevan, Ed., Wiley, New York, N. Y., 1968, Chapter 9; (c) A. Ekstrom, *Radiat. Res. Rev.*, in press.

Mechanisms suggested[4-6] for radical formation by electron attack in γ-irradiated C_2H_5OH include

$$C_2H_5OH_2^+ + e^- \longrightarrow CH_3CHOH + H_2 \quad (1)$$

$$\left.\begin{array}{l} C_2H_5OH_2^+ + e^- \longrightarrow C_2H_5OH + H^* \\ H^* + C_2H_5OH \longrightarrow CH_3CHOH + H_2 \end{array}\right\} \quad (2)$$

$$2C_2H_5OH + e^- \longrightarrow$$
$$C_2H_5O^- + CH_3CHOH + H_2 \quad (3)$$
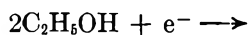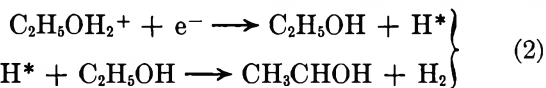
Present information does not allow elimination of any one of these. Since radicals are known to be formed by decay of electrons formed when alkali metals are added to C_2H_5OH glass at 77°K, mechanism 3 must be involved in the radiolyzed glass at concentrations below some minimum level of $[C_2H_5OH_2^+]$.

By contrast with the ethanol glass, no free radicals are formed when trapped electrons in γ-irradiated 3MP are photobleached.[2a]

Effects of Matrix Annealing. The red shift of the spectrum of the trapped electron caused by annealing the matrix before irradiation and the accompanying decrease in electron yield (Figures 10 and 11) are unique as far as we are aware. They indicate that annealing causes a change in the distribution of types of trapping sites and in their average cross section for electron trapping in competition with neutralization or reaction with alcohol molecules. It is not obvious why the relaxation of matrix molecules during annealing should lead to the availability of a greater proportion of relatively weak (large-radius) trapping sites, as implied by the red shift. The relatively rapid decay of the electrons in the annealed sample is qualitatively consistent with the weaker trapping implied by the red shift.

Previous observations of changes in electron-trapping properties with small changes in the matrix include the blue shifts in the spectra of electrons in liquid alcohols with decreasing temperature[13] and with increasing polarity,[14] the blue shift in glassy relative to liquid alcohols and with increasing polarity in solid alcohols,[5a] and the increase in half-life of the trapped electron with increasing sample size (and hence decreasing rate of cooling) in glassy 3MP.[15]

(13) S. Arai and M. C. Sauer, Jr., *J. Chem. Phys.*, **44**, 2297 (1966).

(14) M. C. Sauer, Jr., S. Arai, and L. M. Dorfman, *ibid.*, **42**, 708 (1965).

(15) K. Tsuji and F. Williams, *Int. J. Radiat. Phys. Chem.*, **1**, 383 (1969).

Phenyl and Hydroxyphenyl Radicals. Pulse Radiolysis Study of

Their Spectra and Reactivity

by B. Cercek* and M. Kongshaug[1]

Paterson Laboratories, Christie Hospital and Holt Radium Institute, Manchester 20, England (Received January 5, 1970)

The optical absorption spectra of the phenyl, $C_6H_5\cdot$, and hydroxyphenyl radicals, $HOC_6H_4\cdot$, in aqueous solutions have been obtained. Their spectra resemble those of benzene and phenol in water, but the absorptions are more intense, *e.g.*, the molar extinction coefficients are $\epsilon(C_6H_5\cdot) = 630\ M^{-1}\ cm^{-1}$ at 260 nm and $\epsilon(HOC_6H_4\cdot) = 1950\ M^{-1}\ cm^{-1}$ at 275 nm. The following rate constants have been measured: $k(C_6H_5\cdot + C_6H_5I) = 7 \times 10^1\ M^{-1}\ sec^{-1}$ and $k(HOC_6H_4\cdot + HOC_6H_4Br) = 7 \times 10^7\ M^{-1}\ sec^{-1}$.

Introduction

Within the multitude of organic radicals which have been produced by the technique of pulse radiolysis and their absorption spectra reported there is conspicuous absence of phenyl-type radicals. We now report a pulse radiolysis study in which the optical absorption spectra of the phenyl and hydroxyphenyl radicals were obtained by the dissociative attachment of the hydrated electron, e_{aq}^-, to iodobenzene, C_6H_5I, and to *p*-bromophenol, HOC_6H_4Br, and their reactivity toward the parent compound investigated.

Experimental Section

Irradiation Facilities. A Vickers linear accelerator giving 0.5-μsec pulses of approximately 8-MeV elec-

trons has been used. Doses of about 500 rads per pulse were used. Details of the experimental arrangement have been described before.[2] A grating-type double monochromator has been used to eliminate the distortion of the optical absorption spectra below 270 nm due to scattered light.

Materials. All solutions were prepared using distilled water redistilled from alkaline permanganate. The reagents were used without further purification. Iodobenzene and *p*-bromophenol were Hopkin and Williams Ltd general purpose reagents. The solutions were acidified using Analar grade sulfuric acid. Purification of the reagents (iodobenzene by repeated washing with redistilled water, *p*-bromophenol by repeated recrystallization) did not affect the rate constants for reactions 1 and 2 (discussed in section reactivity of the phenyl radicals).

Dosimetry. The dose given by each pulse was monitored with a secondary emission chamber (SEC). For each set of experiments the SEC was calibrated by means of the $(CNS)_2^-$ absorption at 500 nm in a 10^{-2} M KCNS solution, saturated with oxygen, using the molar extinction coefficient of 7100 M^{-1} cm^{-1} and $G[(CNS)_2^-] = 2.9.$[3]

Analysis. The yields of iodide ions were determined by potentiometric titration using 5×10^{-3} to 2.5×10^{-3} N $AgNO_3$ solutions. A silver indicator and calomel reference electrode were used, and the changes of the potentials were measured using a PYE "Dynacap" pH meter. Its expandable scale allowed accurate readings of 1 mV. Corrections for the blank (unirradiated solutions) were less than 0.2% of the volume of silver nitrate used to titrate an irradiated solution and could therefore be neglected.

We have measured the yields of iodide ions in 2×10^{-4} M deaerated aqueous iodobenzene solution at neutral pH using 0.3 M 2-propanol to scavenge the H and OH radicals. The yield of the halide ions was found to be $G(I^-) = 2.7 \pm 0.1$, corresponding to the yield of the hydrated electron. It has been shown before that the yield of the bromide ions equals the yield of the hydrated electrons.[4,5]

The pH values were measured with a PYE "Dynacap" pH meter using samples of unirradiated solutions directly from the flow system.

Results and Discussion

Absorption Spectra of the Phenyl and Hydroxyphenyl Radicals. The phenyl radicals are produced simultaneously with the products of the reaction of H and OH radicals with the haloaromatic compounds. To separate the spectra of the phenyl and hydroxyphenyl radicals from the H and OH radical products optical absorptions were recorded every 5 nm in 1.4×10^{-4} M iodobenzene and 10^{-4} M *p*-bromophenol solutions about 5 μsec after the end of a 500-rad pulse of radiation under the following conditions. (1) *In deaerated solu-*
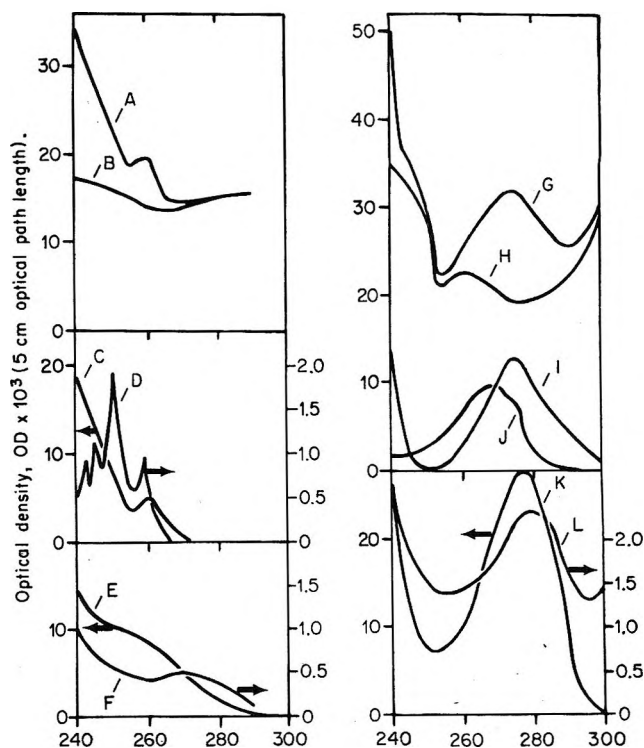
Figure 1. Optical absorption spectra of the species discussed. The arrows refer to the various scales used: ordinate, optical density, $10^3 \times OD$; abscissa, wavelength in nm. A, deaerated 1.4×10^{-4} M iodobenzene, pH 7; 5 μsec after a pulse of 500 rads. B, deaerated and N_2O-saturated 1.4×10^{-4} M iodobenzene, pH 7; 5 μsec after a pulse of 500 rads; normalize to $G(H) = 0.6$ and $G(OH) = 2.7$. C, phenyl radical, pH 7. D, benzene; concentration equal to that of the phenyl radical, pH 7. E, iodobenzene; depletion for $G(-iodobenzene) = 6$ and 500 rads. F, products of the H + C_6H_5I reaction; normalized from $G(H) = 3.3$ to $G(H) = 0.3$ and 500 rads, pH 1. G, deaerated 10^{-4} M *p*-bromophenol, pH 7; 5 μsec after a pulse of 500 rads. H, deaerated and N_2O-saturated 10^{-4} M *p*-bromophenol, pH 7; 5 μsec after a pulse of 500 rads; normalized to $G(H) = 0.6$ and $G(OH) = 2.7$. I, hydroxylphenyl radical, pH 7. J, phenol; concentration equivalent to that of the hydroxyphenyl radical, pH 7. K, *p*-bromophenol; depletion for $G(-p$-bromophenol$) = 6$ and 500 rads. L, products of the H + HOC_6H_4Br reaction, normalized from $G(H) = 3.3$ to $G(H) = 0.3$ and 500 rads.

tions at neutral pH. Spectra were corrected for the depletion of solute, S, assuming $G(-S) = G(e_{aq}^-) + G(OH) + G(H) = 6$. The observed spectra (Figure 1A and G) are the sum of the absorptions due to the phenyl or hydroxyphenyl radicals and the products of the reaction of OH and H radicals with the haloaromatic solutes. (2) *In solutions at pH 1.* Hydrated electrons, e_{aq}^-, were converted into H radicals. Optical

(2) J. P. Keene, *J. Sci. Instrum.*, **41**, 493 (1964).

(3) G. E. Adams, J. W. Boag, J. Currant, and B. D. Michael, "Pulse Radiolysis," M. Ebert, J. P. Keene, A. J. Swallow, and J. H. Baxendale, Ed., Academic Press, New York, N. Y., 1965, p 117.

(4) M. Anbar, F. B. Alfassi, and H. Bregman-Rice, *J. Amer. Chem. Soc.*, **89**, 1263 (1967).

(5) B. Cercek and M. Kongshaug, *J. Phys. Chem.*, **73**, 2056 (1969).

absorptions were recorded in deaerated and oxygen-saturated solutions. Spectra were corrected for the depletion of solute, S, using $G(-S)_{oxic} = 2.9$ and $G(-S)_{anoxic} = 6.5$. Oxygen reacts fast with H radicals $[k(O_2 + H) = 2 \times 10^{10} M^{-1} sec^{-1}]$,[6] but only slowly with both iodohydroxycyclohexadienyl radicals $[k(O_2 + \cdot HOC_6H_5I) = 7 \times 10^6 M^{-1} sec^{-1}]$[7] and the OH addition product of the p-bromophenol $[k(O_2 + \cdot(OH)_2\text{-}C_6H_4Br) = \sim 10^6 M^{-1} sec^{-1}]$.[8] The HO_2 is generally regarded as an unreactive radical which does not react with a variety of organic solutes[9,10] including benzene[11] and only slowly with itself $[k(HO_2 + HO_2) = 6.7 \times 10^5 M^{-1} sec^{-1}]$.[12] Spectra obtained in oxygen-saturated solutions are, therefore, the sum of the spectra of the hydroperoxy radical, HO_2, and of the products of the OH radical reaction; those recorded in anoxic conditions are the sum of the spectra of the products of the H and OH radical reactions. The spectra of the products of the H radical reaction with the iodobenzene and p-bromophenol were obtained by substracting the "oxic" spectrum from the "anoxic" one and adding the spectrum of the HO_2 radical recorded in oxygen-saturated solution at pH 1. The resulting spectra were normalized from $G(H) = 3.3$ to $G(H) = 0.3$, i.e., half of the yield of the H radicals in neutral solutions. They are delineated in Figure 1F and L for iodobenzene and p-bromophenol, respectively. (3) In nitrous oxide, N_2O, saturated solutions at neutral pH. Hydrated electrons, e_{aq}^-, were converted into OH radicals. Spectra were corrected for the depletion of solute assuming $G(-S) = 6$. Under these conditions the yield of OH radicals is twice that in deaerated solutions; the yield of the H radicals is the same as in deaerated solutions, i.e., $G(H) = 0.6$. The sum of the spectra of the products of the H and OH radicals for neutral pH can therefore be obtained by taking half of the absorptions recorded in N_2O-saturated solutions and adding half of the absorptions of the products of the H radicals at neutral pH (Figure 1F or L).

On the basis of these experiments, the spectra of phenyl (Figure 1C) and hydroxyphenyl (Figure 1I) radicals were obtained by subtracting the sum of the absorptions of the H and OH radical products (Figure 1B and H) from the absorptions observed in deaerated solutions at neutral pH (Figure 1A and G).

In the gas phase the absorption bands of the phenyl radical were reported to be in the wavelength region from 430 to 530 nm.[13] In the aqueous phase we could not detect any absorptions of the phenyl radicals in this wavelength region. Our observations, however, do not exclude absorption bands with a molar extinction coefficient of $<50 M^{-1} cm^{-1}$.

It may be of interest to point out that the spectra of the transient products of the H + HOC_6H_4Br (Figure 1L) and of the H + C_6H_5I (Figure 1F) reactions do not correspond to those from the reaction of the hydrated electrons (Figure 1I and C, respectively).

It has been concluded from the steady-state radiolysis results that H atoms debrominate p-bromophenol.[4,5] The different spectra, therefore, suggest that H atoms may debrominate haloaromatic compounds (a) by abstraction of the halide atom by H atoms and/or (b) via a transient product produced by the addition of H atoms to the benzene ring and/or halide atom followed by a reaction yielding halide ions.

Molar Extinction Coefficients. To calculate the molar extinction coefficients of the phenyl, $C_6H_5\cdot$, and hydroxyphenyl, $HOC_6H_4\cdot$, radicals we have assumed that the yields of these radicals equal the yield of the hydrated electron, e_{aq}^-, i.e., $G(C_6H_5\cdot) = G(HOC_6H_4\cdot) = G(e_{aq}^-) = 2.7$. On this basis the molar extinction coefficient of the phenyl radical was found to be 630 $M^{-1} cm^{-1}$ at 260 nm and that of the hydroxyphenyl radical 1950 $M^{-1} cm^{-1}$ at 275 nm; we estimate these values to be accurate to $\pm 20\%$.

Comparison of the Phenyl and Related Benzenoid Absorption Spectra. It may be of interest to compare the absorption spectra cf the phenyl, $C_6H_5\cdot$ (Figure 1C), and hydroxyphenyl, $HOC_6H_4\cdot$ (Figure 1I), radicals with those of the parent aromatic compounds, i.e., benzene, C_6H_6 (Figure 1D) and phenol, HOC_6H_5 (Figure 1J), respectively. The positions of the absorption maxima of the hydroxycyclohexadienyl radicals are related to those of their parent aromatic compounds by a bathochromic shift.[14] It therefore seems likely that the absorption maximum of the phenyl radical at 260 nm is related to the absorption of the benzene centered around the 250-nm band. Our efforts to find a fine structure in the spectrum of the phenyl radical were not successful; the spectral resolution of 3 nm was probably not enough to detect any fine structure in its spectrum. Similarly, the absorption maximum of the hydroxyphenyl radical at 275 nm is related to the absorption of the phenol at 270 nm.

The long wavelength band of benzene and phenol has a low intensity as a consequence of the forbiddenness of the $^1B_{2u} \leftarrow ^1A_{1g}$ transition. The CH bond of benzene is slightly positively polarized in the direction of the hydrogen atom; the removal of an H atom, as in the phenyl radical, results in a small positive charge on the carbon atom.[13] The migration of charge distorts the symmetry, consequently removing some of the

(6) M. Anbar and P. Neta, *Int. J. Appl. Radiat. Isotop.*, **18**, 493 (1967).

(7) B. Cercek, *J. Phys. Chem.*, **72**, 3832 (1968).

(8) B. Cercek and M. Kongshaug, unpublished pulse radiolysis results.

(9) A. O. Allen, "The Radiation Chemistry of Water and Aqueous Solutions," Van Nostrand, Princeton N. J., 1961.

(10) G. Scholes, *Progr. Biophys. Biophys. Chem.*, **13**, 61 (1963).

(11) L. M. Dorfman, I. A. Taub, and R. E. Bühler, *J. Chem. Phys.*, **36**, 3051 (1962).
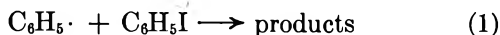
(12) J. Rabani and S. O. Nielsen, *J. Phys. Chem.*, **73**, 3736 (1969).

(13) G. Porter and B. Ward, *Proc. Roy. Soc., Ser. A*, **287**, 457 (1965).

(14) B. Cercek, *J. Phys. Chem.*, **71**, 2354 (1967).

forbiddenness and thus intensifying the absorption. The greater the migration of the charge, the greater the intensification of the optical transition.[15] In agreement we find the absorptions of the phenyl and hydroxyphenyl radicals to be more intense than the absorptions of equal concentration of the benzene and phenol, respectively (compare spectra C and D, I and J in Figure 1). The small intensification of the absorption for the hydroxyphenyl radical suggests only a small distortion of charge relative to phenol.

Reactivity of the Phenyl Radicals. We have converted the hydrated electrons, e_{aq}^-, with nitrous oxide, N_2O, into OH radicals and noticed that the optical absorption at 260 nm in iodobenzene and at 275 nm in *p*-bromophenol solutions decreased about 9% in 200 μsec when doses of 500 rads were delivered. On the other hand, in deaerated solutions of iodobenzene and *p*-bromophenol we observed formation of an absorption; its rate of formation increased with increasing concentrations of the haloaromatic compounds. These observations suggest that the phenyl and hydroxyphenyl radicals react with the iodobenzene and *p*-bromophenol, respectively. To test this hypothesis and to obtain an estimate of the rate constants for reactions 1 and 2, we have assumed that in 10^{-4} M and more concentrated

$$C_6H_5\cdot + C_6H_5I \longrightarrow \text{products} \quad (1)$$

$$HOC_6H_4\cdot + HOC_6H_5Br \longrightarrow \text{products} \quad (2)$$

solutions the phenyl radicals react only with the haloaromatic compounds. Since the decrease in the optical absorption due to the decay of the hydroxycyclohexadienyl radicals was maximally 5% of the total increase in the optical absorption corrections for these effects were neglected. On this basis the observed increase in optical density, $\Delta OD_0(t)$, for a time t, after the pulse, is given by eq I

$$\Delta OD_0(t) = OD_{Ph}(t) + OD_P(t) -$$
$$OD_D(t) - OD_{Ph}(0) = \{P(\infty) - P(t)\}\epsilon_{Ph}l +$$
$$P(t)\epsilon_Pl - P(t)\epsilon_{HA}l - P(\infty)\epsilon_{Ph}l \quad (I)$$

where OD and ϵ denote the optical density and molar extinction coefficient; subscripts Ph, P, D, and HA refer to the phenyl radical, products, solute depletion, and haloaromatic compound, respectively; $P(\infty)$ and $P(t)$ the concentration of product when reaction 1 or 2 is completed and at a time, t, after the pulse; l length of the optical path in centimeters. Substituting $P(\infty)$ and $P(t)$ in the well-known kinetic equation for the pseudo-first-order formation of the product, $\ln\{1 - P(t)/P(\infty)\} = -k[HA]t$, with $P(t) = \Delta OD_0(t)/\{\epsilon_P - \epsilon_{Ph} - \epsilon_{HA}\}l$ and $P(\infty) = \Delta OD_0(\infty)/\{\epsilon_P - \epsilon_{Ph} - \epsilon_{HA}\}l$ derived from eq I, we obtain the following relationship which allows to test our hypothesis, $\ln\{1 - \Delta OD_0(t)/\Delta OD_0(\infty)\} = -k[HA]t$.

We found that the experimental data obeyed this relationship for all concentrations of the haloaromatic compounds studied, *i.e.*, 10^{-4} to 3×10^{-4} M. From the half-lives of the exponential increases of the 260- and 275-nm absorptions after the pulse and the concentrations of the iodobenzene and *p*-bromophenol rate constants k_1 and k_2 were found to be $(7.0 \pm 1.5) \times 10^7$ M^{-1} sec^{-1}.

It has been shown using the technique of esr spectroscopy that phenyl radicals react with aromatic compounds by addition to the benzene ring.[16] It is therefore likely that the products of reactions 1 and 2 are species produced by the addition of the phenyl or hydroxyphenyl radicals to the benzene rings of the iodobenzene or *p*-bromophenol.

(15) H. H. Jaffé and M. Orchin, "Theory and Application of Ultraviolet Spectroscopy," Wiley, London, 1962, p 250.

(16) A. L. J. Beckwith and R. O. C. Norman, *J. Chem. Soc. B*, 403 (1969).

Catalytic Sites for Deuterium Exchange with Benzene over Alumina

by P. C. Saunders[1] and Joe W. Hightower*

Department of Chemical Engineering, Rice University, Houston, Texas 77001 (Received February 13, 1970)

Some of the finer details of the interaction of benzene with the surface of an alumina catalyst have been investigated with the use of deuterium tracers. Exchange of benzene H atoms with D_2 occurred readily at room temperature, but intermolecular redistribution of H and D atoms between C_6H_6 and C_6D_6 occurred at least 10–20 times as rapidly under the same conditions. Both reactions apparently took place on the same sites whose concentration was 6–15×10^{12} sites/cm^2 as determined by CO_2 poisoning. Radioactive $C^{14}O_2$ was used to confirm complete adsorption. Several other compounds (NO, CO, O_2, H_2O, and NH_3) had little poisoning effect on the exchange reaction. The exchange reaction with D_2 exhibited a primary kinetic isotope effect by being faster than C_6D_6–H_2 exchange; the $k_{CH}/k_{CD} = 2$ was attributed to a dissociative exchange mechanism in which CH (or CD) cleavage was rate limiting. Benzene also poisoned the H_2–D_2 equilibration. Speculation about the active sites led to the conclusion that all these exchange reactions perhaps occur on exposed Al^{3+} surface ions.

Introduction

A characterization of the chemical nature of catalytically active sites on alumina has been the object of numerous papers spanning several years. Direct spectroscopic examination of surface functional groups, such as lattice terminating OH groups or Al^{3+} ions, and changes which they undergo during adsorption have led to identification of Lewis acid, Brønsted, electron transfer, and perhaps other sites on alumina. Despite these advances, there remains considerable speculation about which, if any, of these sites are responsible for hydrocarbon catalysis. It is entirely possible that no single type of site is responsible for all reactions and that in some cases different sites must work in coordination to produce the desired catalysis.

For this reason it is important to investigate a range of selected reaction types designed to probe the chemical nature and possibly to determine the concentration of active sites. One such test reaction is the exchange of hydrogen atoms with D_2 under mild conditions. Larson and Hall[2a] studied D_2 exchange with methane, while Pink and coworkers[2b] chose exchange with another paraffin, propane, for their test reaction. Alumina is also an excellent catalyst for exchanging vinyl H atoms in olefins with D_2 without saturation,[3,4] and this technique has been used to prepare relatively pure perdeuterated olefins.[5] The density of active sites was determined for these reactions by selective poisoning techniques.[1,4]

Using D_2 exchange with aromatics as test reactions, McCosh and Kemball[6] found ring H exchange rates over a (probably) χ-alumina sample comparable with the methane rate,[2a] no ring directing effects due to methyl substitution, no multiple exchange, and very slow side group exchange. The purpose of this report is to describe some of the finer details of the exchange of D_2 with benzene[7] carried out over the same γ-, η-alumina catalyst used in the methane[1] and olefin[3-5] reactions.

Experimental Section

Catalyst. The 0.10-g catalyst sample was probably a mixture of γ- and η-alumina prepared from the neutral hydrolysis of very pure aluminum isopropoxide by the MK Research and Development Co. of Pittsburgh, Pa.[8] Its BET-N_2 surface area was 158 m^2/g, and metallic impurities (other than Al) were less than 50 ppm. "Standard pretreatment" included slowly raising the sample temperature under vacuum to 530°, treating it at temperature with 150 Torr O_2 for 1 hr, and evacuating the catalyst for 2 hr to a "sticking" McLeod vacuum. It was then isolated from the vacuum system and cooled to reaction temperature. Both the catalyst and pretreatment are similar to those used in the previous studies.[2a,3-5]

The same catalyst sample was used in all these experiments, the "standard pretreatment" being performed before each experiment. Some irreversible poisoning occurred in the first few reactions, as the exchange activity decreased about 30% between the first and tenth runs starting with a fresh catalyst (see Table I). However, after that the catalyst appeared to be fairly well stabilized, and the initial exchange rates were reproducible to within ±5%.

* To whom all correspondence should be sent.

(1) OCS Training Center, Fort Belvoir, Va.

(2) (a) J. G. Larson and W. K. Hall, *J. Phys. Chem.*, **69**, 3080 (1965); (b) B. D. Flockhart, S. S. Uppal, I. R. Leith, and R. C. Pink, Preprints of Papers from IV International Congress on Catalysis, Moscow, compiled by J. W. Hightower, 1969, p 1429.

(3) J. W. Hightower and W. K. Hall, *J. Catal.*, **13**, 161 (1969).

(4) J. W. Hightower and W. K. Hall, *Trans. Faraday Soc.*, **66**, 477 (1970).

(5) J. G. Larson, J. W. Hightower, and W. K. Hall, *J. Org. Chem.*, **31**, 1225 (1966).

(6) R. McCosh and C. Kemball, *J. Chem. Soc. A*, 1555 (1968).

(7) P. C. Saunders, M.S. Thesis, Rice University, Houston, Texas, 1969.

(8) W. K. Hall and F. E. Lutinski, *J. Catal.*, **2**, 518 (1963).

Table I: Rate Parameters from Isotopic Exchange and Redistribution Reactions over Alumina; Some Poisoning Effects

Run no.	Temp, °C	k_ϕ^a or k_u	M	Poison	Amount poison $\left(\dfrac{\text{molec}}{\text{cm}^2} \times 10^{12}\right)$	k_ϕ^P/k_ϕ or k_u^P/k_u	$t_{1/2}$,[b] mins
				Catalyst aging			
1	20	7.42	1.09				
4	20	6.85	1.07				
5	20	6.61	1.06				
9	20	6.00	1.09				
				C_6H_6–D_2 exchange and poisoning			
11	20	5.32	1.08	CO_2	4.17	0.53	57.2
12	20	5.36	1.06	CO_2	2.63	0.66	56.8
13	20	5.69	1.12	CO_2	5.51	0.44	53.5
14	20	5.23	1.02	CO_2	7.05	0.32	58.2
15	20	5.27	1.09	CO_2	1.46	0.81	57.8
16	20	5.34	1.12	CO_2	8.10	0.24	57.0
17	20	5.42	1.10	CO_2	9.15	0.18	56.2
18	20	5.07	1.10	CO_2	5.52	0.44	60.0
19	20	5.03	1.08	CO_2	11.99	0.06	60.5
20	20	4.99	1.09	CO_2	6.40	0.36	61.0
21	20	5.03	1.09	CO_2	13.20	0.03	60.5
22	20	4.98	1.08	O_2	14.37	0.99	61.4
23	20	4.76	1.05	H_2O	9.02	0.80	64.2
24	20	4.76	1.05	CO	14.77	0.79	63.9
25	20	4.96	1.08	CO	48.92	0.73	61.4
26	20	4.74	1.06	NH_3	14.40	0.88	64.2
27	20	4.96	1.08	NH_3	48.32	0.62	61.4
28	20	5.03	1.05	NO	14.56	0.90	60.5
29	20	5.16	1.06	NO	48.64	0.86	59.0
30	34	6.57	1.04				46.5
31	50	9.13	1.12				33.5
32	10	3.53	1.04				86.6
33	67	13.90	1.14				22.0
				C_6D_6–H_2 exchange			
34	20	2.73	0.99				117.4
35	20	2.75	1.03				116.5
				C_6H_6–C_6D_6 redistribution, poisoning			
36	20	48.7		CO_2			2.9
37	20	41.3		CO_2	10.73	0.13	3.5
38	20	46.9		CO_2	13.20	0.07	3.1
39	20	44.8		CO_2	5.61	0.41	3.2

[a] k_ϕ and k_u represent the number of H (or D) atoms entering 100 molecules per minute.   [b] $t_{1/2}$ is the time required for ϕ or u to reach one-half the equilibrium value.

Reactants. The benzene was 99 + % Fisher B-414 grade which was dried over 5 Å molecular sieves, vacuum distilled, and carefully outgassed before use. Perdeuterated benzene (Merck Sharp and Dohme, Ltd.) was similarly treated and had an isotopic purity of 99.5% D. D_2 gas, which was prepared from Chemical Samples Co. 99.7% D_2O in a Elhygen electrolytic ultrapure deuterium generator, was flowed through a trap thermostated at −195°. Research grade hydrogen was similarly passed through a −195° trap. Helium was purified by diffusion through a quartz thimble manufactured by Electron Technology, Inc.

The gases used as poisons (CO_2, NO, H_2O, NH_3, and

O_2) were outgassed and distilled if condensable or passed through thermostats at −195 or −78°. Radioactive $C^{14}O_2$ was prepared by HNO_3 acidification of Mallinckrodt Nuclear barium carbonate-C-14; concentrated starting material was purified by glpc, outgassed, distilled, and diluted to an appropriate activity level before use.

Equipment. All reactions were carried out in an all-Pyrex recirculation reactor shown in Figure 1. Approximately 85% of the total 354-cc reactor system volume was in the spherical mixing bulb b. In addition to a vertical reactor a, single-action magnetically driven Pyrex pump c (about 300-cc/min capacity), and
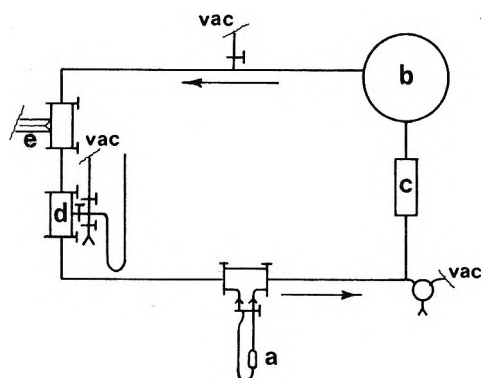
Figure 1. Recirculation system: a, reactor; b, mixing chamber; c, glass pumps; d, poison doser; e, capillary leak to mass spectrometer.

mixing volume, the recirculation loop featured a 1.97-cc bypass doser d located immediately upstream from the catalyst bed. A 2-ft long Kemball-type[9] Pyrex capillary leak e connected the recirculation loop directly to the ion source of the mass spectrometer. This leak was sufficiently small that only 0.3%/hr of a reaction mixture was lost under normal operating conditions (110 Torr in reactor system).

Deuterium analyses were made on an ion-pumped CEC 21-104 mass spectrometer under low-voltage conditions where –H fragmentation was negligibly small (much less than 0.1%). Realtive sensitivities for C_6H_6 and C_6D_6 were measured with a micromanometer and accounted for in the calculations, and the usual C^{13} isotopic impurity corrections were made.

Radioactivity analyses were carried out in a small metal-valve-isolated chamber containing a mercury manometer and separated by a 0.001-in. thick mica window from a gas flow open end Geiger–Muller counter. A Nuclear-Chicago Model 192A Ultrascaler accumulated the pulses for a preset time.

Procedures. After the catalyst had been pretreated, bypassed, and cooled to reaction temperature, a standard benzene–D_2 (10:100 Torr) mixture was thoroughly mixed in the recirculation loop. At time zero the mixture was admitted to the catalyst by manipulation of the two reactor bypass stopcocks, and scans over the mass range from m/e 78 to 85 were taken at regular intervals on the mass spectrometer. In the redistribution experiments, mixtures of 5:5:100 = C_6H_6–C_6D_6–He were used, while the H_2–D_2 equilibrations involved equal amounts of the two reactants whose total pressure was 100 Torr. "Back exchange" reactions made use of C_6D_6–H_2 (10:100 Torr) mixtures.

In the poisoning experiments, a known pressure of the gaseous test compound was first carefully measured into the calibrated doser, and after the reaction rate had become well established (24 min in the exchange experiments and 8 min in the redistribution reactions), the recirculation stream was diverted through the doser, and the poison was carried as a slug directly to the catalyst.

Radioactive CO_2 poison was used as a probe to ascertain whether all the poison was adsorbed on the catalyst. The appearance of radioactivity in the gas phase after $C^{14}O_2$ injection would indicate incomplete adsorption, and specific activity (counts min^{-1} mm^{-1} in counter) measurements of aliquots of the gas phase would determine the fraction of that material adsorbed.

Treatment of Data. The linear Kemball equations[10] were used to describe the course of the exchange reactions, ϕ, of benzene with D_2, and the first-order rate constant k_ϕ is a measure of the number of D atoms entering 100 hydrocarbon molecules per minute. ϕ_∞ represents the statistical equilibrium value of ϕ based on the initial benzene–D_2 ratio (isotope effects[11] were neglected in this treatment). The rate constant for the disappearance of the lightweight material is k_0, and the ratio k_ϕ/k_0 measures the multiplicity, M, of the exchange reaction.

Rate equations for the redistribution reactions are similar to those derived by Bolder, *et al.*[12] An extent of reaction variable, u, was defined as

$$u = \sum_{i=0}^{3} id_i + \sum_{i=4}^{6} (6 - i)d_i$$

where i is the number of D atoms per molecule, and d_i is the fraction of total hydrocarbon atoms which contain i D atoms. The rate constant for the redistribution reaction, k_u, may be determined from the slope of plots of $\ln(u_\infty - u)$ vs. time where u_∞ is the equilibrium (assumed to be a binary distribution) value of u.

The H_2–D_2 rate constant, k_{HD}, was calculated from the slope of $\ln(HD_\infty - HD)$ vs. time plots.

Results

A summary of most of the experimental results is contained in Table I.

C_6H_6–D_2 *Exchange.* After the initial catalyst deactivation (runs 1–10), the activity for C_6H_6–D_2 exchange remained essentially constant ($k_\phi = 5.1 \pm 0.2$ min^{-1}) with a half-time of about 1 hr. In all cases the multiplicity, M, of the reaction was near unity.

CO_2 was an effective poison for this reaction. Whereas the unpoisoned "ϕ plot" remained linear until equilibrium was approached (Figure 2, curve A), addition of CO_2 via the dosing device caused an abrupt break in the curve (Figure 2, curve b) which was followed by a new straight line from which a poisoned rate constant, k_ϕ^p, could be calculated. Figure 3 (curve a) shows the ratio of the rate constants for several runs in which various amounts of CO_2 were added. The titra-

(9) C. Kemball, *Proc. Roy. Soc., Ser. A*, **207**, 539 (1951).

(10) C. Kemball, *Advan. Catal. Relat. Subj.*, **11**, 223 (1957).

(11) E. F. Meyer and C. Kemball, *J. Catal.*, **4**, 711 (1965).

(12) H. Bolder, G. Dallinga, and H. Kloosterziel, *ibid.*, **3**, 312 (1964).
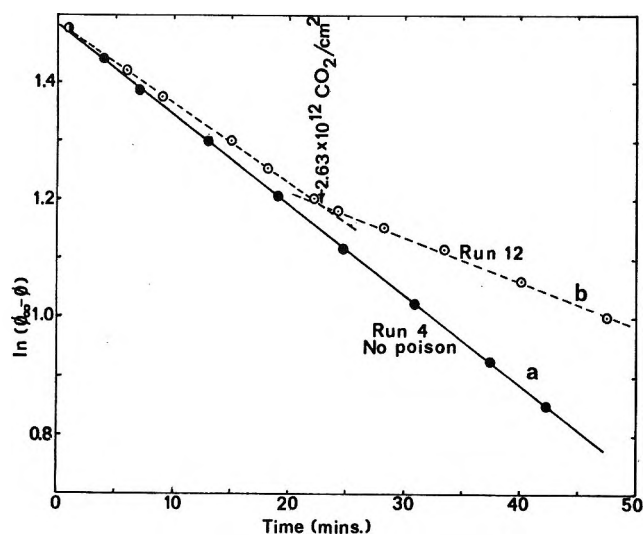
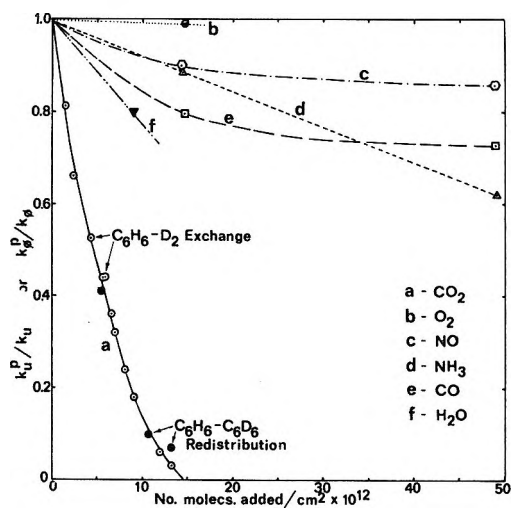Figure 2. Rate curves for $C_6H_6-D_2$ exchange; effect of CO_2 poisoning.

Figure 3. Exchange activity reduction by selected poisons.

tion curve intercept occurs at about 15×10^{12} CO_2 molecules/cm².

None of the other compounds tested was nearly so effective as CO_2 in poisoning the reaction, as indicated by curves b, c, d, e, and f in Figure 3. It is doubtful that a significant fraction of the NO, CO, or O_2 was adsorbed, since mass spectral peaks, although small, were observed for these compounds, and the peak heights were proportional to the poison dose size.

An Arrhenius plot of the rate constants between 10 and 67° (runs 30–33) was linear with an activation energy of 4.3 ± 0.3 kcal/mol.

$C_6D_6-H_2$ Exchange. The reverse exchange reaction, $C_6D_6-H_2$ (runs 34–35), occurred only about half as fast ($k_\phi = 2.74 \pm 0.01$, $t_{1/2}$ = about 2 hr) as did the forward reaction previously described. Again the ϕ plots were linear.

To test for complete adsorption of the CO_2, radioactive $C^{14}O_2$ was used as the poison and the gas phase
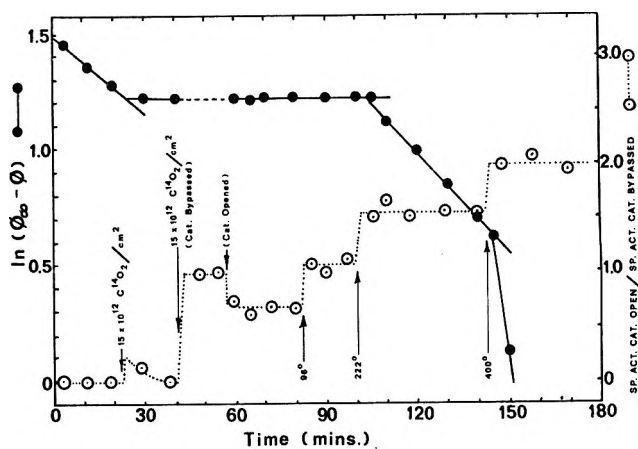
Figure 4. Test for CO_2 adsorption by radioactivity measurements; effect on $C_6H_6-D_2$ exchange rate.

was monitored for radioactivity; the results are shown in Figure 4. At 24 min the "lethal dose" of $C^{14}O_2$, e.g., just enough $C^{14}O_2$ necessary to poison the catalyst completely (note break in ϕ plot), was added via the doser. The first radioactivity measurement at 25 min showed some activity, but after 38 min there was no measurable activity in the gas phase; hence, all the CO_2 was adsorbed. At 42 min the catalyst was bypassed, and a second identical $C^{14}O_2$ poison dose was added. Two measurements (at 47 and 54 min) in the bypassed condition indicated the activity level expected from the first $C^{14}O_2$ dose had there been no adsorption. All activity measurements in Figure 4 are normalized to this value. At 58 min the catalyst was again opened to the recirculation system, and some additional adsorption of $C^{14}O_2$ (about 30% of the second dose) occurred.

Beginning at 83 min, the catalyst temperature was increased rapidly in three separate steps and maintained at the indicated temperature between each jump. At 96° all the $C^{14}O_2$ adsorbed in the second dose and about 12% of the first dose was desorbed. The exchange activity remained poisoned, however, until 50–60% of the adsorbed $C^{14}O_2$ from the first pulse was desorbed at 222°. All the $C^{14}O_2$ was essentially desorbed at 400°, for the specific activity of the gas phase was about double that for a single dose.

$C_6H_6-C_6D_6$ Redistribution. The redistribution of H and D atoms between benzene molecules occurred much more rapidly than did either the $C_6H_6-D_2$ or $C_6D_6-H_2$ exchange reactions. The rate constants were about an order of magnitude greater at 20°, and the times required for half-conversion to equilibrium were $1/20$ as long as that for the $C_6H_6 + D_2$ exchange reaction. CO_2 also poisoned this reaction, and the amount necessary for complete catalyst deactivation (15×10^{12} CO_2 molecules/cm²) was the same as that for the exchange reactions (see solid points, curve a, Figure 3).

H_2-D_2 Equilibration. The rate for H_2-D_2 equilibration was extremely fast as indicated by curve a in Figure
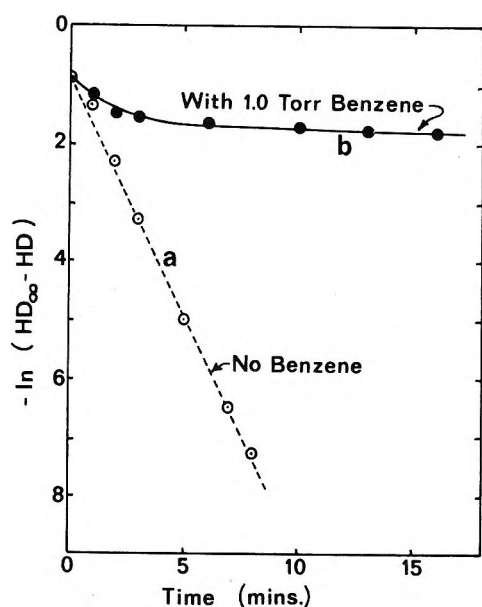
Figure 5. Effect of C_6H_6 on H_2–D_2 equilibration rate.

5. However, when approximately 1 Torr benzene was added to the starting H_2–D_2 mixture, the equilibration reaction was retarded by at least three orders of magnitude (see curve b, Figure 5).

Effect of Deuterated Catalyst. Exchanging the 2 × 10^{14} H atoms/cm^2 intrinsically on the catalyst had no apparent affect on any of the results. The exchange and redistribution rates were identical on both hydrogenated and deuterated catalysts. No exchange between H atoms in the benzene and surface H atoms was observed.

Discussion

These results, coupled with other exchange results[2a,3,4] over an alumina catalyst from the same GA-48 batch which had been treated in an equivalent manner, have clearly demonstrated the ability of alumina to activate CH bonds in hydrocarbons under mild conditions. Furthermore, the catalyst exhibits considerable discrimination between different types of bonds, the order of exchange rates being aromatic ring CH > olefinic vinyl CH[3,4] > paraffinic CH.[2a]

The GA-48 used in these experiments is apparently about two orders of magnitude more active than the catalyst used by McCosh and Kemball,[6] and the activation energy (4.3 kcal/mol) is significantly lower than the value they obtained (6.0 kcal/mol) for the same reaction. Although their absolute activities varied markedly with outgassing temperature, Flockhart, et al.,[2b] found a still higher activation energy (8.7 kcal/mol) for propane exchange with D_2 over a catalyst similar to that used by McCosh and Kemball. These observations illustrate some of the dangers in comparing absolute rate data taken from different catalysts and casts doubt on some of the conclusions drawn by McCosh and Kemball. It appears that rather than hav-

ing the same activation energies, each bond type may have its own unique activation energy with that for aromatic ring being lower than those for olefinic or for paraffinic C–H bonds. While the absolute values may vary from one catalyst to another, the ratio of the activation energies apparently remains about the same in each system. For example, for GA-48 the aromatic ring–paraffinic (methane) ratio is 4.3:5.7 kcal = 0.8, and for the McCosh–Flockhart type catalyst the ratio is 6.0:8.7 kcal = 0.7 for aromatic ring–paraffinic (propane) exchange. Also, the relative exchangeability of the ring H atoms and side group H atoms McCosh and Kemball observed in the alkyl benzenes compares favorably with the relative exchangeabilities of benzene and methane atoms over GA-48 under similar conditions.

All investigators[2–4,6] have observed that the reaction multiplicity, M, is unity and have concluded that the exchange reactions are all stepwise. While this is likely the case, there is another factor which could account for M being one and which could obscure the true nature of the exchange reaction. This factor is the extremely rapid intermolecular redistribution reaction which occurs at a rate 10–20 times as fast as the exchange with D_2. A necessary and sufficient condition for $M = 1$ requires only the maintenance of a statistical equilibrium distribution among all exchangeable positions at all times within the hydrocarbon; this condition was assured by the rapid redistribution reaction regardless of the multiplicity of the initial but slower D_2 exchange reaction. Moreover, this scrambling reaction can also explain the absence of ortho–para-directing effects which McCosh and Kemball[6] did not observe in the ring exchange of alkylbenzenes. The rapid redistribution occurs only among olefinic vinyl[4] and aromatic ring CH bonds; paraffinic CH bonds are not so involved.

The poisoning experiments have supplied considerable information about the concentration and chemical nature of the active sites. Perhaps the most surprising result was the absence of significant poisoning with NO, CO, H_2O, O_2, and NH_3. It is possible that benzene is so strongly adsorbed as to prevent adsorption of these compounds; mass spectral analyses indicated that NO, CO, and O_2 were not adsorbed to an appreciable degree; adsorption of H_2O and NH_3 were not tested. The fact that NO is not a poison does not necessarily rule out the Al^{3+} Lewis acid NO adsorption site, identified by Lunsford[13] using an epr technique, as being operative in these reactions. The site concentration by NO spin density measurements was 4.9 × 10^{12}/cm^2, and Lunsford suggested that they may be the same as the 5.2 × 10^{12}/cm^2 α sites identified by Peri[14] using 1-butene to titrate the adsorbed CO_2 ir spectrum. An-

(13) J. H. Lunsford, *J. Catal.*, **14**, 379 (1969).

(14) J. B. Peri, *J. Phys. Chem.*, **70**, 3168 (1966).

droxyl groups. An important fraction of the hydroxyls are paired, and a distinction is made between "geminal paired," i.e., a pair of hydroxyls on the same silicon atom, and "vicinal pairs" constituted by two hydroxyls located on different but adjacent silicon atoms. The conclusions of Peri were substantiated by considerations on a scale model of a 100 plane of β cristobalite. Assuming that the dehydroxylation is random and that the rearrangements of material during the dehydroxylation are limited to the surface layer, it was shown by a Monte Carlo calculation that a given portion of the hydroxyls must be located in pairs.

Attempts to determine the amount of paired and unpaired hydroxyls, and the relative proportions of geminal and vicinal pairs on the silica gel surface, are mainly based on the reactivity of the surface towards $SiCl_4$, $AlCl_3$, and related compounds. In a study of the silanization of the silica gel surface Snyder and Ward[11] explained their results by assuming the presence of pairs of adjacent hydroxyls, hydrogen-bonded to each other. From the stoichiometry of the hydrolysis of $AlCl_3$ and $SiCl_4$ by surface hydroxyls, Peri and Hensley[10] calculated that after a drying procedure at 400° at least 95% of the hydroxyls are either in geminal or vicinal pairs, while after drying at 600° often more than 85% are still paired. These authors also reconsidered data published by Boehm, et al.,[12] on the reaction between BCl_3 and Aerosil. From these data they calculated that drying at 350° resulted in a surface where 61% of the hydroxyls are still paired. This figure went down to 32% after drying at 550°. Pretreatment of Aerosil at 800° would probably result in a still lower percentage of pairing.

Fripiat and Van Tongelen[13] made an extensive study of the reaction between diborane B_2H_6 and the hydroxyls in silica gel. The reaction mechanism proceeded with the intermediate BH_3 following a stoichiometry 2 OH groups for one B_2H_6 or 1 OH per BH_3. That stoichiometry was generally reached after pretreatments at or above 300°. In these results there is no evidence for the possible existence of geminal paired hydroxyls.

Hertl and Hair[14] made a kinetic study of the hydrolysis of methylchlorosilanes on Cab-O-Sil pretreated at 800°. They concluded that about 60% of the OH's are single, and 40% are in a geminal configuration. Such a severe pretreatment usually yields an ir spectrum with a very narrow OH band at 3750 cm^{-1}. Nevertheless, these authors attempted a decomposition into three components and speculated that a component at 3747 (60% of the total band area) could be due to single OH groups, whereas components at 3751 and 3743 were thought to account for 40% geminal OH groups.

In a recent article, Hertl and Hair[15] described pretreatments destinated to control the content of single and paired hydroxyl groups in Cab-O-Sil. Different gases were adsorbed on these samples and the adsorption isotherms were determined using conventional volumetric and gravimetric techniques. The specific adsorption on the hydroxyl groups was determined from the decrease of the OH band in the ir spectra. It was concluded that nonhydrocarbon gases interact on a 1:2 basis with the hydroxyls in a geminal configuration and on a 1:1 basis with the single hydroxyls. It was estimated that a pretreatment at 800° leaves 1.7 OH/100 Å.[2] The OH distribution is claimed to be 60% geminal paired and 40% single hydroxyls.

From this literature review we conclude that on the surface of thermally treated silica gel, a given percentage of the hydroxyls is probably paired, in "vicinal" or "geminal" configurations, and that the fraction of unpaired hydroxyls increases with the pretreatment temperature. However, there is no systematic agreement on the extent of pairing as a function of the pretreatment temperature. Moreover, the estimations are based on reactions for which the stoichiometry has not been proved unambiguously. Furthermore, the proposed surface structure should allow an explanation, not only of the stoichiometry but also of the mechanism of adsorption reactions, especially for those adsorptions which involve an interaction with the hydroxyl groups.

Investigations of adsorption mechanisms on hydroxyl groups of silica gel generally involve the determination of isosteric heats of adsorption and the observation of $\Delta \nu$, the lowering of the frequency of the OH band in the infrared spectra of silica gels. Numerous works have been devoted to this problem and it is impossible to give an extensive review of that literature here.

Galkin, Kiselev, and Lygin[16] attempted a correlation between $\Delta \nu$ and a quantity ΔQ_a, corresponding to the difference between the heats of adsorption on hydroxylated and dehydroxylated surfaces at a coverage $\theta = 0.5$.

The heat of adsorption of a large series of vapors was determined by Hertl and Hair[17] using an ir spectroscopic technique. At the same time the shift $\Delta \nu$ was recorded. For some compounds the $\Delta \nu$ was found to be related to the ionization potential of the adsorbed molecules. For other compounds a linear relationship between $(\Delta \nu)^{1/2}$ and the heats of adsorption was reported. A fundamental explanation of these relations could not be given. Relations between $\Delta \nu$ and the ionization potential of adsorbed molecules on silica gel were also investigated by Basila.[2] A nonlinear relation was found for a series of methyl-substituted benzenes and for chloromethanes.

(11) L. R. Snyder and J. W. Ward, J. Phys. Chem., **70**, 3941 (1966).

(12) H. P. Boehm, M. Schneider, and F. Arendt, Z. Anorg. Allg. Chem., **320**, 43 (1963).

(13) J. J. Fripiat and M. Van Tongelen, J. Catal., **5**, 158 (1965).

(14) M. L. Hair and W. Hertl, J. Phys. Chem., **73**, 2372 (1969).

(15) W. Hertl and M. L. Hair, ibid., **73**, 4269 (1969).

(16) G. A. Galkin, A. V. Kiselev, and V. I. Lygin, Russ. J. Phys. Chem., **41**, 20 (1967).

(17) W. Hertl and M. L. Hair, J. Phys. Chem., **72**, 4676 (1968).

In this work the heat of adsorption of methyl bromide on a silica gel Aerosil was determined from adsorption isotherms at different temperatures. The isotherms were determined in two ways, following a conventional volumetric procedure, and following a spectroscopic procedure. The heat of adsorption is found to be dependent on the pretreatment conditions and on the coverage. Some conclusions on the structure of the surface will be made. The mechanism of the interaction with the hydroxyls will be discussed and related to the shift in the OH band frequency.

Experimental Section

CH₃Br (Merck p.a.) adsorbed from the gas phase on an Aerosil sample, obtained from the Degussa Co. Its BET area was 238 m²/g. Aliquots of this material were pretreated in a conventional BET high-vacuum system at temperatures of 90, 200, 270, and 500° and evacuated at 10^{-5} to 10^{-6} Torr. CH₃Br adsorption isotherms were determined using a conventional volumetric procedure, and the isosteric heat of adsorption (Q_{vol}) was calculated applying the Clausius–Clapeyron equation.

The same adsorption phenomenon was studied by ir spectroscopy using the technique proposed by Hertl and Hair.[17] This work was performed in a Pyrex cell fitted with CaF₂ windows and very similar to that used by Eberly.[18] The sample, pressed into a thin wafer (≈ 8 mg cm⁻²), could be heated in vacuo to any desired temperature between room temperature and 500° in the spectrometer itself. The temperature of the film was measured by a chromel–alumel thermocouple attached to the stainless steel sample holder. A side arm of the cell was connected to a storage bulb containing CH₃Br, a compensating cell in the reference beam, and a manometer. The pretreatment temperatures were as for the conventional adsorption procedure mentioned above. After cooling to suitable temperatures CH₃Br was adsorbed at increasing pressures. At each adsorption step the spectrum was recorded once between 2000 and 4000 cm⁻¹, and at least 5 times between 3300 and 4000 cm⁻¹. For this Aerosil sample a 3747 cm⁻¹ component is well resolved and the peak height of this component decreased with increasing adsorption of CH₃Br. The decrease of the height of this peak plotted against the CH₃Br pressure was treated as an adsorption isotherm, and the isosteric heat of adsorption, denoted as Q_{ir}, was determined. The peak height was determined with respect to a base line tangent to the spectrum in the region 3400–3700 cm⁻¹. The bond shape of the 3750-cm⁻¹ band is very sharp and does not change during adsorption. For this reason, it was not necessary to use the integrated band area.

Due to the much higher scattering of the experimental points, as compared to the volumetric procedure, the accuracy on Q_{ir} is lower than Q_{vol}. We agree with Hertl and Hair[17] that the accuracy on Q_{ir} is of the order of 1 kcal. Q_{vol} represents the overall adsorption energy

Figure 1. The isosteric heats of adsorption Q_{vol} of CH₃Br on Aerosil as a function of the coverage for different pretreatment temperatures. The broken line at 5.8 kcal represents the heat of liquefaction of CH₃Br.

on the different sites, whereas the Q_{ir} represents only the heat of adsorption on the freely vibrating hydroxyls. Significant changes in the intensity of the broad band of the perturbed hydroxyls could not be determined.

Results

1. *The Heats of Adsorption Q_{vol} and Q_{ir}.* The isosteric heats of adsorption obtained volumetrically (Q_{vol}) are collected in Figure 1 for samples activated by vacuum pretreatments at 90, 200, 320, and 800°. The heat of adsorption depends on the pretreatment conditions and on the coverage. The monolayer coverage in these samples is obtained for an adsorption of ≈ 27 ml g⁻¹ (STP). For the highest pretreatment temperature (800°) the heat of adsorption is lower than 8 kcal mol⁻¹ and tends to the liquefaction energy 5.8 kcal. There is no difference in the heat of adsorption on samples pretreated at 200 and 320°: Q_{vol} decreases from 10 kcal mol⁻¹ at zero coverage to 7.3 at $\theta = 1$. The most pronounced decrease in Q_{vol} is observed for the sample pretreated at 90°: from 18 to ≈ 8 kcal mol⁻¹ at $\theta = 1$. The Q_{vol} values reflect the shape of the isotherms: with increasing pretreatment temperature the isotherms changed gradually from type II to type III (BDDT classification).

In Figure 2 are plotted the values of Q_{ir} as a function of the decrease in peak height of the 3747-cm⁻¹ band. No absolute concentration values can be attributed to the abscissa because the adsorption coefficient of the

(18) P. E. Eberly, Jr., *J. Phys. Chem.*, **71**, 1717 (1967).
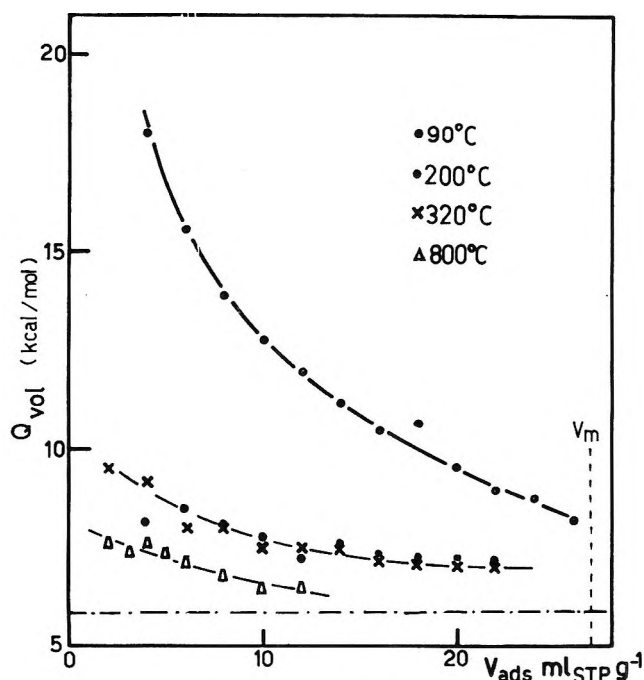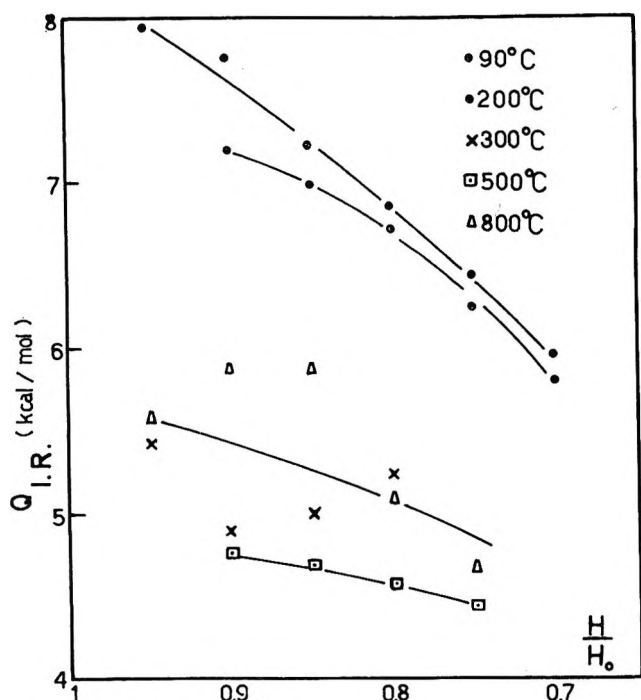
Figure 2. The isosteric heats of adsorption Q_{ir} as a function of coverage for different pretreatment temperatures of the gel. H/H_0 is the ratio of the 3747-cm^{-1} peak height after a particular adsorption to the initial peak height. The broken line at 5.8 kcal represents the heat of liquefaction of CH_3Br.

band was not known. As far as the adsorption coefficient of the OH's does not depend on the temperature of pretreatment, and is independent of the amount of CH_3-Br adsorbed, the abscissa in Figure 2 reflects the degree of coverage of the unperturbed OH groups ($\theta \rightarrow 1$ for $H/H_0 \rightarrow 0$). The maximum pressure that we could realize in the ir cell was 100 mm. Comparison with conventional isotherms indicate that this pressure corresponds to a coverage of less than 0.3. The isotherms determined spectroscopically change from type II to type III almost in the same way as the isotherms determined volumetrically.

A regular decrease of Q_{ir} with coverage is obtained for pretreatments at 90 and 200°, but the Q_{ir} values are systematically lower than Q_{vol}. The difference is especially pronounced for a pretreatment at 90°, but not so important at 200°. The scattering of the results is high for high pretreatments, and values much lower than the liquefaction energy are often obtained.

2. The Frequency Shift $\Delta \nu$ of the 3747-cm^{-1} Band. The free OH groups on silica gel are identified by a sharp ir band generally reported at 3747 cm^{-1}. The perturbed OH groups at the surface or inside the Aerosil globules produce a broad band around 3600 cm^{-1}. Adsorption of CH_3Br caused a decrease in the 3747-cm^{-1} band and the concomitant development of a band at 3627 cm^{-1}. The shift $\Delta \nu$ of 120 cm^{-1} is due to an interaction of adsorbed CH_3Br molecules. $\Delta \nu$ was independent of coverage and pretreatment temperature.

Discussion

A. Nature of the adsorption sites and comparison of Q_{vol} and Q_{ir}. The decrease of both Q_{vol} and Q_{ir} with increasing pretreatment temperatures reflects the modification of the surface of the silica gel. The decrease of both values as a function of the coverage reflects the heterogeneity of the surface.

In principle, three kinds of adsorption sites must be considered: 1, the water molecules. After evacuation at low temperature a given fraction of the surface is still covered with water molecules; 2, the hydroxyl groups. From what is known in the literature we may assume that samples evacuated at moderate temperatures (in our experiments 200–300°) have a surface fully covered with hydroxyls (≈ 4.6 OH/100 Å^2). Further subdivision into paired and unpaired OH groups will be discussed later; 3, a pretreatment at very high temperatures (800°) yields a surface partially covered with hydroxyls (1.4–1.7 OH/100 Å^2) and with siloxane groups resulting from a dehydroxylation.

This differentiation of sites is reflected in the evolution of Q_{vol} (Figure 1) and Q_{ir} (Figure 2) with the pretreatment temperature. At low coverage ($\theta \rightarrow 0$) the difference between Q_{vol} after pretreatments at 90 and 200° suggests that the residual water molecules are the strongest adsorption sites. This is substantiated by the fact that Q_{ir} has the same values for pretreatments at 90 and 200°. The Q_{ir} can only reflect the contribution of the hydroxyls. The difference in Q_{vol} between these pretreatment temperatures must therefore be ascribed to the influence of residual water molecules.

The surface is considered to be fully hydroxylated after the pretreatments at 200 and 320°, and almost free of residual water. For these samples one would expect to find identical values for Q_{vol} and Q_{ir}, but the actual values of Q_{ir} are significantly lower than Q_{vol}. One could invoke the fact that hydrogen-bonded hydroxyls might contribute to the Q_{vol} and account for the difference with Q_{ir}. Our ir spectra gave no evidence that the hydrogen bonded hydroxyls, contributing to a broad band between 3700 and 3000 cm^{-1}, were involved in the reaction, but the intensity and shape of this band are such that small changes could not be detected. We believe that the difference between Q_{ir} and Q_{vol} can be explained in another way and will comment on that point further.

The weakest adsorption sites are the siloxane groups. This is deduced from the fact that for samples pretreated at 800°, Q_{vol} extrapolates to the liquefaction energy. This conclusion is in agreement with the findings of Kiselev[19] following which the nonspecific adsorption on dehydroxylated surfaces produces isosteric heats practically equal to the liquefaction energy. Kiselev[16] has calculated for a great series of gases the difference in the isosteric heat of adsorption ΔQ_A for reac-

(19) A. V. Kiselev, *Quart. Rev. Chem. Soc.*, 15, 116 (1961).

tions on a fully hydroxylated surface and on a dehydroxylated surface, the latter corresponding to the liquefaction energy. That this extra heat reflects the specific interaction with the hydroxyls is substantiated by the fact that these ΔQ_A values could be correlated with the frequency shift $\Delta \nu$ of the hydroxyl band. The comparisons were made at a coverage $\theta = 0.5$. Our data of Q_{vol} at that coverage, taken on the curves for samples pretreated at 200–300° and at 800°, and the observed $\Delta \nu$ (120 cm^{-1}) are in complete agreement with Kiselev's findings.

All these considerations with regard to Q_{vol} make it hard to understand that Q_{ir} can take values lower than the liquefaction energy. Also, the shape of the isotherms (type II) is not in agreement with the low values of Q_{ir}. Moreover, Q_{ir} can only be expected to be equal to Q_{vol} if the adsorption reaction between CH₃Br and the hydroxyls proceeds following a stoichiometry 1:1, or at least if the stoichiometry is constant for all the isotherms used to calculate Q_{ir}. In view of the heterogeneity of the surface, we are not convinced that this condition is satisfied. Further, the procedure used to calculate Q_{ir} assumes that the absorption coefficient of the unreacted hydroxyls is not influenced by the presence of adsorbed molecules on neighboring sites. Because of all these uncertainties in the physical meaning of Q_{ir}, we believe that the variation of Q_{ir} as a function of external factors like pretreatment temperature and coverage may be compared to similar variations in Q_{vol}, but that the absolute values have no obvious meaning. Another reason to avoid a more extensive comparison between Q_{vol} and Q_{ir} is in the rather high inaccuracy on Q_{ir}. Further discussions will therefore be based on the more reliable values of Q_{vol}.

B. The Heterogeneity of the Surface. Paired and Unpaired Hydroxyls. The three curves in Figure 1 indicate that three different types of surfaces are formed by pretreatments at increasing temperatures. As mentioned before, a partially hydrated surface is formed at 90°. The decrease of Q_{vol} with coverage can be understood if at low coverage the most energetic sites are preferentially saturated. It was shown in a previous paragraph that adsorbed water molecules constituted the strongest adsorption sites for H₂O. In the ir spectrum an important component at 3747 cm^{-1} indicates that the surface is not fully covered with adsorbed H₂O. Therefore, the Q_{vol} is supposed to extrapolate to the heat of adsorption on hydroxyl groups for $\theta = 1$ ($V_{ads} \approx 27$ ml g^{-1}). According to Peri's description[9] of the silica gel surface, the OH density at that pretreatment is still very high. The average distance between hydroxyls is such that each CH₃Br can cover statistically two OH groups.

At 200 and 320° no appreciable amount of molecular water is left. The Q_{vol} at $\theta \rightarrow 0$ is almost equal to the values observed for $\theta \rightarrow 1$ on the curve of the sample pretreated at 90°. Therefore it is reasonable to assume

that the most energetic sites after pretreatments above 200° are these sites where two hydroxyls interact with one CH₃Br molecule. The decrease of Q_{vol} with coverage is then understood if we assume that at $\theta \rightarrow 1$, Q_{vol} extrapolates to the heat of adsorption on isolated hydroxyls. Applying the same type of argumentation on the curve obtained on a sample pretreated at 800° we understand that the isolated hydroxyls are covered preferentially and that Q_{vol} tends to the liquefaction energy as the adsorption approaches the monolayer.

This interpretation is in agreement with the present views on the nature of the silica gel surface insofar that we agree that the partially dehydroxylated surface is heterogeneous with respect to the distribution of the hydroxyls. We consider as "paired" the hydroxyls which are at a distance such that they can be covered by one molecule of CH₃Br, and the packing of CH₃Br in this work was 32.4 Å². Our results do not allow a detailed description of the nature of hydroxyl pairs (vicinal or geminal), nor do they allow a calculation of the relative proportions of paired and single hydroxyls. However, considering the shape of the lines in Figure 1, we must conclude that the hydroxyls left at 800° are almost completely isolated, and that at moderate pretreatments (200–300°) the amount of "paired" hydroxyls must be lower than the figures quoted in the literature.[10,14,15]

Taking into account that our Aerosil sample is not necessarily similar to the other gels studied in the literature we are not going to present our data as being in contradiction with the quoted data.[10,14,15] Nevertheless, we wish to make the following remarks. The number of geminal paired hydroxyls[14,15] recently supposed to subsist after pretreatments at elevated temperatures is surprisingly high. These numbers certainly are in agreement with the Monte Carlo treatment as applied by Peri, but it seems to us that a dehydroxylation phenomenon does not necessarily proceed in a random way. Indeed, in geminal paired hydroxyls a simple rotation of one of the hydroxyls around the SiO bond can bring the proton in a suitable position to form a water nucleus with the other OH of the geminal pair. Therefore, geminal pairs could be easier to dehydroxylate than isolated hydroxyls. Furthermore, Peri[10] tries to describe the dehydroxylation by considering only rearrangements restricted to the atoms in the surface layer. It is generally known that dehydroxylation involves sintering and a lowering of the surface area. This suggests that the rearrangements of material during high-temperature dehydroxylations involve more than just the surface of the gel particles.

C. The Mechanism of Interaction between Surface Hydroxyls and Adsorbed Molecules. Hydrogen bonding is generally invoked when the interaction between organic molecules and hydroxyls produces a frequency shift of the OH stretching frequency. Charge transfer[2] was claimed to contribute to the hydrogen bond mecha-

nism. The strength of such an interaction must then be related to the ionization potential I(eV) of the adsorbed molecules. Several authors[2,17,20] could indeed find such relations, and a selection of literature data is collected in Table I. As far as the energy of interaction between

Table I: Selection of Literature Data on $\Delta\nu$ and I (eV) for Several Gases Adsorbed on Silica gel

Gas	$\Delta\nu$	I (eV)	References
(1) Mesitylene	166	8.38	a
	169	8.39	b
(2) Xylene	154	8.45	a
	155	8.45–8.60	c
	156	8.46	b
(3) Toluene	141	8.82	a
	127	8.81	c
	143	8.82	b
(4) Benzene	128	9.25	a
	120	9.1	c
	125	9.23	b
(5) CH_3I	125	9.1	c
(6) CH_3Br	120	10.5	d
(7) CH_3Cl	106	11.28	a
(8) CH_2Cl_2	72	11.35	a
(9) $CHCl_3$	48	11.42	a
	45	11.42	c
(10) CCl_4	40	11.47	a
	45	11.47	c
(11) $(CH_3)_3SiCl$	135	10.07[e]	c
(12) $(CH_3)_2SiCl_2$	90	10.50[e]	c
(13) $(CH_3)SiCl_3$	60	11.17[e]	c
(14) $SiCl_4$	25	11.63[e]	c

[a] See ref 2, Basila. [b] See Kiselev, ref 16 and 20. [c] See ref 17, Hertl and Hair. [d] This paper. [e] These ionization potentials were determined for us by Professors W. C. Price and W. A. Potts.

the surface and the adsorbed molecules is reflected in the frequency shift, correlations between the heat of adsorption and $\Delta\nu$, and between Q and I (eV) may also be expected. Such correlations were indeed reported. Hertl and Hair[17] reported two straight line correlations between Q_{ir} and $(\Delta\nu)^{1/2}$, one relative to compounds with an unpaired electron on p orbitals, the other containing compounds with an unpaired electron in sp^2 and sp^3 orbitals. These correlations were based on a comparison of very different compounds but can be considered to describe a general trend. Kiselev[20] reported a linear relationship between $\Delta\nu$ and Q_{vol}, and between $\Delta\nu$ and I (eV) for a series of methyl substituted benzenes. Basila[2] found nonlinear relations between $\Delta\nu$ and I (eV) for several series of chemical compounds. All these correlations were purely empirical and received no theoretical foundations.

In a critical comparison of the data collected in Table I we found that it is not always possible to fit the data
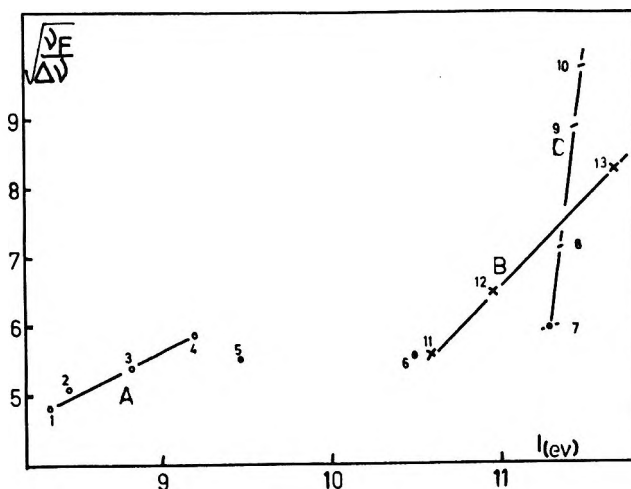
Figure 3. $(\nu_F/\Delta\nu)^{1/2}$ for different homogeneous series of gases adsorbed on silica gel as a function of the ionization potential. For the identity of the points see Table I: A, alkylbenzenes series; B, methylchlorosilanes; C, chloromethanes.

from different sources into the various proposed relations.

A theoretical study of the hydrogen bond, considered as a special case of charge transfer reactions, was made by Puranik and Kumar.[21] The following relation was derived

$$I \text{ (eV)} = \frac{5}{2} \lambda \left(\frac{\nu_F}{\Delta\nu}\right)^{1/2} CS + E + W$$

In this equation C is a constant and ν_F is the original frequency. I (eV) is the ionization potential and S the overlap integral between donor orbital and the molecular orbital of the acceptor molecule. E is the electron affinity of the acceptor molecule, λ is related to the polarity of the acceptor orbital, and W is the net attraction energy between acceptor and donor.

We applied this theory to the literature data in Table I. We are indebted to Professor Price for determining some missing values of ionization potentials which are indicated in Table I. In agreement with this theory a linear relationship between I (eV) and $(\nu_F/\Delta\nu)^{1/2}$ was found in comparisons between compounds with strictly the same donor groups. This relation is shown in Figure 3 for the families of substituted benzenes, chlorosilanes, and chloromethanes. By analogy with the chloromethanes we believe that also for CH_3Br charge transfer is contributing to the adsorption mechanism. The values for CH_3I, CH_3Br, and CH_3I are included in Figure 3, but a direct comparison is not allowed as the donor group is different for the three components. The application of the PK[21] relation to the series of compounds compared by Hertl and Hair did not produce a single relationship.

(20) G. A. Galkin, A. V. Kiselev, and V. I. Lygin, *Trans. Faraday Soc.*, **60**, 431 (1964).

(21) P. G. Puranik and V. Kumar, *Proc. Indian Acad. Sci. Sect. B*, **58**, 29 (1963).

From the straight line behaviors in Figure 3 we may conclude that charge transfer contributes to the interaction between the surface hydroxyls of silica gel and adsorbed organic molecules. The different slopes and intercepts in the same figure further indicate that the entire frequency shift cannot be ascribed to charge transfer. It is indeed generally accepted that hydrogen bonding effects are due both to charge-transfer phenomena and to electrostatic phenomena.

We want to emphasize that it is unlikely to find a single explanation to the mechanism of adsorption on silica gel surfaces. Different mechanisms may contribute to the total energy of adsorptions, the relative importance of which will depend on the specific nature of the adsorbed molecules. The same mechanisms are probably contributing to the $\Delta\nu$ of the OH band. It is not necessary that the contributions of these mechanisms towards the heat of adsorptions and towards $\Delta\nu$ are identical. Attempts to investigate this by comparison between different adsorbed compounds are only valuable if the comparison is made within an homogeneous series of chemical compounds.

The Platinum–Carbon Stretching Frequency for Chemisorbed

Carbon Monoxide

by G. Blyholder* and R. Sheets

Department of Chemistry, University of Arkansas, Fayetteville, Arkansas 72701 (*Received July 13, 1970*)

The infrared spectra of CO chemisorbed on Pt produces bands at 2045, 1815, and 480 cm^{-1}. There has been considerable controversy in the literature about the observation of a band near 480 cm^{-1}. The definiteness of our results is supported by our being able to obtain background spectra before adsorption of CO and the measurement of an isotope shift for the 480-cm^{-1} band which confirms that it is due to the Pt–C stretching motion. In addition, the isotope shifts support a linear Pt–C–O model with the carbon atom attached to the Pt. From changes in the appearance of the evaporated films concurrent with changes in the intensity of the 1815-cm^{-1} band it is suggested that this band is due to CO on highly dispersed Pt. Addition of oxygen produces a band at 560 cm^{-1} which is assigned as a surface oxide.

Introduction

In investigations of the interaction of gases with metal surfaces one of the primary considerations is the determination of the nature of the chemisorption bond to the surface. While a number of techniques give information about the energetics of adsorption, infrared spectroscopy has proven to be a most useful technique for determining the structure of the surface species. While infrared spectroscopy has been quite successful in determining the structure of many complex adsorbed species,[1,2] there have been very few reports of the vibration frequency of the metal-adsorbate bond. Infrared bands for Pt–H,[3] Zn–H,[4] Fe–C,[5] Ni–C,[6] Pt–C,[7–9] and M–O,[10] have been reported.

Considerable controversy and doubt surrounds the reports about stretching frequencies for the Pt–C bond.[11,12] The controversy concerns whether or not it is possible to obtain meaningful infrared spectra in the region of 500 cm^{-1} using silica-supported samples. In those cases where silica-supported samples were not

* To whom correspondence should be addressed.

(1) M. L. Hair, "Infrared Spectroscopy in Surface Chemistry," Marcel Dekker, Inc., New York, N. Y., 1967.

(2) L. H. Little, "Infrared Spectra of Adsorbed Species," Academic Press, New York, N. Y., 1966.

(3) W. A. Pliskin and R. P. Eischens, *Z. Phys. Chem.*, **24**, 11 (1960).

(4) R. P. Eischens, W. A. Pliskin, and M. J. D. Low, *J. Catal.*, **1**, 180 (1962).

(5) G. Blyholder, *J. Chem. Phys.*, **44**, 3134 (1966).

(6) G. Blyholder, Proceedings of the Third International Congress on Catalysis, North Holland, Amsterdam, 1965.

(7) R. P. Eischens and W. A. Pliskin, *Advan. Catal.*, **10**, 1 (1958).

(8) C. W. Garland, R. C. Lord, and P. F. Troiano, *J. Phys. Chem.*, **69**, 1188 (1965).

(9) J. K. A. Clarke, G. M. Farren, and H. E. Rubalcava, *ibid.*, **72**, 327, 2688 (1968).

used the technique was such that no background spectrum could be run, thus leaving open the possibility that the bands reported were due to other species than the Pt–C bond. In no case has the proposed band for the Pt–C frequency been subjected to the test of measuring an isotope shift. We will in fact show that there is a Pt–C stretching frequency where some authors have reported one and that some of the reported bands are due to other species.

Experimental Section

The wide spectral range experimental technique, which has been described in detail elsewhere,[13] consists of evaporating Pt from an electrically heated tungsten filament in an evacuated infrared cell. The metal is deposited in a hydrocarbon oil film on the salt windows of the infrared cell. The gas to be studied is then admitted to the cell and the spectrum of the chemisorbed species is obtained. Spectra are recorded before and after admission of the gas to the cell. Five minutes of pumping has been found sufficient to remove all spectra due to gas phase molecules. For three and four carbon atom molecules, 30 min of pumping may be required to remove molecules dissolved in the oil film. All measurements were taken at room temperature, which is about 25°.

The spectra were obtained using a Perkin-Elmer Model 457 spectrophotometer. This is a grating instrument which scans the region from 4000 to 250 cm^{-1}. No unusual spectrometer settings were used. The CO was passed through an activated charcoal trap cooled with liquid air.

This technique has the advantage that a wide infrared spectral region is available for study. It has the disadvantage that the metal surface is immersed in oil. This oil is apparently only weakly adsorbed since many gases have been found to chemisorb readily on the metal. Essentially, the oil is regarded as a solvent which has weak interactions with the systems of interest. Having a wide spectral range available aids greatly in attempts to determine structure.

Results

The spectral results are recorded in Figures 1 and 2. As shown in curve b of these figures, the result of exposing the sample to 3 Torr of CO for 30 min and then pumping out the gas phase for 2 min produces a strong band at 2045, a medium intensity band at 1815, and a weak band at 480 cm^{-1}. Pumping on the cell for 5 hr leaves the bands at 2045 and 480 cm^{-1} unchanged but gradually (many intermediate spectra were obtained) reduces the intensity of the 1815-cm^{-1} band to the greatly reduced level shown in curve c of Figure 1. During this time the appearance of the metal film changes considerably. Initially the film is light brown in color, the transmission is high, and the background is level. After the 5 hr of pumping the film appeared
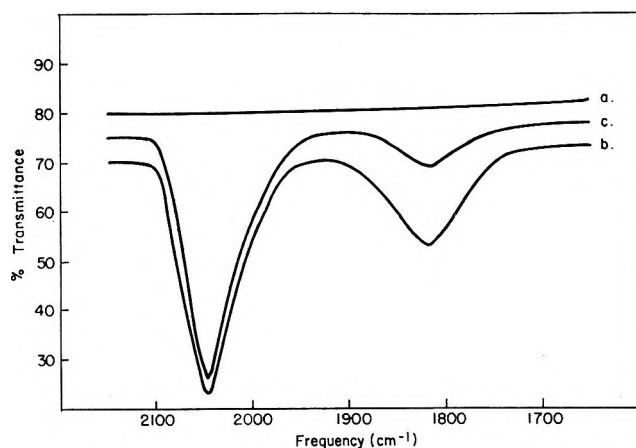
Figure 1. Infrared spectra of CO adsorbed on Pt: curve a, background; curve b, CO added and gas phase pumped out; curve c, after 5 hr of evacuation.
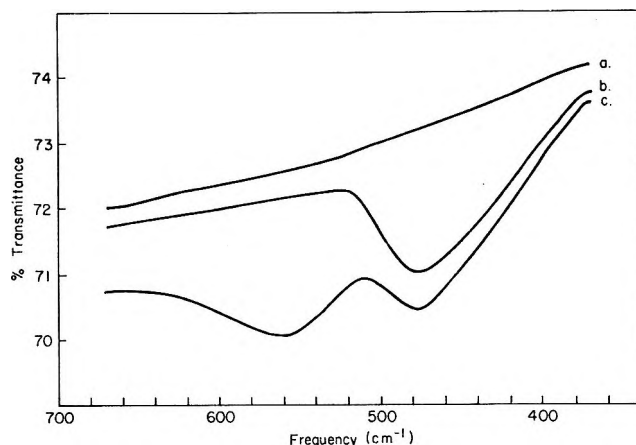
Figure 2. Infrared spectra of CO adsorbed on Pt: curve a, background; curve b, CO added and gas phase evacuated; curve c, after addition of 10 Torr of air for 10 min.

black, the transmission was greatly decreased, and the background sloped toward greater transmission at longer wavelengths.

The introduction of 10 Torr of air to the sample with adsorbed CO followed by 2 min evacuation produces a sample which gives the spectrum shown in curve c of Figure 2. This treatment leaves the bands at 2045, 1815, and 480 cm^{-1} unchanged while producing the new band at 560 cm^{-1}. Subsequent exposure of this sample to an atmosphere of air for 12 hr eliminates all the bands caused by CO adsorption at 2045, 1815, and 480 cm^{-1} except for a small vestage of the 2045-cm^{-1} band but leaves the 560-cm^{-1} band unchanged.

Calculations of the frequency shifts expected from isotopic substitution are presented in Table I. These

(10) G. Blyholder and L. D. Neff, J. Phys. Chem., **70**, 893 (1966); G. Blyholder and L. D. Neff, ibid., **73**, 3494 (1969); G. Blyholder and M. C. Allen, Inorg. Chem., **9**, 302 (1970); G. Blyholder and M. C. Allen, J. Catal., **16**, 189 (1970).

(11) J. F. Ogilvie, J. Phys. Chem., **72**, 2688 (1968).

(12) N. W. Cant and W. K. Hall, ibid., **74**, 1403 (1970).

(13) G. Blyholder, J. Chem. Phys., **36**, 2036 (1962).

Table I: Force Constants (mdyn/Å) and Resulting Frequencies (cm^{-1}) for C^{16}O Adsorbed on Pt Together with Frequency Shifts (cm^{-1}) for Substitution of ^{18}O

Structure	k(C–O)	k(Pt–C)	k(bend)	k(interaction)	V_1	V_2	V_3(band)	ΔV_1	ΔV_2	ΔV_3
Pt–C–O	17.0	1.5	0.2		2082	318	396	47	10	5
Pt–C–O	17.0	1.5	0.3		2082	318	486	47	10	7
Pt–C–O	16.5	2.0	0.3		2063	365	486	46	11	7
Pt–C–O	16.0	3.0	0.3		2054	442	486	44	14	7
Pt–C–O	15.5	3.5	0.3		2035	475	486	42	16	7
Pt–C–O	15.5	4.0	0.3		2046	504	486	41	17	7
Pt–C–O	15.5	3.5	0.3	0.2	2020	478	486	42	16	7
Pt–O–C	17.0	2.0	0.3		2075	368	456	53	10	17
Pt–O–C	17.0	2.5	0.3		2081	411	456	54	12	17
Pt–O–C	17.0	3.0	0.3		2087	449	456	55	13	17

calculations are based on a model of a linear free Pt–C–O system. This type of model has received some formal justification by Grimley.[14] The computer calculations were done with a modified version[15] of a program described Snyder and Schachtschneider.[16] The observed shifts are 45 ± 5 cm^{-1} for the 2045-cm^{-1} band and 13 ± 3 cm^{-1} for the band at 480 cm^{-1}. The values in the table indicate that variation of the force constants over a considerable range and the inclusion of an interaction force constant do not appreciably affect the frequency shifts caused by isotopic substitution.

Discussion

In the C–O stretching region around 2000 cm^{-1} our results are similar to other workers in the appearance of the most intense band above 2000 cm^{-1}. The one different feature of our spectra in this region is the band at 1815 cm^{-1} reaching medium intensity. In their original paper on CO adsorbed on silica-supported metals, Eischens, Pliskin, and Francis[17] reported a very weak band at this position. In a later, more detailed treatment[18] of the C–O stretching region these same authors do not mention any band near 1800 cm^{-1}. Also, Garland, Lord, and Troiano reported[8] a weak band near 1840 cm^{-1} for CO on Pt as well as a strong band at 2053 cm^{-1}.

It has been proposed that a band 100 or 200 wave numbers below 2000 cm^{-1} may be due to CO adsorbed on metal atoms with relatively low coordination numbers.[19] This interpretation fits the known information about the band near 1815 cm^{-1}. Silica-supported samples are heated for long periods during the reduction process so that the metal particles develop a highly crystalline nature with the result that the 1815-cm^{-1} band is very weak. For metal evaporated into a gas as done by Garland, et al., the Pt is less highly crystalline and the 1815-cm^{-1} band a little more intense. For our initial samples evaporated under a vacuum there would be expected to be some Pt metal which is highly dispersed, thus giving a medium-intensity band at 1815 cm^{-1}. The change in appearance and transmission with time of these samples indicates sintering and

crystal growth is occurring, which causes the band at 1815 cm^{-1} to decrease markedly in intensity. When we evaporate Pt into a cell containing He at about 0.5 Torr the 1815-cm^{-1} band is weak.

Based on the facts that we have observed background spectra before admission of CO and that the isotope shift has been observed, this work has established that there really is an infrared band at 480 cm^{-1} for CO adsorbed on Pt. Regardless of the basis for the controversy about the transmission of silica-supported Pt at 500 cm^{-1}, its changes with the admission of gases, and the interference of emitted radiation with transmission observations, there is a band near 480 cm^{-1} as reported.

By analogy to metal carbonyls both bending and stretching vibrations for chemisorbed CO are expected to have frequencies in the 300–600-cm^{-1} region. Therefore, the assignment of a single band in this region as a stretching vibration without further supportive evidence is rather arbitrary. In the only case of CO adsorption on a metal in which the isotope shift has been used to establish assignments, i.e., for CO chemisorbed on Fe, the bending mode is more intense than the stretching mode.[5] However, here comparison of the observed isotope shift given in Table I with the calculated shifts for the stretch and the bend establishes that the 480-cm^{-1} band indeed represents the Pt–C stretching mode. Although there probably was not much doubt, the shift in the C–O stretching frequency confirms that the molecule is attached to the surface via a carbon atom and not an oxygen atom.

A band in the 480-cm^{-1} region was first reported by

(14) T. B. Grimley, *Proc. Phys. Soc., London*, **79**, 1203 (1962).

(15) L. L. Garber, L. B. Sims, and C. H. Brubaker, Jr., *J. Amer. Chem. Soc.*, **90**, 2518 (1968).

(16) R. G. Snyder and J. H. Schachtschneider, *Spectrochim. Acta*, **19**, 117 (1963).

(17) R. P. Eischens, W. A. Pliskin, and S. A. Francis, *J. Chem. Phys.* **22**, 1786 (1954).

(18) R. P. Eischens, S. A. Francis, and W. A. Pliskin, *J. Phys. Chem.*, **60**, 194 (1956).

(19) G. Blyholder, *ibid.*, **68**, 2772 (1964).

Eischens and Pliskin.[7] Their work involved platinum supported in a pressed salt pellet. In addition to bands for CO stretching and the 480-cm^{-1} band, they found bands at 1640 and 655 cm^{-1}. They stated that their method did not exclude air from the sample at all times. The 1640-cm^{-1} band was ascribed to water and the 655-cm^{-1} band at least partially to CO_2. They left the door open to interpreting part of the absorption near 655 cm^{-1} as being due to chemisorbed CO. We find no evidence for infrared absorption in this region which indicates that any band would have to have a quite low intensity. Since they were unable to run a background spectrum there was no way to be sure that the 480-cm^{-1} band was not due to an impurity as, indeed, some of the other bands in their spectrum are.

Garland, Lord, and Troiano,[8] as well as reporting bands at 2053 and 1840 representing C–O stretches, reported bands at 477 and 570 cm^{-1} which they assigned to the Pt–C stretch and the Pt–C–O bend, respectively. Their technique of evaporating the metal into CO gas does not allow a background spectrum to be obtained with the result that bands due to decomposition products and impurities cannot be separated from adsorbed CO spectra. Our results show that the 570-cm^{-1} band is not present when only CO is chemisorbed, indicating that this band is not due to CO. However, this band

does appear when our sample is exposed to oxygen, indicating that it is due to a surface oxide on the Pt. That this should appear in their spectra is not unexpected since exposure of a platinum surface close to the melting temperature for Pt to CO might well be expected to result in cracking of the CO. As the cracking of molecules on hot metal surfaces is a very general catalytic process their procedure would appear to present considerable difficulty in the interpretation of its results.

Since some of the difficulties with different techniques have been discussed, it should be noted that we are aware that our technique is far from being completely satisfactory. Some of its deficiencies have been stated in the section describing the experimental procedure. To summarize, we believe our assignments are correct for the following reasons. (1) We do record background spectra and the bands only appear when CO is added. (2) Treatment with oxygen removes all bands assigned to chemisorbed CO and recovers the original background except for the new absorption around 560 cm^{-1}. (3) The isotope shifts agree with the assignments.

Infrared Spectrum of LiNaF$_2$

by S. J. Cyvin, B. N. Cyvin,

The Technical University of Norway, Trondheim, Norway

and A. Snelson*

IIT Research Institute, Chicago, Illinois 60616 (*Received March 30, 1970*)

The infrared spectra of the vapors over pure NaF and mixtures of NaF + ^{6}LiF and NaF + ^{7}LiF at 900–1000° have been recorded in the spectral region, 4000–190 cm^{-1}, using the matrix isolation technique. Five of the six infrared active frequencies of LiNaF$_2$ have been observed. Assuming C_{2v} symmetry, they are assigned as follows for ^{7}LiNaF$_2$: A$_1$, 660 and 376 cm^{-1}, B$_2$, 589 and 326 cm^{-1}, and B$_1$, 238 cm^{-1}. The results of a normal coordinate analysis on LiNaF$_2$ have been used together with existing ir data to calculate the ir inactive frequencies of planar cyclic Li$_2$F$_2$ and Na$_2$F$_2$.

Introduction

There have been several investigations using the matrix isolation technique of the infrared spectra of the vapor species over lithium fluoride[1] and sodium fluoride[2] at elevated temperatures. The two most important species in both systems are the monomer and planar cyclic dimer. Unfortunately, the spectroscopic selec-

tion rules for the latter allow only three of the six fundamental vibration frequencies to be observed in the infrared, and these data are insufficient to allow a force

constant analysis to be made which might be of use in estimating the Raman active frequencies. Since at the present time there does not appear to be any experimental technique which permits observation of the Raman active frequencies, it was considered worthwhile to investigate the spectrum of the mixed dimer LiNaF₂, which has been identified mass spectroscopically[3] in the vapor over heated mixtures of lithium and sodium fluoride. It is probable that this molecule has a cyclic structure similar to Li₂F₂, in which case all six fundamental vibration frequencies are infrared active, permitting a force constant analysis to be made. These data could then be used as a basis for estimating the infrared inactive frequencies of the pure dimers.

In this paper the results of an investigation on the infrared spectra of the vapor species over mixtures of lithium fluoride and sodium fluoride isolated in neon matrices are presented. For comparison purposes, the spectra of the vapor species over pure lithium fluoride and sodium fluoride in neon matrices were required. Data for the former were available from pervious studies in this laboratory, but for the latter an experimental determination was necessary.

Experimental Section

The matrix isolation cryostat and molecular beam furnace used in the investigation have been described previously.[1] Research grade neon was used as the matrix gas and liquid helium as the refrigerant. Knudsen cells were made of graphite with effusion orifices, 0.037 cm in diameter. In all experiments the ratio of the effusate surface area in the Knudsen cell to the effusion orifice area was approximately 1000:1. Reagent grade sodium fluoride was obtained from Baker and Adamson. ⁶LiF and ⁷LiF was obtained from Oak Ridge National Laboratory with a stated isotopic purity of 99.3% and 99.99%, respectively. Knudsen cell temperatures for both the pure and mixed halide experiments were in the range 900–1000°. Deposition times varied from one to six hours. Matrix gas flow rates were usually about 5 × 10⁻² mol/hr. The spectra were recorded on a Perkin-Elmer 621 spectrophotometer and the reported frequencies are believed accurate to ±1 cm⁻¹.

Results

1. Sodium Fluoride. Eight experiments were performed in which sodium fluoride was vaporized at temperatures between 900 and 1000° and trapped in neon matrices at various dilutions. The spectrum from a typical experiment is shown in Figure 1. Under the best conditions of isolation (highest dilution, longest deposition times) only the peaks shown at a, b, e, g, and h appeared, suggesting that the features at c, d, f, and i result from species formed by agglomeration at lower matrix dilutions. Indeed, the latter four features appeared with a similar intensity as the other absorption
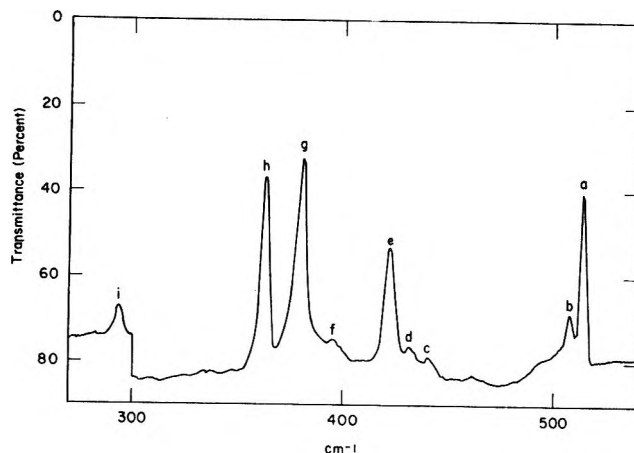
Figure 1. Infrared spectrum of sodium fluoride vapor species in a neon matrix. Deposition time 3 hr at 950°. Matrix dilution approximately 6000:1.

peaks under poor trapping conditions. The weak feature at b did not always occur in the spectrum. Its appearance or nonappearance was not related to changes in matrix dilution in any obvious way. This behavior suggests the presence of some varible impurity in the matrix gas. A similar phenomenon was observed in this laboratory in the matrix isolation spectrum of lithium fluoride.[1]

The spectrum of the sodium fluoride vapor species trapped in a neon matrix is similar to the previously reported spectra in argon, krypton and xenon matrices.[2] The peak a in Figure 1 at 515 cm⁻¹ is assigned to monomeric NaF. The peaks g and h at 380 and 363 cm⁻¹, respectively, are assigned to the two infrared active in-plane vibrations of the dimer Na₂F₂. In the present investigation the far-infrared limit of the spectrometer was 190 cm⁻¹ as opposed to 260 cm⁻¹ in the earlier study. However, no new absorption bands were observed in this region and the infrared active out-of-plane bending frequency of Na₂F₂ is assumed to lie below 190 cm⁻¹.

An assignment for the band at e is difficult. Originally[2] the analogous band in an argon matrix was attributed to a polymer of the type NaₙFₙ with n > 2. Since the original investigation, the existence of a linear dimer Li₂F₂[1,4] has been demonstrated in the lithium fluoride system. The possibility that the band at e be assigned to a linear Na₂F₂ species cannot be excluded. The relative intensity of the band at e under conditions of good isolation with respect to those of the monomer and rhombic dimer suggests that the species responsible for the band is present to the extent of about 10%, assuming equal extinction coefficients for all the species. Mass spectral data for this system[3] put the

(3) R. F. Porter and R. C. Schoonmaker, *J. Chem. Phys.*, **29**, 1070 (1958).

(4) S. Abramowitz, N. Acquista, and I. W. Levin, *J. Res. Nat. Bur. Stand.*, **72A**, 487 (1968).

Figure 2. Infrared spectrum of the vapor species over an equimolar mixture of ^{6}LiF and NaF in a neon matrix. Deposition time, 5 hr at 1000°. Matrix dilution approximately 10,000:1. Absorption bands designated by x and y are due to species containing only pure ^{6}LiF or NaF, respectively.

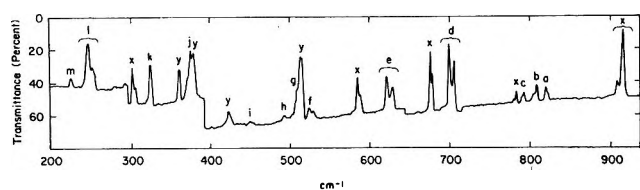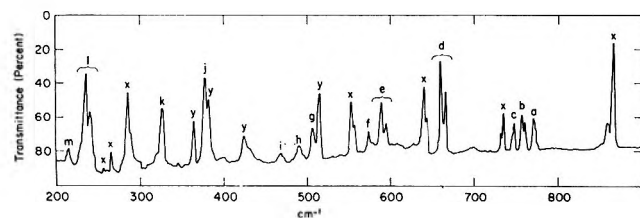Figure 3. Infrared spectrum of the vapor species over an equimolar mixture of ^{7}LiF and NaF in a neon matrix. Deposition time, 6 hr at 1000°. Matrix dilution approximately 7000:1. Absorption bands designated by x and y are due to species containing only pure ^{7}LiF or NaF, respectively.

Table I: Frequencies of Absorption Bands Attributed to ^{6}LiF + NaF and ^{7}LiF + NaF Vapor Species

^{6}LiF + NaF		^{7}LiF + NaF	
Figure designation	Frequency (cm^{-1})	Figure designation	Frequency (cm^{-1})
a	820	a	770
b	808	b	760
			756
c	792	c	747
d	705	d	665
	700		660
e	627	e	595
	621		589
f	529	f	574
	523		
g	508	g	507
h	492	h	490
i	450	i	467
j	377	j	376
k	327	k	326
l	256	l	242
	249		238
m	229	m	217

maximum amount of trimer and tetramer at <1% and gives some support to assigning this band to a linear dimer rather than a higher polymer.

2. Lithium Fluoride and Sodium Fluoride. Eight matrix isolation experiments were performed on equimolar mixtures of ^{6}LiF + NaF and ^{7}LiF + NaF. Matrix dilutions were varied from about 1000:1 to 15,000:1 with deposition times from 1 to 6 hr. Typical spectra for the ^{6}Li and ^{7}Li isotopic species are shown in Figures 2 and 3. Two experiments were performed in which the mole ratios of LiF–NaF were set at 1:2 and 2:1. The resultant spectra were not discernibly different from those in which a 1:1 molar ratio of the fluorides was used except that the intensity of those absorption bands attributed to the pure monomeric or dimeric species of the minor constituent had noticeably lower absorption intensities than when equimolar ratios of the two fluorides were used. Finally, two spectra were obtained of the vapor over a mixture of ^{6}LiF, ^{7}LiF, and NaF in a molar ratio of 1:1:2, respectively. One of these spectra is shown in Figure 3 and it is seen to be essentially a composite of Figures 1 and 2 with the addition of three absorption bands due to the mixed species ^{6}Li^{7}LiF$_2$ and a few other weak features shown at a, d, e, and f. The nonappearance of any new moderately strong absorption bands in these experiments demonstrates that the major vaporizing species consist of monomers and dimers and not higher polymers.

In Table I the frequency of the absorption bands appearing in the spectra of the vapors over ^{6}LiF + NaF and ^{7}LiF + NaF which cannot be assigned to the monomers and dimers of lithium fluoride or sodium

fluoride are listed. On the basis of intensity measurements, pairs of frequencies bracketed together are believed to be the result of matrix splitting of a single fundamental frequency. As might be expected, absorption bands appearing in the ^{6}LiF + NaF spectrum had their counterparts at lower frequencies in the ^{7}LiF + NaF spectrum. One exception to this behavior is the relatively weak doublet at f in the ^{6}LiF + NaF spectrum, which does not appear to have an analog in the ^{7}LiF + NaF system. In the latter system a comparable doublet, if it existed, could be obscured by the intense NaF absorption at y. Another example of this type of behavior occurs for the band at f in the ^{7}LiF + NaF spectrum for which no counterpart is obviously present in the ^{6}LiF + NaF system. Again it is possible that a corresponding band in the ^{6}LiF + NaF spectrum is obscured by the feature at x.

Relative absorption band intensity measurements were used to help assign absorption bands to given molecular species. Fairly large changes in matrix dilutions were used in the various experiments. Prior experience has shown that this can cause small changes in absorption band shape, and it was considered worthwhile to assess the precision that could be expected of the relative intensity measurements which were used in making assignments. To this end relative intensity measurements were made on the known lithium fluoride dimer bands at 676 and 584 cm^{-1} in the ^{6}LiF spectrum. Both these bands exhibit splitting, induced by the matrix environment, having well defined shoulders at 684 and 588 cm^{-1}. The result of the relative intensity measurements from three different spectra for these bands, together with those for species containing ^{6}LiF and NaF, are given in Table II. The standard devia-

Table II: Relative Intensity Measurements for Some of the Absorption Bands Occurring in the Spectrum of the Vapor Species Over a Mixture of LiF and NaF

Frequencies of absorption bands used to derive intensity ratios[a]	Intensity ratios for experiment no.			Standard deviation from the mean ± percentage
	1	2	3	
1. 584/588	1.95	2.16	2.28	4.7
2. 676/684	1.90	2.07	2.30	6.9
3. 676/584	1.94	2.02	2.26	4.8
4. 700/705	1.69	1.84	1.53	5.3
5. 622/627	1.75	1.88	1.61	4.6
6. 249/256	3.55	3.12	3.57	4.4
7. 700/820	6.41	4.78	7.79	13.7
8. 700/808	7.73	4.63	5.76	15.1
9. 700/792	17.5	8.65	10.67	24.3
10. 700/621	2.64	2.54	2.81	3.0
11. 700/523	14.6	7.51	11.6	18.3
12. 700/492	30.9	14.8	32.0	21.4
13. 700/450	32.8	18.2	44.3	23.8
14. 700/327	2.44	2.32	1.97	6.7
15. 700/249	1.34	1.12	1.17	5.8
16. 700/229	10.9	4.63	7.49	23.6
17. 820/808	0.96	0.96	0.74	7.9
18. 820/792	1.20	1.75	1.37	11.1
19. 808/792	2.73	1.69	1.06	26.8

[a] The ratios given in 1, 2, 4, 5, and 6 are for absorption bands which appear to be doublets.

tions listed for the lithium fluoride bands, numbered 1, 2, and 3 in Table II, suggest that intensity ratios for related absorption bands can probably be measured to about ±7% providing no overlapping of absorption bands due to different species occurs. Using this criterion, it appears that the absorption bands numbered 3, 5, 6, 10, 14, and 15 are related. Similar measurements made on the ⁷LiF + NaF system showed a corresponding number of absorption bands to be related. The separation of the maxima in the bands at 705 and 700, 627 and 621, and 256 and 249 cm⁻¹ in the ⁶LiF + NaF spectrum is similar to that in the ⁷LiF + NaF system for the bands at 665 and 660, 595 and 589, and 242 and 238 cm⁻¹. A close similarity in the magnitude of band splitting due to matrix effects has been observed for the three ir active bands of the ⁶Li₂F₂ and ⁷Li₂F₂ cyclic dimers. It appears reasonable to attribute the above pairs of absorption bands in the LiF + NaF spectra to matrix splitting of single fundamental frequencies. This leaves four absorption bands at 700, 621, 327, and 249 cm⁻¹ in the ⁶LiF + NaF spectrum and four in the ⁷LiF + NaF spectrum at 660, 589, 326 and 238 cm⁻¹ which relative intensity measurements suggest are related to the same molecular species in each system.

Further examination of the spectra shown in Figures 2 and 3 shows the presence of an absorption band at j which is partially overlapped by the sodium fluoride dimer band y. By reducing the spectral slit width from

the standard setting of 2.3 cm to 1.2 cm⁻¹, it was possible to resolve these two bands better than is shown in Figures 2 and 3. Although reliable intensity measurements could still not be made on the band at j under these conditions, its intensity was estimated as being at the very least as strong as that of the sodium fluoride dimer band at y.

Finally in Table II, not all possible intensity ratios for all the species which contain NaF + LiF are given. These data have been omitted either because the precision measurement was obviously poor, precluding any possibility of the bands being related, or because the bands were too weak for reliable measurements to be made.

Vibrational Assignment. In the mass spectroscopic investigation of the NaF + LiF system,[3] the most abundant vapor species to be observed were the monomers and dimers, the latter both pure and mixed. Since the structure of the most abundant mixed dimer is not known, a planar cyclic geometry, similar to that in Li₂F₂, was assumed. A mixed dimer of this type has C₂ᵥ symmetry and all six fundamental vibration frequencies are ir active. In the present investigation, four absorption bands in the NaF + LiF system, which intensity measurements showed are related, appeared with similar intensity as the known dimer bands of Li₂F₂ and Na₂F₂, and are assigned to the species LiNaF₂. Relative intensity measurements could not be used to show that the absorption band appearing at j in Figures 2 and 3 was related to any other absorption bands because of its close proximity to a dimer band of Na₂F₂. However, since this band occurs with high intensity, it appears reasonable to assign it to LiNaF₂ also. The result of applying the Teller–Redlich product rule to the five frequencies assigned to the species ⁶LiNaF₂ and ⁷LiNaF₂ is given in Table III. The distribution of the

Table III: The Teller–Redlich Product Rule Applied to the Species ⁶LiNaF₂ and ⁷LiNaF₂

Symmetry species	⁶LiNaF₂	⁷LiNaF₂	Product rule	
			Theoretical	Observed
A₁	700	660		
A₁	377	376	1.072	
A₁				
B₂	621	589		
B₂	327	326	1.064	1.058
B₁	249	238	1.040	1.046

frequencies among the various symmetry species of the C₂ᵥ point group was made to obtain the best fit with the product rule and to yield a consistent set of force constants in the normal coordinate analysis given later. The observed and calculated isotope shifts agree satisfactorily for the B₂ and B₁ modes but cannot be com-

pared for the A_1 frequencies since one of the latter was not observed experimentally. There is some evidence, based on the normal coordinate analysis presented later, that this frequency may be very close to an Na-LiF$_2$ band at about 326 cm^{-1}.

A firm assignment for the absorption bands shown in Figures 2, 3, and 4 resulting from species containing both lithium and sodium fluoride and which cannot be attributed to cyclic LiNaF$_2$ is not possible on the basis of the present data. The features shown at a, b, and c in both Figures 2 and 3 are examples of some of these absorption bands. The absorption bands at x in both spectra, adjacent to the band c, have been assigned to a stretching mode of the linear dimer[4] Li–F–Li–F containing either ^{6}Li or ^{7}Li isotopes. It appears probable that two of the three bands at a, b, and c could arise from linear dimers of the type Li–F–Na–F and Na–F–Li–F each of which might be expected to have an Li–F stretching mode in this region. The possibility of a dimer of the type F–Li–Na–F accounting for one of these three absorption bands is unlikely on thermodynamic grounds. For a molecule of this type of Li–F and Na–F bond energies may reasonably be set at 105 ± 10 and 90 ± 10 kcal, respectively, by comparison with the known bond energies in the lithium fluoride and sodium fluoride monomers and dimers.[5] If this molecule is indeed present in the system in about the same proportion as the linear Li$_2$F$_2$ dimer, an energy of formation of 300 ± 25 kcal is indicated, resulting in a Li–Na bond energy of at least 60 kcal. This compared to the Li–Li and Na–Na bond energies of 26 and 19 kcal, respectively, seems too large. Another possible alternative for the third absorption band might be a trimer containing NaF and LiF. Some evidence in favor of this is the appearance of several new features, shown at a, b, and c in Figure 4, when the vapors over a mixture of ^{6}LiF, ^{7}LiF, and NaF are isolated.

Normal Coordinate Analysis. 1. Lithium Sodium Fluoride. For the purpose of the normal coordinate analysis, LiNaF$_2$ was assumed to have C$_{2v}$ symmetry. The space and internal coordinates are shown in Figure 5. Equilibrium values for the internal coordinates were derived assuming an Li–Na and F–F separation of 2.351 and 2.924 Å, respectively. These values were taken as half the sum of the corresponding distances[6] in the pure dimers Li$_2$F$_2$ and Na$_2$F$_2$. No attempt was made to modify the observed frequencies to take into account matrix frequency shifts, or to make corrections for anharmonic effects. An approximate valence force field, with six force constants corresponding to the potential function $2V = f_r(r_1{}^2 + r_2{}^2) + f_s(s_1{}^2 + s_2{}^2) + R^2 f_\alpha \alpha^2 + S^2 f_\beta \beta^2 + RS f_\gamma (\gamma_1{}^2 + \gamma_2{}^2) + f_x w^2$ was tried in the initial analysis. This function was selected since it permitted some intelligent estimates to be made of the various force constants and had the advantage that some of the force constants were transferable to the dimers Li$_2$F$_2$ and Na$_2$F$_2$. After several trials the
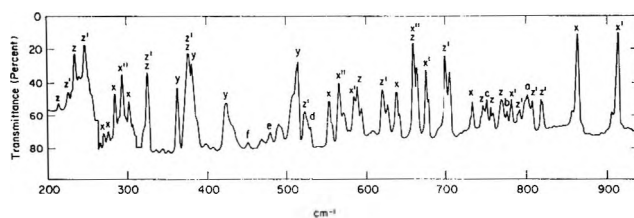
Figure 4. Infrared spectrum of the vapor species over a mixture of ^{6}LiF, ^{7}LiF, and NaF in the molar ratios 1:1:2, respectively. Deposition time, 6 hr at 1030°. Matrix dilution approximately 8000:1. Absorption band designations: x, x′, and x″ species containing ^{7}LiF, ^{6}LiF, and ^{6}LiF + ^{7}LiF, respectively, y, species containing only NaF, z and z′, species containing only NaF + ^{7}LiF and NaF + ^{6}LiF, respectively.
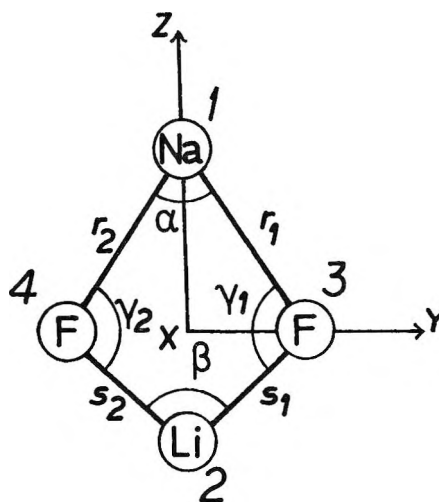
Figure 5. The planar C$_{2v}$ molecular model for LiNaF$_2$. In-plane internal coordinates are indicated. One out-of-plane internal coordinate reads $w = x_1 + x_2 - x_3 - x_4$ in terms of the cartesian displacement. R and S are used to denote the equilibrium Na–F and Li–F distances, respectively.

following values, in mdyne/Å, were found for the force constants: $f_r = 0.53$, $f_s = 0.73$, $f_\alpha = 0.16$, $f_\beta = 0.30$, $f_\gamma = 0.18$, and $f_x = 0.1145$. In Table IV the frequen-

Table IV: Calculated and Observed Frequencies (cm^{-1}) for ^{6}LiNaF$_2$ and ^{7}LiNaF$_2$

| | ^{6}LiNaF$_2$ | | ^{7}LiNaF$_2$ | |
	Calcd	Obsd	Calcd	Obsd
A$_1$	705	700	660	660
A$_1$	376	377	376	376
A$_1$	332		321	
B$_2$	625	621	589	589
B$_2$	327	327	326	326
B$_1$	248	249	238	238

(5) JANAF Thermochemical Tables, The Dow Chemical Co., Midland, Mich.

(6) K. S. Krasnov, V. S. Timoshinin, T. G. Danilova, and S. V. Khandozhko, "Molecular Constants of Inorganic Compounds," Izd. Khimiya, Leningrad, 1968.

cies calculated using these force constants and those observed in the investigation are presented.

For the final analysis a harmonic force field was derived in terms of the following complete set of symmetry coordinates.

$$S_1(A_1) = 2^{-1/2}(r_1 + r_2),$$

$$S_2(A_1) = 2^{-1/2}(s_1 + s_2), \quad S_3(A_1) = R\alpha$$

$$S_1(B_2) = 2^{-1/2}(r_1 - r_2),$$

$$S_2(B_2) = 2^{-1/2}(s_1 - s_2), \quad S(B_1) = w$$

Values for the symmetry force constants were obtained from the valence force constants derived above and then refined to give the best fit to the observed frequencies. The resulting symmetry force constants are given in Table V. They reporduce the observed

Table V: Final Symmetry Force Constants (mdyne/Å) for LiNaF$_2$ (3A$_1$ + B$_1$ + 2B$_2$), Li$_2$F$_2$, and Na$_2$F$_2$ (2A$_g$ + B$_{3g}$ + B$_{3u}$ + B$_{2u}$ + B$_{1u}$)

LiNaF$_2$	1.826			0.1145	0.675	
	-1.450	2.367			0.115	0.812
	1.075	-1.147	1.088			
Li$_2$F$_2$	0.73		0.73	1.752	0.714	0.124
	0.00	0.28				
Na$_2$F$_2$	0.53		0.53	0.987	0.731	0.098
	0.00	0.30				

frequencies of ^{7}LiNaF$_2$, and those of ^{6}LiNaF$_2$ with deviations below 1%. According to the calculation, the experimentally unobserved A$_1$ frequency lies very close to a B$_2$ mode at about 326 cm^{-1}. It is possible that a weak shoulder on the low-frequency side of the B$_2$ mode may be due to the A$_1$ frequency. Although satisfactory agreement between the observed and calculated frequencies has been obtained in the normal coordinate analysis, this cannot be taken as unequivocal evidence in favor of a planar structure for the molecule since it is probable that as good agreement could be obtained with a slightly nonplanar molecular configuration.

2. Lithium Fluoride and Sodium Fluoride Cyclic Dimers. A normal coordinate analysis for these types of molecules, assuming D$_{2h}$ symmetry, has been given elsewhere.[7] The space coordinates were chosen so

that the z and y axes were in the plane of the molecules as in LiNaF$_2$ shown in Figure 5. The ^{7}Li$_2$F$_2$, ^{6}Li$_2$F$_2$ and Na$_2$F$_2$ molecules were analyzed in a similar way to that described above for LiNaF$_2$. The observed infrared active frequencies for ^{7}Li$_2$F$_2$ and ^{6}Li$_2$F$_2$ were obtained from a matrix study[8] and those for Na$_2$F$_2$ from data presented in this paper. Values for f_{LiF} and f_{NaF} were assumed to 0.73 and 0.53 mdyne/Å, respectively, the same as in LiNaF$_2$. In Table V the symmetry force constants corresponding to the symmetry coordinates[7] are given, and the calculated and observed frequencies for the dimers are presented in Table VI.

Table VI: Calculated and Observed Frequencies (cm^{-1}) for ^{6}Li$_2$F$_2$, ^{7}Li$_2$F$_2$, and Na$_2$F$_2$

| | ^{6}Li$_2$F$_2$ | | ^{7}Li$_2$F$_2$ | | Na$_2$F$_2$ | |
	Calcd	Obsd	Calcd	Obsd	Calcd	Obsd
A$_g$	594		551		320	
A$_g$	342		342		287	
B$_{3g}$	559		524		293	
B$_{1u}$	679	678	641	641	380	380
B$_{2u}$	586	585	553	553	363	363
B$_{3u}$	304	303	287	287	178	<190

Since the out-of-plane bending frequency of Na$_2$F$_2$ has not been observed, the force constant for this mode given in Table V was estimated. Two methods were used: (1) the ratio of the stretching mode force constants f_{LiF} and f_{NaF} in the pure cyclic dimers was assumed to be the same as the ratio for the out-of-plane bending mode force constants, and (2) the ratio of the out-of-plane bending force constant for Li$_2$F$_2$ and LiNaF was assumed to be the same as for LiNaF and Na$_2$F$_2$. Values of $f_x = 0.090$ and 0.106 mdynes/Å were obtained, resulting in bending frequencies of 171 and 189 cm^{-1}, respectively. In Tables V and VI the average of these values is given.

(7) S. J. Cyvin, J. Burnvoll, B. N. Cyvin, I. Elvebredd, and G. Hagen, *Mol. Phys.*, **14**, 43 (1968).

(8) A. Snelson, *J. Chem. Phys.*, **46**, 3652 (1967).

Electronic and Electron Spin Resonance Spectroscopic Study of Zinc-Reduced

Di(4-pyridyl) Ketone Methiodides[1a]

by Nicolae Filipescu,[1b] Felix E. Geiger, Charles L. Trichilo, and Fredrick L. Minn

*Department of Chemistry, The George Washington University, Washington, D. C. 20006 and
Goddard Space Flight Center, NASA, Greenbelt, Maryland 20771 (Received July 25, 1970)*

The dimethiodide of the title compound with zinc in degassed acetonitrile formed a stable cation radical whose esr spectrum was fully reconstituted. This radical underwent a slow zero-order subsequent reaction with rate constant $\sim 2 \times 10^{-8}$ mol/(l. hr). The monomethiodide, however, gave a diamagnetic species of the same color which remained stable indefinitely. The mechanism for the reduction is discussed.

The N-methyl iodides I and II of di(4-pyridyl) ketone
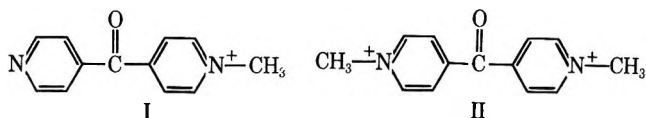
are interesting not only because of their structure and functionality but also because of their striking resemblance to model compounds with known physiological activity.[2] The free radicals derived from compounds I and II are related, for example, to the cationic species obtained from viologens,[3,4] the neutral 1-alkyl-4-carbomethoxypyridinyls,[5] and the paramagnetic anion of di-(4-pyridyl) ketone.[6] Zinc, magnesium, sodium amalgam, and dithionite reduction has been used by Kosower and coworkers[5] to generate free radicals from pyridine derivatives. Here we report the analysis of the electron paramagnetic resonance spectrum of the cation radical obtained on zinc reduction of II and of the uv-visible absorption changes during the reactions of both I and II with the metal in degassed acetonitrile.

Results

Brick-red crystals of dimethiodide II and zinc dust were covered in a closed system with acetonitrile previously degassed by several freeze–thaw cycles under high vacuum. Although compound II is not very soluble in acetonitrile, in the presence of zinc it dissolved to produce a magenta solution which gives the uv-visible absorption shown in Figure 1 (curve 1). The other curves in Figure 1 represent changes in the visible absorption of such a sample in a sealed quartz cell, after the band at λ_{max} 524 nm reached maximum absorbance in curve 1 and no solid II remained. The initially formed compound with λ_{max} at 524 nm changed progressively over several months into a new species with absorption maximum at 480 nm as the solution became red. Whereas the magenta solution was intensely paramagnetic and gave the esr spectrum shown in Figure 2, the red component proved to be diamagnetic. The isosbestic point at 497 nm formed by the curves

reflecting the dark reaction testifies to the absence of consecutive or competitive processes. Both colored species were oxygen sensitive; on admission of air the solution became either brown (from magenta) or gold (from red).

When monomethiodide I and zinc dust were mixed with degassed acetonitrile under vacuum, a magenta of virtually the same color and visible absorption (λ_{max} 523 nm) as that from II was formed. However, this solution did not show the presence of free radicals. Furthermore, the color of the sealed sample remained unchanged indefinitely, to change rapidly to yellow only upon admission of air.

Metal reduction of the parent dipyridyl ketone was not investigated, since the expected species, the corresponding ketyl radical anion, was previously examined.[6,7]

Discussion

The paramagnetic species formed on reduction of dimethiodide II with zinc in acetonitrile is III, a previously unreported radical. Its identity was verified
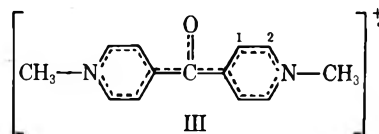
by comparison of electron densities calculated from

(1) (a) Taken in part from work done by C. L. T. for the Ph.D. degree; (b) to whom correspondence should be addressed.

(2) (a) P. Borger, C. C. Black, and A. San Pietro, *Biochemistry*, **6**, 80 (1967); (b) P. Borger and A. San Pietro, *Arch. Biochem. Biophys.*, **120**, 379 (1967); (c) O. Rogne, *Biochem. Pharmacol.*, **16**, 1853 (1967).

(3) C. S. Johnson and H. S. Gutowsky, *J. Chem. Phys.*, **39**, 58 (1963).

(4) A. H. Corwin, R. R. Arellano, and A. B. Chivvis, *Biochim. Biophys. Acta*, **162**, 533 (1968).

(5) (a) E. M. Kosower and E. J. Poziomek, *J. Amer. Chem. Soc.*, **86**, 5515 (1964); (b) E. M. Kosower and J. L. Cotter, *ibid.*, **86**, 5524 (1964); (c) E. M. Kosower and I. Schwager, *ibid.*, **86**, 5528 (1964).

(6) J. C. M. Henning, *J. Chem. Phys.*, **44**, 2139 (1966).

(7) F. L. Minn, C. L. Trichilo, C. R. Hurt, and N. Filipescu, *J. Amer. Chem. Soc.*, **92**, 3600 (1970).
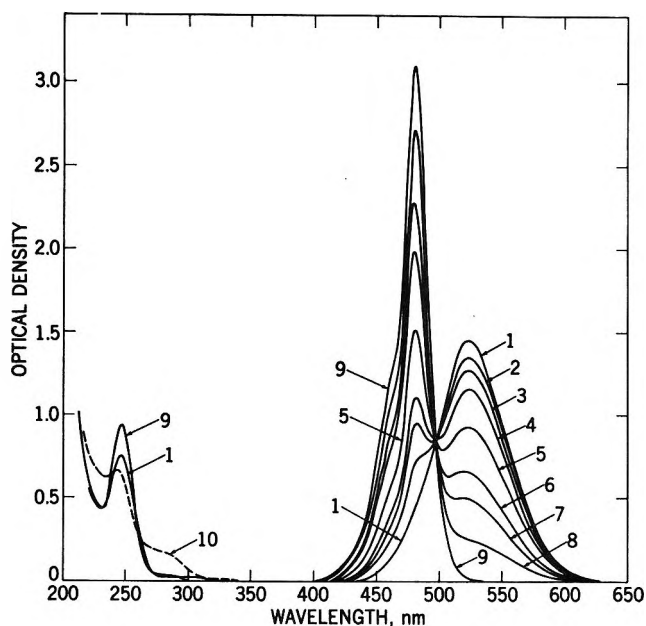
Figure 1. Changes in the uv-visible absorption spectrum of an $\sim 10^{-4}$ M solution of II in degassed acetonitrile in the presence of zinc: 1, after the initial reaction of II with Zn was complete; 2-9, spectra after 364, 603, 874, 1684, 2451, 2607, 3284, and 3837 hr, respectively, in the dark at 298°K following complete reaction of II (numerous intermediate curves were omitted for clarity); 10, after admission of air.

Figure 2. Experimental and simulated esr spectra of di(4-pyridyl) ketone dimethiodide monocation radical III.

Hückel[8] and the more refined McLachlan[9] MO's with those derived from the interpreted esr spectrum shown in Figure 2. The hyperfine splitting constants were found to be $a_H^1 = 0.743 \pm 0.005$, $a_H^2 = 0.629 \pm 0.005$, $a_N = 2.63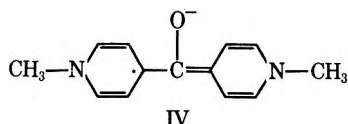4 \pm 0.020$, and $a_{CH_3} = 2.514 \pm 0.020$ Oe. The excellent accuracy of these values was derived from fits with numerous computer simulations. Figure 2 also displays a computer-reconstructed[10] spectrum using these hfs constants, a Lorentzian line shape, and a line width of 65 mOe. Our HMO calculation for molecule III used $\alpha_N = \alpha_C + h\beta$, $\alpha_{C3} = \alpha_C + 0.1h\beta$ for the carbon atoms adjacent to the nitrogens,[3] $\alpha_O = \alpha_C + 2\beta$, $\alpha_{CO} = \alpha_C + 0.3\beta$ for the carbonyl carbon, $\beta_{CN} = \beta_{CC} = \beta$, and $\beta_{CO} = 1.41\ \beta$.[8] A plot of π spin densities ρ^π calculated at the C_1, C_2, and N sites for different values of the parameter h gave reasonable agreement with experimental values around $h = 1.4$, a value comparable to that used for the viologen radicals.[3] Such plots also tended to verify the monocation nature of the radical, since other possibilities, species that may form either upon further reduction of III or upon fission of the molecule, give unacceptable correlation with experimental ρ^π values. For example, a reasonable possibility that had to be removed was anion radical IV, which

$$CH_3-N\overset{\cdot}{\underset{\underset{IV}{}}{\bigcirc}}C\overset{\underset{O^-}{||}}{\bigcirc}N-CH_3$$

could be produced by three-electron reduction of dicat-

ion II. In this case the two types of aromatic hydrogens are theoretically expected to have widely different splitting constants within the range $0.5 \leq h \leq 1.5$; this contradicts experimental findings.

From the spectral changes shown in Figure 1 we were able to examine the kinetics of the reaction in which radical III was slowly converted into a diamagnetic red product. Plots of the reciprocal of the absorbance and the logarithm of the absorbance vs. time gave curves far from straight lines. This ruled out both second- and first-order reaction in free radical, respectively. On the other hand, the graph of optical density vs. time was a nearly perfect straight line, which indicates that the radical-disappearance reaction is zero order with rate constant $\sim 2 \times 10^{-8}$ mol/(l. hr). Since virtually all zero-order transformations are heterogeneous, that is, surface reactions, the value of the rate constant may depend on the condition of the zinc surface. There are only three obvious reactions of III that may occur at the zinc–liquid interface to generate a diamagnetic product, namely, further reduction, disproportionation, or dimerization. Because dimerization is not expected to take place preferentially on the metal surface and disproportionation is essentially equivalent to the III

(8) As suggested, for example, by A. Streitwieser, Jr., "Molecular Orbital Theory for Organic Chemists," Wiley, New York, N. Y., 1961, Chapter 5.

(9) A. D. McLachlan, Mol. Phys., 3, 233 (1960).

(10) Modifications to a program by A. Inzaghi and L. Mongini, European Atomic Energy Commission—Euratom, Report EUR-4064e, 1968.

→ V one-electron reduction, the latter is the most probable pathway. Enolic zwitterion V is expected to be
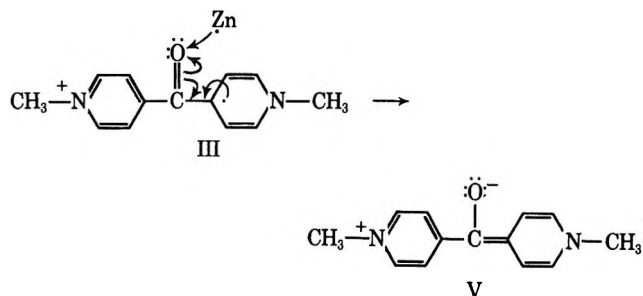
oxygen sensitive and visible absorbing, as observed.

The magenta diamagnetic species formed from the monomethiodide I with zinc is very probably the anion VI formed by the disproportionation of a neutral radi-

cal intermediate VII. This latter species, unlike the charged radical III from dimethiodide II, is expected to be too short-lived for detection by our methods. Elementary MO theory predicts, as observed, that radical
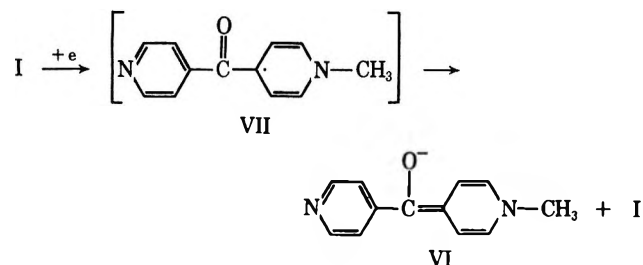
cation III and anion VI should have similar electronic spectra.

Experimental Section

Di(4-pyridyl) ketone and its methiodides were prepared by methods described previously.[7] Degassed solutions in spectrograde acetonitrile (Eastman) were prepared by repeated freeze–thaw cycles under vacuum in either silica absorption cells[11] or 2-mm i.d. esr tubes provided with side reservoirs and constrictions for flame sealing. Degassing was carried out with the solvent in the side bulb and the solids in the sample compartment; they were mixed only after oxygen removal was complete. Uv-visible absorption spectra were recorded on Cary spectrophotometer Model 15 in double-beam mode. Esr spectra were recorded on a modified Varian V-4502 spectrometer with 100-kHz modulation. The microwave bridge of the spectrometer consisted of a circulator in the sample arm and a precision attenuator and phase shifter in the bucking arm. Computer simulations were carried out on an IBM 360/91 computer and drawn by the Cal-Comp Associates plotter; other calculations were performed on an IBM 360/50 computer.

(11) N. Filipescu and F. L. Minn, *J. Chem. Soc.*, B, 84 (1969).

Intensities of the Optical Absorption Spectra of Octahedral

Complexes of the Transition Metal Ions[1]

by A. S. Chakravarty

Saha Institute of Nuclear Physics, Calcutta-9, India, and Mellon Institute, Pittsburgh, Pennsylvania 15213
(Received June 2, 1970)

An attempt has been made to explain the visible absorption bands of the octahedral complexes of the transition metal ions making use of the vibronic interaction mechanism. This work is an extension of the earlier work done by Liehr and Ballhausen. In calculating the oscillator strengths of the electric dipole transitions for the kd^n systems, we have utilized the odd vibrations of the ligands which is responsible for a mixing of some 4p character with the kd^n wave functions of the central metal ion. The necessary integrals have been computed using (1) the hydrogenic, (2) the Slater, and (3) the Richardson-Watson SCF wave functions. The expressions for oscillator strengths involve $f_{d \to p}$, the mean oscillator strength of an ordinary d → p transition. Since it is difficult to obtain it experimentally, we have made a theoretical estimate of it using different amounts of charge delocalization (*i.e.*, covalency). Finally, the oscillator strengths of a few transitions in $3d^n$ hydrated octahedral complexes of the transition metal ions have been estimated assuming 10% charge delocalization, as an example. The agreement between the theory and experiment is good. Lastly, the possible sources of error in the vibronic model have been discussed.

1. Introduction

The origin of the optical absorption spectra of the octahedral complexes of the transition metal ions is not yet completely understood, though it is now generally conceded that the visible absorption bands of such inorganic complexes are vibronically allowed electric dipole transitions among the various kd^n electronic configurations[2a] ($k = 3, 4, 5$). Since at the present time quite a large amount of experimental data on the optical absorption spectra of such complexes is available, it seems worthwhile to make an effort to put forward a suitable theory which explains qualitatively and also to some extent quantitatively the experimentally observed oscillator strengths of such complexes. It is well known that in the absence of symmetry destroying vibronic (vibrational electronic) perturbations, electric dipole transitions between the various d^n electronic states of such complexes are rigorously forbidden[2a] (g $\not\leftrightarrow$ g). Thus to compute the intensities of these electric dipole transitions, it is necessary to consider the mixing of kd^n configurations, $\Psi_g^{(0)}(d)$ with $kd^{n-1}(k+1)p$ configurations, $\Psi_u^{(0)}(p)$, under vibrational perturbations.[2a] Previous calculations of this mixing have confined themselves to Ti^{3+}, V^{3+}, Ni^{2+}, and Cu^{2+} complexes and to the use of hydrogenic wave functions.[2a,b] We have now extended our calculations in several directions. The algebraic structure of the oscillator strengths of the electric dipole transitions of kd^n complexes has been derived. The oscillator strength of a transition i → j has been given in terms of the vibronic part $\theta_{i \to j}$ multiplied by a factor $\lambda(s)$, where $\lambda(s)$ depends on a particular ion of the transition metal complex. It is very interesting to note that though the vibronic part $\theta_{i \to j}$ in

the expressions of the oscillator strengths of different kd^n complexes apparently look different, they can be shown to be ultimately related to that of kd^1 multiplied by different numerical constants in different cases. This happens due to the existing group-theoretical symmetry in the wave functions. The algebraic expressions for the oscillator strengths for both high as well as low spin-allowed transitions of $3d^n$ systems and also the relations of the vibronic parts $\theta_{i \to j}$ of kd^n ($n = 2, ..., 8$) systems with that of kd^1 are listed in Appendexes A and B, respectively.[2c] We shall present here only the expressions of oscillator strengths of kd^1 and kd^9 systems.

The vibronic coupling constants which occur in the algebra are ultimately related with the integrals G_k^l and B_k^l ($l = 1, 3; k = 3, 4, 5$) defined by[3]

$$G_k^l = \int_0^\infty R_{kd}(r) \frac{r_<^l}{r_>^{l+1}} R_{(k+1)p}(r) r^2 dr \qquad (1.1)$$

$$B_k^l = \frac{d}{dr_0} G_k^l$$

where r_0 is the metal–ligand bond distance.[15] We have computed these integrals using (a) hydrogenic type wave functions with a variable effective nuclear charge,

(1) This is a joint work started in collaboration with Dr. Andrew D. Liehr but completed by the author.

(2) (a) A. D. Liehr and C. J. Ballhausen, *Phys. Rev.*, **106**, 1161 (1957); (b) C. J. Ballhausen and A. D. Liehr, *Mol. Phys.*, **2**, 123 (1959); (c) Appendexes A and B have been deposited as Document No. 01146 with the ADI Auxiliary Publications Project, Photoduplication Service, Library of Congress, Washington, D. C. 20540. A copy may be secured by citing the document number and remitting $6.80 for photoprints or $2.00 for 35-mm microfilm. Advance payment is required. Make checks or money orders payable to: Chief, Photoduplication Service, Library of Congress.

(3) A. D. Liehr, *Advan. Chem. Phys.*, **5**, 241 (1963).

Z_{eff}, (b) Slater type of wave functions with variable Z_{eff}, and (c) Richardson, et al., type of SCF wave functions,[4-6] hereafter referred to as approximation a, b, and c, respectively. At the end in Table IX we have calculated the oscillator strengths at 300 and 0°K of the optical absorption spectra of the hydrated complexes of a few transition metal ions using Richardson, et al., wave functions as an example. Later we shall work out many more examples of this sort for a wide variety of ligands as well as for 4d and 5d systems. In practice it is very difficult to find a reasonable estimate of $\lambda(s)$ which contains a number of unknown parameters; the reason for this will be clear shortly.

The above-mentioned $G_k{}^l$ and $B_k{}^l$ integrals have been calculated by using electronic computers but will not be presented here due to lack of space. It is also important to mention that the odd vibrational frequencies of the different type of ligands for the transition metal octahedral complexes which fall in the infrared as well as in the far-infrared regions of the spectrum are not yet known from experiments for all types of so-called ionic complexes we are interested in. We, therefore, have assumed a set of values for them in our calculations of the intensities of $3d^n$ complexes. Later, we shall do detailed calculations for each ion in different environments taking into consideration the partial covalent model instead of the point charge model which we have used here. It is well known by now that the point charge model is not strictly valid even in these magnetically dilute complexes,[7] and the more realistic model is a mixture of purely ionic and purely covalent model. In $\lambda(s)$ we have a parameter $f_{d \to p}$, which is the mean oscillator strength of a d→p transition, and it is not known from experiments. We have, therefore, calculated this parameter assuming a charge delocalization onto the ligands and have used the molecular orbital wave functions[7b] the details of which will be presented later.

Here we would like to mention that from a formal point of view, the vibronic theory outlined here is simple and straightforward. The only difficulty is to make reasonable estimates of the quantities occurring in our final intensity expressions. Koide and Pryce[7c] made a similar attempt to explain the intensities of some optical absorption lines in hydrated Mn^{2+} salts. Later Englman[7d] tried to explain the intensities of the crystal field bands by importing the idea of charge-transfer states, but they[7c,d] have used the matrix sum rule to evaluate the vibronic intensities which can be shown to be not only physically implausible but also mathematically inconsistent.[7e,f] Besides this, it is very hard to understand the physical basis of the charge-transfer wave functions since they cannot even approximately be considered orbitals of isolated ligands. Under these circumstances, his [7d] approach to the problem as well as the results obtained by him are not very meaningful.

In our calculations, on the other hand, we have not

attempted any close agreement with experiments in view of the uncertainties involved in the parameters like $f_{d \to p}$, but nevertheless, we do a theoretical calculation for it introducing the covalency effects in it. From the study of the magnetic susceptibilities of these complexes and also from paramagnetic resonance we have an approximate idea of the amount of covalency in these salts. We therefore have found the value of $f_{d \to p}$ for different percentage of covalency and finally have used the value of $f_{d \to p}$ corresponding to 10% covalency for our final oscillator strength calculations. It is fairly clear that we wanted to study the effect of $3d^{n-1}$ 4p states in the intensities through a vibronic perturbation. This does not mean that other excited p states do not contribute to the intensity, but their contributions would perhaps be much smaller than that of 4p. Besides this there are no other serious assumptions involved in our calculation.

We now pass on to the formal development of the vibronic theory of the electric dipole transitions.

2. The Electric Dipole Transitions

The general principles of symmetry and mechanics which govern the appearance of vibronically allowed bands were laid down by Herzberg and Teller[8] in 1933. However, not until recent years has this theory been put on a concrete basis and applied in a semiquantitative fashion to problems of inorganic complexes. In dealing with the interpretation of the observed optical intensity distribution in the octahedral complexes of the transition metal ions, we shall adopt the same general computation scheme as in Liehr and Ballhausen's paper,[2a] but for the sake of completeness, we shall attempt to give a general outline of the theory involved in such a calculation. The requisite wave functions for the kd^n electronic systems under octahedral symmetry have been determined by standard techniques.[9] In our calculations we shall employ the first-order perturbation theory.

We now assume that the ligands can be approximated by point charges of a certain effective charge q_j and mass m associated with the jth ligand. The electrons

(4) J. W. Richardson, W. C. Nieuwpoort, R. R. Powell, and W. F. Edgell, *J. Chem. Phys.*, **36**, 1057 (1962).

(5) J. W. Richardson, R. R. Powell, and W. C. Nieuwpoort, *ibid.*, **38**, 796 (1963).

(6) J. W. Richardson, private communications (1964). We are thankful to Professor Richardson for sending us the 4p wave functions of the doubly and triply ionized 3d transition metal ions before publication.

(7) (a) J. Owen and J. H. M. Thornley, *Rept. Progr. Phys.*, **29**, 675 (1966); (b) C. A. Coulson, private communications (1968). We express our sincere thanks for his invaluable help in this part of the calculation; (c) S. Koide and M. H. L. Pryce, *Phil. Mag.*, **3**, 607 (1958); (d) R. Englman, *Mol. Phys.*, **3**, 48 (1960); (e) J. S. Griffith, *ibid.*, **3**, 477 (1960); (f) W. E. Hagston, *Proc. Phys. Soc.*, **92**, 1101 (1967).

(8) G. Herzberg and E. Teller, *Z. Phys. Chem.* (*Leipzig*), **21**, 410 (1933).

(9) J. S. Griffith, "The Theory of Transition-Metal Ions," Cambridge University Press, New York, N. Y., 1961.
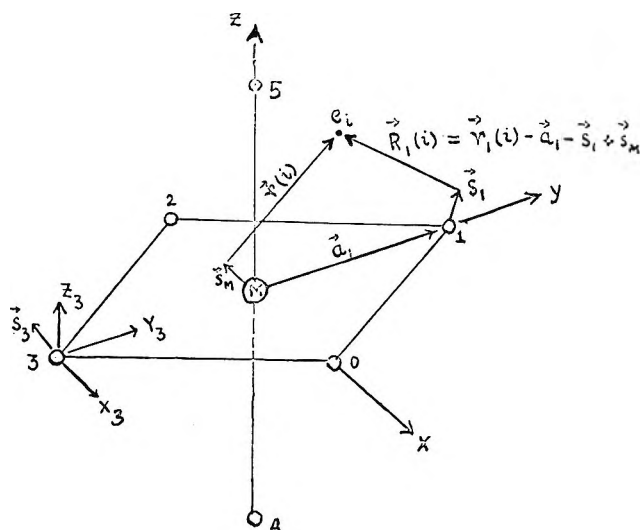
Figure 1. Molecular geometry assumed for hexacoordinated inorganic complexes.[2a]

at radius vector r_i will therefore be perturbed by the charge of the ligands (Figure 1).

From the figure we get for the ith electron

$$\frac{1}{|R|} = \frac{1}{|\vec{r}_i + \vec{s}_M - \vec{s}_j - \vec{a}_j|} \quad (2.1)$$

Expanding this expression and keeping only linear terms in the nuclear displacements $\vec{S}_M$ and $\vec{S}_j$, we get

$$\frac{1}{|R|} = \frac{1}{|\vec{r}_j - \vec{a}_j|}\left\{1 - \frac{(\vec{r}_j - \vec{a}_j)(\vec{s}_M - \vec{s}_j)}{|\vec{r}_i - \vec{a}_j|^2}\right\} \quad (2.2)$$

Taking our octahedral wave functions as our unperturbed wave functions, we thus have for the perturbation term $\mathcal{3C}^{(1)}$ as a function of the normal oscillation Q_k

$$\mathcal{3C}^{(1)}(Q_k) = q_j e^2 \sum_i \sum_j (\vec{s}_j - \vec{s}_M) \cdot \vec{\nabla}_{a_j}\left(\frac{1}{|\vec{r}_i - \vec{a}_j|}\right) \quad (2.3)$$

$\vec{r}_i$ being the radius vector of electron number i (of charge $-e$) and a_j being the position vector of ligand number j, which carries a charge of $(q_j e)$.

By first-order perturbation theory, we now have for the mixing coefficients $\Gamma_{d,p}^{(K)}$

$$\Gamma_{d,p}^{(K)} = -\frac{\langle \Psi_u^0(p)|\mathcal{3C}^{(1)}(Q_K)|\Psi_g^0(d)\rangle}{E_p - E_d} \quad (2.4)$$

with the corresponding first-order wave functions

$$\Psi(d) = \Psi_g^0(d) + \sum_K \sum_p Q_K \Gamma_{d,p}^{(K)}\Psi_u^0(p) \quad (2.5)$$

Now, since the ligands of the transition metal complex are taken to be octahedrally situated point masses and charges (Figure 1), we have the electronic potential energy V, as

$$V(\vec{r}_i, \vec{a}_j) = -\sum_{i,j}\frac{q_j e^2}{|\vec{R}_j(i)|} = -\sum_{i,j}\frac{q_j e^2}{|\vec{r}_i - a_j|} \quad (2.6)$$

In this approximation, the mixing coefficient $\Gamma_{d,p}^K$ is defined by the following relation

$$\sum_K Q_K \Gamma_{d,p}^K = (E_p - E_d)^{-1}\sum_i\sum_{j=0}^{5}(\vec{s}_j - \vec{s}_M) \times$$

$$\nabla_{a_j}\int \Psi_u^0(p)\frac{q_j e^2}{|\vec{r}_i - \vec{a}_j|}\Psi_g^0(d)dr \quad (2.7)$$

the summations being performed over the i different orbitals, the several point charges, and the K different odd normal oscillations.

Since the potential of the ligand oscillations composing the normal oscillation of the entire system will be taken to be harmonic, the intensity in terms of the oscillator strength f, is given by[10]

$$f(d^n, \nu_K \longrightarrow d'^n, \nu_K = 1) =$$

$$1.085 \times 10^{11}(N_{\nu_k}/N)\Delta E_{dn} \times$$

$$|\langle \Psi(d), \nu_K|\vec{r}|\Psi(d'), \nu_K \pm 1\rangle|^2 \quad (2.8)$$

where N_{ν_K} is the molar population in the ground electronic state $\Psi(d)$, of the $(\nu_K + 1)$th harmonic of the normal mode Q_K (frequency ν_K). N is the Avogadro number. We therefore have[11]

$$f(d^n \longrightarrow d'^n) =$$

$$\sum_K\sum_{\nu_K} f(d^n, \nu_K \longrightarrow d'^n, \nu_K \pm 1) =$$

$$1.085 \times 10^{11}\sum_K \coth\left(\frac{h\nu_K}{2kT}\right)\Delta E_{dn} \times$$

$$|\sum_p\langle 0|Q_K|1\rangle\Gamma_{d,p}^K\langle d'|\vec{r}|p\rangle + \Gamma_{d',p}^K\langle d|\vec{r}|p\rangle|^2 \quad (2.9)$$

First we evaluate the electronic integrals, using the antisymmetrized products contained in $\Psi_g^0(d)$ and $\Psi_u^0(p)$ wave functions. Since $\mathcal{3C}^{(1)}$ is a sum of one-electron perturbations, we need only consider the matrix elements between individual d and p wave functions. By summing over the six ligands, we obtain

$$\mathcal{3C}^{(1)} = q_j e^2 \sum_{j=0}^{5}(\vec{s}_j - \vec{s}_M)\cdot$$

$$\nabla_{a_j}\sum_{l=0}^{\infty}\sum_{m=-l}^{l}\frac{4\pi}{2l+1}\frac{r_<^l}{r_>^{l+1}}Y_l^{m*}(\theta_j,\phi_j)\cdot Y_l^m(\theta,\phi) \quad (2.10)$$

We now find the matrix elements

$$\Gamma_{i,j} = \langle(k+1)p_j|\mathcal{3C}^{(1)}(Q_K)|kd_i\rangle \quad (2.11)$$

where $i = xy, xz, yz, x^2 - y^2, z^2$; $j = x, y, z$; $k = 3, 4, 5$, and $K = 3a, b, c$; 4a, b, c; 6a, b, c. The general form of the matrix elements given in expression (2.11) can be determined by investigating the symmetry properties under reflections in the six $x = 0$, $y = 0$, $z = 0$, $x = z$, $y = z$, and $x = y$ planes.[3] We shall not enter into a discussion of this here since they are given

(10) R. S. Mulliken and C. A. Rieke, *Rept. Progr. Phys.*, **8**, 231 (1941).

(11) C. J. Ballhausen, "Introduction to Ligand Field Theory," McGraw-Hill, New York, N. Y., 1962.

by Liehr in detail.[3] We quote his final expressions here.

$$\Gamma_{xy,x} = \gamma_{x,3b}{}^{xy}S_{3b} + \gamma_{x,4b}{}^{xy}S_{4b} + \gamma_{x,6b}{}^{xy}S_{6b}$$

$$\Gamma_{xy,y} = \gamma_{y,3c}{}^{xy}S_{3c} + \gamma_{y,4c}{}^{xy}S_{4c} + \gamma_{y,6c}{}^{xy}S_{6c}$$

$$\Gamma_{xy,z} = 0 \qquad (2.12)$$

$$\Gamma_{x^2-y^2,x} = \gamma_{x,3c}{}^{x^2-y^2}S_{3c} +$$
$$\gamma_{x,4c}{}^{x^2-y^2}S_{4c} + \gamma_{x,6c}{}^{x^2-y^2}S_{6c}$$

$$\Gamma_{x^2-y^2,y} = \gamma_{y,3b}{}^{x^2-y^2}S_{3b} +$$
$$\gamma_{y,4b}{}^{x^2-y^2}S_{4b} + \gamma_{y,6b}{}^{x^2-y^2}S_{6b}$$

$$\Gamma_{x^2-y^2,z} = \gamma_{z,6a}{}^{x^2-y^2}S_{6a}$$

The remaining vibronic perturbation terms are readily obtained from the above expressions by applying a counterclockwise rotation of 120° about the (111) direction.[3] To get the expressions 2.12 from 2.11, we have expressed the nuclear displacements in terms of the symmetry coordinates after evaluating the electronic integrals. In the octahedral point group O_h, only perturbing nuclear displacements of symmetry τ_{1u} and τ_{2u} yield nonzero mixing coefficients.[2a,12] The algebraic forms of the vibronic coupling constants $\gamma_{x,3b}{}^{xy}$, etc., appearing in eq 2.12, computed on the basis of a point charge model,[2b] are given by

$$\gamma_{x,3b}{}^{xy} = \gamma_{y,3c}{}^{xy} = -\frac{1}{\sqrt{5}}\frac{qe^2}{r_0}\left[\frac{9}{7}G_k{}^3 + 2G_k{}^1\right]$$

$$\gamma_{x,4b}{}^{xy} = \gamma_{y,4c}{}^{xy} = -\sqrt{\frac{2}{5}}qe^2\left[-\frac{3}{7}B_k{}^3 + B_k{}^1\right]$$

$$\gamma_{x,6b}{}^{xy} = \gamma_{y,6c}{}^{xy} = -\frac{3\sqrt{5}}{7}\frac{qe^2}{r_0}G_k{}^3$$

$$\gamma_{x,3c}{}^{x^2-y^2} = -\gamma_{y,3b}{}^{x^2-y^2} =$$
$$-\frac{1}{\sqrt{5}}\frac{qe^2}{r_0}\left[-\frac{27}{14}G_k{}^3 + 2G_k{}^1\right] \qquad (2.13)$$

$$\gamma_{x,4c}{}^{x^2-y^2} = -\gamma_{y,4b}{}^{x^2-y^2} =$$
$$-\sqrt{\frac{2}{5}}qe^2\left[\frac{9}{14}B_k{}^3 + B_k{}^1\right]$$

$$\gamma_{x,6c}{}^{x^2-y^2} = -\gamma_{y,6b}{}^{x^2-y^2} = +\frac{3\sqrt{5}}{14}\frac{qe^2}{r_0}G_k{}^3$$

where $G_k{}^l$ and $B_k{}^l$ are given by eq 1.1.

In the electronic integrals given by eq 2.12 we now replace the symmetry coordinates (S_K) with suitable linear combinations of the normal coordinates (Q_K). It is important to note that the τ_{1u} symmetry coordinates S_{jt}, ($j = 3, 4$; $t = $ a, b, c) are, however, not normal coordinates.[12] The normal coordinates of symmetry τ_{1u} can only be determined after assumptions have been made as to the potential energy of the system. If we assume Wilson's valence force potential, we

obtain the following relations connecting the S_{jt} symmetry coordinates to Q_{jt} normal coordinates[2a,12]

$$S_{3t} = \frac{1}{\sqrt{2}}(L_{33}Q_{3t} + L_{34}Q_{4t})$$

$$S_{4t} = L_{43}Q_{3t} + L_{44}Q_{4t} \qquad (t = \text{a, b, c}) \qquad (2.14)$$

where, taking the even vibrational frequencies ν_1, ν_2, and ν_5 equal to 300, 275, and 150 cm^{-1}, respectively, we obtain the odd frequencies[2a,13] $\nu_3 = 137$ cm^{-1}, $\nu_4 = 356$ cm^{-1}, and $\nu_6 = 106$ cm^{-1} and hence it can be shown that[14]

$$L_{33} = 0.295816\sqrt{2} \qquad L_{34} = 0.186319\sqrt{2}$$
$$L_{43} = -0.027619 \qquad L_{44} = 0.296860 \qquad (2.15)$$

Substituting these results in eq 2.9, the final expressions for the oscillator strengths are derived for kd^n octahedral complexes using the approximations a, b, and c mentioned earlier.

We have already seen that the oscillator strengths depend on the evaluation of the vibronic coupling constants, γ's, given by eq 2.13, which are ultimately related with the integrals $G_k{}^l$ and $B_k{}^l$. Using approximation a, Ballhausen and Ancmon[15] have derived the expressions for $G_k{}^l$ and $B_k{}^l$ for $k = 3$ and have computed the integrals for a great range of values of Z_d, Z_p, and $r = r_0/a_0$ (r_0 is the metal–ligand bond distance and a_0 the Bohr radius). We have similarly derived expressions of $G_k{}^l$ and $B_k{}^l$, for $k = 4$ and 5 in the approximation a, and for $k = 3, 4$, and 5 in the approximation b, and only for $k = 3$ in the approximation c.[16] Suffice it to say that we have computed these integrals by electronic computer for a great range of values of Z_d, Z_p, and r (Z_d is the effective charge on 3d, 4d, or 5d wave functions and Z_p is the effective charge on 4p, 5p, and 6p wave functions). When we go through all the steps mentioned so far we get the oscillator strength for transition between two crystal field states i and j as

$$f_{i\to j} = \theta_{ij}\lambda(s)$$

where θ_{ij} involves temperature factor (3.2) and vibronic coupling constants ($\Gamma_{\alpha\beta}{}^K$) (see Appendixes) and $\lambda(s)$ is given by[2a,17]

(12) A. D. Liehr and C. J. Ballhausen, *Ann. Phys.* (N. Y.), **3**, 304 (1958).

(13) In our intensity calculations we have used the above values of the odd frequencies throughout, though it is true that these values will change appreciably depending on the ion and the associated ligands, but since these frequencies fall in the far-infrared region, the experimental data are very scarce. Thus it can be said that a great deal of experimental work is needed to obtain a reliable force potential and hence the normal vibrational frequencies for these complexes.

(14) C. J. Ballhausen, "Electron States in Complexes of the First Transition Group," Thesis, Copenhagen, 1958, p 52.

(15) C. J. Ballhausen and E. M. Ancmon, *Kgl. Danske Videnskab. Selskab, Mat.-Fys. Medd.*, **31**, No. 9 (1958).

(16) This is because the SCF wave functions are not yet available for 4d and 5d ions.

(17) Note that the numerical factor in the expression for $\lambda(s)$ is $^4/_5$ and not $^8/_5$ as given in ref 2a.

$$\lambda(s) = \frac{4}{5} q^2(s) \left[R^2 \frac{\Delta E_{dn}}{\Delta E_{dp}^3} \right] f_{d \to p} \qquad (2.16)$$

where s stands for a particular ion of the transition metals i.e., Ti^{3+}, Cu^{2+}, etc., $q^2(s)$ represents the square of the effective charge associated with the crystal field of the ligands, R the Rydberg constant, ΔE_{dn} is the energy difference (in cm^{-1}) between the two electronic levels between which the transition is taking place, ΔE_{dp}[18] is the mean energy separation of the d and p orbitals, and $f_{d \to p}$ is the mean oscillator strength of an ordinary d→p transition.

The Calculation of q(s) Occurring in Eq 2.16. The relation between Dq[19] and $q(s)$ is given by [20]

$$Dq = \frac{1}{6} q(s) G^4{}_{kd,kd}(Z_d, r_0) \qquad (2.17)$$

where

$$G^l{}_{kd,kd} = \int_0^\infty R_{kd}^2(r) \frac{r_<{}^l}{r_>{}^{l+1}} r^2 dr \qquad (2.18)$$

In approximation a, Ballhausen has computed $G_{3d,3d}^4$ and has mentioned a few values in his thesis.[14] We have computed $G_{kd,kd}^4$ for $k = 3$, 4, and 5 and for a great range of values of Z_d and r, using approximations a, b, and c but, due to lack of space, will not be presented here. In principle, therefore, $q(s)$ can be found out using eq 2.17 when Dq is known from the spectra.

The Calculation of $f_{d \to p}$ Occurring in Eq 2.16. We now concentrate our attention on $f_{d \to p}$, the mean oscillator strength of an ordinary d → p transition occurring in eq 2.16. In performing such calculations for the oscillator strength, it is essential to use the best wave functions which can possibly be found.

From the experiments on the ligand hyperfine interactions, magnetic susceptibilities, and optical spectra we have the most striking demonstration of the existence of covalency in transition metal complexes.[7a] Therefore, strictly speaking, one has to use the molecular orbital approach in the intensity calculations because if there is charge delocalized from the central atom onto the ligands, this will contribute rather a lot to the transition moment integral. The main difficulty is that we do not know the amount of covalency. Different methods of estimating it give different values, but if an approximate value could be estimated by some means, there are two ways in which we could use this information.[7b] The simplest way would be to say that if x per cent of the excited charge cloud is on the ligands and not on the central atom, then the matrix element would be reduced by $\sqrt{x}$. This is because the matrix component is proportional to Ψ and not Ψ^2, but the intensity, which depends on the square of the matrix element, will be reduced by the full x per cent. A better way, suggested by Coulson, would be to say that if on one of the ligand atoms there is a percentage y of the excited electron (taken to be zero in the ground state),

then one would imagine a concentrated δ-function wave function, with y strength at the ligand nucleus. It would then be a simple matter to see what change this made in the matric component $\langle \Psi_{gr} | \vec{r} | \Psi_{Ex} \rangle$. Of course, one has to be careful when taking account of more than one ligand atom, since the phases of the δ functions would have to fit with the symmetry of the excited orbital at each ligand center.

Let us suppose that we deal with a central atom A and one ligand B and also suppose that the atomic orbital φ_A is slightly delocalized onto B. Then the molecular orbital wave function can be written in the form

$$\Psi_{Ex} = C_1 \varphi_A - C_2 \varphi_B$$

where φ_B is some atomic orbital on B. The negative sign indicates an antibonding orbital. If we neglect overlap integrals which will be a reasonable approximation in this type of problem, then

$$C_1^2 + C_2^2 = 1$$

and the fraction of the electron to be found on atom B is C_2^2. This orbital Ψ is the upper state involved in an electronic transition. For the lower state we assume another atomic orbital on A, which we will call χ_A and which we shall assume to be completely localized on atom A. We are now interested in the matric component

$$\langle \Psi_{Ex} | \vec{r} | \chi_{Gr} \rangle$$

The intensity of the absorption will be proportional to the square of this matrix component. If we now expand Ψ_{Ex} in terms of C_1 and C_2, we obtain two terms for the matrix component. The one with C_1 as a factor is an integral centered at the ion site and involves the 4p wave functions of the central paramagnetic ion. The second term having the factor C_2 involves the two-center integrals and is fairly tedious to evaluate.

If we are to make proper calculation of this, we shall need to know the detailed form of φ_B. Even if we knew it, there would result the two-center integrals. We therefore simplify this integral by treating the atomic orbital φ_B as if it were a concentrated point charge at the nucleus B. This is what is meant by calling it δ-function charge. The value of this integral is then given by

$$c_2 \cdot \chi_A \ (\text{at B}) \cdot \vec{r} \ (\text{at B})$$

The result of compressing the atomic orbital φ_B into a point is to take away the necessity to make a detailed integration. The main advantage in adopting this

(18) $E_{dp} \approx R$ for free ions but in complexes this value will be somewhat reduced from the free ion value. For a discussion about this see ref 7.

(19) $10Dq$, by convention, is assumed to be the energy separation of a single d electron under the cubic crystalline electric field produced by the ligands.

(20) C. J. Ballhausen, *Dan. Mat. Rys. Medd.*, 29, No. 4 (1954).

procedure is that we are not required to bother ourselves with the precise form of φ_B.

This is all about a two-atom system for which the calculation is much simpler, but in our case of octahedral symmetry O_h, we have to use the molecular orbitals for our calculation. We assume that the d electrons in the ground state are completely localized on the metal ion but the excited p orbitals form molecular orbitals. One can write, therefore

$$\Psi_{Gr} = \Psi(d)$$

$$\Psi_{Ex}^{(1)} = c_1\phi_M(4p_x) - \frac{c_2}{\sqrt{2}}\phi_L(2p_{z1} - 2p_{z4}) -$$

$$\frac{c_3}{2}\phi_L(2p_{z3} + 2p_{y2} - 2p_{z5} - 2p_{y6})$$

$$\Psi_{Ex}^{(2)} = c_1\phi_M(4p_y) - \frac{c_2}{\sqrt{2}}\phi_L(2p_{z2} - 2p_{z5}) -$$

$$\frac{c_3}{2}\phi_L(2p_{z1} + 2p_{y3} - 2p_{z6} - 2p_{z4})$$

$$\Psi_{Ex}^{(3)} = c_1\phi_M(4p_z) - \frac{c_2}{\sqrt{2}}\phi_L(2p_{z3} - 2p_{z6}) -$$

$$\frac{c_3}{2}\phi_L(2p_{z2} + 2p_{y1} - 2p_{z4} - 2p_{y5})$$

The 4p orbitals are simultaneously σ- and π-antibonding orbitals. The coefficients c_1, c_2, c_3 are difficult to obtain, and there is no absolutely reliable way of getting them. They cannot be gotten by comparison with experimental hyperfine coupling constants,[7] since the results obtained by various methods do not agree mutually. In principle, these coefficients can be roughly obtained by variational methods.[21] We do not calculate these coefficients here but assume certain values for them such that the relation $c_1{}^2 + c_2{}^2 + c_3{}^2 = 1$ is satisfied (neglecting overlap). We have assumed, for simplicity, coefficients are the same for both σ and π bonding, i.e., $c_2 = c_3$. The following three sets of values of c_1 and c_2 are assumed in our calculations which are given in Table I. It is evident from Table I

Table I

Coefficient	Set 1	Set 2	Set 3	Set 4
c_1	1.0	0.9	0.8	0.7
c_2	0.0	0.3082	0.4243	0.5050

that we assume a maximum of 30% of charge delocalization on the ligands, and we believe that this is a very reasonable range within which to work.

For the ground electronic states we take the strong field wave functions for the $3d^n$ metal ions denoted by

χ_M. We have to calculate now the following matrix element

$$\langle \chi_M | \vec{r} | \Psi_{Ex} \rangle$$

This matrix element has to be inserted into the usual expression for the oscillator strength, given by

$$f_{d \to p} = 1.085 \times 10^{11}(E_p - E_d) \times$$

$$|\sum_i \langle \chi_M | \vec{r} | \Psi_{Ex}{}^i \rangle|^2 \quad (2.20)$$

where i denotes the three components of the excited state wave function. We have calculated the oscillator strengths for a $d \to p$ transition given by the above expression by using Richardson, et al., type of SCF wave functions.[4-7] It is easy to show that the metal orbitals of the type $3d_{3z^2-r^2}$ and $3d_{z^2-y^2}$ form only σ bonds with the ligands and $3d_{zy}$, $3d_{yz}$, $3d_{zz}$ form π bonds in O_h symmetry.

We pointed out earlier that we assume a δ function type of wave function at the ligand sites and we consider only the 2p wave functions on the ligand sites. Regarding the use of δ function approximation, the following should be noted. When, for example $2p_\pi$ orbitals are approximated by a δ function, it is not correct to put an equivalent charge at ligand site when we know from basic symmetry argument that there must be a node there. Since there are two regions (also called lobes) where the charge is concentrated, we should replace the total charge-cloud by two point charges, each equal to $e/2$ (one-half the electronic charge) at the centers of the two lobes. This incidentally also takes care of normalization problem associated with δ function. Now the question is where the two points are located? It would seem that they are at radial maxima of $2p_\pi$ orbitals. This, however, is not true. We place them at half the atomic radius for covalent bonding since this represents quite closely the distance at which most of the charge is located. Since we are interested in the so-called ionic complexes, we use the value for the covalent radius of fluorine[22] ($r \sim 0.72$ Å) in our calculations. It is, however, important to note that this procedure is bound to be only an approximation, but our intention is to see how important the delocalization process is and for this purpose the above procedure is good enough. p_σ orbitals are treated in the same way. Explicit use of 2p orbitals on ligands and inclusion of overlap integrals would bring in specific dependence on the ligand nature, and hence the calculations would be very tedious.

Following the above procedure we have calculated the mean oscillator strength for the $d \to p$ transition the expression of which has been given in eq 2.20. It is also to be noted that we need the magnitude of

(21) C. J. Ballhausen and H. B. Gray, "Molecular Orbital Theory," W. A. Benjamin, New York, N. Y., 1965.

(22) C. A. Coulson, "Valence," Oxford University Press, London, 1961.

$E_d - E_p$ for which we use 12 eV, which has been roughly estimated from ionization data with corrections.[7] Table II gives the $f_{d \to p}$ for the $3d^n$ transition metal complexes. We use these values in finding the final intensities of the above mentioned hydrated complexes (see Table X).

Table II: $f_{d \to p}$ for $3d^n$ Complexes of the Transition Metal Ions for Different Sets of Values of c_1 and c_2 Mentioned in Table I. $E_p - E_d$ Has Been Assumed To Be 12 eV

Configuration	Ion	$f_{d \to p}$ (for set 1)	$f_{d \to p}$ (for set 2)	$f_{d \to p}$ (for set 3)	$f_{d \to p}$ (for set 4)
$3d^1$	Ti^{3+}	0.2833	0.2280	0.1884	0.1556
$3d^2$	V^{3+}	0.2510	0.1922	0.1474	0.1095
$3d^3$	V^{2+}	0.2508	0.1940	0.1496	0.1118
	Cr^{3+}	0.0887	0.0677	0.0518	0.0385
$3d^4$	Cr^{2+}	0.3237	0.2459	0.1876	0.1387
	Mn^{3+}	0.1900	0.1495	0.1164	0.0878
$3d^5$	Mn^{2+}	0.2673	0.2070	0.1598	0.1195
	Fe^{3+}	0.1624	0.1278	0.0994	0.0749
$3d^6$	Fe^{2+}	0.2248	0.1751	0.1355	0.1016
	Co^{3+}	0.1418	0.1135	0.0891	0.0678
$3d^7$	Co^{2+}	0.1895	0.1484	0.1151	0.0866
$3d^8$	Ni^{2+}	0.1651	0.1298	0.1010	0.0761
$3d^9$	Cu^{2+}	0.1454	0.1149	0.0896	0.0677

Following the procedure outlined earlier we now list the algebraic expressions for oscillator strengths for kd^1 and kd^9 systems only. The rest are listed in Appendix A.[2c]

kd^1.   *Transition* $^2T_{2g} \to {}^2E_g$.

$$f(a \longrightarrow b) = A(xy)y|x| \sum_K^{3,4,6} \{ [(xy,x;K) +$$

$$(x^2 - y^2,y;K)]^2 + [(x^2 - y^2,x;K) - (xy,y;K)]^2 \}$$

$$f(b \longrightarrow b) = A(xz)z|x| \sum_K \{ [(xz,x;K) +$$

$$(x^2 - y^2,z;K)]^2 + [(x^2 - y^2,x;K)]^2 \}$$

$$f(c \longrightarrow b) = A(yz)y|z| \sum_K \{ [(x^2 - y^2,z;K) -$$

$$(yz,y;K)]^2 + [(x^2 - y^2,y;K)]^2 \}$$

$$f(a \longrightarrow a) = A(xy)y|x| \sum_K \{ [(z^2,y;K) -$$

$$(3^{-1/2})(xy,x;K)]^2 + [(z^2,x;K) - (3^{-1/2})(xy,y;K)]^2 \}$$

$$f(b \longrightarrow a) = A(xz)z|x| \sum_K \{ [(z^2,z;K) -$$

$$(3^{-1/2})(xz,x;K)]^2 + [(z^2,x;K) + 2(3^{-1/2})(xz,z;K)]^2 \}$$

$$f(c \longrightarrow a) = A(yz)z|y| \sum_K \{ [(z^2,z;K) -$$

$$(3^{-1/2})(yz,z;K)]^2 + [(z^2,y;K) + 2(3^{-1/2})(yz,y;K)]^2 \}$$

kd^9.   *Transition* $^2E_g \to {}^2T_{2g}$.

$$f'(b \longrightarrow a) = 2f(a \longrightarrow b)$$

$$f'(b \longrightarrow b) = 2f(b \longrightarrow b)$$

$$f'(b \longrightarrow c) = 2f(c \longrightarrow b)$$

$$f'(a \longrightarrow a) = 2f(a \longrightarrow a)$$

$$f'(a \longrightarrow b) = 2f(b \longrightarrow a)$$

$$f'(a \longrightarrow c) = 2f(c \longrightarrow a)$$

where

$$A = \frac{\Delta E_{dn}}{\Delta E_{dp}}$$

$$(xy)y|x| = f_{xy}{}^{py}|x| = \langle p_y|x|d_{xy} \rangle$$

$$(xy,x;K) = \Gamma_{xy,x}{}^K \text{ etc.}$$

For other kd^n ions see Appendix A.[2o]

In the above expressions for the oscillator strengths, ΔE_{dn} is the energy difference (in cm^{-1}) between the ground and the excited state in which the transition takes place. ΔE_{dn} is usually taken from the experiments on the optical absorption spectra (see Tables VIII and IX).

$$\Delta E_{dp} = E_d - E_p = 12 \text{ eV}$$

Γ's are the vibronic coupling constants given by eq 2.12.

It can be shown from the above expressions for the oscillator strengths that the electron–hole equivalence is not directly applicable here. There is a direct correspondence between kd^n and kd^{5+n} systems and numerous indirect relationships between these and other systems. The above observations are also true in the optical rotatory power calculations.[23]

The oscillator strengths are given in terms of the vibronic part $(\theta_{i \to j})$ multiplied by a factor $\lambda(s)$ defined by eq 3.1 in section 3. By correspondence and indirect relationships between the different kd^n ($n = 2, 3, 4, 5, 6, 7, 8, 9$) systems among themselves as well as with kd^1, we mean the correspondence and the indirect relationships between the vibronic parts $(\theta_{i \to j})$ of the different systems only. In most of the cases these relations can be found out by carefully looking at the expressions, whereas, in some cases, one has to apply the symmetry operators on the vibronic coupling constants Γ's in order to derive the relations.[3] The various interesting relations existing between the $\theta_{i \to j}$'s of the different kd^n systems with those of kd^1 are presented in Appendix B.[2c]

3. Algebraic Formulations of the Oscillator Strengths

The algebraic formulations of the oscillator strengths for different possible transitions (i → j) for kd^n systems are given in this section. The final oscillator strengths $f_{i \to j}$ can be expressed as

(23) A. D. Liehr, *J. Phys. Chem.*, **68**, 665, 3629 (1964).

Table III: Experimental Odd Vibrational Frequencies (ν_3, ν_4, and ν_6 in cm^{-1}) of the XY_6 Complexes of the Transition Metal Ions

Con-figuration	Ion	Complex	ν_3	ν_4	ν_6	References
3d³	Cr³⁺	Cr(NH₃)₆³⁺	...	475	...	a
		Cr(CN)₆³⁻	124	457	95	b
		Cr(CO)₆³⁺	436	661	570	c
3d⁵	Mn²⁺	Mn(H₂O)₆²⁺	170	320–400	85	d
	Fe³⁺	Fe(CN)₆³⁻	387	511	381	e
3d⁶	Co³⁺	Co(NH₃)₆³⁺	325	464	261	f
		Co(CN)₆³⁻	414	365	395	e
		CoF₆³⁻	475	310	...	g
	Fe²⁺	Fe(CN)₆⁴⁻	414	585	402	e
3d⁷	Co²⁺	CoSO₄·7H₂O	252	384	147	h
		K₂Co(SO₄)₂·6H₂O	281	391	147	h
		(NH₄)₂Co(SO₄)₂·6H₂O	252	264	240	h
		Co(H₂O)₆²⁺	170	320	85	d
3d⁸	Ni²⁺	NiSO₄·7H₂O	297	393	134	h
		K₂Ni(SO₄)₂·6H₂O	299	398	134	h
		(NH₄)₂Ni(SO₄)₂·6H₂O	293	385	134	h
		Ni(NH₃)₆²⁺	...	334	...	a
4d³	Mo³⁺	MoF₆³⁻	741	264	190	i
		Mo(CO)₆³⁻	595	368	517	c
4d⁴	Tc³⁺	TcF₆³⁻	748	265	...	a
4d⁵	Ru³⁺	Ru(Cl)₆³⁻	188	346	...	j
		RuF₆³⁻	735	275	188	k
4d⁶	Rh³⁺	RhF₆³⁻	724	283	192	l
5d²	Os⁶⁺	OsF₆³⁻	720	268	230	m
5d³	W³⁺	WF₆³⁻	712	256	216	n
	Re⁴⁺	ReCl₆²⁻	172	313	...	o
		ReBr₆²⁻	118	217	...	o
5d⁴	Os⁴⁺	OsCl₆²⁻	117	314	...	o
	Re³⁺	ReF₆³⁻	715	257	193	p
	Pt⁶⁺	PtF₆³⁻	705	273	211	m
5d³	Ir⁶⁺	IrF₆³⁻	718	276	205	q
5d⁵	Ir⁴⁺	K₂IrCl₆²⁻	184	333	...	q
		(NH₄)₂IrCl₆²⁻	192	327	...	q
5d⁶	Ir³⁺	K₂IrCl₆³⁻	200	296	...	j
	Pt⁴⁺	K₂PtCl₆²⁻	186	344	...	j
		K₂PtBr₆²⁻	78	240	...	j
		K₂PtI₆²⁻	46	186	...	j

^{a} K. Nakamoto, "Infrared Spectra of Inorganic and Coordination Compounds," Wiley, New York, N. Y., 1963. ^{b} H. Hartmann and E. Konig, *Z. Phys. Chem. (Frankfurt am Main)*, **30**, 215 (1961). ^{c} C. W. F. T. Pistorius and P. C. Haarhoff, *J. Mol. Spectrosc.*, **3**, 621 (1959). ^{d} S. Koide and M. H. L. Pryce, *Phil. Mag.*, **3**, 607 (1958). ^{e} I. Nakagawa and T. Shimanouchi, *Spectrochim. Acta*, **18**, 101 (1962). ^{f} T. Shimanouchi and I. Nakagawa, *ibid.*, **18**, 89 (1962). ^{g} M. D. Meyers and F. A. Cotton, *J. Amer. Chem. Soc.*, **82**, 5023 (1960). ^{h} V. Ananthanarayanan, *Z. Phys. Chem. (Leipzig)*, **222**, 102 (1963). ^{i} H. H. Claassen, H. Selig, and J. G. Malur, *J. Chem. Phys.*, **36**, 2888 (1962). ^{j} D. M. Adams and H. A. Gebbie, *Spectrochim. Acta*, **19**, 925 (1963). ^{k} G. Nagarajan, *Indian J. Pure Appl. Phys.*, **2**, 86 (1964). ^{l} B. Weinstock, H. H. Claassen, and C. L. Chernick, *J. Chem. Phys.*, **38**, 1470 (1963). ^{m} B. Weinstock, H. H. Claassen, and J. G. Malm, *ibid.*, **32**, 181 (1960). ^{n} T. G. Burke, D. F. Smith, and A. H. Nielsen, *ibid.*, **20**, 447 (1952). ^{o} L. A. Woodward and M. J. Ware, *Spectrochim. Acta*, **20**, 711 (1964). ^{p} H. H. Claassen, J. G. Malm, and H. Selig, *J. Chem. Phys.*, **36**, 2890 (1962). ^{q} H. C. Mattraw, N. J. Howkins, D. R. Carpenter, and W. W. Sabol, *ibid.*, **23**, 985 (1955).

$$f_{i \to j} = \theta_{i \to j} \lambda(s) \qquad (3.1)$$

where $\theta_{i \to j}$ involves the vibronic coupling constants ($\Gamma_{\alpha\beta}{}^{r_K}$) and represent that part of the formulas given in section 2 which is within the summation sign. This part involves the odd vibrational frequencies ν_K ($K = 3, 4, 6$) of irreducible representations of symmetries T_{1u} and T_{2u} and also the temperature factor[11] (T.F.)

$$\text{T.F.} = \sum_K^{3,4,6} |\langle 0|Q_K|1\rangle|^2 \coth\left(\frac{h\nu_K}{2kT}\right) \qquad (3.2)$$

and

$$\lambda(s) = \frac{4}{5} q^2(s) R^2 \cdot \frac{E_N - E_V}{(E_N - E_p)^2 (E_p - E_V)} f_{N \to p} \qquad (3.3)$$

where N and V are the two vibronically perturbed states and p is the odd perturbing state. If we, however, assume $E_N - E_p \approx E_p - E_V$ then eq 3.3 is the same as eq 2.16. It is important to mention that it is impossible to tabulate $\theta_{i \to j}$ as a function of $Z_{kd,(k+1)p}$ ($k = 3, 4, 5$) for each vibrational frequency $\nu_{3,4,5}$ leaving that frequency unspecified because to calculate the $\Gamma_{\alpha\beta}{}^{r_K}$ one must transform the symmetry coordinates (S_{Kt}, $t =$

a, b, c) to the corresponding normal coordinates (Q_{Kt}) by using eq 2.14. This involves the explicit use of the L matrix. The numerical values of the L matrix cannot be obtained unless the vibrational frequencies ν_3, ν_4, and ν_6 are explicitly specified.[14] Throughout our calculations we have used $\nu_3 = 137$ cm^{-1}, $\nu_4 = 356$ cm^{-1}, and $\nu_6 = 106$ cm^{-1} to calculate the variation of oscillator strength with the effective nuclear charge.[13] The above-mentioned magnitudes for the vibrational frequencies, we believe, are more or less typical for the $3d^n$ octahedral complexes under consideration.[11] In Table III we present the magnitudes of the odd vibrational frequencies obtained from experiments on the various types of complexes of the kd^n ions. A glance at Table III would be sufficient to realize that the odd vibrational frequencies which are responsible for mixing the 4p wave functions with the central 3d wave functions through the vibronic perturbation vary widely in magnitude from complex to complex and from ion to ion. No possible explanation as to why these frequencies differ so much from one another has been put forward by the infrared spectroscopists as yet. Here we should like to make a few remarks about these frequencies. We would like to remark that these frequencies should be a reflection of the bond strengths between the metal and the ligand, or, in other words, the weaker the bond is, less would be the magnitude of the stretching frequency $\nu_4(T_{1u})$. From the electronegative character of the ligands it is fairly well known that fluorine is the most electronegative; therefore the bond strength between fluorine and the central ion must be very weak, and thus ν_4 would be lowest in magnitude among the three. Then comes the aquocoordination and lastly the CN ligand. CN is least electronegative; therefore the bond between the metal and the ligand should be very strong, and hence ν_4 should have the greatest magnitude. This picture agrees with the experimental values quoted in Table III. As regards the variation of ν_3 and ν_6, which are the bending frequencies, we also can give a crude explanation from the electronegativity of the ligand complexes. Since fluorine is most electronegative, the bond strength between the metal and fluorine is consequently weak. Therefore, for the bending of the type YXY (where X is the metal and Y is the ligand) the greater electrostatic repulsion will increase the vibrational frequencies because, due to bending, the metal–ligand bond being weaker, the ligands will be drawn closer and hence the electrostatic repulsion would probably be greater. Thus ν_3 and ν_6 would have much greater magnitudes compared to ν_4 for the fluoride complexes, whereas they would be least in the covalent cyanide complexes and in between for the aquo complexes.

To show the variation of the oscillator strengths with the effective nuclear charge, we have already seen earlier that the vibrational frequencies must be specified at the onset of calculations. Since the frequencies vary considerably from one complex to the other, the best possible thing is to treat every case separately. This is impossible at present since it involves too much labor. In connection with calculation of the L matrix (eq 2.15) we have chosen a representative set of values for $3d^n$ systems,[2a] whereas the work on the $4d^n$ and $5d^n$ systems will be done shortly.

It is clear from eq 3.3 that $\lambda(s)$ contains a number of unknown parameters lumped together, and it is very difficult to get an exact estimate of it. In the point charge model $q^2(s)$ can be obtained using eq 2.17 provided Dq is known from experiments. $E_N - E_V$ is, of course, known from the absorption spectra, but there is no way of knowing $E_N - E_P$, $E_P - E_V$, or $f_{N \to P}$, and, therefore, we have made a theoretical estimate of $f_{d \to p}$ given in Table II. These values have been used to estimate $\lambda(s)$ which have been utilized in finding the magnitudes of the oscillator strengths of the optical absorption spectra of some of the aquo complexes of the $3d^n$ transition metal ions mentioned in Table X.

Table IV gives the variation of $\theta_{i \to j}$ with the effective nuclear charge for the $3d^1$ system at temperature 300 and 0°K (the values for 0°K are given in parentheses) in the approximations a, i.e., using hydrogenic

Table IV: Ti^{3+} ($3d^1$), Transition $^2T_{2g} \to {}^2E_g$, Variation of $\theta_{i \to j}$ with Z_{eff} (3d) at 300 and 0°K^a in Approximation a or b

Z_{eff} (3d) ($Z_{4p} = 5.5$)	$\theta^{2}T_{2g} \to {}^2E_g$ (10^{-4})
3.5	271.7300 (91.2070)
4.0	86.4305 (28.8385)
5.0	41.1130 (14.5335)
6.5	6.7570 (2.6345)
7.5	7.0635 (2.6840)
8.5	6.8230 (2.5635)

^{a} The values in parentheses are at 0°K.

functions, Z_p is kept constant at 5.5 and the metal–ligand distance $r_0 = 2$ Å. $q(s)$ for $\lambda(s)$, assuming the point charge model, can be obtained by using eq 2.17 when $G^4_{kd,kd}$ ($k = 3, 4, 5$) is evaluated. We have also evaluated the integrals $G^4_{kd,kd}$ ($k = 3, 4, 5$) which will be published elsewhere shortly. Table V gives the variation of $\theta_{i \to j}$ for $3d^1$ system in the approximation c. Table VI gives the variations of $\theta_{i \to j}$ with Z_{eff} for the ($4d^1$) system in the approximations a and b. Similarly Table VII gives the $\theta_{i \to j}$ for the $5d^1$ system. The $\theta_{i \to j}$ parts for the systems kd^n can be readily found out from kd^1 ($k = 3, 4, 5$) system by using the relations given in Appendix B.[2c]

Table V: $\theta_{i \to j}$ Using Richardson Wave Functions at 300 and 0°K (See Text)

Configuration	Transition (g → g)	$\theta_{i \to j}$ (× 10⁻⁴) At 300°K	At 0°K
3d¹ (Ti³⁺)	$^2T_2 \to {}^2E$	99.6675	41.6115
3d² (V³⁺)	$^3T_1 \to {}^3T_1$	94.0900	36.2390
	$\to {}^3T_2$	79.3330	36.3660
3d³ (V²⁺)	$^4A_2 \to {}^4T_1$	207.1035	72.0720
	$\to {}^4T_2$	175.7520	84.7410
(Cr³⁺)	$^4A_2 \to {}^4T_1$	141.1035	50.6235
	$\to {}^4T_2$	82.5345	42.5385
3d⁴ (Cr²⁺)	$^3T_1 \to {}^3A_1$	91.8150	45.2980
	$\to {}^3A_2$	123.9410	43.6310
	$\to {}^3E(1)$	71.9180	29.6425
	$\to {}^3E(2)$	56.9180	29.6425
	$\to {}^3T_1(1)$	49.9230	22.4400
	$\to {}^3T_1(2)$	57.9540	22.0240
	$\to {}^3T_2(1)$	57.9540	22.0240
	$\to {}^3T_2(2)$	49.9230	22.4400
	$^5E \to {}^5T_2$	161.8165	66.6965
(Mn³⁺)	$^3T_1 \to {}^3A_1$	41.9150	21.7490
	$\to {}^3A_2$	81.2790	29.1960
	$\to {}^3E(1)$	41.0635	16.9810
	$\to {}^3E(2)$	41.0635	16.9810
	$\to {}^3T_1(1)$	25.8780	11.8050
	$\to {}^3T_1(2)$	35.7190	13.6670
	$\to {}^3T_2(1)$	35.7190	13.6670
	$\to {}^3T_2(2)$	25.8780	11.8050
	$^5E \to {}^5T_2$	92.3955	38.2085
3d⁵ (Mn²⁺)	$^2T_2 \to {}^2A_1$	17.7155	6.2780
	$\to {}^2A_2$	11.6480	5.8330
	$\to {}^2E(1)$	29.3630	12.1105
	$\to {}^2E(2)$	29.3630	12.1105
	$\to {}^2T_1(1)$	97.1920	37.0010
	$\to {}^2T_1(2)$	78.9890	35.6660
	$\to {}^2T_2(1)$	78.9890	35.6660
	$\to {}^2T_2(2)$	97.1920	37.0010
3d⁵ (Fe³⁺)	$^2T_2 \to {}^2A_1$	11.7205	4.2125
	$\to {}^2A_2$	5.3190	2.7765
	$\to {}^2E(1)$	17.0395	6.9890
	$\to {}^2E(2)$	17.0395	6.9890
	$\to {}^2T_1(1)$	60.7210	23.1210
	$\to {}^2T_1(2)$	41.5170	18.8130
	$\to {}^2T_2(1)$	41.5170	18.8130
	$\to {}^2T_2(2)$	60.7210	23.1210
3d⁶ (Fe²⁺)	$^1A_1 \to {}^1T_1$	321.9420	163.2420
	$\to {}^1T_2$	552.3960	196.6920
	$^5T_2 \to {}^5E$	145.7230	59.9890
3d⁶ (Co³⁺)	$^1A_1 \to {}^1T_1$	146.8560	77.1000
	$\to {}^1T_2$	372.8400	134.0220
	$^5T_2 \to {}^5E_2$	86.6160	35.1870
3d⁷ (Co²⁺)	$^2E \to {}^2T_1(1)$	90.3560	37.0460
	$\to {}^2T_1(2)$	90.3560	37.0460
	$\to {}^2T_2(1)$	90.3560	37.0460
	$\to {}^2T_2(2)$	90.3560	37.0460
	$^4T_1 \to {}^4T_2$	101.1100	45.6500
	$\to {}^4T_1$	139.7900	53.1400
3d⁸ (Ni²⁺)	$^3A_2 \to {}^3T_1$	211.9920	75.9180
	$\to {}^3T_2$	95.2230	49.2810
3d⁹ (Cu²⁺)	$^2E \to {}^2T_2$	132.0340	53.4020

Table VI: (4d¹) System, Transition $^2T_{2g} \to {}^2E_g$, Variation of $\theta_{i \to j}$ with Z_{eff} (4d) at 300 and 0°K[a] in Approximations a and b)

Z_{eff} (4d) (Z_{eff} (5p) = 6.0)	$\theta^2T_{2g} \to {}^2E_g$ Approx. a (× 10⁻⁴)	Approx. b (× 10⁻⁵)
4.0	50.8970 (26.0480)	82.4410 (29.9330)
5.0	48.1480 (31.8450)	92.4490 (35.0655)
6.0	103.8345 (54.0840)	81.6480 (32.0205)
7.0	132.0045 (62.4785)	62.4900 (25.0325)
8.0	112.6065 (51.7235)	43.8695 (17.7495)
9.0	72.6895 (33.3415)	29.2970 (11.8640)

[a] The values in parentheses are at 0°K.

Table VII: (5d¹) System, Transition $^2T_{2g} \to {}^2E_g$, Variation of $\theta_{i \to j}$ with Z_{eff} (5d) at 300 and 0°K[a] in Approximations a and b

Z_{eff} (5d) (Z_{6p} = 6.0)	$\theta^2T_{2g} \to {}^2E_g$ Approx. a (× 10⁻⁴)	Approx. b (× 10⁻⁵)
5.00	11.8335 (6.4350)	74.3345 (25.6945)
6.0	34.2115 (11.4195)	95.7445 (34.5480)
7.0	39.8020 (13.6115)	94.5780 (35.5725)
8.0	25.8665 (11.7670)	79.2160 (30.8205)
9.0	21.3870 (14.4750)	59.6730 (23.7800)
10.0	35.0750 (22.3300)	41.9935 (16.9725)

[a] The values in parentheses are at 0°K.

In Tables VIII and IX we mention the experimental oscillator strengths for the different transitions in kd^n systems, the Dq values, and the energy separations of the energy levels between which the transition is taking place. It is important to note that we are dealing with the spin-allowed transitions only. The spin-forbidden transitions are usually much weaker in intensity, and we shall treat these cases in the future. The experimental values of the oscillator strengths have been found out by us from the relevant absorption spectra found by several workers in this field (see the references) assuming Gaussian distribution and using the formula

$$f = 4.6 \times 10^{-9} \epsilon_{max} \nu_{1/2} \qquad (3.4)$$

However, it is important to note that this way of finding the oscillator strengths may introduce a very high percentage of error; the error may be as high as 100% when-

Table VIII: The Experimental Oscillator Strengths, Dq Values, and the Energy Differences of the Complexes of the Transition Metal Ions with Their References

Config-uration	Ion	Complex	Dq, cm^{-1}	Transition $g \rightarrow g$	Energy diff, cm^{-1}	Oscillator strength, f ($\times 10^{-4}$)	Refer-ence
3d^1	Ti^{3+}	Ti(H$_2$O)$_6^{3+}$	2030	$^2T_2 \rightarrow {}^2E$	20,300	1.0	a
		Ti(urea)$_6^{3+}$	1600	$^2T_2 \rightarrow {}^2E$	16,000	4.71	b
3d^2	V^{3+}	V(H$_2$O)$_6^{3+}$	1840	$^3T_{1g} \rightarrow {}^3T_{2g}$	17,100	0.93	c
				$\rightarrow {}^3T_{1g}$	25,200	1.8	
		V^{3+} in Al$_2$O$_3$	1860	$^3T_{1g} \rightarrow {}^3T_{2g}$	17,400	1.88	d
				$\rightarrow {}^3T_{1g}$	25,200	4.29	
		V(urea)$_6^{3+}$	1740	$^3T_{1g} \rightarrow {}^3T_{2g}$	16,250	1.91	c
				$\rightarrow {}^3T_{1g}$	24,200	3.09	
3d^3	V^{2+}	V(H$_2$O)$_6^{2+}$	1180	$^4A_{2g} \rightarrow {}^4T_{2g}$	11,800	0.1	e
				$\rightarrow {}^4T_{1g}$	17,500	0.2	
	Cr^{3+}	Cr(H$_2$O)$_6^{3+}$	1740	$^4A_{2g} \rightarrow {}^4T_{2g}$	17,400	1.98	f
				$\rightarrow {}^4T_{1g}$	24,500	3.02	
		KCr(SO$_4$)$_2 \cdot 12$H$_2$O	1760	$^4A_{2g} \rightarrow {}^4T_{2g}$	17,600	1.6	e
				$\rightarrow {}^4T_{1g}$	24,700	2.2	
		Cr(OX)$_3^{3-}$	1739	$^4A_{2g} \rightarrow {}^4T_{2g}$	17,390	12.27	
				$\rightarrow {}^4T_{1g}$	23,980	24.98	
		Cr(en)$_3^{3+}$	2188	$^4A_{2g} \rightarrow {}^4T_{2g}$	21,880	10.00	g
				$\rightarrow {}^4T_{1g}$	28,570	8.33	
		Cr(NH$_3$)$_6^{3+}$	2150	$^4A_{2g} \rightarrow {}^4T_{2g}$	21,500	6.42	h
				$\rightarrow {}^4T_{1g}$	28,500	6.64	
3d^4	Cr^{2+}	Cr(H$_2$O)$_6^{2+}$	1400	$^5E \rightarrow {}^5T_2$	14,000	1.8	e
	Mn^{3+}	CsMn(SO$_4$)$_2 \cdot 12$H$_2$O	2100	$^5E \rightarrow {}^5T_2$	21,000	1.17	i
3d^6	Fe^{2+}	Fe(H$_2$O)$_6^{2+}$	1040	$^5T_2 \rightarrow {}^5E$	10,400	0.25	j
	Co^{3+}	Co(en)$_3^{3+}$	2320	$^1A_1 \rightarrow {}^1T_1$	21,400	13.84	k
				$\rightarrow {}^1T_2$	29,600	14.35	
		Co(OX)$_3^{3-}$	1800	$^1A_1 \rightarrow {}^1T_1$	16,500	23.59	l
				$\rightarrow {}^1T_2$	23,810	35.20	
		Co(NH$_3$)$_6^{3+}$	2290	$^1A_1 \rightarrow {}^1T_1$	21,070	15.41	m
				$\rightarrow {}^1T_2$	29,600	12.24	
3d^7	Co^{2+}	Co(H$_2$O)$_6^{2+}$	930	$^4T_1 \rightarrow {}^4T_2$	8,200	0.27	n
				$\rightarrow {}^4T_1$	20,000	0.75	k
		CoSO$_4 \cdot 7$H$_2$O	1000	$^4T_1 \rightarrow {}^4T_2$	8,350	0.3	e
				$\rightarrow {}^4T_1$	19,800	0.9	
		Co(NH$_3$)$_6^{2+}$	1010	$^4T_1 \rightarrow {}^4T_2$	9,000	0.26	o
				$\rightarrow {}^4T_1$	21,100	1.38	o
		Co(en)$_3^{2+}$	1100	$^4T_1 \rightarrow {}^4T_2$	9,800	0.53	o
				$\rightarrow {}^4T_1$	21,700	2.81	o
3d^8	Ni^{2+}	Ni(H$_2$O)$_6^{2+}$	850	$^3A_2 \rightarrow {}^3T_2$	8,500	0.22	p
				$\rightarrow {}^3T_1$	14,700	0.35	p
		Ni(NH$_3$)$_6^{2+}$	1075	$^3A_2 \rightarrow {}^3T_2$	10,750	0.53	p
				$\rightarrow {}^3T_1$	17,500	0.70	p
		Ni(en)$_3^{2+}$	1120	$^3A_2 \rightarrow {}^3T_2$	11,200	1.03	p
				$\rightarrow {}^3T_1$	18,350	1.02	p
3d^9	Cu^{2+}	Cu(H$_2$O)$_6^{2+}$	1260	$^2E \rightarrow {}^2T_2$	12,600	2.9	q
		CuSO$_4 \cdot 5$H$_2$O	1300	$^2E \rightarrow {}^2T_2$	13,000	1.4	e
		CuSiF$_6 \cdot 6$H$_2$O	1250	$^2E \rightarrow {}^2T_2$	12,500	1.8	r
		CuSiF$_6 \cdot 6$H$_2$O (78°K)	1333	$^2E \rightarrow {}^2T_2$	13,330	0.66	
4d^1	Nb^{4+}	Nb^{4+}(Cl)$_6$ (13 M HCl)	2090	$^2T_2 \rightarrow {}^2E$	20,900	27.26	s
4d^2	Nb^{3+}	Nb(Cl)$_6^{2+}$	~1980	$^3T_1 \rightarrow {}^3T_2$	18,900	30.64	s
				$\rightarrow {}^3T_1$	22.500	56.15	s
4d^3	Nb^{2+}	Nb(Cl)$_6^{2+}$ (strong HCl)	2270	$^4A_2 \rightarrow {}^4T_2$	22,700	25.25	s
				$\rightarrow {}^4T_1$	Not observed		
	Mo^{3+}	Mo(Cl)$_6^{3-}$	1900	$^4A_2 \rightarrow {}^4T_2$	19,000	7.27	t
				$\rightarrow {}^4T_1$	24,000	16.17	
4d^5	Ru^{3+}	Ru(Cl)$_6^3$	2400	$^2T_2 \rightarrow {}^2A_2$	19,200	7.0	u
				(only this transition is believed to be of crystal field origin)			

Table VIII *(Continued)*

Config-uration	Ion	Complex	Dq, cm^{-1}	Transition $g \rightarrow g$	Energy diff, cm^{-1}	Oscillator strength f ($\times 10^{-4}$)	Refer-ence
		Ru(Br)$_6$$^{3-}$	~2030	$^2T_2 \rightarrow {}^2A_2$	15,300	18.0	u
4d^6	Rh^{3+}	Rh(H$_2$O)$_6$$^{3+}$	2700	$^1A_1 \rightarrow {}^1T_1$	25,500	11.0	
				$\rightarrow {}^1T_2$	32,800	14.0	
		Rh(OX)$_3$$^{3-}$	2640	$^1A_1 \rightarrow {}^1T_1$	25,100	54.0	
		Rh(NH$_3$)$_6$$^{3+}$	3410	$^1A_1 \rightarrow {}^1T_1$	32,700	30.0	
				$\rightarrow {}^1T_2$	39,100	25.0	
		Rh(en)$_3$$^{3+}$	3460	$^1A_1 \rightarrow {}^1T_1$	33,200	48.0	
				$\rightarrow {}^1T_2$	39,600	46.0	
		Rh(Cl)$_6$$^{3-}$	2160	$^1A_1 \rightarrow {}^1T_1$	19,300	14.0	
				$\rightarrow {}^1T_2$	24,300	13.0	
		Rh(Br)$_6$$^{3-}$	2000	$^1A_1 \rightarrow {}^1T_1$	18,100	25.0	
				$\rightarrow {}^1T_2$	22,200	25.0	
5d^6	Ir^{3+}	Ir(Cl)$_6$$^{3-}$	2800	$^1A_1 \rightarrow {}^1T_1$	24,100	12.5	
				$\rightarrow {}^1T_2$	28,100	12.0	
5d^6	Ir^{3+}	Ir(Br)$_6$$^{3-}$	2500	$^1A_1 \rightarrow {}^1T_1$	22,400	37.0	
				$\rightarrow {}^1T_2$	25,800	32.0	
		Ir(en)$_3$$^{3+}$	4140	$^1A_1 \rightarrow {}^1T_1$	40,200	40.0	
				$\rightarrow {}^1T_2$ (not observed)	...	...	
	Pt^{4+}	Pt(Cl)$_6$$^{2-}$	3000	$^1A_1 \rightarrow {}^1T_1$	28,300	70.0	

[a] H. Hartman, et al., Z. Anorg. Allg. Chem., **284**, 153 (1956). [b] H. Hartmann, et al., ibid., **289**, 40 (1957). [c] H. Hartmann and C. Furlani, Z. Phys. Chem. (Frankfurt am Main), **9**, 162 (1956). [d] W. Low, ibid., **13**, 107 (1957). [e] O. G. Holmes and D. S. McClure, J. Chem. Phys., **26**, 1688 (1956). [f] C. K. Jorgensen, Acta Chem. Scand., **8**, 1496 (1954). [g] A. Mead, Trans. Faraday Soc., **30**, 1052 (1934). [h] M. Linhard, Z. Electrochem., **50**, 224 (1944). [i] H. Hartmann and H. L. Schlafer, Z. Naturforsch., **64**, 762 (1951). [j] C. K. Jorgensen, Acta Chem. Scand., **8**, 1507 (1954). [k] C. K. Jorgensen, ibid., **8**, 1495 (1954). [l] A. Mead, Trans. Faraday Soc., **30**, 1054 (1934). [m] H. Kuroya and R. Tsuchida, Bull. Chem. Soc. Jap., **15**, 429 (1940). [n] T. Dreisch and W. Trommer, Z. Phys. Chem. B (Leipzig), **37**, 40 (1937). [o] C. J. Ballhausen and C. K. Jorgensen, Acta Chem. Scand., **9**, 397 (1955). [p] C. K. Jorgensen, ibid., 1362 (1955). [q] J. Bjerrum, C. J. Ballhausen, and C. K. Jorgensen, ibid., **8**, 1281 (1954). [r] R. Pappalardo, J. Mol. Spectrosc., **6**, 554 (1961). [s] D. Cozzi and S. Vivarelli, Z. Anorg. Allg. Chem., **279**, 165 (1955). [t] H. Hartmann and H. J. Schmidt, Z. Phys. Chem. (Frankfurt am Main), **11**, 234 (1957). [u] C. K. Jorgensen, Acta Chem. Scand., **10**, 518 (1956). [v] C. K. Jorgensen, ibid., **10**, 500 (1956); **11**, 151 (1957).

Table IX: The Experimental Results on the Melts

Config-uration	Ion	Complex[a,e]	ν_{max}, cm^{-1}	Transition		Dq	Refer-ence
3d^1	Ti^{3+}	TiCl$_6$$^{3-}$	10,000	$^2T_{2g} \rightarrow {}^2E_g$	~10^{-4} [b]	1150[c]	d
			13,000				
3d^2	V^{3+}	VCl$_6$$^{3-}$	11,000	$^3T_{1g} \rightarrow {}^3T_{2g}$	2.0×10^{-4}	1275	e
			18,020	$^3T_{1g} \rightarrow {}^3T_{1g}$	6.4×10^{-4}		d
3d^3	V^{2+}	VCl$_6$$^{4-}$	7,200	$^4A_{2g} \rightarrow {}^4T_{2g}$	~1.34×10^{-4}	720	d
			12,020	$^4A_{2g} \rightarrow {}^4T_{1g}$	~2.06×10^{-4}		
			19,050	$^4A_{2g} \rightarrow {}^4T_{1g}$	~3.21×10^{-4}		
	Cr^{3+}	CrCl$_6$$^{3-}$	12,500	$^4A_{2g} \rightarrow {}^4T_{2g}$	~8.4×10^{-4}	1250	d, f
			18,500	$^4A_{2g} \rightarrow {}^4T_{1g}$	~14.0×10^{-4}		
	Cr^{3+}	CrF$_6$$^{3-}$	14,600	$^4A_{2g} \rightarrow {}^4T_{2g}$	...	1460	g
			22,300	$^4A_{2g} \rightarrow {}^4T_{1g}$	...		
3d^2	V^{3+}	V(CN)$_6$$^{3-}$	22,200	$^3T_{1g} \rightarrow {}^3T_{2g}$	6.1×10^{-4}	2340	h
			28,600	$^3T_{1g} \rightarrow {}^3T_{1g}$	12.6×10^{-4}		

[a] Chloride complexes in LiCl–KCl eutectic at 400° and the fluoride complex in LiF–NaF–KF eutectic at 650°. [b] Combined oscillator strength. [c] Average Dq. [d] D. M. Gruen and R. L. McBeth in the "Coordination Chemistry of 3d Transition Metal Ions in Fused Salt Solution," Plenary Lectures at VII I.C.C.C., Stockholm, Sweden, 1962. [e] D. M. Gruen and R. L. McBeth, J. Phys. Chem., **66**, 57 (1962). [f] G. Harrington and B. R. Sundheim, Ann. N. Y. Acad. Sci., **79**, 950 (1960). [g] J. P. Young and J. C. White, Anal. Chem., **32**, 799 (1960). [h] J. R. Perumareddi, A. D. Liehr, and A. W. Adamson, J. Amer. Chem. Soc., **85**, 249 (1963).

ever a crystal field band falls near the edge of a charge-transfer band. Also, if the bands are not symmetric, the Gaussian distribution should not be valid in such cases; thus, estimating the oscillator strengths may be extremely difficult.

A Few Examples. In Table X we present the theoret-

Table X: Comparison of Theoretical and Experimental f's in Approximation c (See the Text)

Config-uration	Ion	Transition (g→g)	$\theta_{i \to j}$ (approx. c)^a (× 10^{-4})	$E_i - E_j$,^{b} cm^{-1}	$\lambda(s)^c$ (× 10^{-2})	Theoretical $f \times 10^4$	Experimental^b $f \times 10^4$
3d^1	Ti^{3+}	$^2T_2 \to {}^2E$	99.6675 (41.6115)	20,300	3.42	3.7577 (1.5688)	1.0
3d^2	V^{3+}	$^3T_1 \to {}^3T_1$	94.0900 (36.3660)	25,200	4.85	5.2929 (2.0457)	1.8
		$\to {}^3T_2$	79.3330 (36.3660)	17,100	3.29	3.0283 (1.3882)	1.93
3d^3	Cr^{3+}	$^4A_2 \to {}^4T_1$	141.1035 (50.6235)	24,500	2.37	8.0218 (2.8780)	1.98
		$\to {}^4T_2$	82.5345 (42.5385)	17,400	1.68	3.3329 (1.7174)	3.02
3d^6	Fe^{2+}	$^5T_2 \to {}^5E$	145.7230 (59.9890)	10,400	0.98	1.5794 (0.6519)	0.25
3d^7	Co^{2+}	$^4T_1 \to {}^4T_2$	101.1100 (45.6500)	8,200	0.83	0.9107 (0.4112)	0.3
		$\to {}^4T_1$	139.7900 (53.1400)	20,000	2.02	3.0710 (1.1674)	0.75
3d^8	Ni^{2+}	$^3A_2 \to {}^3T_1$	211.992	·14,700	1.64	3.7343 (1.3740)	0.35
		$\to {}^3T_2$	95.2230 (49.2810)	8,500	0.95	0.9700 (0.5020)	0.22
3d^9	Cu^{2+}	$^2E \to {}^2T_2$	132.0340 (53.4020)	12,600	4.03	5.6433 (2.2825)	2.9

^{a} See Table V. ^{b} See Tables VIII and IX; the experimental f's are at about 20°K for most of the cases. ^{c} $\lambda(s)$ has been calculated using the value of $f_{d \to p}$ assuming 10% covalency from Table II.

ical oscillator strengths calculated in the approximation c, i.e., by using Richardson–Watson's SCF wave functions for the hydrated complexes of the 3d^n transition metals and compare these with the experiment. Here we have used $f_{d \to p}$ from Table II (corresponding to set 2 of Table I) and $E_p - E_d \approx 12$ eV.

From Table X we see that the calculated and observed oscillator strengths are in very reasonable agreement. Our main aim was to see whether the semipoint charge model and the vibronic mechanism are capable of explaining at least qualitatively the observed oscillator strengths of the crystal field bands of the 3d^n octahedral complexes. We can say that within the limits of our approximations involved we are successful in getting a semiquantitative understanding of the observed crystal field spectra. One of the sources of error, and probably one of the main sources, is the odd vibrational frequencies which vary widely for different complexes (Table III). Moreover, the vibrational frequencies quoted in Table III are for the XY$_6$ complex and not for the crystal. Hence the contribution from the optical and acoustical mode in the vibrational frequencies, and hence in the oscillator strengths, cannot be ascertained until and unless experiments are done with crystalline complexes. Therefore, appreciable experimental work is highly desirable in this direction. To the best of our knowledge we do not know of any experiment done in this direction up to the present day.

Considering these approximations mentioned above, we think the agreement with experiment is good. In our later work we plan to work out the oscillator strengths for specific cases using the experimentally observed values for the semiempirical parameters if and when they are available. The vibronic theory outlined in this paper for the kd^n electronic configurations of the transition metal complexes applies equally well to the f^n configurations of the rare earth complexes. A large amount of experimental data on the absorption spectra of the rare earth complexes is now available so that this type of calculations is very desirable. It is well known that the absorption spectra of the rare earths are very sharp compared to those of the transition metal ions, and therefore the oscillator strengths can be found out very precisely from experiments unlike the transition metal spectra. The dipolar and covalent model should be a much more realistic model in calculating the necessary integrals involved in our calculations, and we hope we shall be able to do some work in this model in near future.

A Near-Infrared Spectroscopic Investigation of the Effect of

Temperature on the Structure of Water[1]

by William C. McCabe,[2] S. Subramanian, and Harvey F. Fisher*

Veterans Administration Hospital, Kansas City, Missouri   64128   and Department of Biochemistry, University of Kansas Medical Center, Kansas City, Kansas   66103   (Received June 12, 1970)

Studies on the effect of temperature on the 1.45-μ absorption band of water indicate that water is composed of an equilibrium mixture of not less than two components. One of these components is identified as singly hydrogen-bonded water based on its correlation with singly hydrogen-bonded water in acetone. Another component has a spectral contribution similar to that of ice and, hence, is identified as an "icelike" species.

Introduction

The details of the intermolecular structure in liquid water constitute a subject of vigorous investigation and controversy. Several reviews[3a-c] and monographs[4,5] have appeared in recent years, summarizing the current status of research on the structure of water. The current models of water structure may be broadly divided into two major categories. The first of these treats water essentially as a dielectric continuum[6] while the second category admits the simultaneous existence of at least two species of water, the structural models which Frank has termed "mixture models." The continuum model as proposed by Pople[6] postulated that H bonds will be bent but not broken when water is formed from ice or when the temperature of water is raised. The opponents[7-9] of mixture model have rested their case mainly on the lack of evidence for distinct molecular species from Raman and infrared studies of HDO. In addition, Stevenson[10,11] has pointed out that the fraction of monomer water (which is one of the components in many of the mixture models) in liquid water from 0° to 100° is less than 1%. These studies[7-11] thus lend credence to the continuum model.

Mixture models[12-16] include in their fold at least two kinds of species, a bulky species representing some type of H-bonded structure and a dense species such as monomeric or free water molecules. The experimental support for mixture models, in general, comes from the near-infrared studies of Luck,[17] and Raman spectra of H_2O and HOD studied by Walrafen.[18] Since the mix-

* To whom correspondence should be addressed.

(1) This work was supported in part by a Public Health Service research grant (GM 15188) from the National Institutes of Health and a National Science Foundation grant (GB 3915).

(2) Supported by a predoctoral fellowship from the National Institutes of Health (5-F1-GM-34,000).

(3) (a) H. S. Frank, *Fed. Proc., Fed. Amer. Soc. Exp. Biol., Suppl.,* **24,** 15, S-1 (1965); (b) G. Nemethy and H. A. Scheraga, *J. Chem. Phys.,* **36,** 3382 (1962); (c) E. Wicke, *Angew. Chem. Int. Ed. Engl.,* **5,** 106 (1966).

(4) J. L. Kavanau, "Water and Solute–Water Interactions," Holden-Day, San Francisco, Calif., 1964.

(5) D. Eisenberg and W. Kauzmann, "The Structure and Properties of Water," Oxford University Press, New York, N. Y., 1969.

(6) J. A. Pople, *Proc. Roy. Soc. Ser. A,* **205,** 163 (1951).

(7) T. T. Wall and D. F. Hornig, *J. Chem. Phys.,* **43,** 2079 (1965); T. T. Wall and D. F. Hornig, *ibid.,* **47,** 784 (1967).

(8) M. Falk and T. A. Ford, *Can. J. Chem.,* **44,** 1699 (1966).

(9) E. U. Franck and K. Roth, *Discuss. Faraday Soc.,* **43,** 108 (1967).

(10) D. P. Stevenson, *J. Phys. Chem.,* **69,** 2145 (1965).

(11) D. P. Stevenson, "Structural Chemistry and Molecular Biology," A. Rich and N. R. Davidson, Ed., W. H. Freeman and Company, San Francisco, Calif., 1968, p 490.

(12) H. S. Frank and W. Y. Wen, *Discuss. Faraday Soc.,* **24,** 133 (1957).

(13) L. Pauling, "Nature of the Chemical Bond," Cornell University Press, Ithaca, New York, 1960, p 464.

(14) E. Forslind, *Proc. Int. Congr. Rheol. 2nd,* 1953 (1954).

(15) O. Y. Samoilov, "Structure of Aqueous Electrolyte Solutions and the Hydration of Ions," Consultants Bureau, New York, N. Y., 1965.

ture model is very useful in explaining the properties of aqueous solutions, it needs further study.

If discrete H-bonded species, each with its own absorption properties, exist in liquid water, then the unambiguous isolation and identification of one of these component species would establish the validity of the "mixture model." As pointed out by Luck,[19] it is difficult to achieve this in the OH fundamental vibration region. We have investigated the overtone region for the effect of temperature on the 1.45-μ band of H_2O (assigned to $\nu_1 + \nu_3$)[20] to isolate, if possible, discrete and distinct species.

Experimental Section

The water used in these experiments was deionized tap water which was found in this laboratory to be equivalent to glass-distilled water. Acetone and chloroform were spectroquality reagents from Matheson Coleman and Bell. $NaClO_4$ was obtained from Fisher Scientific Co.

All spectra were recorded using a Cary Model 14R double-beam recording spectrophotometer. The absorption cells were of the insert type, producing pathlengths of either 0.1000 or 0.0500 ± 0.0001 cm. The temperature of water (solution) in the cells was controlled by circulating water from a thermostat through the metallic cell holders to ±0.02°. The final temperature stabilization was followed by setting the monochromator at 1.410 μ and recording the absorbance at this wavelength. The sensitivity at 1.410 μ is approximately 0.0007 absorbance unit per 0.1° change in temperature.

The absorption spectra of water presented in Figure 1 were obtained by recording the absorption of water measured vs. an empty cell. The spectra of water in solution of $NaClO_4$ in water (Figure 7) were also recorded in the same way. In these spectra no correction for variation of reflectance loss with frequency was necessary. The absorbance at 0.7000 μ was zero, within experimental error for 0.1-cm path length of water. The absorbance at 0.7000 μ was assumed to be zero for all spectra and, therefore, plotting the data based on this assumption would constitute a correction for reflectance loss.

The temperature difference spectra presented in Figure 3 were obtained by maintaining the reference cell water at 20° and sample cell water at higher temperatures to obtain temperature differentials of 10, 20, 30, 40, 50, and 60°. The spectra presented in Figures 2 and 3 have been corrected for the density changes of water with temperature and thus represent water spectra at the same concentration in sample and reference cells. The magnitude of this correction is approximately 10% at most frequencies.

The refractive index measurements were made at 546 mμ using a Phoenix–Brice differential refractometer thermostated at 20°.
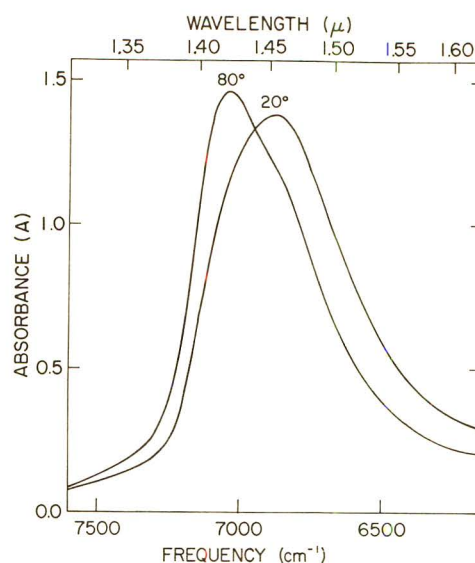

Figure 1. The near-infrared absorption spectrum of water at 20 and 80°. Curve 20° is the spectrum of water at 20° measured vs. the absorption cell. The absorption cell path lengths were 0.1 cm. Curve 80° is the spectrum of water at 80° measured vs. the absorption cell. The absorption cell path lengths were 0.1 cm.

Results and Discussion

A. *Effect of Temperature on the Near-Infrared Spectrum of Water*. The change in the near-infrared absorption of water in the 1.45-μ region from 20 to 80° (Figure 1) cannot be explained by a shift of the entire absorption envelope to higher frequencies. At 80°, there is a definite shoulder at 6850 cm^{-1} (1.460 μ). The appearance of a shoulder at higher temperature indicates that there are at least two component species undergoing change in their relative concentrations with temperature. While Fermi resonance can be cited as a cause for the observed spectral changes with temperature, we shall present an argument later that Fermi resonance is not responsible for the spectral changes caused by temperature change in the 1.45-μ region. It is assumed here and throughout the paper that a spectral change following a temperature change reflects a significant alteration in the structure of water. A critical test of this assumption is made out in the spectra presented in Figure 2. The solid line is the absorption spectrum of a saturated solution of water in $CHCl_3$ at 57 ± 3°. The dotted line is the spectrum of the same solution cooled to 22°. It can be seen that a 35° change in temperature produces a peak shift of only 0.0015 μ (5.5

(16) R. P. Marchi and H. Eyring, *J. Phys. Chem.*, **68**, 221 (1964).

(17) W. A. P. Luck, "Physico-Chemical Processes in Mixed Aqueous Solvents," F. Franks, Ed., Heinemann, London, 1967, Chapter II.

(18) G. E. Walrafen, *J. Chem. Phys.*, **47**, 114 (1967); G. E. Walrafen, *ibid.*, **48**, 244 (1968); G. E. Walrafen, "Hydrogen-Bonded Solvent Systems," A. K. Covington and P. Jones, Ed., Taylor and Francis, London, 1968, p 9.

(19) W. A. P. Luck, *Discuss. Faraday Soc.*, **43**, 134 (1967).

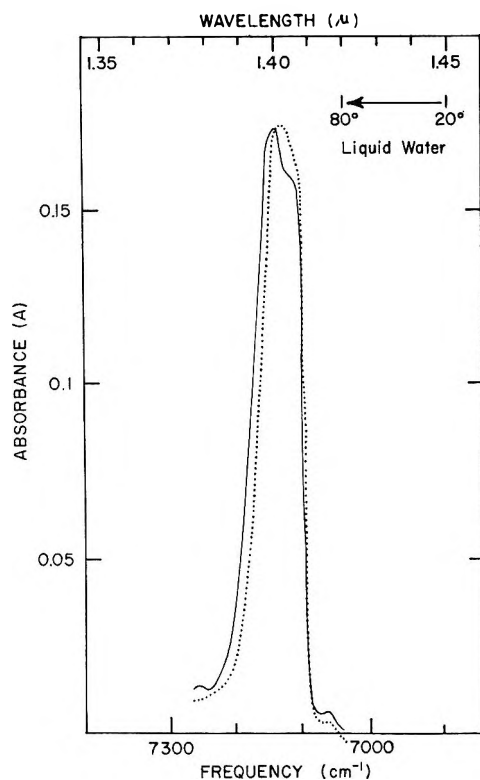(20) H. Yamatera, B. Fitzpatrick, and G. Gordon, *J. Mol. Spectrosc.* **14**, 268 (1964).

Figure 2. The effect of temperature on an isolated absorption band of a solution of structureless water in CHCl₃. The solid line is the spectrum of a saturated solution of water in CHCl₃ at 57 ± 3° measured vs. CHCl₃ at the same temperature. The dotted line is the absorption spectrum of the same system after cooling to 22°; 0.5-cm path length cylindrical cells were used. The arrow in the upper right-hand corner of the figure shows for comparison the spectral shift of liquid water on heating from 20 to 80°.

Figure 3. The near-infrared temperature difference spectra of water at temperature differentials of 10, 20, 30, 40, 50, and 60°. Curves 10, 20, 30, 40, 50, and 60° are the difference spectra for water at 30, 40, 50, 60, 70, and 80 measured vs. water at 20° (the "A" curves); each spectrum was corrected for the difference in density between the sample and reference absorption cells. The absorption cell path lengths were 0.1 cm.

Figure 4. Resolution of a temperature difference spectrum into its component curves. The "A" curve is the temperature difference spectrum for water measured vs. water with a temperature differential of 40°; it is the same as the 40° "A" curve presented in Figure 3. The "B" curve represents the Gaussian distribution of absorption which corresponds to the high-frequency portion of the "A" curve. The "C" curve is the algebraic difference between the "A" and "B" curves plotted in the positive sense.

cm⁻¹). The absorption spectrum of pure water demonstrates a peak shift of 0.030 μ (150 cm⁻¹) for a 60° change. Clearly, the temperature difference alone could not have produced such a shift by a purely spectroscopic effect; it must, then, have produced some alteration in the system which is responsible for the spectral shift. In other words, the effect of temperature change is to produce a structural change in water. The specific explanation for the absence of a significant temperature effect on the spectrum of water in CHCl₃ is apparent. The spectrum of water at its critical temperature (374.5°) exhibits a peak with a maximum at 1.40 μ (see Figure 11). There can be no question that water at its critical temperature must be totally lacking in structure. If water dissolved in CHCl₃ were to exist largely as monomer, it should also absorb at 1.40 μ and this peak should be invariant with temperature. This is precisely what we have observed.

B. The Temperature Difference Spectra. Having established that the spectral change, caused by temperature change, is a sequel to structure change, we proceed to analyze the characteristics of the temperature difference spectra (Figure 3). Each of the temperature difference spectra, "A" curves, in Figure 3 can be resolved
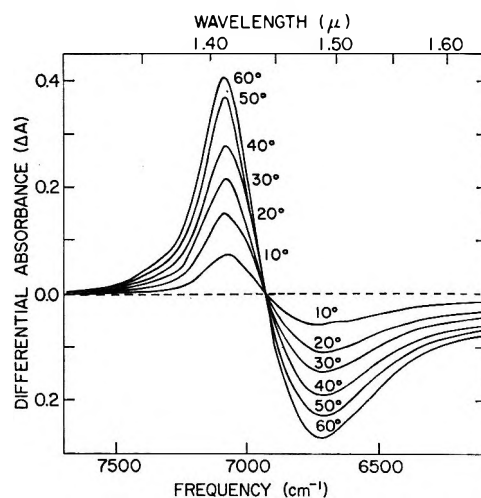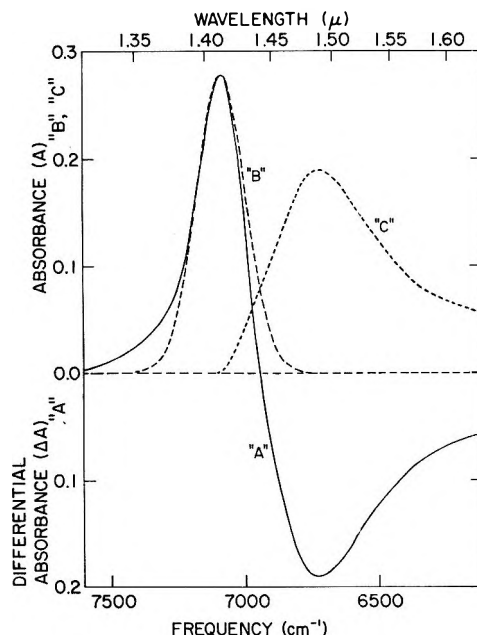
into two component curves, "B" and "C." For the purpose of illustration, the 40° "A" curve has been resolved into its component "B" and "C" curves in Figure 4. Both "B" and "C" curves are plotted in the

Table I: Summary of the Variation in the Absorption Parameters of the "A" Curves with Temperature

Property	Temperature differential (ΔT)					
	10°	20°	30°	40°	50°	60°
$(\nu_0)_{max} \pm 5$ cm^{-1}	7080	7080	7080	7081	7083	7085
$(\nu_0)_{min} \pm 10$ cm^{-1}	6710	6710	6710	6710	6710	6710
$(\Delta A_{\nu_0})_{max}$	0.0738	0.1500	0.2135	0.278	0.369	0.406
$(\Delta A_{\nu_0})_{min}$	0.0560	0.1105	0.1465	0.190	0.229	0.267
$(\Delta \nu_{1/2})_B \pm 10$ cm^{-1}	214	218	218	216	214	216
$[(\nu_0)_{max}]_{av}$			7081 $\pm$ 5 cm^{-1}			
$[(\Delta \nu_{1/2})_B]_{av}$			216 $\pm$ 10 cm^{-1}			
$[(\Delta A_{\nu_0})_{max}/(\Delta A_{\nu_0})_{min}]$	1.318	1.357	1.457	1.463	1.615	1.519
$(\Delta A/\Delta T)_{max}$	0.0074	0.0075	0.0072	0.0070	0.0074	0.0068
$(\Delta A/\Delta T)_{min}$	0.0056	0.0055	0.0049	0.0048	0.0047	0.0045
$(A_\nu)_{H_2O}{}^a$	0.9630	0.9590	0.9550	0.9510	0.9460	0.9400
$[(\Delta A_{\nu_0})_{max}/(A_\nu)_{H_2O}]$	0.077	0.156	0.224	0.292	0.391	0.431

[a] These values have been adjusted to represent the concentration of water in the sample absorption cell. The excess water in the reference absorption cell has been canceled and does not contribute to the spectra presented in Figure 3.

positive sense. All of the "B" and "C" curves are similar in shape.

The "B" curve in Figure 4 represents a Gaussian distribution of absorption, obtained from the "A" curve. The absorption parameters of a Gaussian distribution, namely ν_0, the frequency of absorption maximum, A_{ν_0}, the absorbance at ν_0, and $\Delta \nu_{1/2}$, the half band width, for each of the differential spectra ("A" curve) are listed[21,22] in Table I. The values for ν_0, A_{ν_0}, and $\Delta \nu_{1/2}$ for each of the "A" curves are presented under the headings $(\nu_0)_{max}$, $(\Delta A_{\nu_0})_{max}$, and $(\nu_0)_B$. These represent the high-frequency limb of the "A" curves. For the 40° "A" curve $(\nu_0)_{max}$ is 7081 $\pm$ 5 cm^{-1}, $(\Delta A_{\nu_0})_{max}$ is 0.278, and $(\Delta \nu_{1/2})_B$ is 216 $\pm$ 10 cm^{-1}. The "C" curve (Figure 4) is simply the algebraic difference between the "A" and the "B" curves and plotted (in Figure 4) in the positive sense.

The frequencies at the maxima and minima $(\nu_0)_{max}$ and $(\nu_0)_{min}$ for the "A" curves are invariant with temperature within experimental error (see Table I). The average values for $(\nu_0)_{max}$ and $(\nu_0)_{min}$ are 7081 $\pm$ 5 cm^{-1} ($\sim$1.412 μ) and 6710 $\pm$ 10 cm^{-1} ($\sim$1.49 μ), respectively. The half band widths of the "B" curves are also invariant with temperature within experimental error. The ratio of the absorbance at the maxima to that at the minima for the "A" curves $(\Delta A_{\nu_0})_{max}/(\Delta A_{\nu_0})_{min}$, however, show a significant temperature dependence. There appears to be a discontinuity at 70° ($\Delta T = 50°$). This temperature dependence is too small, however, to be more than a secondary effect of temperature on the structure of water. Therefore, all the data contained in Table I are consistent with the conclusion that water is composed of at least two components. The absorption properties of these two components are represented by the "B" and "C" curves (Figure 4). The total absorption band in the 1.45-μ region (Figure 1) cannot be fitted by a summation of "B" and "C" curves representing the temperature-sensitive components.[23] These

two components, then, cannot be the sole species comprising water structure; there must be some other component which does not show up in the temperature difference spectra. This third component, with an absorption centered around 1.46 μ, contributes about 15% to the total absorption and this contribution is apparently invariant with temperature in the range (20–80°) studied here.

C. Identification of "B" Curve with Water-in-Acetone Spectrum. In order to prove that the resolution of the "A" curves is not arbitrary and that the "B" and "C" curves represent real species, and also to provide meaningful identities for the "B" and "C" curves, it is necessary to equate the resolved curves to physically obtainable species. If one of the curves ("B" curve, for example) is identified with some isolable species of water, the other will also be proved to correspond to another species, through a complementary process.

The absorption spectra for two different concentrations of water in acetone vs. CCl$_4$ in acetone are presented in Figure 5 (curves A and B). These spectra represent the absorption by water in acetone in the 1.45-μ region of absorption by water. The solvent balance between the sample and reference cells was obtained using the nonabsorbing CCl$_4$ as a diluent for acetone in the reference cell.[24]

(21) The Gaussian error function,[22] $A_\nu = A_{\nu_0} \exp(-[\ln 2][2(\nu_0 - \nu)/(\Delta \nu_{1/2})]^2)$, was used to calculate the absorbance at a given frequency, A_ν, for an absorption peak with its frequency of maximum absorbance at ν_0, and with half band width equal to $\Delta \nu_{1/2}$.

(22) R. D. B. Fraser, "A Laboratory Manual of Analytical Methods of Protein Chemistry (Including Polypeptides)," P. Alexander and R. J. Block, Ed., Pergamon Press, New York, N. Y., 1960, p 291.

(23) Studying different overtone bands of H$_2$O, D$_2$O, and HOD, Luck also arrives at the conclusion that the "free" OH and "bonded" OH, in his two-species model, do not add up to 100% [see also W. A. P. Luck, Discuss. Faraday Soc., 41, 141 (1967).] Luck[17] further suggests that there may be a species with energetically unfavorable H bonds which corresponds approximately with our third component.
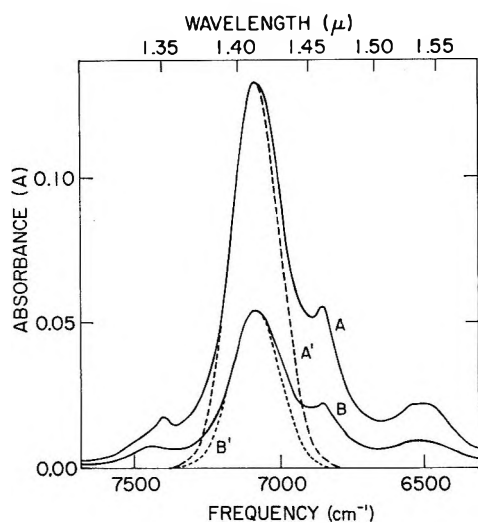
Figure 5. The spectra of water dissolved in acetone. Curve A is the difference spectrum of 25 μl of H_2O in 3 ml of acetone measured *vs.* 25 μl of CCl_4 dissolved in 3 ml of acetone; the concentration of water was 0.462 M. The absorption cell path lengths were 1 cm. The absorption cells were thermostated at 17°. Curve B is similar to curve A; 10 μl of H_2O was used. The concentration of water was 0.184 M. Curves A′ and B′ are the Gaussian distribution of absorption corresponding to the major peaks in curves A and B, respectively.

Figure 6. The variation of refractive index and position of the 1.45-μ absorption peak with mole fraction of water in acetone. The upper curve is a plot of the change in refractive index, Δn, of water–acetone solutions *vs.* mole fraction of water. The lower curve is a plot of the peak position for the 1.45-μ water peak in the spectra of different water–acetone solutions *vs.* mole fraction of water.

The Gaussian distributions of absorption representing the major peak in the 1.45-μ region of water in acetone (curves A′ and B′) are indicated in Figure 5. The corresponding absorption distribution parameters are $\nu_0 = 7075$ cm^{-1} (1.413 μ), $\Delta\nu_{1/2} = 200$ cm^{-1}, and $A\nu_0$ equal to 0.0544 and 0.132. These can be compared with the average values of $\nu_0 = 7081 \pm 5$ cm^{-1} and $\Delta\nu_{1/2} = 216 \pm 10$ cm^{-1} of the "B" curves (Table I). Thus, within experimental error, the absorption represented by the "B" curves and the major peak in the water in acetone absorption spectrum can both be fitted by the same Gaussian distribution of absorption. This indicates that the corresponding water species are equivalent, *i.e.*, they have the same average distribution of kinds and numbers of hydrogen bonds. Lin, *et al.*,[25] studied the environment of water in the system water–acetone–1,2-dichloroethane by solubility, nmr, and dielectric measurements of different water–acetone mixtures and concluded that acetone forms primarily a monohydrate with water by forming an H bond between a hydrogen of water and the carbonyl oxygen.[26]

In Figure 6 two experimental parameters for water–acetone mixtures are plotted *vs.* mole fraction of water: (1) the peak position for the 1.45-μ band and (2) the change in refractive index, Δn.[27] A critical point occurs in both plots at approximately 0.5 mole fraction of water, where a rapid change in slope occurs. This indicates that nonsolvent-bound water increases at higher mole fractions of water. The common feature in both measurements is the stoichiometry of a one-to-one complex between water and acetone. The 1:1 com-
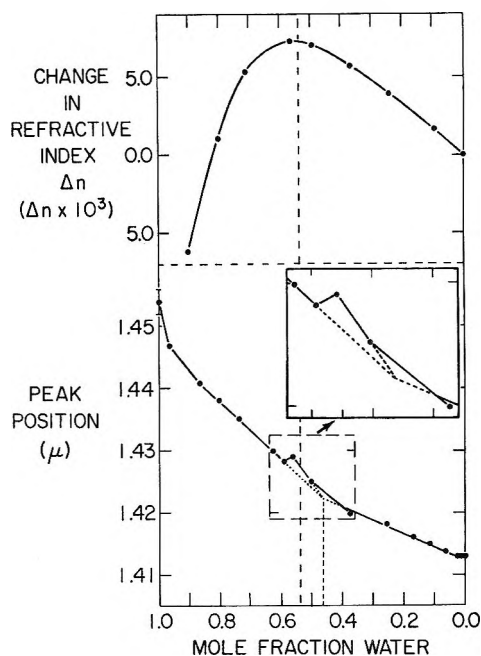
plex, although favored by the studies listed above, cannot be completely established. However, all data are consistent with a 1:1 complex between acetone and water. If the relationship between absorption properties and bonding assumed above is true, then the water species whose absorption is represented by the "B" curve in Figure 4 and the water–acetone complex whose absorption is represented by curves A′ and B′ in Figure 5 are equivalent. If the water–acetone complex is a 1:1 complex, then the water species equivalent to this must be singly hydrogen-bonded molecules of the type D_1A_1 and D_1A_2.[28]

In addition to the major peak at 1.413 μ, the spectrum of water in acetone has other minor peaks at 1.46 and 1.54 μ (Figure 5). These peaks may arise from other combinations or overtones characteristic of the water–

(24) While it is not possible to determine if all of the absorption by the organic solvents was canceled by this balancing procedure, this contribution is small in relation to that of the absorption by water.

(25) T. F. Lin, S. D. Christian, and H. E. Affsprung, *J. Phys. Chem.*, **69**, 2980 (1965); T. F. Lin, S. D. Christian, and H. E. Affsprung, *ibid.*, **71**, 1133 (1967).

(26) W. H. de Jeu, *ibid.*, **74**, 822 (1970).

(27) Refractive index data for water–acetone solutions are also available in the International Critical Tables.

(28) Stevenson[11] described the different water species in terms of a D-donor and A-acceptor notation. D represents the donor (the H atoms of the water molecule are donated for H bonding) and A represents the acceptor (the oxygen atom accepts one or two H atoms for H bonding). In a D_iA_j representation the subscripts i and j can take the values 0, 1, and 2 independently of each other.

acetone complex. In the absence of any evidence for specific assignments of these peaks we prefer to leave these peaks unanalyzed. A case for a 1:2 water-acetone complex may be put forth to account for the minor peaks at 1.46 and 1.54 μ. However, these peaks may not have any bearing to argue for related water species in liquid water, since a water–acetone 1:2 complex is very much different from extensively doubly H-bonded three-dimensional network molecules of water.

D. Water in Aqueous Perchlorate Solution. Buijs and Choppin[29] resolved the 1.2-μ band of H_2O, on the basis of its temperature dependence, into three components representing water molecules with zero, one, and both OH groups H-bonded with other water molecules. Hornig[30] disputed the basic assumption of this work: that the temperature dependence of the band shape around 1.2 μ is due to changing concentrations of different species of water molecules. Hornig argued that if the presence of distinct species could cause structure in a combination band, then their presence must also cause a similar structure in the uncoupled fundamental stretching bands. Since no such structure is exhibited in the fundamental, the temperature dependence of 1.2-μ band shape, he said, must have some other cause. Kauzmann[5] contends that heating shifts the frequencies of the fundamental modes and these shifts alter Fermi resonance between overlapping overtones and combination bands in this region.

Fermi resonance may also be cited for the temperature dependence of the 1.45-μ band of water. The effect of NaClO$_4$ on the 1.45-μ band, however, demonstrates that Fermi resonance is not the cause for spectral change with temperature. Addition of NaClO$_4$ to water is in effect equivalent to increasing the temperature. The similarity of the effect of NaClO$_4$ on the 1.45-μ band of H_2O and on the infrared spectrum of uncoupled OD stretch (HDO in H_2O) described below argues against the influence of Fermi resonance on the 1.45-μ band. The absence of structure in the fundamental water spectrum must be traced to some other reason.[19]

The effect of NaClO$_4$ on the 1.45-μ band of water is to shift the band toward shorter wavelength (higher frequency) besides producing a shoulder on the longer wavelength side (Figure 7). The position of the high-frequency peak is independent of the concentration of perchlorate. To determine the exact position of the high-frequency component, difference spectra of aqueous solutions of NaClO$_4$ vs. water at the same temperature were obtained and these are shown in Figure 8. A sharp peak at 1.415 μ (7067 $\pm$ 5 cm^{-1}) was obtained whose intensity, but not position, depended on the concentration of perchlorate. The position of "B" curves in the temperature difference spectra (Figure 2 and Table I) is almost the same frequency (7081 $\pm$ 5 cm^{-1}). McCabe and Fisher[31] studied the difference spectra of aqueous solutions of several alkali halides. The "hydration" spectra for the alkali halides were re-
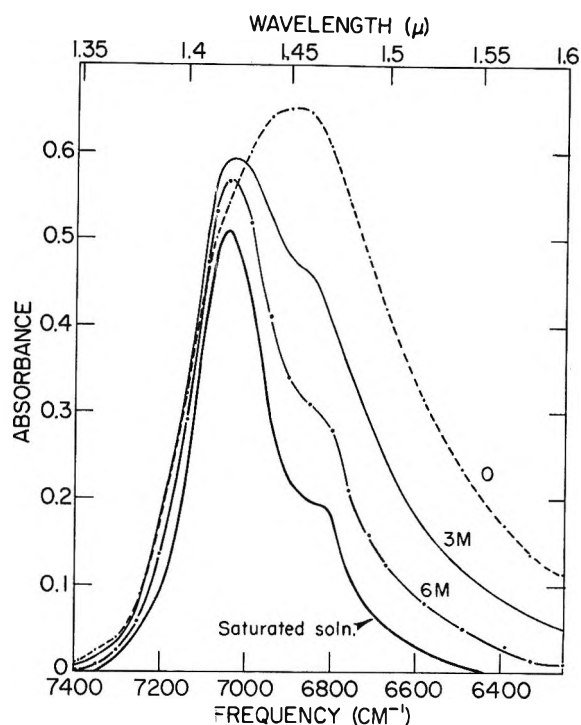

Figure 7. Absorption spectra of water and aqueous solution of NaClO$_4$ in the 1.45-μ region at 20° measured vs. absorption cell. The cell path lengths were 0.05 cm.

solved to correspond to cation and anion "hydrates." The species corresponding to anion hydrate has a frequency of maximum absorption 6997 cm^{-1} (1.429 μ). This would correspond to a water molecule H-bonded to the halide anions. However, in aqueous perchlorate, the difference spectrum has a positive peak at 7067 cm^{-1} (1.415 μ) corresponding to an increase in concentration of some water species already present in water at that temperature. The difference in the frequencies indicates that the water species corresponding to 1.429-μ peak is H-bonded to the anion while that corresponding to 1.415 μ (in aqueous perchlorate) is not H-bonded to the anion. This could be a water molecule H-bonded to another water molecule as correlated by the water in acetone peak at 1.413 μ. This conclusion is supported by the recent Raman spectral studies of aqueous perchlorate solutions by Walrafen.[32] He concludes that while halide anions are hydrated in aqueous solutions, the perchlorate anion does not hydrate to any significant extent.

Kecki, *et al.*,[33] observed that the ν_{O-D} peak of HDO in H_2O was split into two peaks on addition of NaClO$_4$. The high-frequency peak did not change in position but its intensity increased with concentration of NaClO$_4$,

(29) K. Buijs and G. R. Choppin, *J. Chem. Phys.*, **39**, 2035 (1963).

(30) D. F. Hornig, *ibid.*, **40**, 3119 (1964).

(31) W. C. McCabe and H. F. Fisher, *J. Phys. Chem.*, **74**, 2990 (1970).

(32) G. E. Walrafen, *J. Chem. Phys.*, **52**, 4176 (1970).

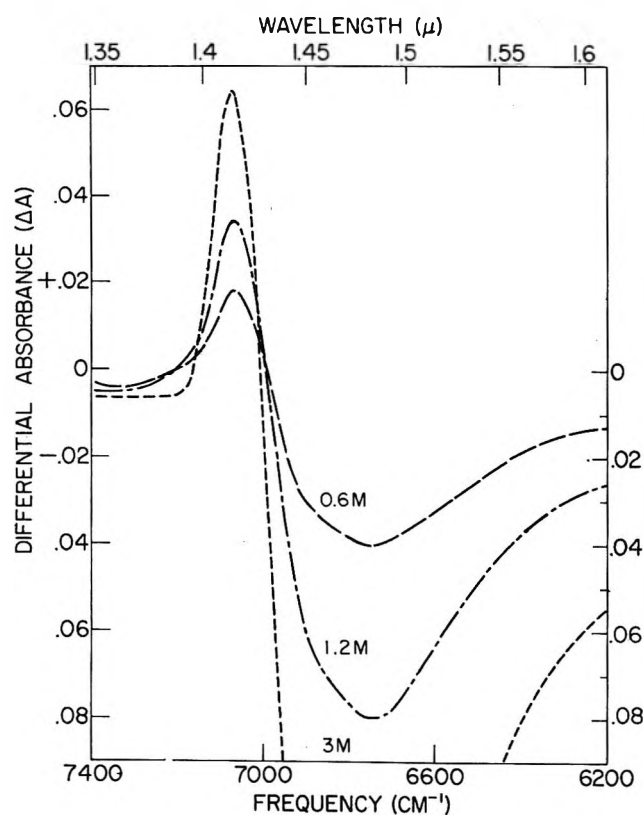(33) Z. Kecki, P. Dryjanski, and E. Kozlowska, *Rocz. Chem.*, **42**, 1749 (1968).

Figure 8. Difference spectra of aqueous solutions of NaClO$_4$ (vs. water) at 20°. Cell path lengths were 0.05 cm.

at the expense of that of the low frequency peak. The splitting was attributed to the structure-breaking action of perchlorate ion. (This splitting is not observed with other anions.) Senior and Verrall[34] obtained an isosbestic point at 2575 cm^{-1} while studying the temperature dependence of the infrared ν_{O-D} band of HDO in H$_2$O. They resolved the peaks (at various temperatures) into two components, one with a $\nu_{max} = 2525$ cm^{-1} (bonded O–D) and the other with $\nu_{max} = 2650$ cm^{-1} (nonbonded O–D). These peak positions concurred with the peak positions of water-in-perchlorate spectra[33] within experimental error thereby implying an analogous situation with addition of perchlorate and increase of temperature.

If it is assumed that the effect of NaClO$_4$ as well as that of temperature is to rupture the "icelike" clusters in water, producing water molecules with only one OH group bonded at the expense of those with both OH groups bonded, then the identity of the species absorbing at 1.415 μ can be established. It is known[35] from infrared studies of dilute solutions of water in CCl$_4$, acetone, and various cyclic ethers that water exists as a single type of species in these solvents and is H-bonded to the oxygen of the ethers or acetone. The high-frequency peak of H$_2$O in perchlorate solution, the major peak of water-in-acetone, and the high-frequency component of H$_2$O in the temperature difference spectra (all in the 1.45-μ region) occur at the same frequency

(7075 $\pm$ 10 cm^{-1}), indicating that the water species absorbing at this frequency may be singly bonded water. That perchlorate ion produces an excess of singly bonded water from doubly bonded water and that it does not produce unbonded water in excess as assumed by Buijs and Choppin[29] is borne out by the fact that water-in-CCl$_4$ (monomer) absorbs[10] at 1.395 μ (7167 cm^{-1}) while water-in-perchlorate has a peak at 1.415 μ (and not at 1.395 μ). The infrared studies of Hartman[36] and Glew, et al.,[35] suggest that monomeric water in liquid water should absorb at almost the same frequency[37] as it does in CCl$_4$ or in liquid water above 200°. Our conclusion as to the effect of perchlorate is also in agreement with the observation of Kecki, et al.,[33] viz., the high-frequency peak of ν_{O-D} of HOD in water "has a frequency too low to represent free monomeric water molecules."

The correspondence between the water-in-acetone peak (Figure 5) and the high-frequency peaks in water–NaClO$_4$ and temperature difference spectra (Figure 3) is also maintained in the $\nu_1 + \nu_2 + \nu_3$ band (ca. 1.2 μ). A temperature increase produces an increase of intensity of the 1.155-μ peak.[17] Water-in-acetone has its major peak at 1.157 μ and addition of perchlorate produces an increase of intensity at 1.157 μ at the expense of the low-frequency envelope of the 1.2-μ band. The monomer peak[10] of water-in-CCl$_4$ is at 1.147 μ and in liquid water above 200° is at 1.148 μ.

All of the foregoing arguments, in effect, give credence to our conclusion that liquid water is composed of at least two components, the high-frequency spectral component being identified as singly bonded water.

E. Identification of "C" Curve With Ice Spectrum. There is a striking similarity in both the peak maxima and overall shapes of the absorption represented by the "C" curve in Figure 4 and the absorption of ice at 0° The near-infrared spectrum of ice[38] is reproduced, in part, in Figure 9. Yamatera, et al.,[20] listed the absorption maximum for ice at 6700 cm^{-1} (1.493 μ). The absorption maximum for the "C" curve in Figure 4 is at 6700 $\pm$ 10 cm^{-1}. It is interesting to note that while curve "B" is Gaussian, curve "C" is not, although it is possible to resolve this curve into Gaussian components. The near-infrared spectrum of ice in the 1.45-μ region,[39]

(34) W. A. Senior and R. E. Verrall, *J. Phys. Chem.*, **73**, 4242 (1969).

(35) D. N. Glew, H. D. Mak, and N. S. Rath, "Hydrogen-Bonded Solvent Systems," A. K. Covington and P. Jones, Ed., Taylor and Francis, London, 1968, p 195.

(36) K. A. Hartman, Jr., *J. Phys. Chem.*, **70**, 270 (1966).

(37) The equivalence of unbonded water in liquid water (D$_0$A$_1$ and D$_0$A$_2$) and water-in-CCl$_4$ in terms of stretching absorption frequencies has also been pointed out by Stevenson (ref 11, p 495) in analogy with studies of NH$_3$ in water and CCl$_4$. So in the study of the 1.45-μ band ($\nu_1 + \nu_3$) the unbonded water molecules (in Buijs and Choppin classification) should absorb at the same frequency as water-in-CCl$_4$ (monomer) does.

(38) W. A. P. Luck, *Ber. Bunsenges. Phys. Chem.*, **69**, 626 (1965).

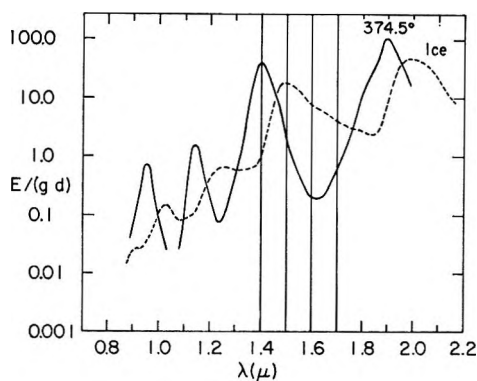(39) W. A. P. Luck and W. Ditter, *Z. Naturforsch.*, **24b**, 482 (1969).

Figure 9. The near-infrared spectra of ice and water at its critical temperature (374.5°). These data have been reproduced, in part, from a paper by W. A. P. Luck, *Ber. Bunsenges. Physik Chem.*, **69**, 626 (1965).
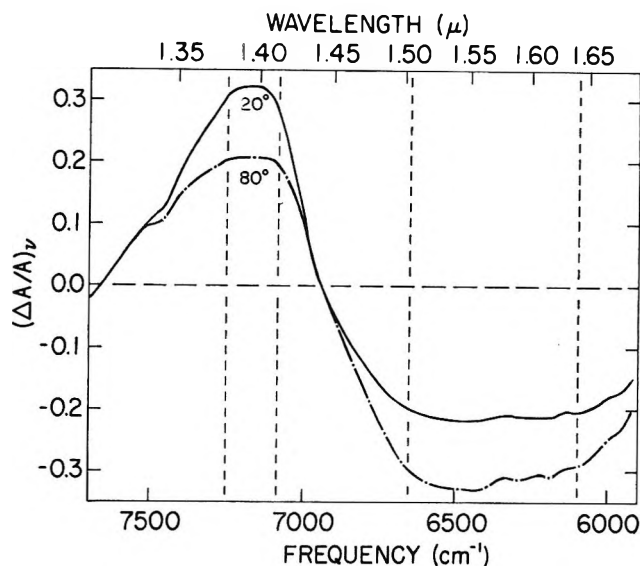

Figure 10. Comparison of the temperature difference spectrum with the spectrum of water at a given temperature. Curves A and B represent plots of the differential absorbance, ΔA, at each frequency, ν, for the 40° "A" curve (Figure 4) divided by the absorbance, A, at each frequency for water at 20 and 80°, respectively.

however, has the same band shape and asymmetry as that of curve "C." So the species corresponding to curve "C" can be termed "icelike." Insofar as the ice spectrum can be resolved into Gaussian components, it is possible that either ordinary ice contains more than a single species or that a single species gives more than one peak. The "icelike" species in water is also subject to the same limitation.

Thus, the "B" and "C" curves in Figure 4 appear to represent the absorption by singly hydrogen-bonded water (D_1A_j) and icelike water (D_2A_j), respectively.

If this interpretation is correct, the data indicate that when the temperature of water is raised, a component of water with an icelike structure is converted into singly hydrogen-bonded water (possibly by way of an invariant intermediate component). This conclusion can be compared to those of Walrafen[18] as follows. (1) Our conclusion that the effect of temperature on the structure of water is represented by the interconversion of two components is in agreement with Walrafen's. (2) Our conclusion that the temperature-vulnerable component is similar to ice agrees well with Walrafen's conclusion that this is "lattice" water. (3) Our conclusion that the temperature-stable component (in this temperature range) is singly bonded water, differs from Walrafen's contention that this component is monomer (nonbonded) water.

Regarding the disagreement in point 3, it can be stated in support of our conclusion that Stevenson[11] and Luck[38] have obtained absorption data indicating very little monomer water in the temperature range from 20 to 80°. The near-infrared absorption peak for water-in-CCl₄ at 7167 cm⁻¹ (1.395 μ) which Stevenson[10] interpreted as due to absorption by monomer water is certainly different from the absorption peak which has been correlated with singly hydrogen bonded water in this paper. The near-infrared absorption peaks for water in CCl₄[40] and for water at its critical temperature, 374.5°[38] are both at 7148 ± 5 cm⁻¹ (∼1.40 μ) for the 1.45 μ($\nu_1 + \nu_3$) absorption band. This indicates that

the major species in equilibrium in liquid water are singly bonded and icelike water.[41] Monomer water may be found in small amounts.

F. Further Justification for a Mixture Model. Stevenson[11] obtained the infrared spectra of HDO in D_2O for the O–D absorption at 23 and 60°. He plotted the data as $(\Delta A/A_{23})_\nu$ vs. ν and pointed out that if a given absorption band represents the summation of two component absorption peaks which are interconvertible with changes in temperature, then this plot should be invariant at the two extremes of the absorption band. The data in Figure 4 are replotted according to Stevenson[11] in Figure 10 as $(\Delta A/A_t)_\nu$ vs. ν for t equal to 20 and 80°. If the absorbance minimum (1.67–1.69 μ) between the ($\nu_1 + \nu_3$), 1.45-μ and the ($\nu_2 + \nu_3$), 1.93-μ absorption bands is taken as the low-frequency limit of the ($\nu_1 + \nu_3$) band, then the criterion imposed by Steven-

(40) The spectrum for water in CCl₄ (plus a small amount of acetone) measured *vs.* CCl₄ (plus a small amount of acetone) in the $\nu_1 + \nu_3$ (1.45 μ) and $\nu_2 + \nu_3$ (1.93 μ) absorption band regions is an unpublished observation by the authors. Stevenson[11] listed the maxima for water-in-CCl₄ in the 1.45-μ and 1.93-μ regions as 7165 cm⁻¹ (1.890 μ) and 5285 cm⁻¹ (1.892 μ), respectively. Luck's results for water at its critical temperature are 7153 cm⁻¹ (1.398 μ) and 5291 cm⁻¹ (1.890 μ), respectively. We obtained the values 7143 cm⁻¹ (1.400 ± 0.001 μ) and 5283 cm⁻¹ (1.893 ± 0.001 μ), respectively, for the position of these peaks.

(41) As stated under section B, there is a third spectral component (which is temperature independent) which we cannot assign specifically to any structural species in water, for want of available evidence. The emphasis made in this paper is *not* that water consists of only two species but that it consists of discrete species which can be spectroscopically identified. Alternate interpretations can be given for the interconversion of "B" and "C" component species with temperature involving the invarient component but the broad features outlined by our classification of "singly bonded" and "icelike" water may still be valid.

son that $\Delta A / A_t$ be constant at the extremes is satisfied to a close approximation for the low-frequency region of the $(\nu_1 + \nu_3)$ band. There is, however, a significant slope in the region of the absorption band limit (1.67–1.69 μ). It is further significant that the agreement holds for 20 and 80° as well. Therefore, the "C" curve in Figure 4 does appear to represent the water component whose absorption corresponds to the low-frequency limb of the $(\nu_1 + \nu_3)$ band. The data presented for the high-frequency extreme of the $\nu_1 + \nu_3$ band appears to be sufficient to rule out any significant overlap between the "B" and "C" curves in this region since $(\Delta A / A_{80})_\nu$ is constant over a significant region (150 cm^{-1}). The fact that both $(\Delta A / A_{20})_\nu$ and $(\Delta A / A_{80})$ vs. ν plots have a significant slope in the region above 7250 cm^{-1} suggests that there is an additional absorption peak in this region. It should be emphasized that most of this absorption is at higher frequencies ($\sim 1.33\ \mu$) than the absorption by water vapor ($\sim 1.38\ \mu$). In any case, it appears that as the contribution from the "B" curve increases, the value for $(\Delta A / A_t)_\nu$ becomes constant over a wider range of frequencies. Based on these considerations, it is concluded that the results of this treatment of the data are consistent with the concept of a mixture model for water. We suggest, however, that part of the lack of invariance in the term $(\Delta A / A_t)_\nu$ for the high-frequency extreme (ca. 1.38 μ) may be due to an almost constant concentration of nonbonded water.

The data in Figure 3 and Table I indicate the conversion of one component into another at the instance of a change in temperature. The isosbestic point which is essential to this conclusion occurs at 6933 cm^{-1} (1.442 μ). This apparent isosbestic point, while necessary, cannot be considered as proof of a one to one conversion. Worley and Klotz[42] observed an isosbestic point at 6512 cm^{-1} (1.468 μ) in their study of the effect of temperature and salts on the near-infrared spectrum of HDO in H$_2$O. While the differences between O–H absorption in H$_2$O and HDO could be significant in this region, their intermolecular structures must be quite similar. Thus, the association of the isosbestic point with an intermolecular structural transition seems valid. Isosbestic points have also been observed by Walrafen[18] and Hartman[36] in their studies on the effect of temperature on the Raman and infrared spectra of HDO and H$_2$O.

Worley and Klotz[42] obtained a value of 2.37 kcal/mol for the enthalpy of conversion of one component to the other (bonded OH to nonbonded OH). Walrafen[18] obtained an enthalpy of 2.5 ± 0.6 kcal/mol for the same process (bonded OD to nonbonded OD) from his studies on the effect of temperature on the Raman spectra of HOD in H$_2$O. The data on the effect of temperature on the 1.45-μ band of H$_2$O were plotted according to Worley and Klotz[42] in Figure 11. A value for $\Delta H^\circ = 2.18$ kcal/mol was obtained from this plot.
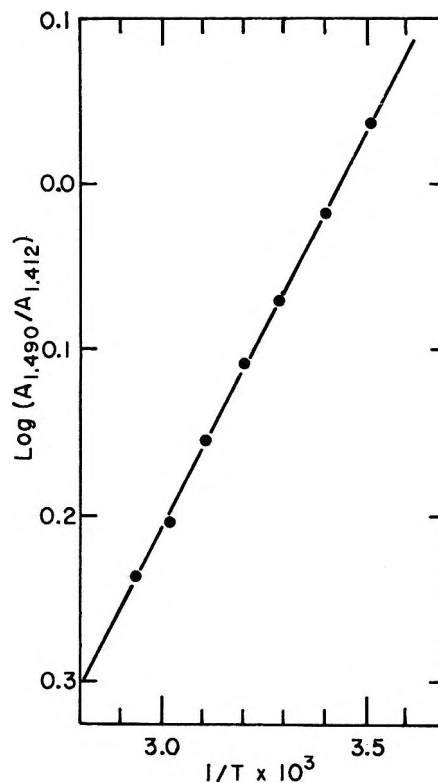

Figure 11. The logarithm of the absorbance ratio $A_{1.490}/A_{1.412}$ (A_{6710}/A_{7081}) plotted vs. $1/T$. The values for A_λ were determined from the values for $(\Delta A)_{\nu_0}$ given in Table I and the values for $A_{1.412}$ and $A_{1.490}$ for water at 20° (Figure 1). For 0.1 cm path length of water at 20°, $A_{1.412} = 0.987$ and $A_{1.490} = 1.076$. The solid circles, ●, represent experimental points.

As indicated by Walrafen,[18] this agreement is significant; it supports the concept of a temperature-sensitive equilibrium between two structural species in water.

Conclusion

It appears that liquid water consists of close-packed discrete "icelike" clusters of varying numbers of water molecules in equilibrium with each other as envisaged by the "flickering cluster" model[12] except for the fact that the fraction of monomeric water is very small. The bulk of water molecules in liquid water must be engaged in H bonding involving one or both OH groups. Water molecules with both OH groups bonded will be found in the interior of clusters while those with only one OH group bonded will be at the periphery. Even though they may be parts of a single entity, they constitute spectroscopically distinct species (at least in the near-infrared region). The surface molecules (with one OH bonded) absorb at a higher frequency than the interior ones (both OH groups bonded). The effect of perchlorate or temperature rise would be to break up the clusters, thereby decreasing the ratio of low-frequency

(42) J. D. Worley and I. M. Klotz, J. Chem. Phys., 45, 2868 (1966).

species to the high-frequency species. This causes the cluster size to decrease with temperature. The production of more surface molecules at the expense of interior ones with temperature appears to proceed through an intermediate species which has a constant spectral contribution in the temperature range 20–80°.

Copper Nuclear Magnetic Resonance Study of Cyanocuprate(I)

Ions in Solution.   Formation of Polynuclear Species

and of Mixed Complexes

by Takeo Yamamoto,* Hiroki Haraguchi,[1] and Shizuo Fujiwara

Department of Chemistry, Faculty of Science, University of Tokyo, Hongo, Tokyo 113, Japan   *(Received February 25, 1970)*

Aqueous solutions of copper(I) cyanide with an excess of alkali cyanide were studied by means of copper-63 and -65 nmr. Copper nmr signals were detected when the cyanide to copper ratio was larger than 4. The nmr line width decreased with an increase in the above ratio. It was concluded that (1) the dominant species $Cu(CN)_4{}^{3-}$ retains the tetrahedral symmetry in solution, (2) $Cu(CN)_3{}^{2-}$, or $Cu_2(CN)_6{}^{4-}$, has a distorted tetrahedral structure and therefore makes little contribution to the nmr line width even though it is the largest in amount among the minor species, and (3) polynuclear species such as $Cu_2(CN)_5{}^{3-}$ largely determine the nmr line width. The formation of mixed complexes of Cu(I) with the cyanide ligand and several other ligands was also found to increase the nmr line width. It was indicated that the values of $K_m = [Cu(CN)_3L^{(2+n)-}][CN^-]/[Cu(CN)_4{}^{3-}][L^{n-}]$ are in the order $(NH_2)_2CS > SCN^- > I^- \gtrsim NH_3 > Br^- > Cl^- \gtrsim (NH_2)_2CO$, where K_m for SCN^- was estimated to be about 1×10^{-3}.

Introduction

Copper-63 and -65 nmr of solid Cu(I) compounds has been reported in copper(I) halides[2,3] and in potassium tetracyanocuprate(I).[4] However, there have been few nmr studies on aqueous solutions of copper(I) salts.[5] In the present work, the copper nmr is studied in aqueous solutions of copper(I) cyanide in the presence of an excess of alkali cyanide. The line width, which strongly depends on the concentrations of cyanide and of copper(I) ions, is discussed in terms of the composition and the ligand exchange of the complexes in the solution.

The line width is also observed to increase in the presence of other potential ligands such as thiourea, thiocyanide, iodide, ammonia, bromide, chloride, or urea. The effect can be explained in terms of the formation of weak mixed complexes $Cu(CN)_3L^{n-}$.

Experimental Section

Commercial reagent grade chemicals were used throughout the experiment. The concentrations (in molar units) of copper and cyanide ions are denoted by m and l, respectively. The estimated error in the ratio l/m was ±0.05. This value will be used in Figure 3.

Nmr signals were measured by using two bridge-type spectrometers operating at 6.1403 MHz and 15.086 MHz, respectively. The narrower signals were measured by the side band method at either 500- or 1000-Hz field modulation frequency. The broader signals were recorded as the first derivative lines with 35.5-Hz modulation. For weak signals, the modulation amplitude was varied by 5-db increments and the peak-to-peak intensity and line width were measured for each modulation amplitude. The intensity *vs.* modulation amplitude and the line width *vs.* amplitude curves were compared with the theoretical curves calculated for the Gaussian and the Lorentzian lines,[6] and the line width extrapolated to zero modulation amplitude was obtained graphically. Most of the observed line shapes

are Lorentzian within experimental error, though some of the narrower lines have shapes between Gaussian and the Lorentzian. Therefore, all the experimental lines were assumed to have the Lorentzian line shape in the following discussion. The error due to the discrepancy was included in the estimation of errors shown in Figures 1, 2, and 3.

The peak-to-peak separation of the first derivative lines will be referred to as the line width in the following discussion. The magnitude of the inhomogeneity of the magnetic field was estimated from the line width of ^{23}Na signals and was subtracted from the observed line width. The inverse of the transverse relaxation time $1/T_2$ is given by multiplying the line width obtained above with $\sqrt{3}\,\pi$.

Powdered copper(I) chloride was used as an external reference in the chemical shift measurements.

The viscosities of sample solutions were measured with an Ostwald viscometer at 20°.

The copper nmr signal was too broad to be detected (line width $\geq$ 5000 Hz) with the spectrometers used in the present study, when either potassium tetracyanocuprate(I) or sodium tetracyanocuprate(I) was dissolved in water. As alkali cyanide was added to the solution, the signal became observable at a field (8.20 ± 0.08) × 10^2 ppm lower than that of powdered copper(I) chloride.

For a quantitative study, three stock solutions were made dissolving 3, 4.5, and 6 mol each of potassium cyanide, 1.5 mol each of sodium cyanide, and 1.5 mol each of copper(I) cyanide in water and diluting to 1 l. Sample solutions with different l values and/or different m values from the above solutions were made by mixing aliquots of the stock solutions with each other and/or with water. Chemical shifts were identical for all the samples within experimental error.

In Figure 1, examples of the spectra are shown for samples with $m = 1.5\ M$. When l/m is equal to or smaller than 4, no signal is observed. At $l/m = 4.1$, a broad signal becomes observable. The line becomes considerably narrow at $l/m = 4.2$. The line width at $l/m = 6$ is about 85 Hz.

In Figure 2, the inverse of the ^{63}Cu nmr relaxation time, $1/T_2$, obtained from the line width after applying the correction for the inhomogeneity of the field, is plotted against the ratio of the total concentration of cyanide to that of copper, l/m. It is seen there that $1/T_2$ increases rapidly as l/m decreases toward 4.

The dependence of the line width on the observing radiofrequency was studied by measuring several samples both at 6.1403 MHz and at 15.086 MHz. When the correction for the inhomogeneity of the magnetic field was applied, the line widths (in frequency units) were identical at the two frequencies within experimental error.

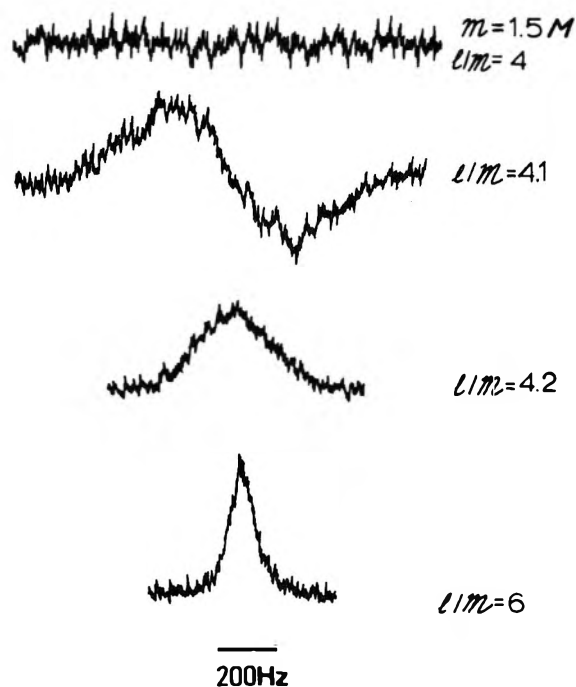The line width was found to increase with increasing temperature for all the samples studied. For example,

Figure 1. Copper-63 nmr spectra of aqueous solutions of cyanocuprate(I) ions: m, the total concentration of copper(I); l, the total concentration of cyanide.
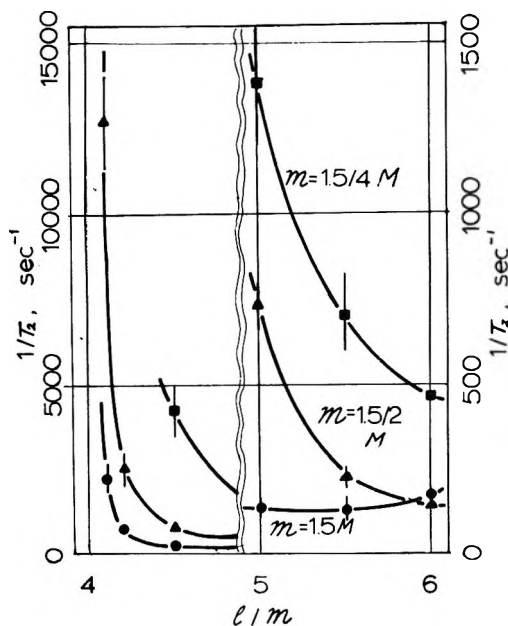

Figure 2. The inverse of the relaxation time of copper-63 vs. the ligand to metal ratio in cyanocuprate(I) solutions. The perpendicular bars are the estimated errors.

the line width for a sample with $m = 1.5\ M$, $l/m = 4.1$, was 230 Hz at 0° and 420 Hz at 20°.

The effect of the viscosity of the solution was studied by changing the ratio of the concentration of sodium cyanide to that of potassium cyanide, keeping the total cyanide concentration constant. For $m = 1\ M$, $l/m = 4.2$, for $m = 1.5\ M$, $l/m = 4.5$, and for $m = 2\ M$,

$l/m = 5.0$, the line width increased linearly with the viscosity.

In order to find the dependence of the relaxation time on the nuclide, the relative intensities of the first derivative lines, I_{65} and I_{63}, were measured for ^{65}Cu and ^{63}Cu at the same frequency of 6.1403 MHz. The same experimental condition was maintained except for changing the magnitude of the static magnetic field. The ratio of the two intensities, I_{65}/I_{63}, was measured as it is much more sensitive to the change in the relaxation time than the ratio of the line widths themselves. The observed ratio and the estimated error were

$$I_{65}/I_{63} = 0.71 \pm 0.08$$

The effect of other potential ligands on the line width was measured by mixing equal aliquots of an aqueous solution of 2 M cuprous cyanide and 8 M potassium cyanide and the aqueous solution of one of the following substances of concentration $2L$ M: lithium chloride, sodium bromide, sodium iodide, sodium thiocyanide, ammonia, urea, and thiourea. The concentration of the resulting solution was assumed to be L M in the potential ligand, $m = 1$ M and $l/m = 5$, neglecting the small change in the liquid volume. For all the potential ligands, the line width increased with L. The results will be discussed below.

Discussion

Mechanism of the Broadening. The copper chemical shift observed here agrees with the shift reported for solid potassium tetracyanocuprate(I).[4] It is evident that the sharp absorption in samples with large values of l/m is the signal from the dominant species, $Cu(CN)_4{}^{3-}$. From the rapid increase in the line width as l/m decreases toward 4, it is also clear that the broadening is associated with chemical exchange of $Cu(CN)_4{}^{3-}$ with other species whose presence in the solution increases as the amount of CN^- decreases.

When the jth species has a quadrupole coupling constant e^2Qq_j/h, an asymmetry factor η_j, and a correlation time of the rotational Brownian motion τ_{cj}, the intrinsic relaxation time of the species, T_{2j}, due to the quadrupole coupling is given by[7]

$$1/T_{2j} = 3.95(e^2Qq_j/h)^2[1 + (\eta_j{}^2/3)]\tau_{cj} \quad (1)$$

provided that the correlation time is sufficiently short so that $(e^2Qq_j/h)\,\tau_{cj} \ll 1$.

When there is fast chemical exchange between $Cu(CN)_4{}^{3-}$ and the other minor species $j, j = 1, \ldots n$, the apparent relaxation time T_2 obtained from the observed line width of the main part of the spectrum is related to the chemical shifts and the intrinsic relaxation times of the minor species, as[8]

$$1/T_2 = 1/T_{2a} + \sum_j (1/\tau_{aj}) \times$$
$$\frac{(1/T_{2j})^2 + p_j/(T_{2j}\tau_{aj}) + (\Delta_j)^2}{(1/T_{2j} + p_j/\tau_{aj})^2 + (\Delta_j)^2} \quad (2)$$

where T_{2a} and T_{2j} are the intrinsic relaxation times of copper atoms in $Cu(CN)_4{}^{3-}$ and in the jth minor species, respectively, τ_{aj} is the average time before one copper atom goes from the main species into the jth species, p_j is the small population of copper nuclei present in the jth species, and Δ_j is the copper chemical shift of the jth species from $Cu(CN)_4{}^{3-}$.

If the chemical exchange is sufficiently fast and the chemical shift terms in eq 2 are negligible, the equation is simplified to

$$1/T_2 = 1/T_{2a} + \sum_j (p_j/T_{2j}) \quad (3)$$

Equations 1 and 3, together with the values of the natural abundance of ^{65}Cu and ^{63}Cu, give the ratio of the intensities of first derivative lines for the two nuclides

$$(I_{65}/I_{63})_{calcd} = 0.751$$

The above value agrees with the observed one, suggesting the validity of the mechanism assumed above. Equations 1 and 3 are also in agreement with the observed linear dependence of the line width on viscosity and its independence from the observing radiofrequency. Furthermore, as the equilibrium of eq 4 shown below is endothermic,[9] an increase in temperature results in an increase in the calculated line width according to eq 1 and 3, in agreement with the observed result.

In conclusion, the broadening of the copper nmr line is caused by the presence of some minor species with large intrinsic line widths, which undergo fast chemical exchange with the dominant species $Cu(CN)_4{}^{3-}$. The broad line widths of the minor species are determined by the quadrupole interaction of the nuclei with the surrounding electric field gradients.

Structure of the Cyanide Complexes. The dissociation of $Cu(CN)_4{}^{3-}$ ion into the lower cyanides

$$Cu(CN)_4{}^{3-} \rightleftharpoons Cu(CN)_3{}^{2-} + CN^- \quad (4)$$

$$Cu(CN)_3{}^{2-} \rightleftharpoons Cu(CN)_2{}^- + CN^- \quad (5)$$

has been studied extensively.[10] In the present study, the results of Penneman and Jones[9] are used because they have studied solutions with higher total copper concentrations than most of the others. An extended Debye-Hückel formula for the activity coefficients is used together with the equilibrium constants and the enthalpies of formation to calculate the concentration constants for the solutions used in the present study. The results at 20° are

(7) A. Abragam, "The Principles of Nuclear Magnetism," Oxford, England, 1961, p 314.

(8) T. J. Swift and R. E. Connick, *J. Chem. Phys.*, **37**, 307 (1962).

(9) R. A. Penneman and L. H. Jones, *ibid.*, **24**, 293 (1956).

(10) L. G. Sillén and A. E. Martell, Ed., "Stability Constants of Metal-ion Complexes," The Chemical Society, London, England, 1964, p 110.

$$K_4 = \frac{[Cu(CN)_4{}^{3-}]}{[Cu(CN)_3{}^{2-}][CN^-]} = 10^{2.46} \ldots 10^{2.53}$$

$$K_5 = \frac{[Cu(CN)_3{}^{2-}]}{[Cu(CN)_2{}^-][CN^-]} = 10^{5.10} \ldots 10^{5.13}$$

Approximate values, $K_4 = 3 \times 10^2$ and $K_5 = 1 \times 10^5$, will be used in the following discussion.

Brigando[11] has suggested that Cu(I)–Cu(I) polynuclear complexes are formed at low temperatures in solutions of low concentrations of free cyanide ions. However, Penneman and Jones[9] have not observed the formation of polynuclear ions. As the system we studied has higher concentrations of the metal ions than in the above two cases, it is probable that polynuclear species exist in the solutions.

In the present system where $l/m \geq 4$, the concentrations of all the minor species are small compared to m. Therefore, the population p_{ij} of a minor species $Cu_i(CN)_j{}^{i-j}$ may be written as follows

$$p_{ij} = K_{ij} \cdot (m)^{j-3i-1} \cdot (x)^{j-4i} \tag{6}$$

where K_{ij} is a concentration equilibrium constant

$$K_{ij} = \frac{[Cu_i(CN)_j{}^{i-j}][CN^-]^{4i-j}}{[Cu(CN)_4{}^{3-}]^i}$$

and $x = (l/m) - 4$.

If it is assumed that τ_{cj} is proportional to the bulk viscosity of the sample solution, η_{bulk}, the inverse of the relaxation time for each species divided by η_{bulk}, $1/(T_{2j}\eta_{bulk})$, should be independent of the composition of the solution. The above quantity for $Cu(CN)_4{}^{3-}$ ion is obtained by assuming that the contribution of the minor species to the observed line width is negligible when $m = 1.5 \, M$ and $x \geq 1.5$. It is

$$1/(T_{2a}\eta_{bulk}) = (65 \pm 15) \; sec^{-1} \, cP^{-1}$$

for ^{63}Cu. When the ionic radius is taken as 4.6 Å[12] and the Stokes model is used to calculate the rotational correlation time for the ion, the quadrupole coupling constant including the asymmetric contribution is calculated from the above value

$$(e^2 Q q_a/h)[1 + (\eta_a{}^2/3)]^{1/2} = 0.4 \; MHz$$

The above value of the coupling constant shows that the tetrahedral symmetry of $Cu(CN)_4{}^{3-}$ ions in the solid[13] is well retained in solution.

By using the above value for $1/(T_{2a}\eta_{bulk})$, the contribution of the minor species to the broadening may be evaluated

$$(1/T_2 - 1/T_{2a})/\eta_{bulk} = \sum_j [p_j/(T_{2j}\eta_{bulk})]$$

The above quantity will be called the reduced broadening in the following discussion. In Figure 3, the reduced broadening for ^{63}Cu is plotted against $x = (l/m) - 4$. It is seen from Figure 3 that the values for $m = 1.5$,
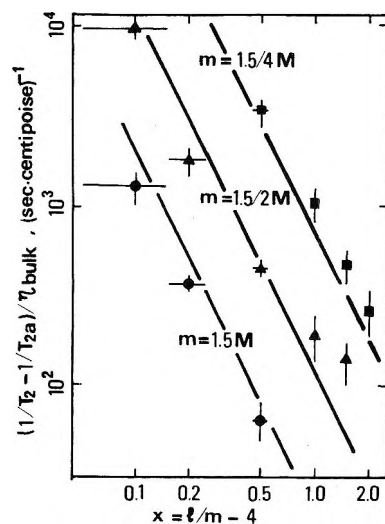

Figure 3. The reduced broadening vs. the ligand to metal ratio in cyanocuprate(I) solutions. The perpendicular and the horizontal bars are the estimated errors. The solid straight lines are $(1/T_2 - 1/T_{2a})/\eta_{bulk} = 57.0 \times m^{-2.5} \, x^{-2.0}$.

1.5/2 and 1.5/4 M make approximately three parallel lines,

$$(1/T_2 - 1/T_{2a})/\eta_{bulk} = 57 \cdot (m)^{\mu_{obsd}} \cdot (x)^{\chi_{obs}}$$

where

$$\mu_{obsd} = -2.5 \pm 0.5; \; \chi_{obsd} = -2.0 \pm 0.5$$

The minor species which largely determine the magnitude of the reduced broadening are likely to be polynuclear species with low j/i ratios such as $Cu_2(CN)_5{}^{3-}$. This ion would give $\mu_{calcd} = -2$ and $\chi_{calcd} = -3$. These values are not in quantitative agreement with the observed data. The disagreement may be explained in the following way. The contribution from $Cu(CN)_3{}^{2-}$ relative to the one from $Cu_2(CN)_5{}^{3-}$ becomes important at low m and high x values, whereas the effect of higher polymers such as $Cu_3(CN)_7{}^{4-}$ as well as the breakdown of the approximation used in deriving eq 6 becomes appreciable at low x values.

The concentration of $Cu(CN)_2{}^-$ estimated from the equilibrium constants K_4 and K_5 is too small to give the observed broadening, if we assume reasonable values of τ_{cj} and $(e^2 Q q_j/h)$ for this species.

According to eq 3 and 6, $Cu(CN)_3{}^{2-}$ and $Cu_2(CN)_6{}^{4-}$ give $\mu_{calcd} = -1$, $\chi_{calcd} = -1$ and $\mu_{calcd} = -1$, $\chi_{calcd} = -2$, respectively. The disagreements between these sets of values and the observed set of values are large enough to disqualify $Cu(CN)_3{}^{2-}$ and $Cu_2(CN)_6{}^{4-}$ as species which contribute significantly to the reduced broadening. This, in turn, means that a $Cu(CN)_3{}^{2-}$ ion does not have a planar triangle coordination of the

(11) J. Brigando, Bull. Soc. Chim. Fr., 503 (1957).

(12) Cu–C–N = 3.1 Å,[13] van der Waals radius of N = 1.5 Å.

(13) R. B. Roof, Jr., A. C. Larson, and D. T. Cromer, Acta Crystallogr., Sect. B, 24, 269 (1968).
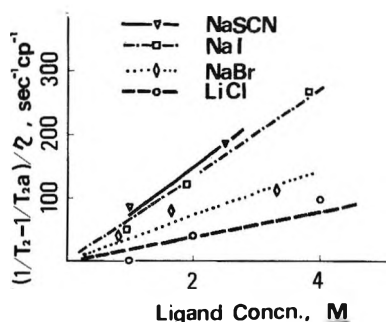
Figure 4. The reduced broadening *vs.* the concentration of ionic potential ligands in a solution with $l/m = 5$, $m = 1$ M.

ligands as in the case of solid potassium dicyanocuprate-(I).[12] In fact, if we assume $r_j = 4.6$ Å, $K_4 = 3 \times 10^2$, and $(e^2Qq_j/h)[1 + (\eta_j^2/3)]^{1/2} = 60$ MHz[14] for the fictitious planar ion $Cu(CN)_3{}^{2-}$ in solution, the contribution from this species to the reduced broadening at $m = 1.5$ M and $x = 0.5$ would be 6.4×10^3 sec^{-1} cP^{-1}, which is more than 50 times as large as the observed value.

The Effect of Mixed Complex Formation. The above conclusion is supported by the effect of other potential ligands on the line width. The reduced broadening $(1/T_2 - 1/T_{2a})/\eta_{bulk}$ due to several potential ligands is plotted against the ligand concentration in Figure 4 and Figure 5. In all the experiments, the total copper and the cyanide concentrations were 1 M and 5 M, respectively. It is seen that for each ligand the reduced broadening is approximately proportional to the concentration of the ligand. This may be explained by assuming a formation of mixed complexes

$$Cu(CN)_4{}^{3-} + L^{n-} \rightleftharpoons Cu(CN)_3L^{(2+n)-} + CN^- \quad (7)$$
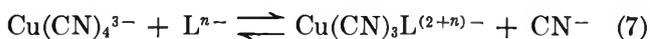
where $n = 0$ or 1. Then, the gradient of a line in Figure 4 or Figure 5 is $K_m/(T_{2m}\eta_{bulk})$ where

$$K_m = \frac{[Cu(CN)_3L^{(2+n)-}][CN^-]}{[Cu(CN)_4{}^{3-}][L^{n-}]}$$

and T_{2m} is the intrinsic relaxation time of copper in the mixed complex species.

The values of $K_m/(T_{2m}\eta_{bulk})$ obtained by a least-squares fitting of the experimental data are shown in Table I, together with the reported values of

$$\beta_2 = \frac{[CuL_2{}^{1-2n}]}{[Cu^+][L^{n-}]^2}$$

There is a strong correlation between the two values for the ligands studied. This suggests that the values of K_m have the same order as the values of β_2 and of $K_m/(T_{2m}\eta_{bulk})$, namely

$(NH_2)_2CS > SCN^- > I^- \gtrsim$
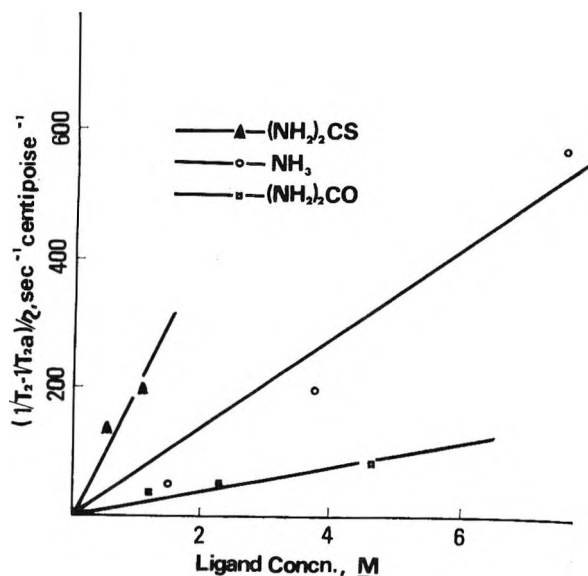
$\qquad NH_3 > Br^- > Cl^- \gtrsim (NH_2)_2CO$

Figure 5. The reduced broadening *vs.* the concentration of nonionic potential ligands in a solution with $l/m = 5$, $l = 1$ M.

Table I: Relative Efficiency of Mixed Ligands in Broadening the Copper Nmr Line Width, $K_m/(T_{2m}\eta_{bulk})$

Ligand	$K_m/(T_{2m}\eta_{bulk})$	log β_2
CN$^-$		16–20.78
$(NH_2)_2CS$	282	
SCN$^-$	75	12.11
NH$_3$	71	8.85
I$^-$	69	8.72–11.2
Br$^-$	37	5.92
Cl$^-$	20	4.60–5.52
$(NH_2)_2CO$	19	

Cooper and Plane[15] have suggested that $Cu(CN)_3{}^{2-}$ has a planar triangle coordination, on the basis of the absence of distinct Raman lines corresponding to mixed complexes in solutions which contain $Cu(CN)_3{}^{2-}$ and one of several potential ligands, including thiocyanate, as the dominant species. However, the present result indicates that mixed complexes are formed, though in rather low concentrations, in the solutions. In fact, if we assume a reasonable value of $T_{2m}\eta_{bulk} = 1 \times 10^{-5}$ sec cP for the thiocyanate ligand

$$\frac{[Cu(CN)_3SCN^{3-}]}{[Cu(CN)_3{}^{2-}][SCN^-]} = K_4 \cdot K_m \simeq 0.2, \text{ or } K_m \simeq 10^{-3}$$

which may be too small for the observation of the mixed complex species by the Raman method.

(14) G. L. McKown and J. D. Graybeal, *J. Chem. Phys.*, **44**, 610 (1966).

(15) D. Cooper and R. A. Plane, *Inorg. Chem.*, **5**, 16 (1966).

Aqueous Dissociation of Squaric Acid

by Lowell M. Schwartz* and Leland O. Howard

Department of Chemistry, University of Massachusetts, Boston, Massachusetts 02116   (*Received August 10, 1970*)

The dissociation constants of squaric acid in aqueous solution have been measured by potentiometric titration. The values found at 25° were about 0.6 for pK_1 and 3.480 ± 0.023 for pK_2. The latter value corresponds to a $\Delta G°$ of 4.748 ± 0.031 kcal/mol. The dissociation constants were also measured as functions of temperature in order to determine the standard molar enthalpies and entropies of dissociation. The values found for the second dissociation were $\Delta H° = -3.028$ kcal/mol and $\Delta S° = -26.08$ cal/mol. Since pK_1 was found to be significantly less than previous reported values, it appears that squaric acid is even stronger than previously thought.

Introduction

The unusual strength of the dibasic acid 1,2-dihydroxycyclobutenedione, commonly known as "squaric acid," has stimulated a number of investigations of its aqueous ionization equilibria.[1-4] pK_2 values at 25° are reported variously as 2.2,[1] 2.89 ± 0.02,[2] 3.21 ± 0.03,[3] and 3.48 ± .02,[4] but these differences to some extent reflect differences in ionic strength of the aqueous media used. However, a pK_2 value in this range should be readily measurable by pH potentiometric titration and agreement should be expected. On the other hand, the first dissociation, reported as $pK_1 = 1.7 \pm 0.03$[3] and 1.2 ± 0.2,[4] is more difficult to determine by this technique. Accuracy in pK_1 requires a significant concentration of undissociated squaric acid which in turn requires highly concentrated solutions. Even near the solubility limit of about 0.17 M the acid is largely dissociated and impurities and small errors in pH measurement propagate as large errors in the calculated pK_1 values. Also activity coefficients are unknown at these ionic strengths and may be estimated only from semiempirical correlations.

In this work we attempt to verify the thermodynamic pK_2 value and, in spite of the difficulties just mentioned, to establish pK_1 to whatever accuracy that pH potentiometric titration affords. MacDonald[4] attempts to analyze the energetics of the aqueous dissociation reactions by comparing pK values of squaric acid with those of oxalic acid. The analysis is highly conjectural and would benefit from additional experimental information. In particular we measure the dissociation constants as functions of temperature and thereby can determine the standard molar enthalpies and entropies of dissociation *via* the thermodynamic relations

$$\frac{d \ln K}{dT} = \frac{\Delta H°}{RT^2} \tag{1}$$

$$\Delta G° = -RT \ln K \tag{2}$$

$$\Delta G° = \Delta H° - T\Delta S° \tag{3}$$

Experimental Section

Squaric acid was purchased from Aldrich Chemical Co. in several lots. After drying at 100° under vacuum, each was titrated with carbonate-free 0.1 M NaOH standardized in the usual way with potassium acid phthalate. Squaric acid samples whose molecular weight analyzed to within 0.4% of the value 114.06 were accepted as sufficiently pure and used in the pK determinations. Samples of acid were dissolved in conductivity water from a calibrated pipet to make solutions varying in concentration from 0.12 to 0.17 M. Each solution was kept under nitrogen atmosphere from the time of its preparation to the completion of the titration. The titrations were done with 0.2226 M carbonate-free NaOH and pH readings were recorded after each addition of base only when the temperature returned to within 0.05° of the desired value. The pH meter was a Beckman model 76 with Beckman 39303 or Corning 476022 glass electrode and Corning 476002 calomel reference electrode. Since critical pH values for pK_1 determination are in the range 1 to 2, the pH meter was standardized with 0.1000 M HCl whose pH is 1.10[5] at all temperatures covered in this study. In addition we checked the pH meter calibration near 4.0 with 0.05 M potassium acid phthalate[5] and between pH 1.1 and 2.5 by measuring the pH of the 0.1000 M HCl titrated with standardized NaOH. pH values of the HCl–NaCl solutions were calculated using activity coefficients for HCl from the Debye–Hückel equation with the "ion size parameter" a_i interpolated from the data given by Bates[5] on page 55. These values generally agreed with

* To whom correspondence should be addressed.

(1) J. D. Park, S. Cohen, and J. R. Lacher, *J. Amer. Chem. Soc.*, **84**, 2919 (1962).

(2) P. H. Tedesco and H. F. Walton, *Inorg. Chem.*, **8**, 932 (1969).

(3) D. T. Ireland and H. F. Walton, *J. Phys. Chem.*, **71**, 751 (1967).

(4) D. J. MacDonald, *J. Org. Chem.*, **33**, 4559 (1968). In a private communication D. J. MacDonald states that his reported $pK_1 = 1.2 \pm 0.2$ is in error due to a miscalculation and that valid pK_1 values cannot be obtained from his experiments.

(5) R. G. Bates, "Electrometric pH Determinations," Wiley, New York, N. Y., 1954.

the pH meter readings to within 0.01 pH unit and since this degree of accuracy was all we could expect with the apparatus, no corrections were made.

We experienced sporadic trouble with the pH measuring system in squaric acid solutions of pH 1.5 or less, but not in HCl–NaCl solutions of similar acidity. The pH reading suddenly began to drop and fluctuate with the rate of stirring. The effect occurred frequently below room temperature and less so above. We localized the trouble in the calomel reference electrode and suspect that undissociated squaric acid was adsorbing into the fiber junction. Since upon washing the tip of the calomel electrode in distilled water the pH system recovered, we adopted the procedure of pipetting 2-ml samples of water onto the electrode tip whenever the trouble occurred, pausing a few minutes, and proceeding with the titration. The calculation method accommodated the solution volume changes due to these small water additions.

Calculations

The method of computing the equilibrium constants is basically the same as that used by MacDonald.[4] The thermodynamic constants K_1 and K_2 are defined by

$$K_1 = \frac{\gamma_{\pm}^2[H^+][HSq^-]}{\gamma_0[H_2Sq]} \tag{4}$$

and

$$K_2 = \frac{\gamma_{\pm}[H^+]\gamma_=[Sq^=]}{\gamma_{\pm}[HSq^-]} \tag{5}$$

where [H$_2$Sq], [HSq$^-$], and [Sq$^=$] represent the molar concentrations of the undissociated squaric acid, bisquarate ion, and squarate ion, respectively, $\gamma_{\pm}$ the mean activity coefficient of the singly charged species, $\gamma_= = \gamma_{\pm}^4$ the activity coefficient for the squarate ion, $\gamma_0 = 10^{0.1I}$ the activity coefficient[6] for undissociated squaric acid, and I the ionic strength. The ionic activity coefficients were estimated by the semiempirical correlation

$$\log \gamma_{\pm} = -D\left(\frac{I^{1/2}}{1 + I^{1/2}} - 0.3I\right) \tag{6}$$

developed by Davies[7] and reported to represent the activity coefficients of fifty 1:1 electrolytes at 25° and 0.1 M with an average deviation of 1.6%. The temperature variation of ionic activity coefficients was assumed to be included in the temperature variation of the Debye–Hückel coefficient D, whose values were taken from Robinson and Stokes'[8] Appendix 7.1.

After incorporating the usual mass and charge balance relationships, the system of equations is soluble when applied to two solutions, one from before the first equivalence point in the titration (denoted by subscript b), and one from after (denoted by subscript a). In this form the dissociation constants are computed from

$$K_1 = \frac{C_bA_a - C_aA_b}{A_bB_a - A_aB_b} \tag{7}$$

and

$$K_2 = \frac{B_bC_a - B_aC_b}{C_bA_a - C_aA_b} \tag{8}$$

where (excluding subscripts b or a)

$$A = 2C° - [Na^+] - [H^+]$$

$$B = (C° - [Na^+] - [H^+])\gamma_= [H^+]$$

$$C = -([Na^+] + [H^+])\gamma_{\pm}^2[H^+]^2\gamma_=/\gamma_0$$

$C°$ = stoichiometric molar concentration of squaric acid

$$[H^+] = 10^{-pH}/\gamma_{\pm}$$

A digital computer program was written to carry out the calculations. The sodium ion and stoichiometric acid concentrations were calculated at each recorded point in the titration. The volumes of the solutions were assumed additive and to vary with temperature in the same manner as pure water. Calculations were made of K_1 and K_2 by pairing each reading before with each reading after the first equivalence point. For each pair of readings estimated solution ionic strengths led to values of K_1 and K_2 calculated according to eq 7 or 8. These equilibrium constants were then used to calculate [HSq$^-$] and [Sq$^=$] in each of the two solutions which permitted more accurate estimates of ionic strength. This iteration continued until pK_1 and pK_2 were each invariant to within 5×10^{-4}.

In the course of the computer calculation, it is possible that differences between nearly equal quantities could produce some pK values of questionable validity. These derive from solutions in the immediate vicinity of the first equivalence point and the end point where [H$_2$Sq] and [HSq$^-$] are small. Consequently, pK values were rejected if derived from titration volumes within 10% of these points.

We have tested the experimental and calculational techniques by titrating Matheson Coleman and Bell reagent ACS grade oxalic acid and found pK_1 = 1.31 ± 0.06 and pK_2 = 4.24 ± 0.01, which compare favorably with literature values pK_1 = 1.28[9] and pK_2 = 4.266.[10]

Results

Little variation was observed in the several pK_1 values calculated by pairing a single reading before the first equivalence point with all the readings after. Sim-

(6) J. N. Butler, "Ionic Equilibrium," Addison-Wesley, Reading, Mass., 1964.

(7) C. W. Davies, "Ion Association," Butterworths, London, 1962.

(8) R. A. Robinson and R. H. Stokes, "Electrolyte Solutions," 2nd ed (revised), Butterworths, London, 1959.

(9) L. S. Darken, J. Amer. Chem. Soc., 63, 1007 (1941).

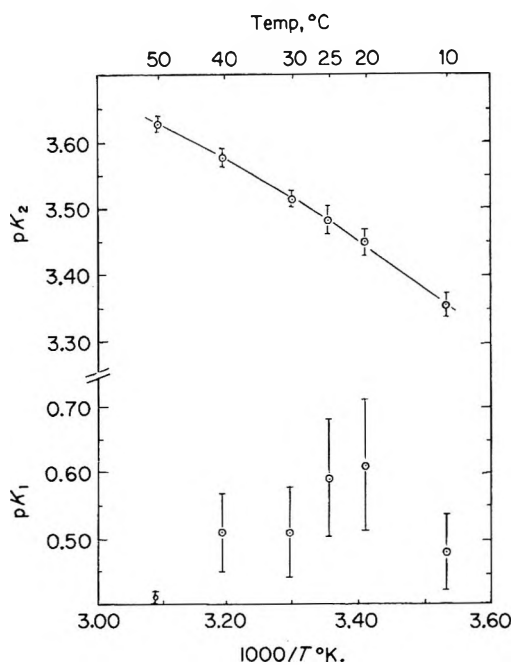(10) G. D. Pinching and R. G. Bates, J. Res. Nat. Bur. Stand., Sect. A, 40, 405 (1948).

Figure 1. Results of squaric acid titrations plotted as pK_1 and pK_2 vs. $1/T°K$. The curve through the pK_2 values is $pK_2 = -1937/T + 14.25 - 0.01434T$.

Table I: Results of Squaric Acid Titrations at Temperatures from 10 to 50°. N_b and N_a are the Total Number of Titration Solutions Contributing to the Averages $\overline{pK_1}$ and $\overline{pK_2}$, Respectively

Temp, °C	$pK_1 \pm s$	N_b	$pK_2 \pm s$	N_a	Number of titrations
10	0.48 ± 0.06	2	3.351 ± 0.019	6	1
20	0.61 ± 0.10	3	3.444 ± 0.019	14	2
25	0.59 ± 0.09	11	3.480 ± 0.023	13	2
30	0.51 ± 0.07	13	3.511 ± 0.010	19	3
40	0.61 ± 0.06	7	3.575 ± 0.013	7	1
50	0.41 ± 0.01	6	3.624 ± 0.009	6	1

that pK_1 in the vicinity of room temperature is about 0.55 ± 0.15, which is significantly less than other estimated values[3,4] indicating that squaric acid is even stronger than previously thought.

The availability of the digital computer program makes it convenient to test the sensitivity of the pK values to various uncertainties in the experimental measurements and the calculating equations. The uncertainties which we estimate in this study and the resulting effect on pK_1 and pK_2 are shown on Table II. A

Table II: Computed Effects of Uncertainties on pK Results

Estimated uncertainty		Approximate effect on	
		pK_1	pK_2
pH value	0.02 unit	0.12	0.02
Solution volumes	0.02 ml	0.01	0.01
Reagent purity (assuming inert impurities)	0.4%	0.13	0.02
Temperature	0.05°	Nil	Nil
Ionic activity coeff correlation eq 6	2%	0.04	0.03

ilarly, the several pK_2 values corresponding to a given solution late in the titration were insensitive to points early in the titration. This reflects the fact that the two dissociation constants are sufficiently separated that readings before the first equivalence point largely determine pK_1 and readings after determine pK_2. Consequently, the several pK values calculated from a single reading were averaged and then treated statistically as follows: (a) averages $\overline{pK_1}$ and $\overline{pK_2}$ were calculated from the above set of averages (included were data from other titrations at a single temperature if duplicate titrations were done); (b) the standard deviation

$$s = \left[\frac{\sum_i (pK_i - \overline{pK})^2}{N - 1} \right]^{1/2}$$

was calculated; (c) any pK value whose deviation from $\overline{pK}$ exceeded $2s$ was rejected (a total of 2 pK_1 and 3 pK_2 values were rejected in this way); (d) in the case of rejection in (c) a new average and standard deviation were calculated.

The results are summarized in Table I and plotted in Figure 1. In the table, N_b is the number of readings before the first equivalence point utilized in the final calculation of $\overline{pK_1} \pm s$ and N_a related similarly to $\overline{pK_2} \pm s$. The $\overline{pK_2}$ values show a clear temperature dependence and can be fitted by the three-parameter function

$$pK_2 = \frac{-1937}{T} + 14.25 - 0.01434T \qquad (9)$$

which is the curve in Figure 1. The temperature dependency of pK_1 is uncertain. It appears, however,

comparison of these results with the standard deviations in Table I shows that the statistical treatment of the data generates uncertainty values that are well within the limits based on our estimates of propagated errors. However, little can be said about inaccuracy in these reported pK values resulting from deviations of the activity coefficients of squaric acid ionic species from Davies' correlation, eq 6.

The fitted eq 9 was used to calculate standard molar Gibbs free energy, enthalpy, and entropy of the second dissociation using eq 1, 2, and 3. At 25° these are

$$\Delta G° = 4.748 \pm 0.031 \text{ kcal/mol}$$

$$\Delta H° = -3.028 \text{ kcal/mol}$$

$$\Delta S° = -26.08 \text{ cal/mol-deg}$$

On the basis of estimated limiting slopes through the 25° pK_2 value, we conclude that $\Delta H°$ is uncertain to about 15% and $\Delta S°$ to about 6%. The unusual strength of squaric acid, however, is in the first dissociation, and a clearer understanding of this phenomenon awaits more accurate measurements probably by some other technique. In this laboratory we are attempting to measure the first ionization conductometrically.

Thermodynamics of Binary Liquid Mixtures by Total Intensity

Rayleigh Light Scattering.   II

by Harvie H. Lewis, Raymond L. Schmidt, and H. Lawrence Clever*

Chemistry Department, Emory University, Atlanta, Georgia 30322 (*Received March 26, 1970*)

Rayleigh scattering and depolarization were measured for benzene–methanol, benzene–propanol-2, and benzene–n-dodecane solutions. The gradient of the concentration dependence of refractive index, $\Delta n/\Delta X$, was directly measured as a function of composition for the solutions by differential refractometry. The measurements were combined with total intensity light scattering and depolarization data to obtain activity coefficients and excess Gibbs free energies of mixing which were compared with results from vapor pressure measurements for the alcohol-containing solutions. The excess free energy of mixing from light scattering at 0.5 mole fraction was 4% below the accepted vapor pressure value for benzene–methanol and 16% below for benzene–propanol-2. The benzene–n-dodecane solutions appear to have a negative excess free energy of mixing over part of the composition range. The light scattering method, at best, can give only approximate thermodynamic values for solutions with a negative excess free energy of mixing.

Rayleigh scattering from liquids and liquid solutions is an active field of study with a constant reevaluation of the theoretical equations as they apply to liquids.[1-4] Over the past several years there have been several studies of Rayleigh scattering from binary nonelectrolyte solutions of small molecules. In these studies either the Rayleigh scattering and depolarization measured for the solution were treated to obtain activity coefficients of the components and excess Gibbs free energy of mixing[5-7] or properties of the solutions were used to calculate a predicted Rayleigh scattering which was compared with experiment.[8,9] Studies of the second type have also been carried out on aqueous electrolyte solutions.[10]

This work is a further study of the relationship between Rayleigh scattering and the thermodynamic properties of binary nonelectrolyte solutions, with particular attention to the contribution of the gradient of the concentration dependence of refractive index to the relationship.

The total Rayleigh scattering, R_{90}, can be separated into an isotropic contribution, R_{is}, and an anisotropic contribution, R_{an}, by the Cabannes relation. In pure liquids the isotropic scattering is due to density fluctuations, R_d. In solutions two further terms contribute to the isotropic scattering, a concentration fluctuation, R_c, and a density–concentration fluctuation cross term, $R^\#$. The total isotropic Rayleigh scattering from a solution is the sum $R_{is} = R_d + R_c + R^\#$ with

$$R_d = (\pi^2/2\lambda_0^4)kTK_t[N(\partial\epsilon/\partial N)_t]^2 \qquad (1)$$

* To whom correspondence should be addressed.

(1) D. J. Coumou, E. L. Mackor, and J. Hijmans, *Trans. Faraday Soc.*, **60**, 1539 (1964).

(2) A. Litan, *J. Chem. Phys.*, **48**, 1052, 1058 (1968).

(3) M. Kerker, "The Scattering of Light and Other Electromagnetic Radiation," Academic Press, New York, N. Y., 1969.

(4) D. McIntyre and J. V. Sengers in "Physics of Simple Liquids," H. N. V. Temperley, J. S. Rowlinson, and G. S. Rushbrooke, Ed., North-Holland Publishing Co., Amsterdam, 1968, Chapter 11.

(5) D. J. Coumou and E. L. Mackor, *Trans. Faraday Soc.*, **60**, 1726 (1964).

(6) R. L. Schmidt and H. L. Clever, *J. Phys. Chem.*, **72**, 1529 (1968).

(7) R. S. Myers and H. L. Clever, *J. Chem. Thermodynamics*, **2**, 53 (1970).

(8) G. D. Parfitt and J. A. Wood, *Trans. Faraday Soc.*, **64**, 805 2081 (1968).

(9) M. S. Malmberg and E. R. Lippincott, *J. Colloid Interface Sci.*, **27**, 591 (1968).

(10) B. A. Pethica and C. Smart, *Trans. Faraday Soc.*, **62**, 1890 (1966).

$$R_c = (\pi^2/2\lambda_0^4)kTVX_1(\partial\epsilon/\partial X_2)^2/(\partial\mu_2/\partial X_2) \quad (2)$$

$$R^\# = (\pi^2/\lambda_0^4)kTK_t[N(\partial\epsilon/\partial N)_t][C_2(\partial\epsilon/\partial C_2)] \quad (3)$$

where λ_0 is the wavelength of the incident light in a vacuum, V is the molar volume, X_1 and X_2 are the mole fractions of components 1 and 2, respectively, μ_2 is the chemical potential of component 2, ϵ is the optical dielectric constant ($\epsilon = n^2$, where n is the refractive index at wavelength λ_0), K_t is the isothermal compressibility, C_2 is the concentration of component 2 in g/cc, N is the number density, k is the Boltzmann constant, and T is the absolute temperature.

In an ideal solution, by definition, $\partial\mu_2/\partial X_2 = RT/X_2$ and R_c becomes the ideal concentration scattering, R_{id}, where

$$R_{id} = (\pi^2/2\lambda_0^4)VX_1X_2(\epsilon\partial/\partial X_2)^2/N_a$$
$$= (2\pi^2/\lambda_0^4)VX_1X_2(n\partial n/\partial X_2)^2/N_a \quad (4)$$

where N_a is Avogadro's number.

For a real solution the ratio of ideal to real concentration scattering is

$$R_{id}/R_c = (X_2/RT)(\partial\mu_2/\partial X_2)$$
$$= (X_2/RT)(RT/X_2 + \partial\mu_2^E/\partial X_2) \quad (5)$$

where $\partial\mu_2^E = RT \partial \ln f_2$ with μ_2^E and f_2 being the excess chemical potential and activity coefficient, respectively, due to component 2 in the solvent reference state. Rearrangement and integration of eq 5 gives

$$\ln f_2 = \int_1^{x_2} (1/X_2)(1 - R_{id}/R_c)dX_2 \quad (6)$$

The activity coefficient of component 1 is obtained from a similar set of equations and the excess Gibbs free energy is calculated from

$$\Delta G^E = RT (X_1 \ln f_1 + X_2 \ln f_2) \quad (7)$$

The relationship between the concentration fluctuation contribution to isotropic scattering, R_c, and chemical potential is clear and direct, but converting Rayleigh scattering data into activity coefficients of the solution components is a multistepped process with potential errors in every step. If one accepts the theoretical equations some of the possible sources of error include (1) both the reliability of the Cabannes relation and the experimental uncertainty in the solution depolarization values used to partition R_{90} into R_{is} and R_{an}; (2) uncertainties in the calculated values of R_d and $R^\#$ which are required to obtain R_c from the difference function $R_c = R_{is} - R_d - R^\#$; (a) uncertainties in the calculated values of R_d came from uncertainties in the values of solution isothermal compressibilities and in values of the function $N(\partial\epsilon/\partial N)_t$ and (b) uncertainties in the calculated values of $R^\#$ include the same terms important to R_d plus uncertainties in the solution refractive index and the gradient of the composition dependence of refractive index; (3) uncertainties in the

calculated values of R_{id}, used to form the R_{id}/R_c ratio, which came from uncertainties in values of the solution refractive index and values of the refractive index–composition slope in the term $n\partial n/\partial X_2$.

To obtain activity coefficients of binary solutions from Rayleigh light scattering data one should measure or have available, in addition to the solution Rayleigh scattering and depolarization, the solution isothermal compressibilities, the optical dielectric constant–number density slope, the solution refractive indices, the refractive index–composition slope, and the solution densities. Neither we nor others have measured all these solution properties. Many of them have been approximated from theoretical or semiempirical relations. For example, (1) the pure liquid isothermal compressibilities, when not available in the literature, are found from the pure liquid Rayleigh scattering.[11] The solution isothermal compressibilities are then assumed to be additive in volume fraction. (2) The number density dependence of the optical dielectric constant is calculated from the Clausius–Mosotti equation multiplied by an empirical dense media correction factor.[6,11] Recently a somewhat improved correction factor has been suggested.[12] (3) The solution refractive indices have been estimated from the Lorentz–Lorenz equation. The dn/dx and dn/dc values were obtained either by differentiation of a quadratic fit to the calculated refractive indices as a function of composition or alternatively dn/dx was calculated directly from a differentiated form of the Lorentz–Lorenz equation, which required an accurate density gradient of the solution.

In this work a direct experimental determination of $\Delta n/\Delta x$ was made, and the resulting values were used in the calculation of activity coefficients and excess free energies of mixing from the Rayleigh scattering and depolarization values.

Experimental Section

Materials. Benzene, Mallinckrodt, was distilled on a 20-plate stainless steel helices packed column. *n*-Dodecane, Phillips, 99 mol %, was shaken with concentrated H_2SO_4, washed until neutral to litmus, and distilled at 63 ± 2 mm pressure, 130°. A freezing point curve indicated liquid-soluble, solid-insoluble impurity at 0.12 mol %. Methanol, Fisher reagent grade, was distilled from over CaO before use. Propanol-2, Fisher 99 mol %, was distilled twice from over CaO.

Solution Preparation. Solutions for the measurement of $\Delta n/\Delta x$ were prepared by weight in special weighing bottles[13] with care taken to correct for any vapor loss. Δx varied from 0.005 to 0.1 with most values falling near 0.02.

Light scattering measurements were as described in earlier work.[6,11]

(11) R. L. Schmidt, *J. Colloid Interface Sci.*, **27**, 516 (1968).

(12) G. H. Meeten, *Nature*, **218**, 761 (1968).

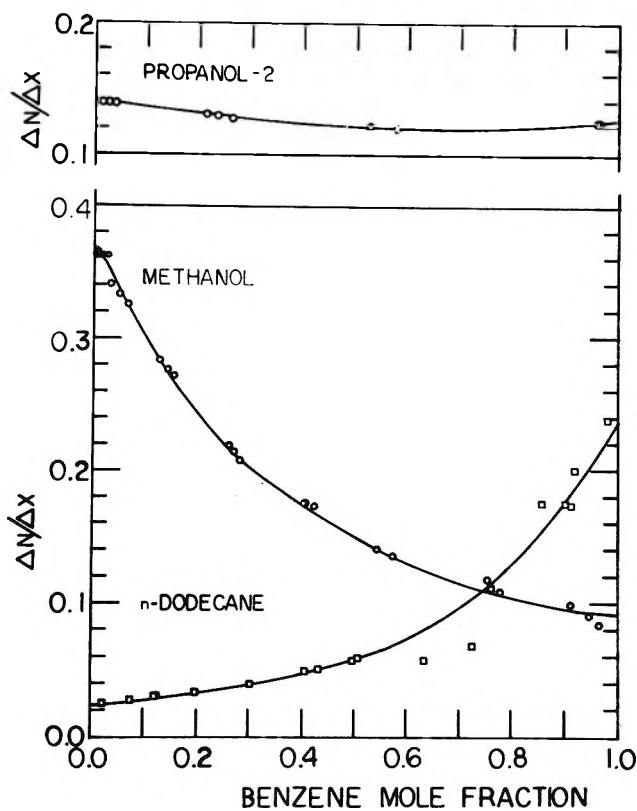(13) R. Battino, *J. Phys. Chem.*, **70**, 3408 (1966).

Figure 1. Experimental $\Delta n/\Delta x$ vs. mole fraction, 25°, 546 mμ.
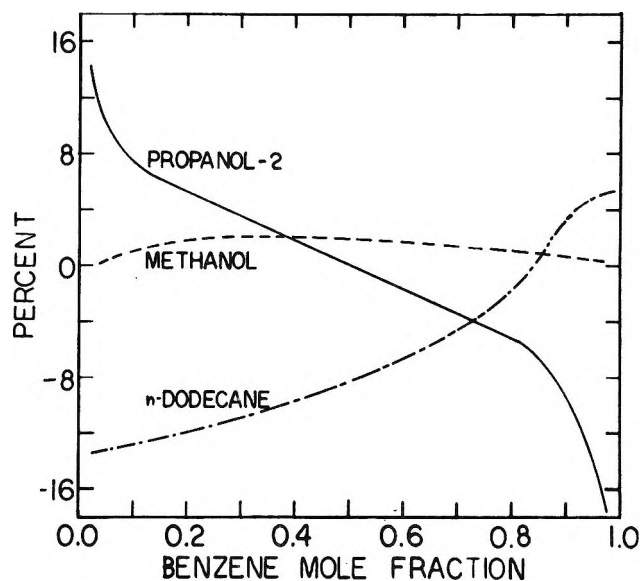

Figure 2. Per cent difference $[(\Delta n/\Delta x)_{\text{exptl}} - (\Delta n/\Delta x)_{\text{calcd L-L}}]100/(\Delta n/\Delta x)_{\text{exptl}}$ vs. mole fraction.

Differential Refractometer. Direct determination of values of $\Delta n/\Delta x$ were made on a Brice–Phoenix Model BP-2000-U differential refractometer. The instrument was calibrated with KCl solutions,[14] and temperature was controlled to 25.0 ± 0.1°.

Results and Discussion

Values of $\Delta n/\Delta x$ determined experimentally are shown in Figure 1. Values from the smoothed curve are in Table I where a refractive index–composition table is constructed using the 546-mμ refractive index of benzene at 25° of 1.5020.[15] The values appear reasonable, and the benzene–methanol results are in good agreement with literature values.[16]

The Lorentz–Lorenz (L–L) equation is generally accepted for the calculation of solution refractive indices.[17] However, to obtain the refractive index–composition gradient, $\Delta n/\Delta x$, the use of the L–L equation is found to be unsatisfactory. The direct differentiation of the L–L equation yields an expression which is unduly sensitive to values of the density-composition gradient. The per cent deviation, $[(\Delta n/\Delta x)_{\text{exptl}} - (\Delta n/\Delta x)_{\text{calcd}}$L–L$]100/(\Delta n/\Delta x)_{\text{exptl}}$, is shown in Figure 2. With the exception of the benzene–methanol solutions the errors are quite large, rising to 16% at the composition extremes.

Values of the refractive index[16] at 546 mμ and $\Delta n/\Delta x$ calculated from the Lorentz–Lorenz equation agree well with experiment for the methanol–benzene solutions. The refractive index is in error 0.091 and 0.074% at 0.5

and 0.25/0.75 mole fractions, respectively. The addition of a term ax_1x_2 to the Lorentz–Lorenz equation with $a = 5.5 \times 10^{-3}$ makes the agreements with experiment almost quantitative (average deviation 0.005%). Both the L–L and the modified L–L equation reproduced $\Delta n/\Delta x$ to 1–3%.

The Lorentz–Lorenz equation is not strictly applicable to the liquid phase. The regular pattern of the deviations of the experimental data from the Lorentz–Lorenz equation suggests we use an equation with corrections for the closeness of approach of the molecules found in the liquid state. Bottcher[18] suggested that the induced dipole in the molecule would also induce a dipole in its surroundings producing what he called the reaction field which enhances the polarizability of the molecule. The reaction field is a function of the radius of the cavity occupied by the molecule and of the refractive index. A computer program was written to calculate the refractive index of a binary solution from Bottcher's total molar polarization equation and an assigned value of the cavity radius for the reaction field calculation. The L–L equation was used to approximate the value of the refractive index for the reaction field, and the cavity radius was calculated assuming the molecules were spheres occupying the total molar volume. The effective polarizabilities of benzene and methanol were increased 10 and 6%, respectively, by the reaction field. The refractive indices calculated

(14) A. Kruis, *Z. Phys. Chem. (Leipzig)*, **34B**, 1 (1936).

(15) A. F. Forziati, *J. Res. Nat. Bur. Stand.*, **44**, 373 (1950).

(16) S. E. Wood, S. Langer, and R. Battino, *J. Chem. Phys.*, **32**, 1389 (1960).

(17) W. Heller, *J. Phys. Chem.*, **69**, 1123 (1965).

(18) C. J. F. Bottcher, "Theory of Electric Polarization," Elsevier, Amsterdam, 1952, Chapter VI.

Table I: Smoothed Values of $\Delta n/\Delta X$ and Calculated Refractive Indices of 546 mμ and 25°

Benzene mole fraction X_2	Propanol-2–benzene		Methanol–benzene		n-Dodecane–benzene	
	$\Delta n/\Delta X$	n_{5461}	$\Delta n/\Delta X$	n_{5461}	$\Delta n/\Delta X$	n_{5461}
	$(0.1246)^d$	$(1.3774)^b$	$(0.1741)^d$	$(1.3279)^b$	$(0.0805)^d$	$(1.4215)^a$
0.00	...	1.3767	...	1.3278	...	1.4226
0.05	0.138	...	0.340	...	0.026	...
0.10	...	1.3905	...	1.3618	...	1.4252
0.15	0.132	...	0.268	...	0.031	...
0.20	...	1.4037	...	1.3886	...	1.4283
0.25	0.128	...	0.219	...	0.037	...
0.30	...	1.4165	...	1.4105	...	1.4320
0.35	0.125	...	0.187	...	0.044	...
0.40	...	1.4290	...	1.4292	...	1.4364
0.45	0.122	...	0.162	...	0.052	...
0.50	...	1.4412	...	1.4454	...	1.4416
0.55	0.121	...	0.141	...	0.065	...
0.60	...	1.4533	...	1.4595	...	1.4481
0.65	0.120	...	0.123	...	0.085	...
0.70	...	1.4653	...	1.4718	...	1.4566
0.75	0.121	...	0.109	...	0.110	...
0.80	...	1.4774	...	1.4827	...	1.4676
0.85	0.122	...	0.099	...	0.146	...
0.90	...	1.4896	...	1.4926	...	1.4822
0.95	0.124	...	0.094	...	0.198	...
1.00	...	1.5020^c	...	1.5020^c	...	1.5020^c

[a] Pure liquid refractive index at 5461 Å calculated from n–λ and $\partial n/\partial t$ data in Timmermans. [b] Reference 16. [c] Refractive index of benzene at 25° and 5461 Å from ref 15. [d] Slope if refractive index is linear in mole fraction.

from Bottcher's total molar polarization equation agreed with experiment within 0.035%, which is a substantial improvement over the L–L equation agreement. However, the Bottcher equation was very sensitive to small changes in the cavity radius. Although promising, the Bottcher approach was pursued no further at this time.

The light scattering measurements are reported in Table II. Values of R_{id} were calculated using smoothed values of the experimental $\Delta n/\Delta x$ values. Thermodynamic results for benzene–methanol are given in Table III where the excess free energies are compared with the accepted literature values[19] and with values obtained using $\Delta n/\Delta x$ values approximated from the Lorentz–Lorenz refractive indices of the solution. The use of the experimental $\Delta n/\Delta x$ values did not alter appreciably the free energy of mixing of benzene–methanol at 0.5 mole fraction. However, the overall shape of the free energy–composition curve was improved with values being consistently 4% low except in the dilute solutions where differences approached 10%.

Measurements on benzene–propanol-2 solutions were made at temperatures of 25 and 43.7°. Activity coefficients and excess free energies of mixing are given in Table IV. The free-energy results parallel but are 16% below values obtained in a careful vapor pressure study.[20]
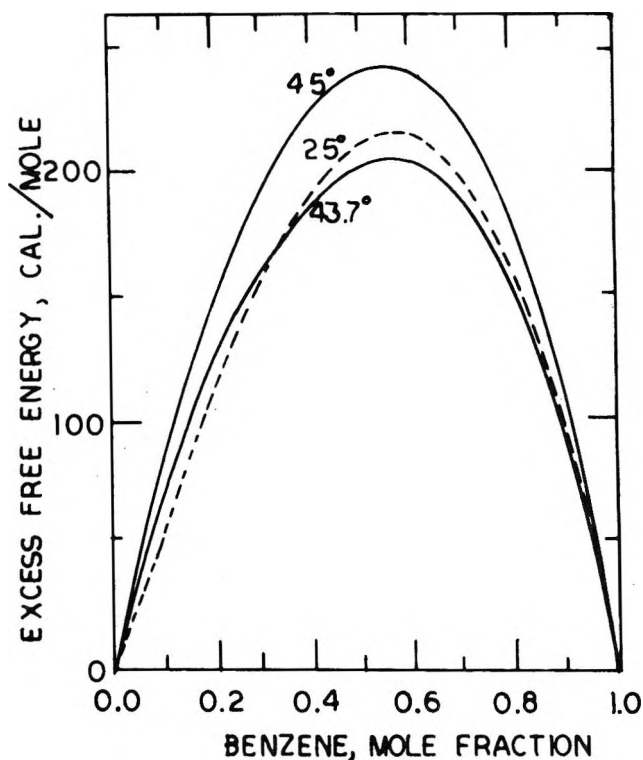

Figure 3. Propanol-2–benzene solutions; a comparison of excess free energy of mixing vs. mole fraction: upper curve, 45° from vapor pressure measurements, ref 20; lower curves, 25 and 43.7° from light scattering measurements.

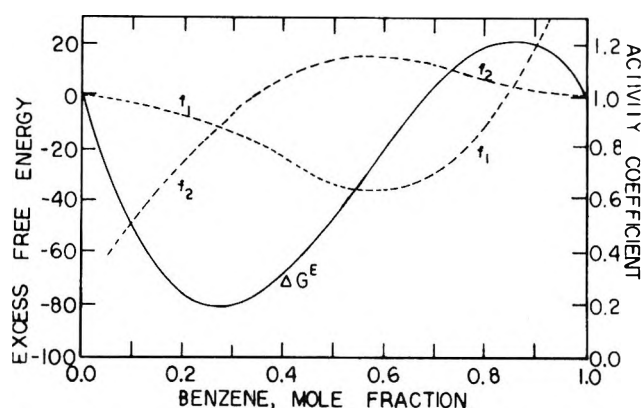**Table II:** Total Intensity Rayleigh Scattering and Depolarization

Mole fraction X_2	436 mμ $R_{90} \times 10^6$, cm⁻¹	ρ_μ	546 mμ $R_{90} \times 10^{-6}$, cm⁻¹	ρ_μ
Methanol (1)–benzene (2), 25°				
0.0000	8.60		3.10	0.047[a]
0.0275	12.85	0.093[a]	4.50	0.093[a]
0.0585	18.20	0.119[a]	6.45	0.119[a]
0.2235	47.95	0.131[a]	16.30	0.131[a]
0.2905	59.70	0.125[a]	21.00	0.125[a]
0.4400	84.50	0.124	28.90	0.120
0.5740	95.85	0.133	32.55	0.134
0.8250	62.15	0.277	21.10	0.271
0.9155	49.70	0.385	16.85	0.377
0.9500	47.75	0.393	16.15	0.393
1.000	46.50	0.420	16.10	0.410
Propanol-2 (1)–benzene (2), 25°				
0.000	9.75	0.06	3.51	0.05
0.043	...	...	4.63	0.10
0.155	20.9	0.17	7.1	0.17
0.157	23.3	0.19	8.1	0.16
0.218	26.7	0.185	9.1	0.16
0.319	37.0	0.175	12.0	0.165
0.395	44.0	0.185	14.9	0.18
0.461	51.0	0.175	16.6	0.17
0.477	51.0	0.185	16.8	0.175
0.645	59.3	0.21	19.7	0.20
0.681	61.4	0.21	20.3	0.215
0.834	55.6	0.295	18.6	0.29
0.912	49.5	0.365	16.7	0.35
0.935	49.9	0.385	·17.3	0.39
0.971	...	...	16.7	0.425
1.000	46.5	0.42	16.1	0.41

Mole fraction X_2	436 mμ $R_{90} \times 10^6$, cm⁻¹	ρ_μ	546 mμ $R_{90} \times 10^{-6}$, cm⁻¹	ρ_μ
Propanol-2 (1)–benzene (2), 43.7°				
0.000	10.95	0.06	3.90	0.05
0.026	11.4	0.10	...	...
0.038	...	...	4.4	0.08
0.043	...	...	4.9	0.10
0.155	21.7	0.145	7.5	0.13
0.218	25.8	0.185	...	...
0.319	35.3	0.185	11.6	0.18
0.395	41.2	0.185	13.3	0.18
0.461	46.8	0.185	15.4	0.185
0.477	46.6	0.185	15.2	0.175
0.645	55.3	0.21	18.1	0.20
0.681	56.5	0.235	19.1	0.235
0.834	54.5	0.305	18.4	0.295
0.912	51.1	0.365	17.5	0.35
0.935	50.9	0.39	17.6	0.385
0.971	...	...	17.5	0.405
1.000	50.1	0.43	17.5	0.425
n-Dodecane (1)–benzene (2), 30°				
0.000	18.0	0.24	5.75	0.175
0.040	18.7	0.27	5.95	0.23
0.397	28.1	0.315	9.05	0.28
0.419	29.1	0.31	9.35	0.275
0.592	35.3	0.30	11.5	0.32
0.708	42.0	0.315	13.9	0.305
0.831	49.2	0.32	16.4	0.315
0.884	50.0	0.325	16.7	0.30
0.920	50.3	0.34	16.9	0.315
0.964	50.0	0.38	16.8	0.34
0.990	48.3	0.40	16.5	0.375
1.000	49.5	0.415	16.8	0.41

[a] From data reported in ref 5.

Table III: Excess Free Energy of Mixing and Activity Coefficients of Methanol (1)–Benzene (2) Solutions at 25°

X_2	ln f_1	ln f_2	ΔG^E, cal/mol[a] (1)	(2)	(3)
0.0	0.0	...	0	0	0
0.1	0.0174	1.502	98	106	108
0.2	0.0698	1.205	176	197	188
0.3	0.1545	0.950	233	238	246
0.4	0.269	0.738	270	274	283
0.5	0.414	0.560	289	293	301
0.6	0.603	0.406	287	289	299
0.7	0.864	0.266	264	267	274
0.8	1.24	0.142	214	220	223
0.9	1.81	0.0431	130	140	137
1.0	...	0.0	0	0	0

[a] (1), R_{id} calculated using experimental $\Delta n/\Delta X$ values; (2), R_{id} calculated using $\Delta n/\Delta X$ values approximated from Lorentz-Lorenz equation; (3), ref 19.

Figure 4. *n*-Dodecane–benzene solutions, 30°; excess free energy and activity coefficients *vs.* composition.

It was disappointing to find that use of the smoothed experimental $\Delta n/\Delta x$ values actually made the agreement 3% poorer than use of $\Delta n/\Delta x$ values approximated from the Lorentz–Lorenz equation.

(19) G. Scatchard and L. B. Ticknor, *J. Amer. Chem. Soc.*, **74**, 3724 (1952).

(20) I. Brown, W. Fock, and F. Smith, *Aust. J. Chem.*, **9**, 364 (1956).

Table IV: Activity Coefficients and Excess Free Energies of Mixing for Propanol-2–Benzene, and n-Dodecane–Benzene Solutions by Rayleigh Light Scattering

Mole fraction benzene X_2	f_1	f_2	ΔG^E, kcal/mol
Propanol-2 (1)–benzene (2), 25°			
0.1	1.00	2.51	0.05
0.2	1.01	2.38	0.11
0.3	1.05	2.13	0.15
0.4	1.13	1.86	0.19
0.5	1.28	1.59	0.21
0.6	1.53	1.38	0.22
0.7	1.96	1.21	0.20
0.8	2.56	1.09	0.16
0.9	3.86	1.02	0.09
Propanol-2 (1)–benzene (2), 43.7°			
0.1	1.01	2.95	0.08
0.2	1.04	2.27	0.13
0.3	1.10	1.88	0.16
0.4	1.18	1.65	0.19
0.5	1.29	1.47	0.20
0.6	1.50	1.32	0.20₅
0.7	1.85	1.18	0.19
0.8	2.46	1.08	0.15
0.9	3.46	1.01	0.08
n-Dodecane (1)–benzene (2)			
0.1	0.98	0.52	−0.05
0.2	0.92	0.74	−0.08
0.3	0.85	0.94	−0.08
0.4	0.79	1.07	−0.07
0.5	0.75	1.14	−0.05
0.6	0.75	1.15	−0.02
0.7	0.79	1.12	0.00₅
0.8	0.92	1.06	0.02
0.9	1.18	1.02	0.02

The temperature coefficient of the excess free energy gave values of $T\Delta S^E$ and ΔH^m which agreed well with literature values at 0.3, 0.4, 0.5, and 0.6 mole fraction alcohol. For example, at 0.5 mole fraction ΔH^m and $T\Delta S^E$ are 370 and 170, respectively, from our data and 393 and 152, respectively, from the literature.[20] However, at high alcohol mole fraction the temperature coefficient of ΔG^E goes negative (Figure 3) while the literature $T\Delta S^E$ values indicate a positive temperature coefficient of ΔG^E at all compositions at 45°. There is ample evidence in the literature of a change in sign of $T\Delta S^E$ with composition going to all negative values as temperatures decrease for benzene–ethanol[18,19] toluene–ethanol,[20,22] and methylcyclohexane–ethanol[21,22] solutions. Thus this change in the temperature ΔG^E may be real for the benzene–propanol-2 solutions, but the uncertainty in our ΔG^E values at high alcohol concentration allows no reliable calculation.

Activity coefficients and excess free energies of mixing of the n-dodecane–benzene solutions are given in Table IV and Figure 4. Over much of the composition range $R_c < R_{id}$. When this occurs uncertainties in the R_{id}/R_c ratio become large and the activity coefficients of less than unity that are obtained are not as reliable as the activity coefficients greater than unity. Thus the thermodynamic values by light scattering are at best only an indication of what may be happening in the n-dodecane–benzene system. The negative free energy is contrary to what is found in most aromatic–aliphatic hydrocarbon solutions,[23] although other hydrocarbon solutions, e.g., n-dodecane–cyclohexane solutions, do show a negative excess free energy.[24]

It is apparent that the use of experimental $\Delta n/\Delta x$ values does not lead to particularly improved values of activity coefficients and excess free energies of mixing from light scattering measurements. Thus, other approaches must be sought to improve our understanding of the light scattering technique. An obvious place to attack is the $d\epsilon/dN$ term and to a lesser extent the solution isothermal compressibility. Both terms contribute to the density fluctuation part of the isotropic scattering. An experimental approach is to measure the pressure dependence of refractive index and use equations with N and p as independent variables

$$R_d \cong (\pi^2/2\lambda_0^4)(kT/K_t)(\partial\epsilon/\partial p)_t^2$$

A theoretical approach[25] would be the use of Onsager's equation for the internal field for the calculation of the density dependence of refractive index

$$\rho(\partial\epsilon/\partial\rho) = (\epsilon - 1)(2\epsilon^2 + \epsilon)/(2\epsilon^2 + 1)$$

which would result in larger values for R_c and improve results for solutions in which the light scattering technique gives low experimental values. The measurement of depolarization needs improvement. The use of laser sources[26] may be the answer to improved depolarization measurements.

(21) C. B. Kretschmer and R. Wiebe, *J. Amer. Chem. Soc.*, **71**, 1793, 3176 (1949).

(22) S. C. P. Hwa and W. T. Ziegler, *J. Phys. Chem.*, **70**, 2572 (1966).

(23) J. S. Rowlinson, "Liquids and Liquid Mixtures," Academic Press, New York, N. Y., 1959, p 149.

(24) J. D. Gomez-Ibanez, J. J. C. Shieh, and E. M. Thorsteinson, *J. Phys. Chem.*, **70**, 1998 (1966).

(25) G. Oster, *Chem. Rev.*, **43**, 358 (1948).

(26) R. C. C. Leife, R. S. Moore, and S. P. S. Porto, *J. Chem. Phys.*, **40**, 3741 (1964).

Chemical Potential Interaction Parameters in Charge-Unsymmetric

Mixtures of Molten Salts[1]

by J. Braunstein,* K. A. Romberger, and R. Ezell[2]

Reactor Chemistry Division, Oak Ridge National Laboratory, Oak Ridge, Tennessee 37830   (*Received April 20, 1970*)

The applicability of conformal ionic solution theory to the interaction parameters for chemical potential in charge-unsymmetric molten salt mixtures is demonstrated. The experimental interaction parameter, $\lim_{x \to 0} (\mu_{\text{alkali halide}}{}^{E}/x^2)$, evaluated for mixtures of alkali fluoride with alkaline earth fluoride or of alkali chloride with alkaline earth chloride, is shown to vary linearly, as predicted by theory, with the ion size parameter $\delta = (d_1 - d_2)/d_1 d_2$, where d_1 and d_2 are the sums of cation and anion radii of the univalent and divalent salts, respectively. Mixing enthalpy dependence on δ is rationalized by a simple physical model.

Introduction

Kleppa, et al.,[3,4] have demonstrated the utility of the interionic distance parameter $\delta = (d_1 - d_2)/d_1 d_2$ in correlating enthalpies of mixing in charge-unsymmetric molten salt mixtures, e.g., mixtures of alkali and alkaline earth salts with a common anion. d_1 and d_2 are the sums of cation and anion radii in the pure univalent and divalent salts, respectively. The correlation has a theoretical basis in the conformal ionic solution theory (CIS), extended to charge-unsymmetric mixtures by Davis,[5] predicting that the limiting molar excess free energy or enthalpy, A, should have the form

$$\lim_{x \to 0} \frac{\Delta A^{E}}{x(1-x)} = \bar{A}_2{}^{E}(x=0) = [\Omega]\delta + U \qquad (1)$$

where x is the mole fraction of divalent salt; Ω and U are combinations of unevaluated integrals occurring in the configurational partition function and its derivatives and contain the temperature and pressure dependence (and are different for free energy or enthalpy). For charge-symmetric salt mixtures, the first-order term in δ vanishes, and CIS predicts that the molar excess thermodynamic quantities are proportional to the square of δ.[6]

$$\lim_{y \to 0} \frac{\Delta A^{E}}{y(1-y)} = \bar{A}_2{}^{E}(y=0) = [\Omega]\delta^2 \qquad (2)$$

For the most part, curiously, the CIS correlation has been tested only with the excess enthalpy. This has been the case even when free energy data were available for a more general test and enthalpies were derived from temperature coefficients of emf rather than calorimetrically.[7] Guion,[8a] however, has demonstrated the fit of the charge-symmetric expression to excess free energies in binary univalent nitrate mixtures. Prior to Davis' extension of CIS to charge unsymmetric systems, Holm[8b] correlated chemical potential interaction parameters, $[\mu_1{}^{E}/x^2]_{x=0}$, with an empirical parameter re-

lated to differences of ionic potentials for several charge-unsymmetric fluoride mixtures. $\mu_1{}^{E}$ is the excess chemical potential of solvent (univalent) and x is the mole fraction of solute (divalent).

In this paper we demonstrate for the first time the applicability of CIS to chemical potential interaction parameters in charge-unsymmetric systems. We show that experimental values of $[\mu_1{}^{E}/x^2]_{x=0}$ vary linearly, as predicted by theory, with the conformal ionic solution parameter δ for the alkali–alkaline earth fluoride systems considered by Holm, four additional ones, and several chloride systems. It is furthermore not necessary to assume the symmetric solution relation for the excess free energy, $G^{E} = ax(1-x)$, which would imply $[\mu_2{}^{E}]_{x=0} = [\mu_1{}^{E}/x^2]_{x=0}$, in order to derive the CIS correlation for the interaction parameter. Davis' first-order expression for the composition dependence of the free energy of mixing, from which he derives eq 1 by a limiting process, contains quantities (θ_{12} and α_{12}) relating to the configurational partition function and its derivatives, for the mixture and for the pure salts (see reference 5b, eq 2.25). By developing the Taylor series expansion of the first-order expression in powers of the solute concentration, it follows readily that $[\mu_1{}^{E}/x^2]_{x=0}$ should have the form of the right-

* To whom correspondence should be addressed.

(1) Research sponsored by the U. S. Atomic Energy Commission under contract with the Union Carbide Corporation.

(2) ORAU Summer Student Trainee from University of Arkansas, 1969.

(3) J. Holm and O. J. Kleppa, *Inorg. Chem.*, 8, 207 (1969).

(4) O. J. Kleppa and F. G. McCarty, *J. Phys. Chem.*, 70, 1249 (1966).

(5) (a) K. D. Luks and H. T. Davis, *Ind. Eng. Chem. Fundam.*, 6, 194 (1967); (b) H. T. Davis, *J. Chem. Phys.*, 41, 2761 (1964).

(6) H. Reiss, J. L. Katz, and O. J. Kleppa, *ibid.*, 36, 144 (1962).

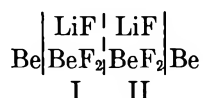(7) G. D. Robbins, T. Førland, and T. Ostvold, *Acta Chem. Scand.*, 22, 3002 (1968).

(8) (a) J. Guion, *J. Chim. Phys.*, 64, 1635 (1967); (b) J. Holm, *Electrochim. Acta*, 11, 351 (1966).

hand side of eq 1. We also present in this paper a heuristic physical rationalization of the form of eq 1 for the enthalpy or energy.

Results

Data on chloride mixtures were reported by Robbins, et al.,[7] from emf measurements. Data on fluorides were taken mostly from the accurate cryoscopic measurements of Cantor[9] with NaF as the solvent.

Data on the LiF–BeF$_2$ system were obtained by us from new measurements of the LiF liquidus which will be discussed more completely in a subsequent publication. The liquidus temperatures and compositions were obtained from discontinuities, on initiation of LiF precipitation, in the slopes of emf–temperature plots at constant overall composition, and of isothermal emf–composition plots.[10a,b] A concentration cell with transference, with beryllium electrodes, was employed.

$$\begin{array}{c|c|c|c} & \text{LiF} & \text{LiF} & \\ \text{Be} & \text{BeF}_2 & \text{BeF}_2 & \text{Be} \\ & \text{I} & \text{II} & \end{array}$$

This cell, used in the determination of transference numbers, has been described previously.[10a] The new liquidus data are presented in Table I and supplement previous data in this system.[10c]

Table I: Liquidus Temperature and Compositions in the LiF–BeF$_2$ System between 0.12 and 0.22 Mole Fraction BeF$_2$

Mole fraction BeF$_2$ (x_{BeF_2})	Liquidus temperature, °C
Equilibrium Saturating Phase:	LiF
0.1188	784.7
0.1215	782.9
0.1371	770.6
0.1404	767.9
0.1574	753.2
0.1625	747.9
0.1853	723.9
0.1894	718.0
0.2053	699.5
0.2066	698.0
0.2140	688.2
0.2220	678.0

Excess chemical potentials of LiF ($\mu_{\text{LiF}}^{\text{E}}$ at temperature T) were calculated from the data in Table I by means of the eq 3.

$$\mu_{\text{LiF}}^{\text{E}} = -RT \ln (1 - x) + L\left(\frac{T}{T_{\text{m}}} - 1\right) +$$

$$C\left(T_{\text{m}} - T + T \ln \frac{T}{T_{\text{m}}}\right) + \frac{b}{2}(T_{\text{m}} - T)^2 \quad (3)$$

The heat of fusion, L, melting point, T_{m}, and heat

capacity of solid and liquid LiF were taken from the JANAF tables.[11] The difference of heat capacities was fitted by the expression $C_{\text{p}}^{\text{l}} - C_{\text{p}}^{\text{s}} = C + bT$. The interaction parameter was obtained by extrapolation to $x = 0$ of a plot of $\mu_{\text{LiF}}^{\text{E}}/x^2$ vs. x^2. This plot, which covered a broader range of compositions than is usual in the calculation of interaction parameters, appeared linear and showed less scatter than plots in which the abscissa was x, thus suggesting the form $\mu_{\text{LiF}}^{\text{E}} = ax^2 + bx^4$ over the rather extended range of the measurements. Graphical extrapolation was employed rather than a least-squares analysis in order to give higher weight to compositions close to the extrapolated limit.

The interaction parameters of NaF in the systems reported by Cantor[9] were obtained by short extrapolation to $x = 0$ of plots of $\mu_{\text{LiF}}^{\text{E}}/x^2$ vs. x or x^2. (No apparent difference in linearity or scatter was evident in the plots vs. x or x^2 in this system, possibly because the range of the measurements was not sufficiently large to distinguish between cubic and quartic terms in $\mu_{\text{LiF}}^{\text{E}}$. In any case the uncertainty of the extrapolated interaction parameter was within the uncertainty of the correlation, about 0.5 kcal/mol.)

The excess chemical potentials of alkali fluoride in CsF–BeF$_2$, RbF–BeF$_2$, and KF–BeF$_2$ were estimated from phase diagrams,[12] thus having greater uncertainty than the cryoscopic results obtained at temperatures closer to the melting point, but they serve to extend the range of values of δ in the correlation. The heat capacity terms in eq 2 were neglected, and the interaction parameter was taken as the value of $\mu_{\text{alk.F}}^{\text{E}}/x^2$ at about 10 mol % solute.

For the chlorides, the interaction parameters were calculated from the reported coefficients in expressions for the excess free energy of mixing.[7]

Discussion

Figure 1 shows the interaction parameters plotted vs. δ for the chloride systems and for the fluoride systems. Pauling radii[13] of the ions were used to calculate d_1 and d_2. Thus the conformal ionic solution theory provides a useful correlation of excess thermodynamic functions in charge-unsymmetric molten salt mixtures, not only for enthalpies but for chemical potentials as well. The chlorides show considerably more scatter

(9) S. Cantor, J. Phys. Chem., 65, 2208 (1961).

(10) (a) K. A. Romberger and J. Braunstein, Inorg. Chem., 9, 1273 (1970); K. A. Romberger and J. Braunstein, MSRP Semiannual Progress Report, Feb 28, 1970, ORNL-4548, p 161; Aug 31, 1969, ORNL-4449, p 138; (b) H. A. Oye, Acta Chem. Scand., 18, 361 (1964). (c) R. E. Thoma, H. Insley, H. A. Friedman, and G. M. Hebert, J. Nucl. Mater., 27, 166 (1968).

(11) "JANAF Thermochemical Tables," D. R. Stull, Ed., PB 168 370, Clearing House for Federal Scientific and Technical Information, Springfield, Va., Aug 1965.

(12) R. E. Thoma, Ed., "Phase Diagrams of Nuclear Materials," ORNL Report No. 2548, 1959.

(13) L. Pauling, "The Nature of the Chemical Bond," 3rd ed, Cornell University Press, Ithaca, N. Y., 1960, p 514.
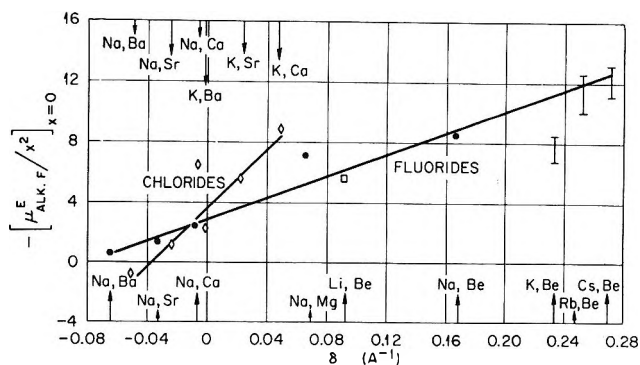
Figure 1. Interaction parameter for the limiting excess chemical potential of alkali halides in common anion mixtures of alkali and alkaline earth halides vs. the ion size parameter. Arrows at top and the symbols ◊ correspond to chlorides. Arrows at bottom and the symbols ● and □ refer to fluorides.
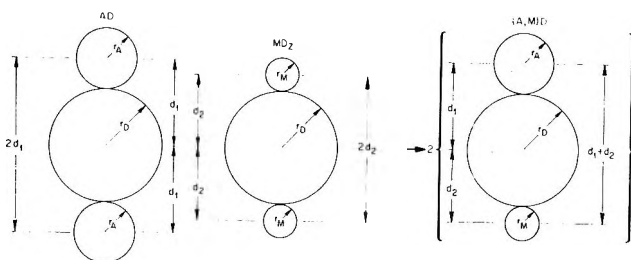

Figure 2. Simplified representation of change of next-nearest neighbor cation coulomb repulsion energy on mixing two salts of differing charge type with a common anion.

than the fluorides, although a smaller range of values of δ is covered and although the excess enthalpy data for the chlorides showed little scatter.[7] Although a quantitative accounting of the apparently much higher slope of the chloride interaction parameters is not yet feasible, the greater polarizability of chloride (than fluoride) may be a contributing factor. The unusual properties of BeF_2-rich mixtures,[3,10,14] related to the network structure of BeF_2 and its breakdown by alkali fluorides, are not manifested in the effect of BeF_2 in dilute solution on the chemical potential of the alkali fluoride solvent. By contrast, interaction parameters for transition metal fluorides (Cu^{2+}, Fe^{2+}, Ni^{2+}, Co^{2+})[15] in NaF show excess stability which may be related to the d electrons and ligand field effects.

Finally, we would like to point out that application of eq 1 to the enthalpy of charge-unsymmetric mixtures can be rationalized physically in a simple if nonrigorous manner with the Førland mixing model.[16] This simple Coulombic model suggested proportionality of enthalpy interaction parameters in charge-symmetric mixtures to a parameter related to δ^2, but has not been applied previously to charge-unsymmetric mixtures.[17-19] Consider the change of Coulomb repulsion energy of a pair of cations separated by an anion for the mixing of a univalent salt A^+D^- with a divalent salt of the same anion, $M^{2+}D_2^-$.

$$(A^+D^-A^+) + (M^{2+}D^-M^{2+}) \longrightarrow 2(A^+D^-M^{2+})$$

The energy change per pair of mixed triplets for the simplified process illustrated in Figure 2 is

$$\Delta E = \left[2\left(\frac{Z_1 Z_2}{d_1 + d_2}\right) - \frac{Z_2^2}{2d_2} - \frac{Z_1^2}{2d_1} \right] e^2$$

Setting the cation charges, Z_1 and Z_2, equal to 1 and 2 and rearranging

$$\Delta E = \left[-\frac{1}{2d_1} - \frac{2(d_1 - d_2)}{d_2(d_1 + d_2)} \right] e^2 \qquad (4)$$

The principal variation in this equation is in the term $(d_1 - d_2)$. The first term on the right-hand side is constant for a given univalent solvent, although its magnitude is much higher than the observed energies for mixtures of salts for which $d_1 - d_2 = 0$. The simple physical model thus predicts an excess energy and enthalpy of form similar to the result (eq 1) derived more rigorously from conformal ionic solution theory.

(14) B. F. Hitch and C. F. Baes, Jr., *Inorg. Chem.*, **9**, 201 (1969).

(15) S. Cantor and W. T. Ward, *J. Phys. Chem.*, **67**, 1868 (1963).

(16) T. Førland, "Thermodynamic Properties of Fused Salt Systems," in "Fused Salts," B. R. Sundheim, Ed., McGraw-Hill, New York, N. Y., 1964, p 77; J. Braunstein, "Ionic Interactions: Dilute Solutions to Molten Salts," S. Petrucci, Ed., Academic Press, New York, N. Y., in press.

(17) NOTE ADDED IN PROOF. A recent work[18] containing an application of the ionic model has come to our attention. That work also discusses the polarization energy[19] but fails to point out the relation of the model to the equations of conformal ionic solution theory. Also, it assumes regular solution behavior by neglecting the difference between enthalpy and free energy interaction parameters.

(18) C. Vallet, Thesis, Université d'Aix Marseille, Marseille, France, 1970.

(19) J. Lumsden, *Discuss. Faraday Soc.*, **32**, 138 (1961).

A Study of Adsorption on Single Crystals by Internal

Reflectance Spectroscopy

by Gary L. Haller* and Richard W. Rice

Department of Engineering and Applied Science, Yale University, New Haven, Connecticut 06520
(Received July 10, 1970)

The usefulness of internal reflection spectroscopy in studies of adsorption on surfaces of known structure is demonstrated for the case of alcohol adsorption on single-crystal α-aluminum oxide. The molecular orientation of a Langmuir–Blodgett deposited calcium stearate monolayer and n-amyl alcohol at submonolayer coverages on a $(41\bar{5}0)$ surface was determined qualitatively. Adsorption isotherms have been measured at several temperatures between 30 and 120° on three faces of α-aluminum oxide. The resulting isosteric heats of adsorption are 13, 19, and 26 kcal/mol at $\theta = 0.4$ on the (0001), $(11\bar{2}3)$, and $(41\bar{5}0)$ faces, respectively. An adsorption site involving a coordinatively unsaturated pair of Al^{3+} ions and an O^{2-} ion is postulated. A good correlation between the calculated number of such sites and the saturation coverage at 120° and between the extent of coordinative unsaturation of the pair site and heat of adsorption on the three surfaces is obtained.

Introduction

There now exists a very extensive literature on the infrared spectra of molecules adsorbed on surfaces.[1] Most of this work involves high-area amorphous oxides or metals supported on such oxides. The high area is required in order to obtain detectable infrared absorption in the transmission spectroscopy used. By utilizing internal reflection spectroscopy[2] (irs), it is possible to work with very small surface areas and maintain a detectable signal by requiring the infrared beam to be multiply reflected through the surface.

In general, metal oxides are transparent in the infrared and many which are of catalytic interest can be obtained as large single crystals. When these crystals are used as internal reflection prisms, it becomes possible to obtain infrared spectra of molecules adsorbed on surfaces of known structure. Moreover, the electric field amplitudes at the internally reflecting interface are different in the three spatial directions and are a function of beam polarization and angle of reflection.[3] Thus, it is possible to determine the average orientation of the adsorbed molecule by measuring the absorption as a function of polarization and angle of reflection. The simultaneous measurement of adsorptive capacity, heat of adsorption, and molecular orientation as a function of the structure of the adsorbing surface should allow deductions concerning the stereochemistry of the adsorption sites to be made.

The utility of infrared irs for the study of adsorption on single crystals will be demonstrated for the case of alcohol adsorption on α-aluminum oxide. Aluminas of various structures are often used as catalyst supports and/or catalysts. High-purity α-aluminum oxide (synthetic sapphire) is inexpensive and large crystals are readily available. These considerations and the LEED[4] investigations of surface structure on mechan-

ically polished and chemically or thermally etched α-aluminum oxide dictated the selection of this oxide for the initial work.

Adsorption isotherms and isosteric heats of adsorption of n-amyl alcohol have been obtained on the (0001), $(11\bar{2}3)$, and $(41\bar{5}0)$[5] faces of α-aluminum oxide. These faces were chosen on the basis of their distinguishing crystallographic features. They are, respectively, the hexagonal close-packed oxide plane (slip plane), the plane normal to the growth direction of the crystal, and a plane parallel to the c axis (normal to slip plane). The molecular orientation of a Langmuir–Blodgett deposited calcium stearate monolayer and n-amyl alcohol at submonolayer coverages on the $(41\bar{5}0)$ crystal has been investigated both before and after chemical etching of the surface. The deposited stearate monolayer is used as a model system for the orientation work. The orientation of deposited monolayers has been measured by other techniques[6] and these constitute an in-

* To whom correspondence should be addressed.

(1) (a) M. L. Hair, "Infrared Spectroscopy in Surface Chemistry," Marcel Dekker, New York, N. Y., 1967; (b) L. H. Little, "Infrared Spectra of Adsorbed Species," Academic Press, New York, N. Y., 1966; (c) R. P. Eischens and W. A. Pliskin, *Advan. Catal.*, 10, 1 (1958).

(2) N. J. Harrick, "Internal Reflection Spectroscopy," Interscience, New York, N. Y., 1967.

(3) Reference 2, p 51.

(4) (a) J. M. Charig, *Appl. Phys. Lett.*, 10, 139 (1967); (b) C. C. Chang, *J. Appl. Phys.*, 39, 5570 (1968); (c) J. M. Charig and D. K. Skinner, "Proceedings of the Conference on the Structure and Chemistry of Solid Surfaces," G. A. Somorjai, Ed., Wiley, New York, N. Y., 1969, p 34; (d) C. C. Chang, "Proceedings of the Conference on the Structure and Chemistry of Solid Surfaces," G. A. Somorjai, Ed., Wiley, New York, N. Y., 1969, p 77; (e) T. M. French and G. A. Somorjai, *J. Phys. Chem.*, 74, 2489 (1970).

(5) The (hkil) indexes refer to the hexagonal unit cell and describe the structure of the reflecting surface within $\pm^1/_2°$. No deterioration in surface polish was observed during the course of experiments except as noted below.

dependent check on the theoretical electric field amplitude equations used in the irs work. Moreover, the observed alcohol absorbances can be converted to absolute surface coverages with a minimum number of assumptions by utilizing the measured absorbance of the deposited monolayer.

Experimental Section

Apparatus. All spectra were recorded on a Beckman IR 12 at a resolution of 5 cm^{-1} or better. Polarization of the beam was accomplished using a Perkin-Elmer wire grid polarizer. The irs cell,[7] manufactured by Wilks Scientific Corp., can be heated in excess of 600° and evacuated to below 10^{-7} Torr with the vacuum system used in this work. The cell consists of a stainless steel circular chamber with vacuum, gas inlet, and two window ports on the side. The crystal is clamped into a stainless steel block suspended from the lid which is sealed to the main body of the chamber with a gold "O" ring. Two heater wells with a thermocouple well between them are bored through the lid into the block from outside the chamber. When a crystal is clamped into position, it is in good thermal contact along its edges and enclosed except for the ends. This design reduced the temperature gradient along the crystal and between the crystal and thermocouple to less than 5° even at temperatures above 400°. The windows are in the form of flanged plugs machined out of KBr. When they are in position, they protrude into the chamber and nearly contact the crystal so that the contribution from gas-phase absorbance is negligible. The vacuum seal between the windows and chamber is made with a viton "O" ring.

Reagents. Aluminum oxide single crystals were flame fusion grown from 99.98% Al$_2$O$_3$ powder and were supplied, cut, and polished by the Adolf Meller Co. Unless stated to the contrary, the crystals used are 52 $\times$ 20 $\times$ 0.5-mm prisms with the ends beveled to 45° to form entrance and exit apertures; they provide about one hundred 45° internal reflections. The major faces[5] were polished with diamond dust to an average roughness of 100 Å (measured by Meller). Fisher certified reagent alcohol was dried over Davison 4A molecular sieves and used without further purification. Stearic acid labeled 99% pure was used as received from Nutritional Biochemicals Corp. Distilled water used in monolayer preparation was double ion-exchanged, passed through an organic removal filter, and then distilled. All other chemicals used were of laboratory reagent grade.

Procedure. An outgassing at 500° under vacuum below 1 $\times$ 10^{-6} Torr for 8 hr was adopted as the standard pretreatment. Alcohol vapor was admitted and/or exhausted in increments and allowed to equilibrate for 15 min before the spectrum was recorded at $\times$10 ordinate scale expansion.
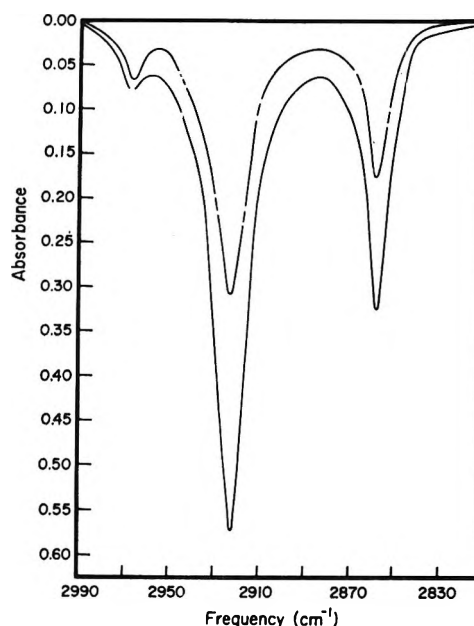
In experiments requiring a deposited monolayer, the

Figure 1. Absorbance spectra for a calcium stearate monolayer on (41$\bar{5}$0) α-Al$_2$O$_3$: - - -, parallel polarized beam; ———, perpendicularly polarized beam.

Blodgett method[8] was used. The prisms were outgassed under the conditions given above, removed from the vacuum chamber, and immediately submerged in a prepared calcium carbonate buffer, pH 9. Stearic acid was spread above the crystal from a hexane solution, compressed with an oleic acid piston, and allowed to equilibrate about 10 min. The crystal was then drawn through the compressed calcium stearate monolayer mechanically at a rate of 1 cm/min and immediately returned to the vacuum chamber.

Results and Discussion

Deposited Monolayers. A monolayer was considered useful when the water-supported monolayer change in area during deposition was within 10% of the geometric area of the crystal. The spectrum of a typical calcium stearate monolayer deposited on the (41$\bar{5}$0) crystal is given in Figure 1. The perpendicular to parallel absorbance ratio, $A_\perp/A_{||}$, for the asymmetric methylene stretch (2918 cm^{-1}) is 1.90 and, as discussed below, indicates that the stearate molecules are oriented nearly normal to the surface of the crystal. This is the expected orientation for deposited monolayers.[6] An upper limit for the absorbance ratio can be estimated from the calculated electric field amplitudes at the interface but in the rarer medium assuming unit elec-

(6) (a) G. L. Gaines, Jr., "Insoluble Monolayers at Liquid-Gas Interfaces," Interscience, New York, N. Y., 1966; (b) J. W. Menter and D. Tabor, *Proc. Roy Soc. Ser. A*, **204**, 514 (1950); (c) L. H. Germer and K. H. Storks, *J. Chem. Phys.*, **6**, 280 (1938).

(7) A. Yelon and G. L. Haller, "Growth, Structure, and Properties of Surface Oxides," Final Report on Grant RSA-69-8, Connecticut Research Commission.

(8) K. B. Blodgett, *J. Amer. Chem. Soc.*, **57**, 1007 (1935).

tric field for the radiation propagating within the crystal.[3,9,10] Perpendicular polarization will set up an electric field with an amplitude

$$E_y = \frac{2 \cos \theta}{[1 - n_{31}{}^2]^{1/2}} = 1.75$$

across the 20-mm width of the crystal. Parallel polarization will give rise to elliptical polarization with amplitude components

$$E_x = \frac{2(\cos \theta)[\sin^2 \theta - n_{31}{}^2]^{1/2}}{(1 - n_{31}{}^2)^{1/2}[(1 + n_{31}{}^2) \sin^2 \theta - n_{31}{}^2]^{1/2}} = 1.20$$

along the 52-mm length and

$$E_z = \frac{2(\cos \theta \sin \theta)n_{32}{}^2}{(1 - n_{31}{}^2)^{1/2}[(1 + n_{31}{}^2) \sin^2 \theta - n_{31}{}^2]^{1/2}} = 0.96$$

normal to the crystal face. If the stearate molecule is normal to the surface, the C–H bonds of the methylene groups will be in a plane parallel to the crystal surface. The fact that the adsorbance ratio for the asymmetric stretch (2918 cm^{-1}) and the symmetric stretch (2856 cm^{-1}) are the same implies that the methylene groups are randomly oriented in this plane as has been found for built-up multilayers by electron diffraction.[6b,o] The absorbance is proportional to the square of the electric field amplitude so the predicted absorbance ratio for perfect orientation is $A_\perp/A_{||} = E_y{}^2/E_z{}^2 = 2.13$. The ratio of 1.90 is in good agreement with this prediction considering surface roughness on the molecular scale. The fact that the ratio is as high as is found is probably accounted for by the ability of compressed films to bridge over surface roughness of the crystals.[11] Another limiting case is that obtained for completely random orientation.

$$\frac{A_\perp}{A_{||}} = \frac{E_y{}^2}{E_x{}^2 + E_z{}^2} = 1.28$$

This is in very good agreement for the absorbance ratio of 1.23 obtained for a thin film of stearic acid formed when the crystal is immersed in a dilute hexane solution and dried. Implicit in the above calculations is the assumption that the energy loss per reflection is small; i.e., the electric fields are not much perturbed by absorption at the interface. This assumption is justified and the reproducibility of our monolayers is demonstrated in Figure 2 by the good linear relationship between absorbance[12] and number of reflections.

OH Absorbances. The background spectrum of the (4150) crystal is shown in Figure 3 and is typical of the single crystal aluminum oxide used in this study. All three crystals are opaque in the infrared below 2100 cm^{-1}, are free of surface O–H and C–H absorbances after outgassing at 500°, and exhibit sharp bands due to O–H in the bulk of the crystal. The numbers and intensity of these internal bands are properties of the individual crystals. The observed frequencies and
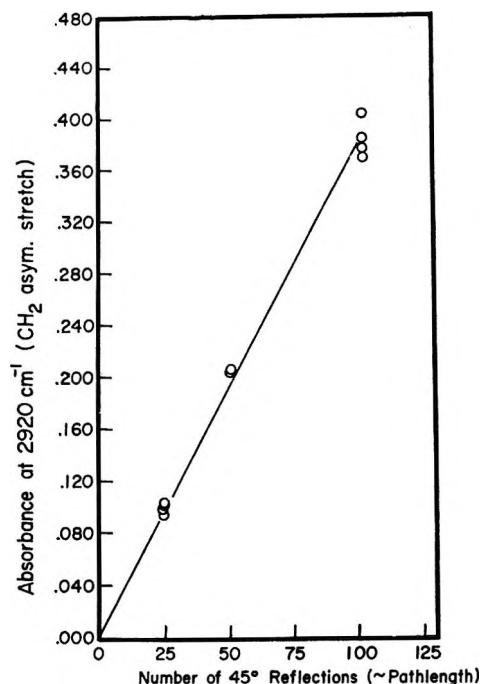
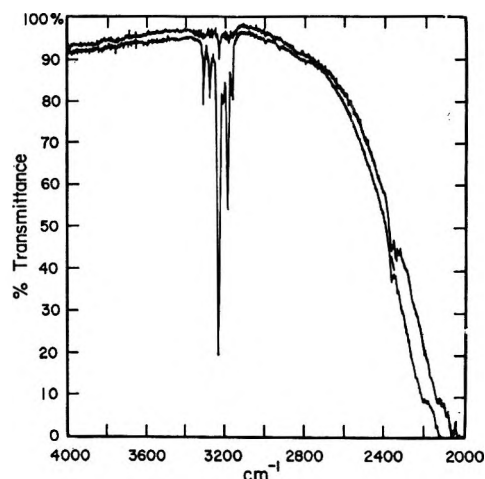Figure 2. Absorbance for calcium stearate monolayer as a function of number of reflections through the monolayer.

Figure 3. Transmittance spectra for clean (41̄50) α-Al$_2$O$_3$: upper curve, perpendicular polarization; lower curve, parallel polarization.

relative intensities for respective crystals are 3166, 3187, 3218, 3233, and 3280 cm^{-1} (weak) for (0001),

(9) Perpendicular and parallel polarization refer to the orientation of the electric field vector of the radiation propagating in the crystal relative to the plane defined by the incident and internally reflected beam.

(10) θ is the angle of incidence and is equal to 45°. $n_{31} = n_3/n_1$ and $n_{32} = n_3/n_2$. The indices of refraction for aluminum oxide, n_1, and gas phase, n_3, are 1.70 and 1.00, respectively. The value of n_2 used was 1.5 for both monolayer [A. C. Hall, *J. Phys. Chem.*, **74**, 2742 (1970)] and alcohol. For calculations concerning water or surface OH, $n_2 = 1.3$ (bulk water) was assumed.

(11) J. J. Bikerman, *Proc. Roy. Soc. Ser. A*, **170**, 130 (1939).

(12) Except for spectra given in Figures 1, 3, 5, and 11, absorbances are those obtained with the partially polarized beam of the spectrometer measured at the band maximum.
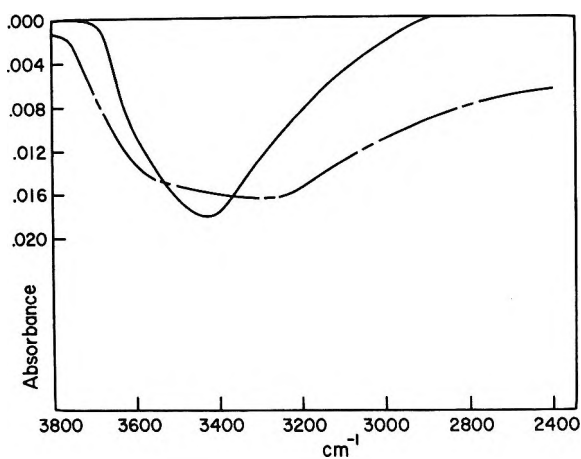
Figure 4. Absorbance spectra for water on (0001) α-Al$_2$O$_3$ at 30°: (a) ——, weakly adsorbed; (b) - - -, more strongly adsorbed.

3166, and 3280 cm^{-1} (medium) for (11$\bar{2}$3), and 3166, 3187, 3218, 3233, and 3313 cm^{-1} (strong) for (41$\bar{5}$0). This internal O–H impurity is probably associated with metal impurities and/or aluminum ion vacancies.[13] None of the internal O–H bands are affected by adsorption on the surface or the outgassing procedure, but presumably are deuterium exchangeable above 1000°.[14]

Figure 4 depicts the absorbance measured for surface OH. When the crystals are evacuated for a few minutes at room temperature, a considerable amount of physically adsorbed water is removed, Figure 4a. When the crystal is subsequently heated to 500° under a vacuum, a further decrease in absorbance below 3600 cm^{-1} results, Figure 4b. Most of the desorption of this strongly bound OH occurs below 370°. The physically adsorbed water is rapidly reversible but OH removed at high temperatures requires several hours at ambient water vapor pressure to return to its former state. Accordingly, the physically adsorbed water readily exchanges with D$_2$O at room temperature while other adsorbed water (probably held as surface hydroxyls) exchanges only very slowly.

The very large polarization effect indicated in Figure 3 is characteristic of all such absorptions in the three crystals and indicates that the O–H dipole is in the close-packed oxygen plane (perpendicular to the c axis). This is particularly easy to see in the case of the (41$\bar{5}$0) crystal. The geometry used will place the c axis normal to the plane of incidence of the reflected beam. Thus, parallel polarization (electric field normal to the c-axis) results in a very large absorbance while the absorbance for perpendicular polarization (electric field parallel to c axis) is near zero.

If the structure of the surface is represented by the structure of bulk below it (evidence that suggests that this is essentially the case is given below), the surface OH would be expected to be oriented parallel to the surface on the (0001) crystal, nearly parallel on the (11$\bar{2}$3) crystal, and about the normal to the surface on the (41$\bar{5}$0)

crystal. Experimentally, all absorbance due to strongly bound surface OH is found to be consistent with a randomly oriented dipole. An explanation for this and the very broad bands observed (compare Figure 4 to Figure 3) can be given in terms of the mobility of the protons on the surface of the crystals. (Hydrogen bonding also causes band broadening, but it is difficult to imagine the surface OH more extensively hydrogen-bonded than the internal OH). The large band widths that result when boehmite (monohydrate of aluminum oxide) is heated have been attributed to proton delocalization.[15] At elevated temperatures discrete vibrational energy levels above a specified level disappear and the probability of proton tunneling through the potential energy barrier approaches the absorption frequency. We observe a very similar behavior for internal OH in α-aluminum oxide. At temperatures around 400° these absorptions are very broad and slightly shifted to higher frequency (due to the thermal expansion of the crystal unit cell). If a proton is mobile at 400° within the crystal lattice, it is reasonable to expect surface proton mobility at room temperature and, therefore, broad peaks which appear to be the absorbances of randomly oriented dipoles.

In contrast to the strongly bound surface OH, the physically adsorbed water does appear oriented. This does not imply an absence of mobility in this layer, but suggests molecular movement with a preferred orientation relative to the surface. If we assume that the molecular water moves randomly across the surface but hydrogen bonding always directs the hydrogens (or the oxygen) toward the surface, we can estimate the angle between the plane defined by the water molecule and the plane of the surface. For the (0001) crystal, this angle is about 11°. Another indication that this physically adsorbed water is in close association with the alumina surface is the position of the absorbance maximum. The absorbance maximum of the physically adsorbed water is shifted 30–50 cm^{-1} to higher frequency relative to bulk water at the same temperature. This result may be interpreted as a consequence of diminished intermolecular hydrogen bonding due to the unfavorable geometry imposed by interaction with the surface.

One other kind of hydroxyl absorption, the isolated OH absorbing in the 3700-cm^{-1} region observed on high-area γ-alumina,[1,16] should be mentioned. These were not seen on the single crystals except in two instances. An absorption at 3750 cm^{-1} was recorded on the (41$\bar{5}$0)

(13) (a) F. K. Volynets, V. G. Vorobev, and E. A. Sidorova, Zh. Prikl. Spektrosk., 10, 981 (1969); (b) R. F. Belt, J. Appl. Phys., 38, 2688 (1967).

(14) R. Müller and Hs. H. Günthard, J. Chem. Phys., 44, 365 (1966).

(15) J. J. Fripiat, H. Bosmans, and P. G. Rouxhet, J. Phys. Chem., 71, 1097 (1967).

(16) J. B. Peri and R. B. Hannan, ibid., 64, 1526 (1960).

crystal after repolishing and on the (11$\bar{2}$3) crystal after heating it above 1000° in hydrogen. This peak was broad on the (41$\bar{5}$0) crystal on which physically adsorbed water remained and was sharp (comparable to the internal OH) on the (11$\bar{2}$3) crystal which did not exhibit any other surface OH absorbance. The 3750-cm^{-1} band was removed from both crystals on heating to 500° under vacuum and did not reappear when the crystals were exposed to water vapor.

Alcohol Adsorption. The spectrum in the CH stretching region of *n*-amyl alcohol adsorbed on the (41$\bar{5}$0) crystal at 1.12 Torr pressure, Figure 5, suggests an ordering in the adsorbed layer. The absorbance ratio for asymmetric stretch of the CH$_2$ group (2935 cm^{-1}) is about 1.6, *i.e.*, the average amyl alcohol molecule is probably more or less erect but not as near the normal to the surface as is calcium stearate. The absorbance ratio for adsorbed amyl alcohol was somewhat lower on the (0001) and (11$\bar{2}$3) crystals and the interpretation is complicated by depolarization within these crystals,[17] but the absorbed alcohols are clearly ordered here too. More quantitative calculations concerning the average dipole orientation can be made if the absorbance ratio is measured at more than one angle of reflection (the optical system used in this work restricted measurements to 45°).

Experimentally, it was noted that absorbance ratios for the asymmetric stretch of the terminal CH$_3$ group of straight-chain hydrocarbons are rather less sensitive than those for the CH$_2$ group to the orientation of the molecule. Therefore, the ratio of the absorbance of the asymmetric CH$_3$ stretch for *n*-amyl alcohol (2965 cm^{-1}) absorbed from the gas phase to that observed for the deposited stearate monolayer is taken as a measure of the fractional surface coverage θ. It should be pointed out that θ defined in this manner is a fraction of the total surface covered and not the fractional coverage of surface sites capable of chemisorbing alcohol. $\theta = 1$ is equivalent to one molecule/20 Å^2 [18] or 5 × 10^{14} molecules/cm^2. Isotherms obtained on all three crystals at 30 and 120° are shown in Figures 6 and 7, respectively. Below $\theta = 0.1$ there always remains some alcohol irreversibly adsorbed which is removed by heating to higher temperatures. The calculated isosteric heats of adsorption at $\theta = 0.4$ are given in Table I. Isosteres at various coverages on the (0001) crystal are shown in Figure 8 and are representative of those obtained on the other crystals. *n*-Amyl al-
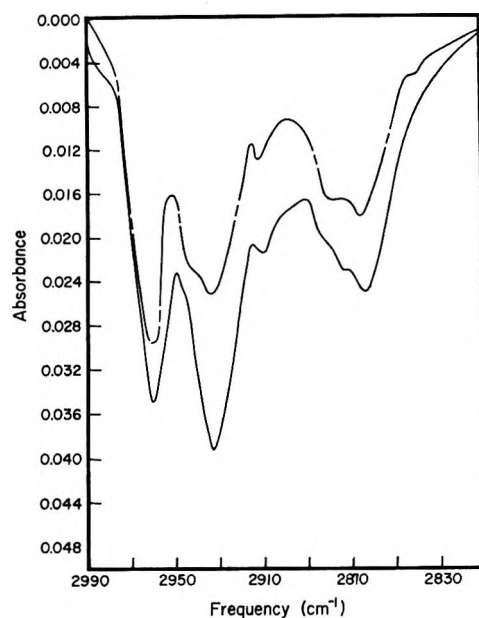

Figure 5. Absorbance spectra for 1.12 Torr of *n*-amyl alcohol on (41$\bar{5}$0) α-Al$_2$O$_3$ at 30°: – – –, parallel polarization; ——, perpendicular polarization.
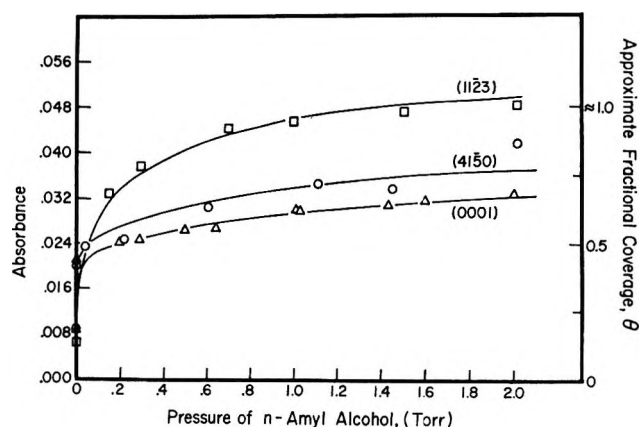

Figure 6. Adsorption isotherms of *n*-amyl alcohol on three crystal faces of α-Al$_2$O$_3$ at 30°.

cohol has been chosen for discussion because it gives reasonably intense CH$_2$ stretch absorbance (indicating orientation) and the CH$_3$ group is sufficiently removed from the terminal oxygen so that perturbation corrections on the calculated coverages are unnecessary.[19]

Table I

Crystal orientation	Isosteric heat of adsorption, $\theta = 0.4$, kcal/mol
(0001)	13
(11$\bar{2}$3)	19
(41$\bar{5}$0)	26

(17) It is not possible to find an orientation of a birefringent crystal such as aluminum oxide which will provide a unique index of refraction for the geometry used in this work. In principle, the beam is double refracted and split into an ordinary and extraordinary ray. The refractive indices for the ordinary and extraordinary rays are not too different for aluminum oxide, being 1.7023 and 1.6943, respectively, at 24° and 3.303 μ. Thus, beam divergence is much less a problem than is strain introduced in the polishing operation. Each crystal was checked for beam depolarization by placing a beam polarizer before the crystal entrance and a second polarizer rotated 90° after the crystal exit. Both the (0001) and (11$\bar{2}$3) crystal depolarized about 30% of the beam but the (41$\bar{5}$0) crystal was free of depolarization effects.

(18) Reference 8a, p 162.

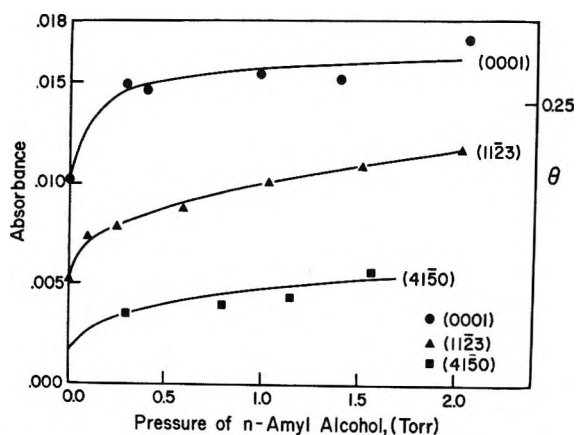(19) H. V. Drushel, W. L. Senn, Jr., and J. S. Ellerbe, *Spectrochim. Acta,* 19, 1815 (1963).

Figure 7. Adsorption isotherms of n-amyl alcohol on three crystal faces of α-Al_2O_3 at 120°.

Figure 8. Isosteres for (0001) α-Al_2O_3.

Figure 9. Adsorption isotherms for (11$\bar{2}$3) α-Al_2O_3 at 30° after various treatments.

If one corrects for perturbation of the CH_3 group and plots θ as a function of reduced pressure, all of the straight-chain C_1 through C_5 alcohols result in a common isotherm within experimental error. In addition, the isosteric heat of adsorption of n-butyl alcohol is the same as n-amyl alcohol on the (0001) crystal.

Before attempting to discuss the adsorptive capacity and heats of adsorption on the three crystals in terms of their surface structure, we must consider the question of surface disorder. LEED studies of mechanically polished (0001) surfaces have been reported by several authors[4] and Chang[4d] has also investigated the (11$\bar{2}$3) surface. The polished surfaces always give weak and diffuse diffraction before heating under vacuum. After heating to between 600 and 800° LEED patterns which have the symmetry of the parent planes are obtained; above 800° the (0001) surface rearranges. To assess the reproducibility of the polishing operation, we determined the n-amyl alcohol adsorption isotherm
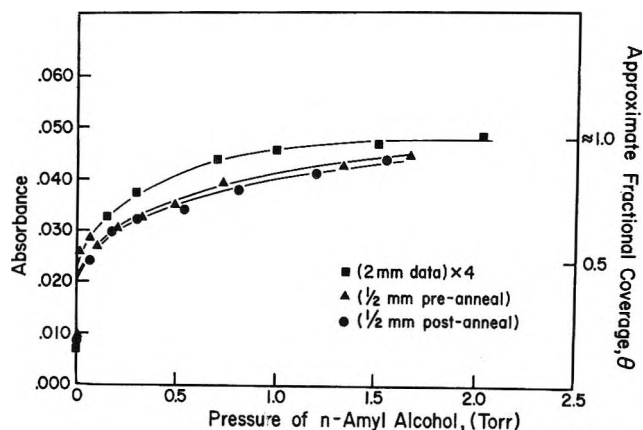
on a 2-mm (11$\bar{2}$3) crystal, repolished the crystal to 0.5 mm, and again measured the isotherm. The amount of alcohol adsorbed at low coverages was not much changed, but the coverage was about 10% lower on the 0.5-mm crystal at pressures above 0.1 Torr as is shown in Figure 9. Subsequently the 0.5-mm (11$\bar{2}$3) crystal was annealed above 1000° in flowing hydrogen, exposed to air at room temperature, and outgassed under vacuum in the usual way. The isotherm of n-amyl alcohol before and after this treatment was the same within experimental error. Of course, this could imply that we have reproducibly contaminated surfaces since our vacuum never exceeds 1×10^{-8} Torr, although the LEED work on the (0001) surface indicates a bulk structure at the surface even at much higher pressures.[4c] We hope to check this in the near future by converting to an ultrahigh-vacuum system. It should also be pointed out that, with hindsight, one would choose the heat of adsorption instead of an individual isotherm to probe changes in the surface.

Another method of eliminating surface disorder on mechanically polished crystals is chemical etching. When the (0001) surface was etched with phosphoric acid at 400°, a good LEED pattern was obtained.[4b] The same treatment applied to our (41$\bar{5}$0) crystal resulted in microscopic etch lines. The highly faceted surface exposes surface of unknown orientation and results in considerable energy loss at higher frequencies due to surface scattering. We report it because it results in an interesting change in orientation of adsorbed alcohol. Figure 10 shows the isotherms before and after etching the (41$\bar{5}$0) surface. Figure 11 is the spectrum in the CH stretching region of n-amyl alcohol adsorbed on the etched (41$\bar{5}$0) surface at 1.12 Torr and is to be compared with Figure 5. The absorbance ratio, $A_\perp/A_\parallel$ for the CH_2 asymmetric stretch is now 1.1 compared to 1.6 before etching. The low ratio and the significant difference between the ratios for the asymmetric and symmetric CH_2 stretch[20] are
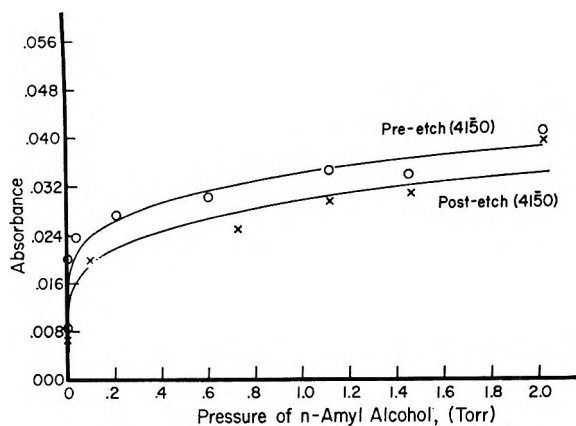
Figure 10. Adsorption isotherms at 30° for (41$\bar{5}$0) α-Al$_2$O$_3$ before and after etching in phosphoric acid at 400°.

both consistent with ordered molecules more or less lying down on the surface.

The simplest correlation involving surface structure might be one between number of sites on a given surface and molecules adsorbed by that surface. We will assume that the adsorption site requires one or more surface aluminum ions which are coordinatively unsaturated (coordination number less that 6, the bulk coordination number) and use structural arguments similar to those proposed for α-chromium oxide.[21] The α-oxides of both aluminum and chromium have trigonal structures that can be represented as a hexagonal close-packed oxide ion lattice with two-thirds of the octahedral holes filled by metal ions. If we form the (0001) surface by cleaving the crystal through a plane of close-packed oxide ions, half of the oxide ions of this plane must be moved to each surface formed in order to maintain electrical neutrality. Each Al^{3+} in this surface would be five-coordinate but could return to full coordination by adsorption of a water molecule. Movement of a proton from the adsorbed water molecule to an adjacent oxide ion results in a surface of close-packed hydroxide ions. If we reverse this step and desorb a water molecule by condensing any hydroxide and adjacent proton, we generate two five-coordinate surface Al^{3+} ions and one two-coordinate O^{2-} ion[22] (O^{2-} is four-coordinate in the bulk). We take these coordinative unsaturated Al^{3+} ions and the accompanying O^{2-} ion as our site for dissociative adsorption of alcohol. The number of such potential sites is just the number of pairs of Al^{3+} under the close-packed hydroxide surface [i.e., the number of Al^{3+} pairs in any (0001) plane of the bulk]. We can imagine a similar arrangement on the (11$\bar{2}$3) and (41$\bar{5}$0) surfaces and again calculate the number of potential sites as the number of Al^{3+} pairs in the respective planes of the bulk. These calculated densities of potential sites[23] are tabulated along with the measured saturation coverages at 120° (extrapolation of the linear portion of the isotherms in Figure 7 to zero pressure) in Table II.

Table II

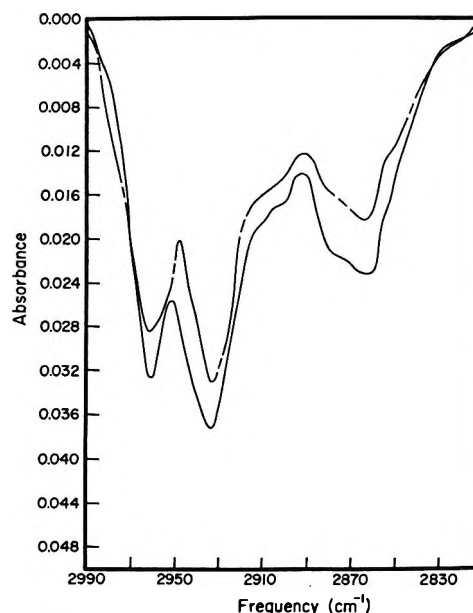| Crystal orientation	Al^{3+} pair sites, $\times 10^{14}$ cm^{-2}	Saturation coverage, 120°, $\times 10^{14}$ cm^{-2}	Saturation coverage/ Al^{3+} pair sites
(0001)	5.09	1.5	0.29
(11$\bar{2}$3)	2.45	0.83	0.34
(41$\bar{5}$0)	1.22	0.31	0.25

Figure 11. Absorbance spectra for 1.12 Torr of n-amyl alcohol on (41$\bar{5}$0) α-Al$_2$O$_3$ at 30° after etching in phosphoric acid at 400°.

We chose saturation coverages to minimize the effect of the varying heats of adsorption and the isotherms at the highest temperature measured to avoid contribution from physical adsorption (hydrogen bonding to hydroxide or oxide not directly involving Al^{3+} ions).[24]

The ratio of adsorbed alcohol molecules to calculated number of sites is suprisingly constant from surface to surface, being about 0.3 at 120°. This constancy may be, in part, fortuitous in light of the differences in the Al^{3+} pair sites on the three surfaces. The Al^{3+}–Al^{3+}

(20) The dipole changes for the symmetric and asymmetric stretch of CH$_2$ lie in the H-C-H plane and are normal to each other. Therefore, if the CH$_2$ group can rotate freely about the axis of the carbon backbone of the molecule or if the molecules are randomly oriented, the ratios $A_\perp/A_\parallel$ (symmetric stretch) and $A_\perp/A_\parallel$ (asymmetric stretch) will be equal.

(21) R. L. Burwell, Jr., G. L. Haller, K. C. Taylor, and J. F. Read, Advan. Catal., **20**, 1 (1969).

(22) Reference 21, p 9.

(23) (a) A hexagonal unit cell with a = 4.7589 Å and c = 12.991 Å was used to calculate site densities. Perfect close-packing of O^{2-} with an average O^{2-} diameter of $a/\sqrt{3}$ and a spacing between close-packed planes of $c/6$ was assumed; (b) R. E. Newham and Y. M. DeHaan, Z. Kristallogr., **117**, 235 (1962).

(24) R. O. Kagel, J. Phys. Chem., **71**, 844 (1967).

distance is smaller on the (41$\bar{5}$0) surface than on the other two surfaces (2.65 Å compared to 2.79 Å).[23b] The average coordination number for the pair of Al^{3+} ions in the site is approximately 9, 7, 5,[25] and the average area per site is 20, 40, and 80 Å^2 on the (0001), (11$\bar{2}$3), and (41$\bar{5}$0), respectively. Presumably these differences will be reflected in the strength of bonding to a much greater degree than they are in the saturation coverages. In fact, the heats of adsorption increase as coordination of the pair site and intermolecular repulsion decrease (area per site increases) as would be expected, and, as previously emphasized,[26] there will be a contribution from bonding of the proton that will be a function of the unsaturation of the oxide ion to which it bonds, but it is not possible to define the stereochemistry precisely.

The assumed dissociative adsorption has been previously proposed for alcohol adsorption of γ-aluminum oxide[24] and appears justified on α-aluminum oxide by the high heats of adsorption. The formation of a weak band like that recorded for the strongly bound OH, Figure 4b, accompanies alcohol adsorption and is additional evidence for dissociation. Since this band is not affected by the manner or degree to which the alcohol is dried and does not appear when ether is adsorbed, it is not likely due to water impurity in the alcohol.[27,28]

(25) J. K. MacKenzie and J. F. Nicholas, *J. Phys. Chem. Solids,* **23,** 197 (1962).

(26) R. L. Burwell, Jr., J. F. Read, K. C. Taylor, and G. L. Haller, *Z. Phys. Chem.,* **64,** 18 (1969).

(27) NOTE ADDED IN PROOF. Dr. J. T. Kummer has kindly brought to the authors' attention the work of Dr. Y.-F. Y. Yao.[28] The heat of adsorption of CH_3OH on micro single crystals of α-Al_2O_3 was measured calorimetrically. The heat of adsorption of methanol falls from an initial value of 31 to 10 kcal/mol at BET monolayer coverage. A qualitative comparison between the two sets of results is made difficult by the differing outgassing temperatures (Yao outgassed at 900°) and the fact that only 80% of the exposed surface of the micro crystals was of the (0001) orientation. However, if we attempt to normalize surface coverages by comparing coverage beyond the point where alcohol can be desorbed at room temperature the agreement is not unreasonable.

(28) Y.-F. Y. Yao, *J. Phys. Chem.,* **69,** 3930 (1965).

The Formulation of Transition State Theory for a Reaction Proceeding

by Simultaneous Mechanisms with a Common Transition State.

I. Simple Direct Formulation

by Margaret Robson Wright and P. G. Wright*

Department of Chemistry, The University, Dundee, Scotland   (*Received January 14, 1970*)

If alternative paths of reaction involve a common transition state, each contribution to the rate is given by a transition state expression incorporating an additional factor. In this respect, a "nonequilibrium" transition state theory is required. For both thermal and nonthermal conditions, this factor can be equated to the fractional contribution to the rate in conditions in which there is equilibrium between the alternative sets of reactants. The bearing of this formulation on the reaction between hydrogen and iodine is considered. However, for this particular reaction it seems likely that the two conceivable mechanisms would involve different transition states.

1. Introduction

Some cases have recently been discussed[1-4] in which, for reasons associated with the symmetry of the activated complex, the correct application of transition state theory is not quite straightforward. Another situation involving special features would arise if there were a reaction capable of proceeding by parallel mechanisms having a common transition state. This question has been considered,[4-6] in particular, in connection with the reaction[7] between hydrogen and iodine.

Consider, for definiteness, a reaction in which L_2 and M_2 give 2LM at an overall rate which might include contributions from both of two distinct mechanisms

$$L_2 + M_2 \xrightarrow{k_{mol}} 2LM \qquad (1)$$

and

$$L_2 + 2M \xrightarrow{k_{at}} 2LM \qquad (2)$$

The overall rate would be

$$k_{mol}[L_2][M_2] + k_{at}[L_2][M]^2$$

For a *thermal* reaction, with

$$[M]^2/[M_2]$$

equal to the equilibrium constant K for the dissociation of molecular to atomic M, the overall rate would take the form

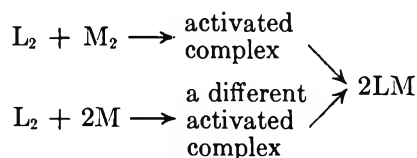$$k_{th}[L_2][M_2]$$

with

$$k_{th} = k_{mol} + k_{at}K$$

In other circumstances (such as a photochemical reaction), the more general expression for the overall rate is required.

$$k_{mol}[L_2][M_2] + k_{at}[L_2][M]^2$$

In a discussion of the experimental results[7] for the reaction between hydrogen and iodine, Noyes[5,6] has considered two conceivable cases for such a system. (i) The activated complex formed in reaction 1 (molecular mechanism) might be the same as that formed in reaction 2 (atomic mechanism)

$$
\begin{array}{c}
L_2 + M_2 \\
\searrow \\
\text{activated} \longrightarrow 2LM \\
\text{complex} \\
\nearrow \\
L_2 + 2M
\end{array}
$$
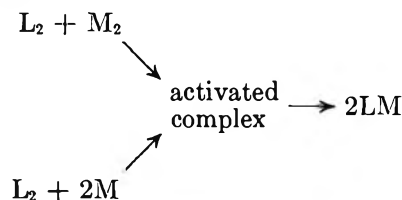
(ii) Reaction 1 might proceed only *via* an activated complex different from that in reaction 2

$$
\begin{array}{l}
L_2 + M_2 \longrightarrow \text{activated complex} \searrow \\
\qquad\qquad\qquad\qquad\qquad\qquad 2LM \\
L_2 + 2M \longrightarrow \text{a different activated complex} \nearrow
\end{array}
$$

The discussion which follows relates to the *first* of these alternatives, a situation which could be represented very roughly by a potential energy contour diagram with two reactant valleys leading to a common col (Figure 1).

* To whom correspondence should be addressed.

(1) E. W. Schlag, *J. Chem. Phys.*, **38**, 2480 (1963).

(2) E. W. Schlag and G. L. Haller, *ibid.*, **42**, 584 (1965).

(3) D. M. Bishop and K. J. Laidler, *ibid.*, **42**, 1688 (1965).

(4) J. N. Murrell and K. J. Laidler, *Trans. Faraday Soc.*, **64**, 371 (1968).

(5) R. M. Noyes, *J. Chem. Phys.*, **47**, 3097 (1967).

(6) R. M. Noyes, *ibid.*, **48**, 323 (1968).

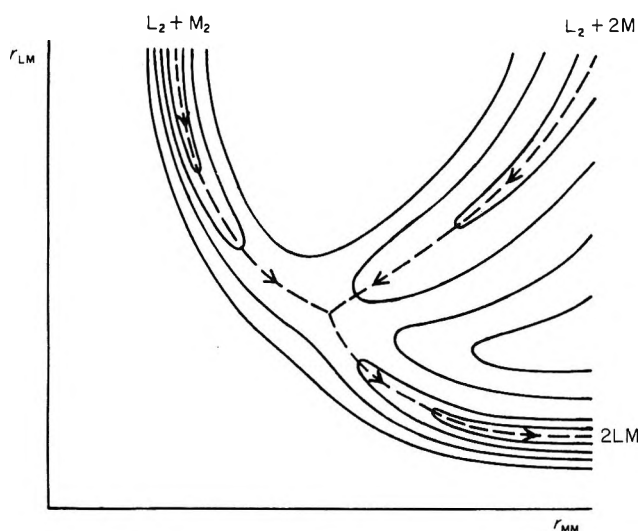(7) J. H. Sullivan, *ibid.*, **46**, 73 (1967).

Figure 1. Schematic potential energy contour diagram for reaction by simultaneous molecular and atomic mechanisms proceeding *via* a common transition state: abscissa, r_{MM}; ordinate, r_{LM}.

Noyes[6] has considered *inter alia* whether it might not be that for such a situation an approach based on transition state theory is invalid in principle. It will be argued here that it is by no means inappropriate to describe such a reaction in terms of transition state theory, and explicit attention will be given to what is the correct formulation.

There seems to be no dispute as to the propriety of applying transition state theory in case ii, in which the activated complexes for the two mechanisms are different.

2. A Spurious Formulation

In the first of his two papers, Noyes[5] drew attention to an argument to the effect that if molecular and atomic mechanisms proceed *via* a common transition state, then (i) the rate constant k_{mol} for the reaction occurring *via* the molecular mechanism 1 is always given by

$$\frac{kT}{h} \exp[-(G_{X\ddagger} - G_A{}^{\ominus})/RT] \qquad \text{(Noyes'[5] eq 4)}$$

where A represents the reactants $L_2 + M_2$ in reaction 1, and X represents the activated complex; (ii) the rate constant k_{at} for the reaction occurring *via* the atomic mechanism 2 is always given by

$$\frac{kT}{h} \exp[-(G_{X\ddagger} - G_B{}^{\ominus})/RT] \qquad \text{(Noyes'[5] eq 5)}$$

where B represents the reactants $L_2 + 2M$ in reaction 2; (iii) the rate constant k_{th} for the overall thermal reaction is always given by

$$\frac{kT}{h} \exp[-(G_{X\ddagger} - G_A{}^{\ominus})/RT]$$

(iv) since in the thermal reaction there is equilibrium with respect to the dissociation $M_2 \rightleftharpoons 2M$ (equilibrium constant K), it then follows that

$$k_{th} = k_{mol} = k_{at}K$$

These expressions 4 and 5 cited by Noyes are, however, not generally exact. The former gives k_{mol} only if the atomic mechanism makes no contribution to the overall thermal rate. Similarly, the latter gives k_{at} only if the molecular mechanism makes no contribution to the overall thermal rate. They do not apply if there are contributions from two distinct mechanisms (molecular and atomic) with a common transition state.

The spurious relations cited seem to arise from a view that if transition state theory is to be applied to a mechanism

$$L_2 + M_2$$
$$\searrow$$
$$\text{activated} \longrightarrow 2LM$$
$$\nearrow \text{complex X}$$
$$L_2 + 2M$$
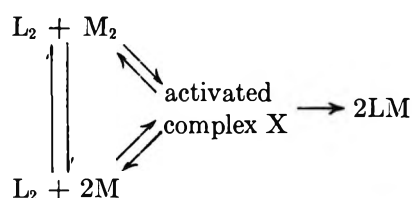
then it is necessary that (i) whenever a reaction proceeding even in part by way of $L_2 + M_2 \rightarrow \ldots$ is considered, whether for thermal or for nonthermal conditions, the quotient of concentrations

$$[X]/[L_2][M_2]$$

must be equated to its equilibrium value, the equilibrium constant for the process $L_2 + M_2 \rightleftharpoons X$, and simultaneously that (ii) whenever a reaction proceeding even in part by way of $L_2 + 2M \rightarrow \ldots$ is considered, the quotient of concentrations

$$[X]/[L_2][M]^2$$

must similarly always be equated to *its* equilibrium value.

Save, however, for the thermal reaction (when X is virtually in equilibrium both with $L_2 + M_2$ *and* with $L_2 + 2M$), such is *not* the case. If (as in a photochemical reaction) there fails to be equilibrium in the reaction $M_2 \rightleftharpoons 2M$ ($[M]^2/[M_2] \neq K$), there is no more cogent reason for equating $[X]/[L_2][M]^2$ to $\{K$ for $L_2 + 2M \rightleftharpoons X\}$ than there is for equating $[X]/[L_2][M_2]$ to $\{K$ for $L_2 + M_2 \rightleftharpoons X\}$; and it is *not possible* for *both* equalities to hold.

For in *all* circumstances

$$\frac{[X]}{[L_2][M_2]} = \frac{[X]}{[L_2][M]^2} \cdot \frac{[M]^2}{[M_2]}$$

and in particular

$$\{K \text{ for } L_2 + M_2 \rightleftharpoons X\} =$$
$$\{K \text{ for } L_2 + 2M \rightleftharpoons X\} \cdot K$$

It then follows that if $[M]^2/[M_2] \neq K$, then, with one

of the other quotients equal to the corresponding K, the remaining one cannot be.

From the fact that in applications of transition state theory *to simple cases in which there is only one set of reactants from which the activated complex can be formed*

$$\frac{[\text{activated complex}]}{[\text{reactants}]} = \left(\frac{[\text{activated complex}]}{[\text{reactants}]}\right)_{eq}$$

it does *not* follow that such a relation must necessarily hold in the form of the theory appropriate to other cases. Rather, any such "equilibrium assumption" is to be replaced by (rate at which a given set of reactants, by passing through the critical configuration of the activated complex, is converted into a given set of products) = (rate at which this occurs in an equilibrium mixture in which each species of this particular set of reactants is present in a concentration equal to that in which it is present in the actual reacting mixture).

The present case, in fact, is one of the situations in which it becomes important that transition state equations can[8-10] be formulated without appeal to any "equilibrium assumption."

3. Simple Consistent Formulation for a Reaction Proceeding by Simultaneous Mechanisms with a Common Transition State

In a reaction proceeding by simultaneous mechanisms with a common transition state, let θ_{mol} denote the fraction of the total rate which *in the thermal reaction* is due to the molecular reaction 1 ($L_2 + M_2 \to ...$), and θ_{at} the fraction which *in the thermal reaction* is due to the atomic reaction 2 ($L_2 + 2M \to ...$).

$$\theta_{mol} + \theta_{at} = 1$$

The *overall* rate of reaction can *always* be formulated as $\nu[X]$ where ν is the overall frequency of breakdown of the activated complexes, irrespective of whether they were formed in reaction 1 or in reaction 2, to give products.

The molecular contribution to the overall thermal rate is therefore

$$\theta_{mol}\nu[X]_{thermal}$$

With the overall thermal rate $\nu[X]_{thermal}$ equal to

$$[L_2][M_2]\frac{kT}{h}\exp[-(G_{X\ddagger} - G_A{}^\ominus)/RT]$$

since the molecular contribution to it is $k_{mol}[L_2][M_2]$, it follows that

$$k_{mol} = \theta_{mol}\frac{kT}{h}\exp[-(G_{X\ddagger} - G_A{}^\ominus)/RT]$$

Similarly, by considering the atomic contribution

$$\theta_{at}\nu[X]_{thermal}$$

to the overall thermal rate, it is found that on the same basis

$$k_{at} = \theta_{at}\frac{kT}{h}\exp[-(G_{X\ddagger} - G_B{}^\ominus)/RT]$$

It is these equations, and not those that were cited by Noyes,[5] that furnish a consistent formulation in terms of transition state theory. Noyes'[5] expression 4 would hold if $\theta_{mol} = 1$, and expression 5 if $\theta_{at} = 1$, but neither is correct if θ_{mol} and θ_{at} both lie in the range $0 < \theta < 1$. In fact, the expressions omitting θ's follow direction from the "equilibrium assumption," which is here inappropriate.

The conditions of the thermal reaction have here been considered in order to obtain expressions for the two individual rate constants k_{mol} and k_{at}. Having been evaluated, these rate constants can now be employed to write down an expression for the rate in nonthermal conditions

$$[L_2][M_2]\theta_{mol}\frac{kT}{h}\exp[-(G_{X\ddagger} - G_A{}^\ominus)/RT] +$$

$$[L_2][M]^2\theta_{at}\frac{kT}{h}\exp[-(G_{X\ddagger} - G_B{}^\ominus)/RT]$$

For example, consider a photochemical reaction with M_2 dissociated to M to a greater extent than in a thermal system. Of the total rate, a fraction less than θ_{mol} would be due to reaction 1 ($L_2 + M_2 \to ...$), and a fraction *greater* than θ_{at} would be due to reaction 2 ($L_2 + 2M \to ...$).

The need for factors θ is implicit in some earlier discussions.[1-3]

4. Application to the Reaction between Hydrogen and Iodine

Sullivan[7] conducted experiments on the photochemical reaction between hydrogen and iodine at temperatures at which the thermal reaction would be negligible. He thereby determined k_{at} over a range of relatively low temperatures and found by extrapolation that the thermal rate at higher temperatures could be fully accounted for as due to the atomic reaction alone.

$$H_2 + 2I \longrightarrow 2HI$$
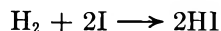
If both $H_2 + I_2$ and $H_2 + 2I$ could form the *same* activated complex, the analysis of section 3 above would be applicable. Sullivan's[7] results would then indicate that, within experimental error, $\theta_{mol} = 0$ and $\theta_{at} = 1$.

However, it would be widely expected that, if there really were potential energy contours as in Figure 1, $H_2 + I_2$ would be capable of conversion into the activated complex, and so to products—which would give a value of θ_{mol} *not* vanishingly small.

This consideration suggests that it could very well be

(8) M. A. Eliason and J. B. Hirschfelder, *J. Chem. Phys.*, **30**, 1426 (1959).

(9) J. Ross and P. Mazur, *ibid.*, **35**, 19 (1961).

(10) K. J. Laidler and J. C. Polanyi, *Progr. Reaction Kinetics*, **3**, 1 (1965).
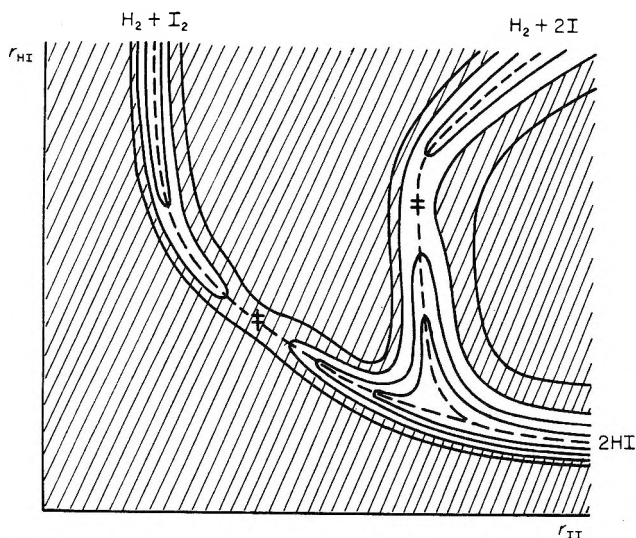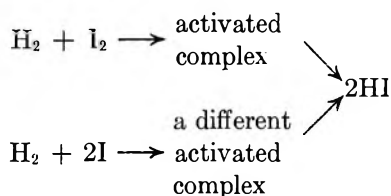
Figure 2. Schematic potential energy contour diagram for the reaction between hydrogen and iodine, on the assumption that a barrier lies between $H_2 + I_2$ and the activated complex of a termolecular atomic mechanism $H_2 + 2I \rightarrow \ldots$. The shading denotes the region for which the potential energy exceeds a certain value lying between those for the two activated complexes: abscissa, r_{II}; ordinate, r_{HI}.

that the reaction between hydrogen and iodine is not an instance of the situation envisaged above, but is of the type

$$H_2 + I_2 \longrightarrow \begin{array}{l}\text{activated}\\\text{complex}\end{array} \searrow$$
$$\hspace{3cm} 2HI$$
$$\begin{array}{l}\text{a different}\\ H_2 + 2I \longrightarrow \begin{array}{l}\text{activated}\\\text{complex}\end{array}\end{array} \nearrow$$

with a barrier lying between $H_2 + I_2$ and the activated complex of the atomic mechanism. Such a situation can be illustrated roughly by a potential energy contour diagram (Figure 2).

If such be the case, then, of the two distinct activated complexes, that formed from $H_2 + 2I$ is so much the more stable that there is no appreciable contribution from any molecular mechanism. Sullivan's results imply a difference in stability corresponding to a standard free-energy difference of at least 3 kcal mol^{-1}.

Relation to the Reverse Reaction. The forward reaction (hydrogen + iodine → ...) may be considered in relation to the reverse reaction (decomposition of HI).

If the molecular mechanism 1 and the atomic mechanism 2 were to proceed *via* a common transition state, then the reverse reactions

$$2HI \longrightarrow H_2 + I_2 \hspace{2cm} (-1)$$
$$2HI \longrightarrow H_2 + 2I \hspace{2cm} (-2)$$
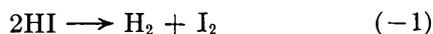
would necessarily proceed *via* a common transition state, capable of dissociating either into $H_2 + I_2$ or into $H_2 + 2I$. The rates of these reactions would then

be in the ratio of transmission coefficients (κ_{-1} and κ_{-2}, say), and the quantities θ would necessarily satisfy the equation

$$\theta_{mol}/\theta_{at} = \kappa_{-1}/\kappa_{-2}$$

If, on the other hand, each of (1) and (2) has its own distinct transition state, then so also must (-1) and (-2). That is, encounter of two HI molecules could, in principle, produce either an activated complex giving rise to $H_2 + I_2$ or a *different* activated complex giving rise only to $H_2 + 2I$. This possibility is exemplified in Figure 2.

Finally, it may be noted that formation of HI by the atomic mechanism might well occur not in a single step

$$H_2 + 2I \longrightarrow 2HI$$
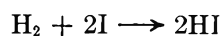
but as a sequence of two steps[4,7]

$$H_2 + I \rightleftharpoons H_2I$$
$$H_2I + I \longrightarrow 2HI$$
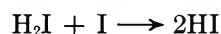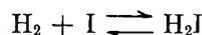
involving an intermediate H_2I of a type which has been invoked[11-13] in studies on the recombination of atomic iodine. Were such the case, the reverse reaction would proceed by the conversion of 2HI into $H_2I + I$, the H_2I thus formed decomposing only subsequently.

5. No Paradox

Both in his preliminary note[5] and in his full final paper,[6] Noyes raised a question as to whether there might be some basic paradox associated with transition state theory. Now consider, from this standpoint, each of the alternative mechanisms.

(i) *If* molecular and atomic mechanisms proceed through a common transition state, then Sullivan's experiments show that (in the present notation) θ_{mol} is zero, within experimental error, and θ_{at} unity. There is no paradox here. The point is perfectly easy to understand on the present formulation when the appropriate fractions θ_{mol} and θ_{at} are included in the transition state equations.

(ii) On the other hand, the two mechanisms might proceed through different transition states. Noyes[6] regards this as not *in itself* involving any difficulty in principle. However, *if* there are two distinct transition states, then Sullivan's results require that the transition state for the molecular mechanism is the higher by at least 3 kcal mol^{-1}. This, Noyes considers, might lead to difficulties in the following respects. (a) Of all transition states which might be envisaged, the planar trapezoidal

$$\begin{array}{c}\text{I}\text{--------}\text{I}\\ \diagdown \hspace{0.3cm} \diagup \\ \text{H}\text{---}\text{H}\end{array}$$
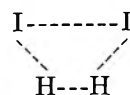
(11) E. Rabinowitch, *Trans. Faraday Soc.*, **33**, 283 (1937).

(12) O. K. Rice, *J. Chem. Phys.*, **9**, 258 (1941).

(13) G. Porter and J. A. Smith, *Proc. Roy. Soc. Ser. A*, **261**, 28 (1961).

has widely been assumed to be likely to be the most stable and to be directly accessible both from $H_2 + I_2$ and from $H_2 + 2I$. If the most stable transition state, whether it be this or some other, is directly accessible both from $H_2 + I_2$ and from $H_2 + 2I$, then doubt is cast on the possibility of there being two distinct transition states, especially if they differ by as much as 3 kcal mol^{-1}. Acceptance of such an argument would lead back to point i previously. (b) Energetic arguments have been proposed[6] suggesting that if there are two distinct transition states, then they are unlikely to differ by as much as 3 kcal mol^{-1}. Again acceptance of this argument leads back to point i.

Neither a or b is at all compelling; the fact that they lead to a paradox seems adequate reason for rejecting them. The reasoning relies throughout on nothing more than considerations of *plausibility*. Each indi-

vidual statement in the analysis might *a priori* be either correct or incorrect.

In this connection, it is of particular interest that, according to Hoffmann,[14] a direct molecular conversion $H_2 + I_2 \rightarrow 2HI$ would for reasons of symmetry *not* be expected to proceed through the trapezoidal transition state.

(14) R. Hoffmann, *J. Chem. Phys.*, **49**, 3739 (1968).

The Formulation of Transition State Theory for a Reaction Proceeding by Simultaneous Mechanisms with a Common Transition State.

II.　Propriety of the Analysis

by P. G. Wright* and Margaret Robson Wright

Department of Chemistry, The University, Dundee, Scotland　　(*Received January 14, 1970*)

It is shown, for a reaction proceeding by simultaneous mechanisms, that (i) straightforward considerations of molecular encounters require that, even if there is a common transition state, the total rate is always expressible as a sum of distinct contributions from the several mechanisms. (ii) These considerations suggest strongly that each such contribution will be of the conventional kinetic form. (iii) A variant derivation of transition state equations indicates that the total rate is always a sum of distinct contributions, each of the conventional form; this is inferred *within* the framework of a formulation of transition state theory. (iv) It is physically possible (even though the geometry is mathematically exceptional) for the potential energy surface to be of the form which is required if there is to be a common transition state.

1.　Introduction

In a preceding communication,[1] a discussion has been given of the formulation of transition state theory for a reaction proceeding by simultaneous mechanisms (*e.g.*,[2] molecular and atomic) but with both mechanisms having the same transition state. The discussion proceeded on the *assumption* that it is proper to apply transition state theory to such a reaction, and, taking this for granted, presented a consistent formulation for each of the mechanisms.

The present purpose is to examine certain aspects of the propriety of such a procedure. In view of the

doubts raised by Noyes,[3] such an enquiry seems needful. The topics considered in particular are the propriety, for such a reaction, of expressing the total rate as a sum of distinct contributions each of the conventional kinetic form; the propriety of so doing within the context of transition state theory; and the possibility, in principle, of there being a potential energy surface of

* To whom correspondence should be addressed.

(1) M. R. Wright and P. G. Wright, *J. Phys. Chem.*, **74**, 4394 (1970).

(2) J. H. Sullivan, *J. Chem. Phys.*, **46**, 73 (1967).

(3) R. M. Noyes, *ibid.*, **47**, 3097 (1967); **48**, 323 (1968).

such geometry as would allow two paths of reaction to proceed by way of a common transition state.

This discussion is concerned with the propriety, and not with the practical utility, of applying transition state theory to such reactions. The fact that it seems necessary to fall back on quantities θ related to transmission coefficients impairs the utility of the theory (at least until some further theory provides means whereby they may be predicted) but does not invalidate it.

2. Discussion in Terms of Molecular Encounters

It is demonstrable by straightforward consideration of molecular encounters that only if an improbable situation obtains can it fail to be admissible to express the total rate in a conventional additive form, such as[1]

$$k_{mol}[L_2][M_2] + k_{at}[L_2][M]^2$$

The argument, assuming nothing about the activated complex, holds irrespective of whether the molecular and atomic contributions to the rate involve two distinct transition states or the same transition state.

Adopt the procedure, commonly used when treating chemical reactions and other phenomena in a gas not in equilibrium, of considering the translational motions of the molecules classically but the internal motions in terms of quantum states. On this basis, out of the molecules of species a, a certain fraction will be in internal quantum state α and have components of velocity in the short ranges u_a to $u_a + \delta u_a$, v_a to $v_a + \delta v_a$, w_a to $w_a + \delta w_a$. This fraction may be written $F_{a\alpha}(u_a,v_a,w_a)\delta u_a \delta v_a \delta w_a$, where the function $F_{a\alpha}$ may, or may not, depart appreciably from the Maxwell–Boltzmann form appropriate to a gas in equilibrium.

For each possible set of reactants there will be a certain probability that an encounter of reactant molecules will lead to reaction. This probability will depend on the velocities and internal quantum states of the reactant molecules, but will be *independent* of the *distribution* of velocities, of the distribution of internal quantum states, and of chemical composition.

It follows that, of encounters a + b in which the molecule a is in internal quantum state α and has components of velocity in short ranges as above, and the molecule b is in internal quantum state β and has components of velocity in short ranges u_b to $u_b + \delta u_b$, v_b to $v_b + \delta v_b$, w_b to $w_b + \delta w_b$, the number per unit volume per unit time which lead to reaction must be of the form

$$\omega_{a\alpha b\beta}(c_a,c_b)n_a F_{a\alpha}(c_a)n_b F_{b\beta}(c_b)\delta u_a \delta v_a \delta w_a \delta u_b \delta v_b \delta w_b$$

where c_a has for brevity been written for (u_a,v_a,w_a); n_a,n_b are the total numbers of molecules of species a,b per unit volume, and $\omega_{a\alpha b\beta}(c_a,c_b)$ is a factor of proportionality, independent of the *distributions* of velocities and internal quantum states and of chemical composition. (It is related to the probability that an encounter will lead to reaction.) The total number of

pairs of molecules a + b reacting per unit volume per unit time is therefore equal to

$$\sum_\alpha \sum_\beta \int \ldots \int \omega_{a\alpha b\beta}(c_a,c_b)n_a F_{a\alpha}(c_a) \times n_b F_{b\beta}(c_b)du_a \ldots dw_b$$

For a reaction between L_2 and $M_2 \rightleftharpoons 2M$, the total rate would be given by the sum of two such contributions: one just as above, with a = L_2, b = M_2, and the other of the analogous form for ternary encounters a + b + c, with a = L_2, b = M, c = M.

The two expressions, respectively, include factors $n_{L_2}n_{M_2}$ and $n_{L_2}n_M{}^2$, but otherwise can depend on experimental conditions only through the distributions of velocities and internal quantum states. In particular, *only if* change in experimental conditions leads to alteration in the distribution of velocities or of internal quantum states, of one or both of L_2 and M, can there fail to be a distinct atomic rate $k_{at}[L_2][M]^2$ (compare Sullivan[4]).

3. An Explicit Treatment within the Framework of a Formulation of Transition State Theory

To a situation corresponding to a potential energy contour diagram of the kind assumed in the preceding communication, apply the following variant (see Eyring, Walter, and Kimball[5]) of the more usual derivations of transition state equations. Treat motion along a reaction coordinate classically, and all other degrees of freedom in terms of quantum states. Let α denote quantum states (with respect to these degrees of freedom) of reactants A, β of reactants B, and γ of products C. Of molecules A (or, for $L_2 + M_2 \rightarrow \ldots$, pairs of molecules) there will be a certain number per unit volume which are in quantum state α and lie along an element δr_A of the reaction coordinate (for A) while moving with momentum between p_A and $p_A + \delta p_A$ toward the col. This number per unit volume may be written

$$f_{A\alpha}(r_A,p_A)\delta r_A \delta p_A$$

Consider a region in the reactant valley *remote from the col*. Then $f_{A\alpha}(r_A,p_A)$ will approximate very closely to its equilibrium value

$$\text{constant} \cdot [A]e^{-\epsilon\alpha/kT}e^{-p_A{}^2/2m_A kT}$$

(where m_A is the relevant reduced mass and [A] denotes the relevant product of concentrations in cases where more than one reactant molecule participates).

Consequently, of molecules A (or pairs of molecules, etc.) in quantum state α and moving with momentum between p_A and $p_A + \delta p_A$ along the reaction coordinate toward the col, the number per unit volume per unit time which pass through a given value of r_A

(4) J. H. Sullivan, *J. Chem. Phys.*, **47**, 3098 (1967).

(5) H. Eyring, J. Walter, and G. E. Kimball, "Quantum Chemistry," Wiley, New York, N. Y., 1944, pp 306, 307.

$$\frac{(p_A/m_A)}{\delta r_A} f_{A\alpha}(r_A, p_A) \delta r_A \delta p_A$$

will approximate very closely to

$$\text{constant} \cdot [A] e^{-\alpha/kT} e^{-p_A^2/2m_A kT} p_A \delta p_A$$

Of these molecules, a certain fraction $\kappa_{\alpha\gamma}$ will be converted into products C in quantum state γ (with respect to degrees of freedom other than motion along the reaction coordinate).

It follows that the total number of molecules A (or pairs of molecules, etc.) converted into products C per unit volume per unit time is equal (very nearly) to

$$\int_0^\infty \sum_\alpha \sum_\gamma \kappa_{\alpha\gamma} \cdot \text{constant} [A] e^{-\alpha/kT} e^{-p_A^2/2m_A kT} p_A dp_A$$

This expression is the same as would apply if there were no possibility that C might also be formed from reactants B. It reduces to the simple form

$$\text{constant} \cdot [A]$$

unless the $\kappa_{\alpha\gamma}$ vary with one or more of the concentrations [A], [B], [C]—a variation that is in no way to be expected.

Thus, the total rate of formation of C is inferred, *within the framework of a formulation of transition state theory*, to be expected to take the form

$$k'[A] + k''[B]$$

(for the reaction between L_2 and $M_2 \rightleftharpoons 2M$

$$k_{mol}[L_2][M_2] + k_{at}[L_2][M]^2)$$

irrespective of whether or not there is equilibrium with respect to interconversion of A and B (here $M_2 \rightleftharpoons 2M$). There seems, then, to be little doubt that such an algebraic expression may properly be applied to both thermal and photochemical reactions (as in Sullivan's work) and that the procedure is compatible with transition state theory.

4. Possibility of a Potential Energy Surface Having the Geometry Necessary to There Being a Common Transition State

It has been suggested[6] that an activated complex will lie on one reaction coordinate only (and not on two as has been assumed possible here) and that the situation to be expected is that of three valleys separated by three distinct cols. A plateau, however, is allowed as an exceptional limiting situation (associated with the vanishing of one or more second derivatives of the potential energy with respect to normal coordinates) but dismissed as "unlikely to arise in practice."

The case of a (very small) plateau is the special geometry here assumed possible for a potential energy surface. There is no compelling physical reason for asserting that the mathematically exceptional situation will *never* arise. Indeed (i) The central point of the mathematical argument (based on an expansion by Taylor's theorem) used by Murrell and Laidler[6] is that a surface having three valleys meeting in a common "bifurcating col," or plateau, is an exceptional limiting case of a surface having three valleys and three distinct cols. (It is derivable by fusion of the distinct cols, that is, by shrinking and eventual disappearance of the central "mound.") (ii) A plateau corresponds to there being a coordinate of free internal rotation. Murrell and Laidler suggest that it is unlikely that free rotations in an activated complex could render it capable of dissociating into alternative sets of products, and cite an example where it assuredly would not. However, it seems entirely possible that in some cases an activated complex

$$\begin{array}{c} L\text{---}M \\ \diagup \\ M\text{---}L \end{array}$$
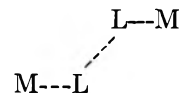
(if exhibiting free internal rotation) would be capable of forming alternative products $L_2 + 2M$ or $L_2 + M_2$.

The points made by Murrell and Laidler are to be read as a general guide to what ordinarily is to be expected, and not as completely rigid requirements.

(6) J. N. Murrell and K. J. Laidler, *Trans. Faraday Soc.*, **64**, 371 (1968).

Some Counting Theorems Concerning the Distribution of

Intrachain Elements on Self-Avoiding Walks

by F. T. Hioe*

Department of Chemistry, University of California, San Diego, La Jolla, California 92037 (*Received May 11, 1970*)

Self-avoiding random walks on a lattice have been studied analytically by a generating function method. A set of theorems is derived to facilitate the recursive enumeration of the distribution of separations of intrachain elements using the generating functions associated with a restricted class of closed graphs. One of these theorems is shown to have an important application to the problem of determining the number of polygons on a lattice. The results can be used to further the study of self-avoiding chain configurations with particular application to polymers.

1. Introduction

The self-avoiding walk problem, with particular application to the theory of polymer configurations[1] and to the theory of the susceptibility of an Ising Ferromagnet,[2] has been studied extensively in recent years.[3] It has been well established from exact enumeration methods[4] and Monte Carlo calculations,[5] for example, that the mean square end-to-end length, $\langle R_n{}^2 \rangle$, of a self-avoiding walk of n steps tends asymptotically to the form

$$\langle R_n{}^2 \rangle \sim A n^\gamma \quad (1.1)$$

where A is a constant depending on the lattice and γ is very close to or possibly exactly equal to $^3/_2$ and $^6/_5$ in two and three dimensions, respectively. A full introduction to the subject appears in the references cited above. More recently, Wall and Whittington[6] applied a generating function technique to the study of the distribution of the end points of short self-avoiding random chains on the diamond and face-centered cubic lattices. Defining the walk generating function $G_n(\alpha,\beta,\gamma)$ as

$$G_n(\alpha,\beta,\gamma) = \sum_{x,y,z} N_n(x,y,z)\alpha^x\beta^y\gamma^z \quad (1.2)$$

where $N_n(x,y,z)$ is the number of self-avoiding walks which, starting at the origin, have reached the point (x,y,z) after n steps, Wall and Whittington found that, for walks up to 10 steps on the diamond lattice, it was possible to express the successive G_n in terms of the lower order generating functions in the form given by

$$G_{2n} = g^*G_{2n-1} - \sum_{k=1}^{n-1} a_{2k}G_{2n-2k} - u_{2n}G_0 \quad (1.3)$$

and

$$G_{2n+1} = gG_{2n} - \sum_{k=1}^{n} a_{2k}G_{2n-2k+1} \quad (1.4)$$

where u_{2n} is the number of returns of $2n$ steps and the a_{2k}'s are associated with the number of ring closures to points other than the origin; g and g^* correspond to the

two types of step vectors on the diamond lattice and are given by

$$g = \alpha\beta\gamma + \alpha\beta^{-1}\gamma^{-1} + \alpha^{-1}\beta\gamma^{-1} + \alpha^{-1}\beta^{-1}\gamma \quad (1.5)$$

$$g^* = \alpha^{-1}\beta^{-1}\gamma^{-1} + \alpha^{-1}\beta\gamma + \alpha\beta^{-1}\gamma + \alpha\beta\gamma^{-1} \quad (1.6)$$

It was found, however, that eq 1.3 and 1.4 no longer hold exactly for higher values of n (>10). For $n = 11$, for example, eq 1.3 and 1.4 must be modified by recognizing another factor to represent a particular type of three-step walk, and for $n = 12$, two new factors must be defined to represent two particular types of four-step walks. The number of such additional factors increases rapidly with increasing n, and consequently the expansion for G_n becomes unmanageably complicated for large n.

In this paper, the problem of deriving the generating function, G_n, will be re-formulated. The use of the generating function technique is generalized for the study of the distribution of the intrachain elements in a self-avoiding walk. A set of theorems is derived that enable the generating functions corresponding to the distribution of any pair of elements in a self-avoiding walk to be enumerated recursively from the generating functions associated with the distribution of the corre-

(1) See, *e.g.*, F. T. Wall, L. A. Hiller, and W. F. Atchison, *J. Chem. Phys.*, **23**, 913 (1955).

(2) See, *e.g.*, C. Domb, National Bureau of Standards (U. S.) Miscellaneous Publication 273, Washington, D. C., 1965, p 29.

(3) For the more recent literature, see, *e.g.*, F. T. Wall, S. Windwer, and P. J. Gans, *J. Chem. Phys.*, **38**, 2220 (1963); C. Domb, J. Gillis, and G. Wilmers, *Proc. Phys. Soc. (London)*, **85**, 625 (1965); S. F. Edwards, *ibid.*, **85**, 613 (1965); H. Reiss, *J. Chem. Phys.*, **47**, 186 (1967); J. L. Martin, M. F. Sykes, and F. T. Hioe, *ibid.*, **46**, 3478 (1967); C. Domb and F. T. Hioe, *ibid.*, **51**, 1915 (1969).

(4) C. Domb, *ibid.*, **38**, 2957 (1963).

(5) F. T. Wall and L. A. Hiller, *Ann. Rev. Phys. Chem.*, **5**, 267 (1954).

(6) F. T. Wall and S. G. Whittington, *J. Phys. Chem.*, **73**, 3953 (1969).

sponding pair of elements on a restricted class of closed graphs.

Some basic ideas concerning the use of the generating functions for representing the distribution of a pair of elements on a self-avoiding chain and on some other types of graphs are first outlined in sections 2 and 3. The theorems are derived in section 4. Two important corollaries are given in section 5, and the conclusion appears in section 6.

This paper, which is rather mathematical, will be followed by two other papers that depend in part on this one, but which can be read and used without reference to the details herein.

2. Generating Functions for Representing the Distribution of a Specified Pair of Elements on a Self-Avoiding Walk

Consider in general a finite d-dimensional lattice and let us denote the lattice point by $x = (x_1, x_2, \ldots, x_d)$. Let $N_n(x)$ be the number of walks which reach the point x after n steps. Introducing d intermediates $\alpha_1, \alpha_2, \ldots, \alpha_d$, the generating function for the end points of an n step walk $G_n(\alpha_1, \alpha_2, \ldots, \alpha_d)$, which we shall denote more simply by $G_n(\alpha)$, is defined by

$$G_n(\alpha) = \sum_x N_n(x)\alpha_1^{x_1}\alpha_2^{x_2}\ldots\alpha_d^{x_d} \quad (2.1)$$

$G_0(\alpha) = 1$ by definition. It is clear that the total number of n step walks c_n is given by

$$c_n = G_n(1, 1, \ldots, 1) \quad (2.2)$$

and that

$$c_n\langle x_i^r\rangle_n = \left[\left(\alpha_i\frac{\partial}{\partial\alpha_i}\right)^r G_n(\alpha)\right]_{\alpha_1,\alpha_2,\ldots,\alpha_d=1} \quad (2.3)$$

where $\langle x_i^r\rangle_n$ is the mean rth power of the x_i coordinate of the end point of the walk, and more generally

$$c_n\langle x_{i_1}^{r_1}x_{i_2}^{r_2}\ldots x_{i_m}^{r_m}\rangle_n = \left[\left(\alpha_{i_1}\frac{\partial}{\partial\alpha_{i_1}}\right)^{r_1} \times \right.$$
$$\left.\left(\alpha_{i_2}\frac{\partial}{\partial\alpha_{i_2}}\right)^{r_2}\ldots\left(\alpha_{i_m}\frac{\partial}{\partial\alpha_{i_m}}\right)^{r_m} G_n(\alpha)\right]_{\alpha_1,\alpha_2,\ldots,\alpha_d=1} \quad (2.4)$$

For example, consider a three-dimensional lattice with cubic symmetry; we have, using the more usual notation (x,y,z) for the coordinates, and (α,β,γ) for the intermediates

$$c_n\langle R_n^2\rangle = 3c_n\langle x^2\rangle_n =$$
$$3\left[\alpha\frac{\partial}{\partial\alpha}\alpha\frac{\partial}{\partial\alpha}G_n(\alpha,\beta,\gamma)\right]_{\alpha=\beta=\gamma=1} \quad (2.5)$$

$$c_n\langle R_n^4\rangle = 3c_n\langle x^4\rangle_n + 6c_n\langle x^2y^2\rangle_n =$$
$$3\left[\left(\alpha\frac{\partial}{\partial\alpha}\right)^4 G_n(\alpha,\beta,\gamma)\right]_{\alpha=\beta=\gamma=1} +$$
$$6\left[\left(\alpha\frac{\partial}{\partial\alpha}\right)^2\left(\beta\frac{\partial}{\partial\beta}\right)^2 G_n(\alpha,\beta,\gamma)\right]_{\alpha=\beta=\gamma=1} \quad (2.6)$$

where $\langle R_n^2\rangle$ and $\langle R_n^4\rangle$ are the mean-square end-to-end distance and the mean fourth moment of the n step walks.

We see that $G_n(\alpha)$ is a function which conveniently expresses the distribution of the nth element (the end point) of the walk about the zeroth element (the origin) of the walk. An obvious generalization of the concept would be to define a generating function to represent the relative distribution of a pair of elements at i and j steps, respectively, from the origin along a walk of n steps. We define this walk generating function $G_n(i,j;\alpha)$ by

$$G_n(i,j;\alpha) = \sum_{x^{(ij)}} N_n(x^{(ij)})\alpha_1^{x_1^{(ij)}}\alpha_2^{x_2^{(ij)}}\ldots\alpha_d^{x_d^{(ij)}} \quad (2.7)$$

where $x^{(ij)} = (x_1^{(ij)}, x_2^{(ij)}, \ldots, x_d^{(ij)}) = (x_1^{(j)}, x_2^{(j)}, \ldots, x_d^{(j)}) - (x_1^{(i)}, x_2^{(i)}, \ldots, x_d^{(i)})$ represents the coordinates $(x_1^{(j)}, x_2^{(j)}, \ldots, x_d^{(j)})$ of the jth elements with respect to the coordinates $(x_1^{(i)}, x_2^{(i)}, \ldots, x_d^{(i)})$ of the ith element. That is, the generating function, $G_n(i,j;\alpha)$, gives the distribution of the jth element about the ith element in a walk of n steps starting from the origin.

For some particular values of i and j, the generating functions $G_n(i,j;\alpha)$ may be conveniently expressed in terms of the generating functions $G_{j-i}(\alpha)$. For example, it is readily seen that

$$G_n(i,i;\alpha) = c_nG_0(\alpha)$$
$$G_n(i,i+1;\alpha) = c_nG_1(\alpha)/q \quad (2.8)$$

and

$$G_n(0,n;\alpha) = G_n(\alpha)$$

where c_n is the total number of n step walks, and q is the lattice coordination number. In general, however, $G_n(i,j;\alpha)$ is a function of i and j, and not simply of $|j - i|$. For a uniform lattice, it is clear from symmetry that

$$G_n(i,j;\alpha) = G_n(n - j, n - i;\alpha) \quad (2.9)$$

From $G_n(i,j;\alpha)$, the mean-square separation $\langle R_{ij}^2\rangle_n$ and the mean fourth moment $\langle R_{ij}^4\rangle_n$, etc., between the ith and the jth elements can be obtained by differentiation in a manner exactly parallel to the examples given in eq 2.5 and 2.6. To get an idea of how $G_n(i,j;\alpha)$ would vary with i and j, we observe[7-9] that for a given n and a given value of $|j - i|$, the mean-square separation $\langle R_{ij}^2\rangle_n$ between the ith and the jth elements is largest when i and j are symmetrical about the midpoint, $n/2$, of the walk.

Another quantity of considerable physical significance is the correlation,[9] $\langle u_iu_j\rangle_n$, between the ith step vector u_i and the jth step vector u_j in a self-avoiding walk

(7) F. T. Wall and J. J. Erpenbeck, *J. Chem. Phys.*, **30**, 634, 637 (1959).

(8) C. Domb and F. T. Hioe, *ibid.*, **51**, 1915 (1969).

(9) C. Domb and F. T. Hioe, *ibid.*, **51**, 1920 (1969).

of n steps; this correlation is defined as the mean of the scalar product of u_i and u_j over all walks of n steps. It is easy to see that $\langle u_i u_j \rangle_n$ can be derived for all i and j subject to the conditions $1 \leqslant i < j \leqslant n$ provided $\langle R_{ij}^2 \rangle_n$ is known wherever $0 \leqslant i < j \leqslant n$. Thus the generating functions $G_n(i,j;\alpha)$ are also useful for the study of the correlation in a self-avoiding walk.

3. Generating Functions for Representing the Distribution of a Specified Pair of Elements on Other Types of Graph

The concept of introducing a generating function to represent the distribution of a pair of elements can be readily extended to the distribution of elements on other types of graphs. Our purpose in this section is to define such generating functions for a class of closed graphs which are relevant to the analysis of the walk generating functions $G_n(i,j;\alpha)$. The class of closed graphs consists of polygons, θ graphs, and dumbbells[10] (see Figure 1).

Let us first consider the polygons. Because there are n starting points and two directions, the lattice constant[10] of an n-sided polygon, p_n, is related to the number of n-step self-avoiding returns, u_n, by

$$p_n = u_n/2n \qquad (3.1)$$

The return generating function, $u_n(i,j;\alpha)$, associated with elements i,j is defined in exactly the same way as the general walk generating function $G_n(i,j;\alpha)$, with the numbers of walks replaced by the numbers of returns. From symmetry, we have

$$u_n(i,j;\alpha) = u_n(i+k,j+k;\alpha) \qquad (3.2)$$

where k is any integer. That is to say, $u_n(i,j;\alpha)$ is a function of $|j - i|$ and hence

$$u_n(i,j;\alpha) = u_n(0,j-i;\alpha) \qquad (3.3)$$

Noting the relation between p_n and u_n given by eq 3.1, we define the polygon generating function, $p_n(i,j;\alpha)$ ($= p_n(i+1,j+1;\alpha) = \ldots = p_n(0,j-i;\alpha)$) by

$$p_n(i,j;\alpha) = u_n(i,j;\alpha)/2n \qquad (3.4)$$

It is clear that the generating functions $u_n(i,j;\alpha)$ and $p_n(i,j;\alpha)$ so defined reduce to u_n and p_n, respectively, on setting the intermediates $\alpha_1 = \alpha_2 = \ldots = \alpha_d = 1$.

Consider now a θ graph, $(r \cdot s \cdot t)_\theta$. Let us first describe the notation that we shall use for denoting a specified pair of elements on the graph. To do so, we make use of a single path starting from one of the principal (junction) points and ending at the other principal point (since the two principal points are equivalent, we need not distinguish one from the other), and which traverses the given θ graph completely in $n = r + s + t$ steps. The positions of the elements of interest are specified by their respective distances along the path as measured from the starting point. It can be readily seen that starting from one of the principal points, there
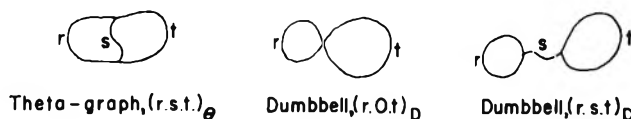

Figure 1. θ graph and dumbbells.

are six possible ways in which one can traverse the graph completely in $n = r + s + t$ steps, the three branches r, s, and t of the graph being regarded as distinct (i.e., given three different colors, say), even if two or all of them are equal. In this way, given a pair of elements on the graph, there are six possible ways in which they can be represented. These representations may be denoted as

$$[(r \cdot s \cdot t/\text{path } 1)_\theta(i_1,j_1)], \quad [(r \cdot s \cdot t/\text{path } 2)_\theta(i_2,j_2)],$$

$$\ldots, \quad [(r \cdot s \cdot t/\text{path } 6)_\theta(i_6,j_6)] \qquad (3.5)$$

where the i's and j's are the numbers of steps along the paths from the starting points of the respective elements. The generating function giving the relative distribution of the two elements for all of the ways that the given θ graph may be imbedded on the lattice will be denoted by

$$[(r \cdot s \cdot t/\text{path } k)_\theta(i_k,j_k;\alpha)] \qquad (3.6)$$

assuming that a particular path k has been chosen to represent the positions of the two elements on the graph. It is naturally convenient to define this generating function in such a way that, on putting $\alpha_1 = \alpha_2 = \ldots = \alpha_d = 1$, it reduces to the lattice constant of the θ graph $(r \cdot s \cdot t)_\theta$.

This seemingly complicated way of denoting the positions of a pair of elements on a θ graph proves to be very systematic as far as analyzing the walk generating function $G_n(i,j;\alpha)$. This is true because of the importance in our analysis of the θ graph generating function associated with a pair of values i,j, $[(r \cdot s \cdot t)_\theta \cdot (i,j;\alpha)]$, defined by

$$[(r \cdot s \cdot t)_\theta(i,j;\alpha)] = \frac{1}{6} \sum_{k=1}^{6} [(r \cdot s \cdot t/\text{path } k)_\theta(i,j;\alpha)] \qquad (3.7)$$

The function $[(r \cdot s \cdot t)_\theta(i,j;\alpha)]$ is determined from a pair of values i and j. It should be noticed that the six terms on the right-hand side of eq 3.7 are not necessarily all different. The factor $1/6$ has been inserted in the definition so that the generating function $[(r \cdot s \cdot t)_\theta(i,j;\alpha)]$ reduces to the lattice constant $(r \cdot s \cdot t)_\theta$ of the graph on setting $\alpha_1 = \alpha_2 = \ldots = \alpha_d = 1$.

The generating function representing a pair of elements on a dumbbell will be defined in a rather similar fashion. For a dumbbell $(r \cdot s \cdot t)_D$, the two principal points are not equivalent (we shall regard the two principal points as nonequivalent even if $r = t$, and for the

(10) M. F. Sykes, J. W. Essam, B. R. Heap, and B. J. Hiley, *J. Math. Phys.*, **7**, 1557 (1966).

dumbbell $(r \cdot 0 \cdot t)_D$, the principal point will be regarded as being made up of two principal points adjoining one another), but there are two equivalent starting directions from either principal point; accordingly, there are four possible (unequivalent) paths for traversing the graph completely in $n = r + s + t$ steps. Thus the distribution of a specified pair of elements on the graph can be represented by a generating function denoted by

$$[(r \cdot s \cdot t/\text{path } k)_D(i_{k:}j_k; \alpha)] \qquad (k = 1, 2, 3, \text{ or } 4) \quad (3.8)$$

Of importance in our analysis of the walk generating function $G_n(i,j; \alpha)$ is the dumbbell generating function $[(r \cdot s \cdot t)_D(i,j; \alpha)]$ associated with a pair of values defined by

$$[(r \cdot s \cdot t)_D(i,j; \alpha)] = \frac{1}{4} \sum_{k=1}^{4} [(r \cdot s \cdot t/\text{path } k)_D(i,j; \alpha)] \quad (3.9)$$

Notice again that the four terms on the right-hand side of eq 3.9 are not necessarily all different. Also, the generating function $[(r \cdot s \cdot t)_D(i,j; \alpha)]$ reduces to the lattice constant $(r \cdot s \cdot t)_D$ of the graph on setting $\alpha_1 = \alpha_2 = \ldots = \alpha_d = 1$.

For convenience in later use, we define

$$V_n(i,j; \alpha) = 12 \sum_n [(r \cdot s \cdot t)_\theta(i,j; \alpha)] + 8 \sum_n [(r \cdot s \cdot t)_D(i,j; \alpha)] \quad (3.10)$$

where the sums on the right-hand side are taken over all θ graphs and dumbbells of order n.

In the ensuing discussion, we shall for convenience of notation drop the α from our notation and denote $G_n(i,j; \alpha)$ by $G_n(i,j)$, etc., and denote $G_n(\alpha)$ simply by G_n.

4. The Theorems

A chain counting theorem, derived by Sykes,[11] asserts a recurrence relation for c_n, the total number of self-avoiding walks of n steps on a lattice, in terms of a restricted class of closed graphs. More explicitly, the theorem states that

$$c_n - 2\sigma c_{n-1} + \sigma^2 c_{n-2} = -u_n + u_{n-1} + 12 \sum_n (r \cdot s \cdot t)_\theta + 8 \sum_n (r \cdot s \cdot t)_D \quad (4.1)$$

where $\sigma = q - 1$, q being the coordination number of the lattice, u_n is the number of self-avoiding returns of n steps, $(r \cdot s \cdot t)_\theta$, and $(r \cdot s \cdot t)_D$ represent the lattice constants of the θ graph $(r \cdot s \cdot t)$ and dumbbell $(r \cdot s \cdot t)$ and the summations on the right-hand side of eq 4.1 are taken over all the θ graphs and dumbbells of order n on the lattice. For the detailed derivation of this theorem, reference should be made to Sykes' paper.

By adopting a procedure which in principle is exactly parallel to that used by Sykes, we shall now set out to derive recurrence relations for $G_n(i,j)$. The
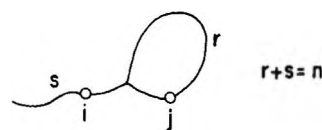

Figure 2. Tadpole $T_s^{(r)}(i, j)$.

analysis will be divided into three parts as: (1) for $i \geqslant 1, j \leqslant n - 1$; (2) for $i = 0, j \leqslant n - 1$; and (3) for $i = 0, j = n$. We shall consider a uniform lattice on which all lattice points are equivalent. The method, however, may easily be adapted to a more general lattice. Let us begin by considering case (1) for $i \geqslant 1$, $j \leqslant n - 1$.

Theorem 1.

$$G_n(i,j) - \sigma G_{n-1}(i,j) - \sigma G_{n-1}(i - 1, j - 1) + \sigma^2 G_{n-2}(i - 1, j - 1) = -u_n(0, j - i) + u_{n-1}(0, j - i) + V_n(i,j)$$

$$(n \geqslant 3, i \geqslant 1 \text{ and } i + 1 \leqslant j \leqslant n - 1) \quad (4.2)$$

Proof. Consider $G_{n-1}(i,j)$ and the effect of adding one step, which we may do in σ ways, to the end point of the $(n - 1)$st step. We have

$$G_n(i,j) = \sigma G_{n-1}(i,j) - 2 \sum_{s=1}^{n-3} T_s^{(n-s)}(i,j) - 2n p_n(i,j) \quad (4.3)$$

where $T_s^{(r)}(i,j)$ represents the distribution of the jth element about the ith element on a tadpole as represented graphically in Figure 2. It is defined in such a way that it reduces to the lattice constant of the tadpole $T_s^{(r)}$ on setting the intermediates $\alpha_1 = \alpha_2 = \ldots = \alpha_d = 1$. $p_n(i,j)$ is the polygon generating function defined in the preceding section. If we consider $G_{n-2}(i - 1, j - 1)$ and the effect of adding one step to the end point of the $(n - 2)$nd step, we have

$$G_{n-1}(i - 1, j - 1) = \sigma G_{n-2}(i - 1, j - 1) - 2 \sum_{s=2}^{n-3} T_{s-1}^{(n-s)}(i - 1, j - 1) - 2(n - 1) p_{n-1}(i - 1, j - 1) \quad (4.4)$$

We shall now eliminate the tadpoles from eq 4.3 and 4.4. To do this, consider the effect of adding one step to the tail of the tadpole $T_{s-1}^{(r)}(i - 1, j - 1)$. We have

$$T_s^{(r)}(i,j) = \sigma T_{s-1}^{(r)}(i - 1, j - 1) - F_s^{(r)}(i,j)$$

$$(\text{for } s - 1 \geqslant 1) \quad (4.5)$$

and

$$T_1^{(r)}(i,j) = r(\sigma - 1) p_r(i - 1, j - 1) - F_1^{(r)}(i,j) \quad (4.6)$$

(11) M. F. Sykes, *J. Math. Phys.*, **2**, 52 (1961).

where $F_s^{(r)}(i,j)$ is a linear sum of the generating functions giving the distribution of element j about element i on θ graphs and dumbbells of order $r + s$. From (4.5) and (4.6), we have

$$\sum_{s=1}^{n-3} T_s^{(n-s)}(i,j) - \sigma \sum_{s=2}^{n-3} T_{s-1}^{(n-s)}(i-1,j-1) =$$

$$(n-1)(\sigma-1)p_{n-1}(i-1,j-1) -$$

$$\sum_{s=1}^{n-3} F_s^{(n-s)}(i,j) \quad (4.7)$$

Subtracting σ times (4.4) from (4.3), and substituting (4.7) into the result, we obtain

$$G_n(i,j) - \sigma G_{n-1}(i,j) - \sigma G_{n-1}(i-1,j-1) +$$

$$\sigma^2 G_{n-2}(i-1,j-1) = -u_n(0,j-i) +$$

$$u_{n-1}(0,j-i) + 2\sum_{s=1}^{n-3} F_s^{(n-s)}(i,j) \quad (4.8)$$

It remains to establish the form of the summation in (4.8). It can be shown, following the analysis as outlined by Sykes, that

$$2\sum_{s=1}^{n-3} F_s^{(n-s)}(i,j) = V_n(i,j) \quad (4.9)$$

where the function $V_n(i,j)$ is defined by eq 3.10. Theorem 1 is thus proved.

The problem of determining the distribution of a pair of elements on a chain has now been transformed into that of determining the distribution of the corresponding pair of elements on a restricted class of closed graphs. Clearly the enumeration problem has been considerably simplified because such graphs are far less numerous than the chains of the same order.

We now proceed to discuss case (2) for $i = 0$, $j \leqslant n - 1$. Let g ($= G_1$) denote the generating function corresponding to the distribution of the end points of 1 step walk.

Theorem 2.

$$G_n(0,j) - gG_{n-1}(0,j-1) - \sigma G_{n-1}(0,j) +$$

$$\sigma gG_{n-2}(0,j-1) + \sigma G_{n-2}(0,j-2) -$$

$$\sigma^2 G_{n-3}(0,j-2) = -u_n(0,j) + u_{n-1}(0,j) +$$

$$u_{n-1}(0,j-2) - u_{n-2}(0,j-2) +$$

$$V_n(0,j) - V_{n-1}(1,j-1)$$

$$(n \geqslant 4, 2 \leqslant j \leqslant n-1) \quad (4.10)$$

For $n = 3$, the recurrence relation for $G_n(0,j)$ is given by

$$G_3(0,2) - gG_2(0,1) + \sigma qG_0 = -u_3(0,1) \quad (4.11)$$

Proof. For $j = 1$, we have

$$G_n(0,1) = c_n G_1/q \quad (4.12)$$

We shall assume that $j \geqslant 2$ in the following discussion.

Consider $G_{n-1}(0,j-1)$ and the effect of multiplying this function by $g(= G_1)$, the generating function corresponding to the distribution of the end points of one-step walks. This has the effect of shifting the end points by one step. We have

$$G_n(0,j) = gG_{n-1}(0,j-1) - G_{n-1}(1,j-1) -$$

$$2\sum_{s=1}^{n-3} T_s^{(n-s)}(n-j,n) - 2np_n(0,j) \quad (4.13)$$

where the second term on the right-hand side results from the immediate reversals. If we consider the multiplication of $G_{n-2}(0,j-1)$ by g, we obtain

$$G_{n-1}(0,j) = gG_{n-2}(0,j-1) - G_{n-2}(1,j-1) -$$

$$2\sum_{s=2}^{n-3} T_{s-1}^{(n-s)}(n-1-j,n-1) -$$

$$2(n-1)p_{n-1}(0,j) \quad (4.14)$$

To eliminate the tadpoles from eq 4.13 and 4.14, we consider the addition of one step to the tadpole $T_s^{(r)}(n-j,n)$. We obtain

$$T_s^{(r)}(n-j,n) = \sigma T_{s-1}^{(r)}(n-1-j,n-1) -$$

$$F_s^{(r)}(0,j) \quad (s \geqslant 2) \quad (4.15)$$

and

$$T_1^{(r)}(n-j,n) = (\sigma-1)rp_r(0,j) - F_1^{(r)}(0,j) \quad (4.16)$$

from which we have

$$\sum_{s=1}^{n-3} T_s^{(n-s)}(n-j,n) -$$

$$\sigma \sum_{s=2}^{n-3} T_{s-1}^{(n-s)}(n-1-j,n-1) =$$

$$(n-1)(\sigma-1)p_{n-1}(0,j) -$$

$$\sum_{s=1}^{n-3} F_s^{(n-s)}(0,j) \quad (4.17)$$

Subtracting σ times (4.14) from (4.13), substituting (4.17) into the result, and using Theorem 1 for $G_{n-1}(1,j-1) - \sigma G_{n-2}(1,j-1)$, we have

$$G_n(0,j) - \sigma G_{n-1}(0,j) - gG_{n-1}(0,j-1) +$$

$$\sigma gG_{n-2}(0,j-1) + \sigma G_{n-2}(0,j-2) -$$

$$\sigma^2 G_{n-3}(0,j-2) = -u_n(0,j) + u_{n-1}(0,j) +$$

$$u_{n-1}(0,j-2) - u_{n-2}(0,j-2) + V_n(0,j) -$$

$$V_{n-1}(1,j-1) \quad (4.18)$$

Equation 4.18 is the recurrence relation for case (2) for all $n \geqslant 4$. The second part of Theorem 2 for $n = 3$ can be readily proved in a similar way.

If we define an operator Λ by

$$\Lambda G_n(0,j) = G_n(0,j) -$$

$$gG_{n-1}(0,j-1) + \sigma G_{n-2}(0,j-2) \quad (4.19)$$

then Theorem 2 can be conveniently stated in the following symbolical form

$$\Lambda[G_n(0,j) - \sigma G_{n-1}(0,j)] =$$
$$[-u_n(0,j) + u_{n-1}(0,j)] -$$
$$[-u_{n-1}(0,j-2) + u_{n-2}(0,j-2)] +$$
$$V_n(0,j) - V_{n-1}(1,j-1) \quad (4.20)$$

We now come to case (3) for $i = 0$, $j = n$. This is the case for the distribution of the end points about the origin, G_n.

Theorem 3.

$$G_n - 2gG_{n-1} + g^2G_{n-2} + 2\sigma G_{n-2} - 2\sigma g G_{n-3} +$$
$$\sigma^2 G_{n-4} = -u_n(0,0) + 3u_{n-1}(0,1) - 2u_{n-2}(0,0) -$$
$$u_{n-2}(0,2) + u_{n-3}(0,1) + V_n(0,n) -$$
$$2V_{n-1}(0,n-2) + V_{n-2}(1,n-3) \quad (n \geqslant 5) \quad (4.21)$$

For $n < 5$, the recurrence relations for G_n are given, respectively, by

$$G_1 - gG_0 = 0$$
$$G_2 - gG_1 + qG_0 = 0$$
$$G_3 - gG_2 + \sigma G_0 = -u_3(0,0) \quad (4.22)$$
$$G_4 - 2gG_3 + g^2G_2 - \sigma q G_0 = -u_4(0,0) + 3u_3(0,1)$$

Proof. Consider gG_{n-1} and gG_{n-2}. We have

$$G_n = gG_{n-1} - G_{n-1}(0,n-2) -$$
$$2\sum_{s=1}^{n-3} T_s^{(n-s)}(0,n) - 2np_n(0,0) \quad (4.23)$$

and

$$G_{n-1} = gG_{n-2} - G_{n-2}(0,n-3) -$$
$$2\sum_{s=2}^{n-3} T_{s-1}^{(n-s)}(0,n-1) - 2(n-1)p_{n-1}(0,0) \quad (4.24)$$

To eliminate the tadpoles from (4.23) and (4.24), we consider $gT_{s-1}^{(r)}(0,n-1)$. We have

$$T_s^{(r)}(0,n) = gT_{s-1}^{(r)}(0,n-1) -$$
$$T_{s-1}^{(r)}(1,n-1) - F_s^{(r)}(0,n) \quad (s \geqslant 2) \quad (4.25)$$
$$T_1^{(r)}(0,n) = grp_r(0,0) - 2rp_r(0,1) - F_1^{(r)}(0,n) \quad (4.26)$$

and thus

$$\sum_{s=1}^{n-3} T_s^{(n-s)}(0,n) - g\sum_{s=2}^{n-3} T_{s-1}^{(n-s)}(0,n-1) =$$
$$g(n-1)p_{n-1}(0,0) - 2(n-1)p_{n-1}(0,1) -$$
$$\sum_{s=2}^{n-3} T_{s-1}^{(n-s)}(1,n-1) - \sum_{s=1}^{n-3} F_s^{(n-s)}(0,n) \quad (4.27)$$

Subtracting g times (4.24) from (4.23) and substituting (4.27) into the result, we obtain

$$G_n - 2gG_{n-1} + g^2G_{n-2} + G_{n-1}(0,n-2) -$$
$$gG_{n-2}(0,n-3) = 2\sum_{s=2}^{n-3} T_{s-1}^{(n-s)}(1,n-1) +$$
$$4(n-1)p_{n-1}(0,1) - 2np_n(0,0) +$$
$$2\sum_{s=1}^{n-3} F_s^{(n-s)}(0,n) \quad (4.28)$$

However

$$2\sum_{s=2}^{n-3} T_{s-1}^{(n-s)}(1,n-1) =$$
$$-[G_{n-1}(0,n-2) - gG_{n-2}(0,n-3)] -$$
$$G_{n-2}(1,n-3) - 2(n-1)p_{n-1}(0,1) \quad (4.29)$$

thus

$$G_n - 2gG_{n-1} + g^2G_{n-2} +$$
$$2[G_{n-1}(0,n-2) - gG_{n-2}(0,n-3)] +$$
$$G_{n-2}(1,n-3) = 2(n-1)p_{n-1}(0,1) -$$
$$2np_n(0,0) + 2\sum_{s=1}^{n-3} F_s^{(n-s)}(0,n) \quad (4.30)$$

If we now rewrite $[G_{n-1}(0,n-2) - gG_{n-2}(0,n-3)]$ by using Theorem 2 in which we replace n by $n-1$ and substitute $n-2$ for j, and if we also rewrite $G_{n-2}(1,n-3)$ by using Theorem 1 in which we replace n by $n-2$, and substitute 1 for i and $n-3$ for j, remembering that $G_{n-3}(1,n-3) = G_{n-3}(0,n-4)$, we obtain finally eq 4.21 which can be written in a more symmetrical form as

$$[G_n - gG_{n-1} + \sigma G_{n-2}] - g[G_{n-1} - gG_{n-2} +$$
$$\sigma G_{n-3}] + \sigma[G_{n-2} - gG_{n-3} + \sigma G_{n-4}] =$$
$$[-u_n(0,0) + u_{n-1}(0,1)] -$$
$$2[-u_{n-1}(0,1) + u_{n-2}(0,0)] +$$
$$[-u_{n-2}(0,2) + u_{n-3}(0,1)] +$$
$$V_n(0,n) - 2V_{n-1}(0,n-2) + V_{n-2}(1,n-3) \quad (4.31)$$

A similar analysis readily gives the recurrence relations (4.22) for $n < 5$.

Using the operator defined by eq 4.19, it is readily verified that Theorem 3 can be conveniently stated in the following symbolical form

$$\Lambda^2 G_n = f_n \quad (n \geqslant 5) \quad (4.32)$$

where f_n denotes the right-hand side of eq 4.31.

Let us consider in a little more detail the contributions to the right-hand side of eq 4.21. The contributions from the polygons involve the distribution of a pair of elements which are separated by not more than two steps. The summations within $V_n(0,n)$ are taken over the generating functions associated with θ graphs and dumbbells of order n with respect to a pair of points falling precisely on the two principal points. The summa-

tions within $V_{n-1}(0, n-2)$ are taken over the generating functions associated with θ graphs and dumbbells of order $n-1$ with respect to a pair of points one of which is at one of the principal points and the other is at one step away from the other principal point. The summations within $V_{n-2}(1, n-3)$ are taken over the generating functions associated with θ graphs and dumbbells of order $n-2$ with respect to a pair of points which are at one step away from the two respective principal points. Therefore in order to derive G_n, only the distribution of a certain pair of elements on a very restricted class of closed graphs need be determined. This fact makes the recurrence for G_n particularly interesting. We shall discuss some of its important consequences in the next section.

The set of recurrence relations expressed by Theorems 1–3 will now enable us to calculate $G_n(i, j)$, for $0 \leq i < j \leq n$, recursively from the generating functions associated with the distribution of the corresponding pair of points on a restricted class of closed graphs which are far less numerous than the walks themselves. These recurrence relations will be referred to as the "generalized chain counting theorem."

Denoting the recurrence relation for c_n, eq 4.1, by, let us say, A_n, it is interesting to note that by setting the intermediates $\alpha_1 = \alpha_2 = \ldots = \alpha_d = 1$, Theorem 1 reduces to A_n, Theorem 2 reduces to $A_n - A_{n-1}$, and Theorem 3 reduces to $A_n - 2A_{n-1} + A_{n-2}$.

Combining Theorems 1–3, we readily derive recurrence relations for two other important generating functions, $K_n(\alpha)$ and $L_n(\alpha)$, defined by

$$K_n = \sum_{j=1}^{n} G_n(0, j) \qquad (4.33)$$

and

$$L_n = \sum_{i=0}^{n-1} \sum_{j>i}^{n} G_n(i, j) \qquad (4.34)$$

We shall refer to these recurrence relations as Theorems 4 and 5

Theorem 4.

$$[K_n - gK_{n-1} + \sigma K_{n-2}] -$$
$$\sigma[K_{n-1} - gK_{n-2} + \sigma K_{n-3}] -$$
$$[G_n - gG_{n-1} + \sigma G_{n-2}] -$$
$$\left[\frac{1}{q}(c_n - \sigma c_{n-1})G_1 - (c_{n-2} - \sigma c_{n-3})G_0 \right] =$$
$$\sum_{j=2}^{n-1}[-u_n(0, j) + u_{n-1}(0, j)] -$$
$$\sum_{j=0}^{n-3}[-u_{n-1}(0, j) + u_{n-2}(0, j)] +$$
$$\sum_{j=2}^{n-1}[V_n(0, j) - V_{n-1}(1, j-1)] \qquad (4.35)$$

Theorem 5.

$$[L_n - 2\sigma L_{n-1} + \sigma^2 L_{n-2}] - 2[K_n - \sigma K_{n-1}] + G_n =$$
$$\sum_{j=1}^{n-2}(n - j - 1)[-u_n(0, j) + u_{n-1}(0, j)] +$$
$$\sum_{i=1}^{n-2} \sum_{j>i}^{n-1} V_n(i, j) \qquad (4.36)$$

Theorems 4 and 5, together with Theorem 3 for G_n, constitute a set of recurrence relations which enable K_n and L_n to be calculated recursively.

It will be recognized that the second-order moments, $\langle Q_n^2 \rangle$ and $\langle S_n^2 \rangle$, of the generating functions K_n and L_n, defined by

$$\langle Q_n^2 \rangle = (n + 1)^{-1} \sum_{j=1}^{n} \langle R_{0j}^2 \rangle_n \qquad (4.37)$$

and

$$\langle S_n^2 \rangle = (n + 1)^{-2} \sum_{i=1}^{n-1} \sum_{j>i}^{n} \langle R_{ij}^2 \rangle_n \qquad (4.38)$$

are the mean-square distance of an element of the walk from the origin of the walk and the mean-square distance of an element of the walk from the center of mass of the walk, respectively. The behaviors of these two quantities have been studied[7,8] for self-avoiding walks on various two- and three-dimensional lattices, and they have been shown[9] to give useful information about the correlations among the steps of the walks.

5. Two Important Corollaries

In this section, we shall discuss two important corollaries which stem directly from Theorem 3.

Corollary 1. The generating function, G_n, can be derived recursively from the generating functions corresponding to θ graphs and dumbbells. To be more specific, Corollary 1 states that the contribution from the polygon terms on the right-hand side of Theorem 3 are derivable from the lower order walk generating functions and need not be computed separately. This corollary can be stated in another way as follows.

Corollary 1A. The number of self-avoiding returns u_n (and consequently the number of polygons p_n on a lattice) can be derived recursively from the generating functions corresponding to θ graphs and dumbbells. The θ graph and dumbbell generating functions required for the determination of u_n are those which contribute to the walk generating functions G_n.

Before we proceed to the proof of these two statements, let us indicate the significance of Corollary 1A. The problem of determining the number of polygons on a lattice is of great interest in its own right. It has application to the study of the properties of a ring-polymer,[12] to the study of the effect of excluded volume on

(12) J. L. Martin, M. F. Sykes, and F. T. Hioe, *J. Chem. Phys.*, 46, 3478 (1967).

phase transition in biopolymers,[13] and to the study of the critical properties of cooperative assemblies.[14] In many of these problems, including the problem of deriving the walk generating function G_n discussed in the previous section, much of the difficulty comes from the necessity of counting the numerous non-self-intersecting returns on the lattice. Now Corollary 1A states that the counting can in fact be transformed into that involving only the θ graphs and dumbbells, even though the distribution of a certain pair of elements on the graphs must now be recorded in the process of counting. Data on the θ graphs and dumbbells have application also to many other problems.[14]

We now prove Corollaries 1 and 1A. The polygon generating functions which contribute to the right-hand side of Theorem 3 consist of the three following types

$$u_n(0,0) \qquad (= u_n G_0)$$
$$u_n(0,1) \qquad (= u_n G_1/q) \qquad (5.1)$$
$$u_n(0,2)$$

We want to show that all these may be derived if we know the walk generating functions G_n of order $n - 2$ and $n - 1$, and the θ graph and dumbbell generating functions contributing to the walk generating functions of order $n - 2$, $n - 1$, and n. For the first two types in (5.1), it is easy to see that they are determined if only G_{n-1} is known, for the number of n-step self-avoiding returns u_n is equal to the number of $n - 1$ step walks whose end points are at one step away from the origin. Thus u_n is derivable from G_{n-1}, and so are $u_n(0,0)$ and $u_n(0,1)$.

Consider now the generating functions $u_n(0,2)$. (For lattices such as the diamond or the honeycomb lattice for which there is only one type of two-step walk, $u_n(0,2)$ is clearly equal to $u_n G_2/q(q-1)$ and is therefore derivable from G_{n-1}.) We want to show that, given G_{n-2} and certain θ graph and dumbbell generating functions of order $\leqslant n$, the generating function $u_n(0,2)$ can be derived. Consider the expansion of G_2 on a given lattice and let us group the terms of the expansion according to sets of symmetrical lattice points which are the end points of the walks. Assume that

$$G_2 = a_1 g_2{}^{(1)} + a_2 g_2{}^{(2)} + \ldots + a_k g_2{}^{(k)} \qquad (5.2)$$

where each of the generating functions $g_2{}^{(1)}$, $g_2{}^{(2)}$, $\ldots$, $g_2{}^{(k)}$ represents a set of symmetrical lattice points which are the end points of some two-step walks, and a_1, a_2, $\ldots$, a_k are constants corresponding to the numbers of walks which reached the respective lattice points. For the simple quadratic lattice, for example

$$G_2 = (\alpha_1{}^2 + \alpha_1{}^{-2} + \alpha_2{}^2 + \alpha_2{}^{-2}) +$$
$$2(\alpha_1\alpha_2 + \alpha_1\alpha_2{}^{-1} + \alpha_1{}^{-1}\alpha_2 + \alpha_1{}^{-1}\alpha_2{}^{-1}) \qquad (5.3)$$

and we have $a_1 = 1$, $g_2{}^{(1)} = \alpha_1{}^2 + \alpha_1{}^{-2} + \alpha_2{}^2 + \alpha_2{}^{-2}$,

$a_2 = 2$ and $g_2{}^{(2)} = \alpha_1\alpha_2 + \alpha_1\alpha_2{}^{-1} + \alpha_1{}^{-1}\alpha_2 + \alpha_1{}^{-1}\alpha_2{}^{-1}$. If we now consider the expansion of G_{n-2} and write out those terms corresponding to the lattice points which may be reached by two-step walks from the origin, and assume that we have

$$G_{n-2} = \ldots + (b_1 g_2{}^{(1)} + b_2 g_2{}^{(2)} +$$
$$\ldots + b_k g_2{}^{(k)}) + \ldots \qquad (5.4)$$

then it can be shown that

$$u_n(0,2) = (a_1 b_1 g_2{}^{(1)} + a_2 b_2 g_2{}^{(2)} + \ldots +$$
$$a_k b_k g_2{}^{(k)}) - 4 T_1{}^{(n-2)}(0,2) -$$
$$8 \sum_n [(r \cdot 0 \cdot l)_\mathrm{D}(1,n-1)] \qquad (5.5)$$

where the summation on the right-hand side is taken over all dumbbells of type $(r \cdot 0 \cdot l)_\mathrm{D}$ of order n on the lattice. The tadpole generating function in (5.5) can be expressed in terms of generating functions associated with polygon of order $n - 2$ and generating functions associated with θ graphs of type $(1,x,y)_\theta$ of order $n - 1$. We have

$$T_1{}^{(n-2)}(0,2) = g(n-2) p_{n-2}(0,1) -$$
$$(n-2) p_{n-2}(0,0) - (n-2) p_{n-2}(0,2) -$$
$$\sum_{n-1} \{3[(1,x,y)_\theta(0,n-2)] - (1,x,y)_\theta G_0\} \qquad (5.6)$$

where the summation on the right-hand side of (5.6) is taken over all θ graphs of type $(1,x,y)_\theta$ of order $n - 1$ on the lattice. Corollaries 1 and 1A are thus proved.

The second corollary which we shall discuss concerns the respective contributions from the polygons, θ graphs, and dumbbells to the numbers of self-avoiding walks reaching various points of the lattice. We shall also give a rather unexpected result regarding the "tail" of the distribution.

It is obvious that the number of n-step walks which arrive at points which cannot be reached by less than n steps is not affected by the excluded volume restriction and is therefore the same for an n-step self-avoiding walk as for an n-step unrestricted walk. It is convenient to imagine a shell which contains such lattice points and to refer to this shell as the nth layer. Similarly, we recognize the $(n-1)$st, $(n-2)$nd, $\ldots$, 1st layers which contain those lattice points which cannot be reached by less than $n-1$, $n-2$, $\ldots$, 1 steps (For the loose-packed lattices, the only layers encountered are n, $n-2$, $\ldots$, etc.). It is of interest to see how the polygons, θ graphs, and dumbbells contribute to the numbers of walks reaching points of the various layers. For n-step walks arriving at points of the $(n-1)$st layer, the number of walks is still the same for a self-avoiding walk as for an unrestricted walk. For walks arriving at points of

(13) D. Poland and H. A. Scheraga, *J. Chem. Phys.*, **45**, 1456 (1966).

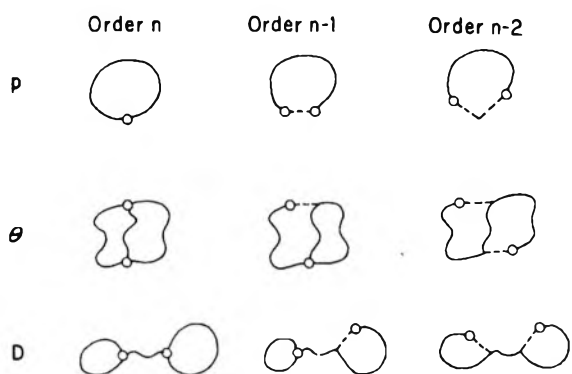(14) See, *e.g.*, C. Domb, *Advan. Phys.*, **9**, 149 (1960).

Order n   Order n-1   Order n-2

p

θ

D

Figure 3. Contributions to G_n. Broken lines, ---, represent one unit step.

the $(n - 2)$nd layer, the numbers are clearly different for an n-step self-avoiding walk and for an n-step unrestricted walk. However, the two numbers are simply related in this case, for we need only subtract off the number of immediate reversals from the number corresponding to an unrestricted walk to obtain the number of self-avoiding walks. For this reason, we shall refer to the region covered by the nth, $(n - 1)$st, and $(n - 2)$nd layers as the "free" region by which we mean that the number of self-avoiding walks arriving at this region can be very simply derived. For walks arriving at points other than those of the nth, $(n - 1)$st, and $(n - 2)$nd layers, other considerations have to be taken into account and it is generally thought that the numbers cannot be derived so simply and thus one has to be satisfied that the free region is only three steps wide. However, we find that the free region is in fact more than three steps wide. To be more precise, we have the following.

Corollary 2. For a self-avoiding walk of n steps, the polygons contribute only to those walks whose end points are at no greater than 2 steps from the origin, the θ graphs contribute to those walks whose end points are at no greater than $[n/3]$ steps from the origin ($[n/3]$ denotes the integer part of $n/3$), and the dumbbells contribute to those walks whose end points are at no greater than $n - 6$ steps for a general close-packed lattice, $n - 8$ steps for a general loose-packed lattice, and $n - 12$ steps for the honeycomb or the diamond lattice, from the origin. The free region is 6 steps wide for a general close-packed lattice, 8 steps wide for a general loose-packed lattice, and 12 steps wide for the honeycomb and the diamond lattice.

To prove this corollary, we have only to examine the contributions to the right-hand side of Theorem 3 which are represented graphically in Figure 3, where the elements of interest are marked by small circles and the broken lines represent one unit step. By considering the maximum distance of separation between the two elements of interest, remembering that the smallest loop is a triangle on a general close-packed lattice, a square on a general loose-packed lattice, and a hexagon on the

honeycomb or the diamond lattice, the first part of the corollary then becomes apparent. Now

$$n - 6 > \left[\frac{n}{3}\right] \text{ if } n > 9 \text{ (close-packed lattices)}$$

$$n - 8 > \left[\frac{n}{3}\right] \text{ if } n > 12 \text{ (loose-packed lattices)} \quad (5.7)$$

$$n - 12 > \left[\frac{n}{3}\right] \text{ if } n > 18 \text{ (honeycomb or diamond lattice)}$$

Thus, for a general close-packed lattice, if $n > 9$, the numbers of walks arriving at points of the nth, $(n - 1)$st, $(n - 2)$nd, ..., $(n - 5)$th layers are completely free of the contributions from the polygons, θ graphs, and dumbbells and are therefore given by the difference equation

$$\Lambda^2 G_n = 0 \quad (5.8)$$

provided that some initial conditions are satisfied. The initial conditions would include the contributions from those polygons and θ graphs which occur before $n > 9$. However, once these initial conditions are correctly given, the difference eq 5.8 gives the correct numbers of walks reaching the free region for any value of n, and similarly for a general loose-packed lattice and the diamond (or the honeycomb) lattice for which the free regions are 8 and 12 steps wide, respectively. Thus, we shall divide the region around the origin of a self-avoiding walk of n steps into four parts and denote them by I, II, III, and IV, respectively, where I denotes the region between the 0th and 2nd layers, II denotes the region between the 3rd and $[n/3]$th layers, III denotes the region between the $([n/3] + 1)$th and $(n - t)$th layers, where $t = 6$ for the close-packed lattices, $t = 8$ for the loose-packed lattices, and $t = 12$ for the honeycomb or diamond lattice, and IV denotes the region between the $(n - t + 1)$th and nth layers. The types of graph contributing to the numbers of walks arriving at the various parts are now given in Table I, where p, θ,

Table I: Types of Graphs Contributing to the Numbers of Walks Arriving at the Various Parts

I	II	III	IV
p, θ, D	θ, D	D	Free

and D denote the polygons, θ graphs, and dumbbells, respectively.

The argument given above clearly applies also to the projection of the radial distribution onto one dimension (such as the x-coordinate distribution discussed by Domb, *et al.*[15]).

(15) C. Domb, J. Gillis, and G. Wilmers, *Proc. Phys. Soc. (London)*, **85**, 625 (1965).

6. Conclusion

The set of recurrence relations, which we have derived as theorems, simplifies the problem of enumerating the distribution of intrachain elements in a self-avoiding walk model polymer chains. In addition, certain useful corollaries have been proved, of which Corollary 1A is particularly helpful. This corollary simplifies the problem of determining the number of polygons on a lattice and therefore has numerous applications to problems arising in chemistry and physics.

Use has been made of the theorems developed herein to assist in the exact determination of the end-to-end lengths of self-avoiding walks on a diamond lattice. This has been done for walks up to 20 steps, the results of which are the subject of the next paper in this series.

The Distribution of End-to-End Lengths of Self-Avoiding

Walks on the Diamond Lattice

by F. T. Wall* and F. T. Hioe

Department of Chemistry, University of California, San Diego, La Jolla, California 92037   (*Received May 11, 1970*)

Exact data on the distribution of end-to-end lengths of self-avoiding walks on the diamond lattice have been obtained for walks up to 20 steps using a counting theorem derived by one of the authors. It is suggested that the limiting x-coordinate distribution, $F(x)$, can be well represented by a function of the form A exp $-(|x|)^\nu$, which was first put forward by Domb, Gillis, and Wilmers for representing the distribution of self-avoiding walks on the simple cubic lattice with $\nu = \frac{5}{2}$. It is conjectured that ν, the principal parameter of the distribution function, depends only on the dimensionality of the lattice. The amplitude A is found to depend on the lattice structure, and an estimate of A for the diamond lattice is given.

1. Introduction

The distribution of end points of a self-avoiding walk has been studied by a number of authors.[1-6] The problem has been approached both analytically[4-6] and numerically.[1-3] These studies have provided strong evidence that the distribution subject to the self-avoiding constraint deviates significantly from the Gaussian distribution which is applicable to a normal unrestricted walk. Much information concerning the shape of the distribution has been provided by the numerical analysis undertaken by Domb, Gillis, and Wilmers.[1] These authors undertook direct enumerations on a computer for walks up to 18 steps on the two-dimensional square lattice (nearly 125 million walks) and up to 13 steps on the three-dimensional simple cubic lattice (nearly 950 million walks) and concluded that the limiting distribution of the end points of the walks for one component, $F(x)$, can be well fitted by a function of the form

$$F(x) = A \text{ exp } -(|x|)^\nu \qquad (1.1)$$

where $\nu = 4$ for the square lattice and $\nu = \frac{5}{2}$ for the simple cubic lattice. They also conjectured that the circular and spherical symmetry properties for the limit-

ing space distribution applicable to walks of a larger number of steps hold for self-avoiding walks as well as for those that are unrestricted. It would naturally be of interest to see how the function (1.1) applies to walks on other lattices, and in particular to see if the exponent ν is lattice sensitive. No extensive investigations of the kind carried out by Domb, Gillis, and Wilmers seem to have been undertaken for other lattices. The main difficulty in this kind of approach is clearly the enormous computing time required for carrying out the

(1) C. Domb, J. Gillis, and G. Wilmers, *Proc. Phys. Soc.*, **85**, 625 (1965).

(2) J. Mazur, *J. Res. Nat. Bur. Stand.*, **69A**, 355 (1965); *J. Chem. Phys.*, **43**, 4354 (1965).

(3) F. T. Wall and S. G. Whittington, *J. Phys. Chem.*, **73**, 3953 (1969).

(4) S. F. Edwards, *Proc. Phys. Soc.*, **85**, 613 (1965); National Bureau of Standards Miscellaneous Publication 273, Washington, D. C., 1965, p 225.

(5) H. Reiss, *J. Chem. Phys.*, **47**, 186 (1967).

(6) H. Yamakawa, *ibid.*, **48**, 3845 (1968).

enumerations because of the enormous number of walks involved.

Recently, Hioe[7] derived a set of counting theorems which considerably simplifies the enumeration problem connected with determining the distribution of intra-chain elements in a self-avoiding walk. These theorems transform the enumeration of the walks into one of analyzing a class of closed graphs which are far less numerous than the walks. With the aid of these theorems, we have been able to derive the exact distribution of end points of self-avoiding walks of up to $n = 20$ steps on the diamond lattice using a reasonable amount of computer time (the number of distinct walks for $n = 20$ is over 3 billion). Indeed, with this new approach, it is possible to continue the enumeration a good deal further. We have not gone beyond $n = 20$ because it is felt that the results up to $n = 20$ are reasonably adequate for our present purpose. Besides the great saving in time, another major advantage of this new method is that it provides other data, such as the lattice constants of various types of graphs,[8] which are useful to many other problems. We have also made use of the set of counting theorems in the study of the various second-order moments associated with the distribution of intra-chain elements of the walks.[9] The results of this investigation are published in another paper.[10]

In this paper, we restrict ourselves entirely to the study of the end-to-end distribution of self-avoiding walks on the diamond lattice. We first establish, in section 2, the spherical symmetry property of the distribution. The moments of the distribution are then analyzed in section 3. In section 4 we estimate the amplitude of the distribution, and finally the conclusions are given in section 5. The paper by Domb, Gillis, and Wilmers will be frequently referred to in the following discussion and, for convenience, we shall refer to it as [1].

2. Spherical Symmetry

It is important first of all to establish if the distribution of end points of a self-avoiding walk tends asymptotically to spherical symmetry, for if this property can be established, the space distribution of the walks can be conveniently studied through its projection on a rectangular coordinate. This is so because, for a spherically symmetrical distribution, the radial distribution of the walk is related to the projected distribution on a single Cartesian coordinate by [1,3]

$$\rho(x) = -2xF'(x) \qquad (2.1)$$

where $\rho(x)dx$ denotes the probability distribution of the walks arriving at a total distance x from the origin and $F(x)dx$ denotes the probability distribution of the walks with one coordinate equal to x. The x-coordinate distribution $F(x)$ is symmetrical about $x = 0$ and it is known to be Gaussian for a normal unrestricted walk.

The study of $F(x)$ for self-avoiding walks is therefore particularly appropriate.

We follow the criteria given in [1] for testing the spherical symmetry of a distribution. Consider the tth moment $\mu_t(\theta_1,\theta_2,\theta_3)$ about an arbitrary axis whose direction angles are $\theta_1,\theta_2,\theta_3$. $\mu_t(\theta_1,\theta_2,\theta_3)$ is given by

$$\mu_t(\theta_1,\theta_2,\theta_3) = [(y\cos\theta_3 - z\cos\theta_2)^2 +$$

$$(z\cos\theta_1 - x\cos\theta_3)^2 +$$

$$(x\cos\theta_2 - y\cos\theta_1)^2]^{t/2} \qquad (2.2)$$

The value of this moment would be independent of θ_1, θ_2, and θ_3 if the distribution is spherically symmetrical. We define the spherical symmetry coefficient $\sigma_{\alpha\beta\gamma}$ as

$$\sigma_{\alpha\beta\gamma} = \frac{\langle x^\alpha y^\beta z^\gamma \rangle}{\langle R^{\alpha+\beta+\gamma} \rangle} \qquad (2.3)$$

where $R = (x^2 + y^2 + z^2)^{1/2}$. For a spherically symmetrical distribution, $\sigma_{\alpha\beta\gamma}$ is given by

$$\sigma_{\alpha\beta\gamma} = s_{\alpha\beta\gamma} =$$

$$\frac{1}{2\pi} \frac{\Gamma\left[\frac{1}{2}(\alpha+1)\right]\Gamma\left[\frac{1}{2}(\beta+1)\right]\Gamma\left[\frac{1}{2}(\gamma+1)\right]}{\Gamma\left[\frac{1}{2}(\alpha+\beta+\gamma)+\frac{3}{2}\right]} \qquad (2.4)$$

Table I: Spherical Symmetry Coefficients for Self-Avoiding Walks on the Diamond Lattice

n	$\sigma_{4,0,0}{}^{(n)}$	$\sigma_{6,0,0}{}^{(n)}$	$\sigma_{4,2,0}{}^{(n)}$
1	0.111111	0.037037	0.037037
2	0.166667	0.083333	0.041667
3	0.181868	0.102265	0.034300
4	0.188172	0.114912	0.032895
5	0.191425	0.121957	0.031624
6	0.193350	0.126624	0.030918
7	0.194617	0.129671	0.030436
8	0.195507	0.131881	0.030116
9	0.196162	0.133486	0.029875
10	0.196662	0.134733	0.029698
11	0.197055	0.135700	0.029558
12	0.197371	0.136487	0.029448
13	0.197630	0.137125	0.029356
14	0.197846	0.137660	0.029282
15	0.198029	0.138109	0.029219
16	0.198185	0.138494	0.029166
17	0.198320	0.138824	0.029120
18	0.198437	0.139119	0.029081
19	0.198541	0.139379	0.029047
20	0.198632	0.139609	0.029018
∞	0.200000	0.142857	0.028571

(7) F. T. Hioe, *J. Phys. Chem.*, **74**, 4401 (1970).

(8) M. F. Sykes, J. W. Essam, B. R. Heap, and B. J. Hiley, *J. Math. Phys.*, **7**, 1557 (1966).

(9) C. Domb and F. T. Hioe, *J. Chem. Phys.*, **51**, 1915, 1920 (1969).

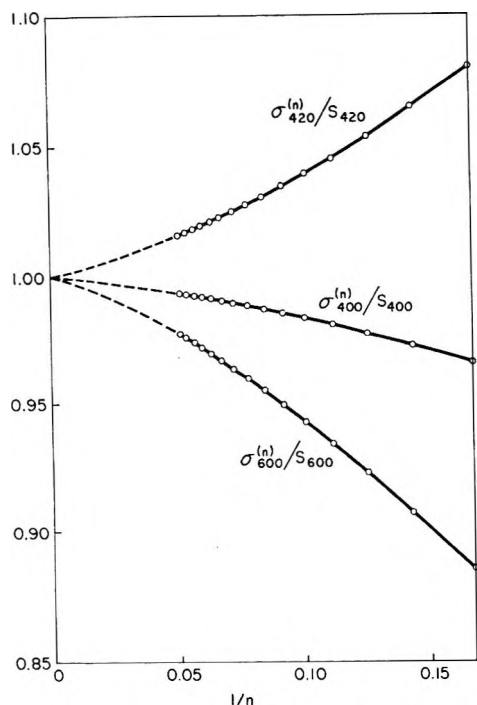(10) F. T. Wall and F. T. Hioe, *J. Phys. Chem.*, **74**, 4416 (1970).

Figure 1. $\sigma_{420}^{(n)}/s_{420}$, $\sigma_{400}^{(n)}/s_{400}$, and $\sigma_{600}^{(n)}/s_{600}$ vs. $1/n$ for self-avoiding walks on the diamond lattice.

It can be readily shown that substitutions of $s_{\alpha\beta\gamma}$ into (2.2) reduce the moment $\mu_t(\theta_1,\theta_2,\theta_3)$ into a value μ_t which is independent of the direction angles θ_1, θ_2, and θ_3 of the reference axis. Using eq 2.4, we obtain

$$s_{4,0,0} = {}^1/_5 = 0.2$$

$$s_{6,0,0} = {}^1/_7 = 0.1428 \ldots \qquad (2.5)$$

$$s_{4,2,0} = {}^1/_{35} = 0.0285 \ldots \text{ etc.}$$

The spherical symmetry coefficients $\sigma_{\alpha\beta\gamma}^{(n)}$ for self-avoiding walks of n steps on the diamond lattice have been derived for various values of α, β, and γ and these are presented in Table I. It will be observed that the values of $\sigma_{\alpha\beta\gamma}^{(n)}$ rapidly approach the corresponding values of $s_{\alpha\beta\gamma}$ as n increases, indicating that the distribution rapidly becomes spherically symmetrical. The rapidity with which the various $\sigma_{\alpha\beta\gamma}^{(n)}$ approach the corresponding $s_{\alpha\beta\gamma}$ is clearly illustrated in Figure 1, where the ratios $\sigma_{\alpha\beta\gamma}^{(n)}/s_{\alpha\beta\gamma}$ are plotted against $1/n$. This is consistent with the finding reported in [1] for self-avoiding walks on the simple cubic lattice. Our results therefore lend further support to the conjecture that the spherical symmetry property of the limiting distribution for normal unrestricted walks is not changed by the self-avoiding condition.

3. Moments of the Distribution

Having established the spherical symmetry property of the limiting space distribution, we now consider the distribution on the x coordinate $F(x)$. The results up to $n = 20$ are reproduced in Tables II and III, in each

of which $c_n(l)$ is the number of walks with x coordinate equal to l. The total numbers of walks, c_n, are given in the last columns of the tables. (The results up to $n = 11$ have already been reported by Martin,[11] but they are included here for convenience of comparison.) A plot of the distribution for $n = 20$, together with that corresponding to a normal unrestricted walk, is shown in Figure 2. In the diagram, the abscissa x is given by

$$x = l/\langle x_n^2 \rangle^{1/2} \qquad (3.1)$$

where $\langle x_n^2 \rangle$ is the mean-square x component of the length of the n step walk, each step vector of the walk being assumed to be of a unit length. The corresponding height of the function $p_n(x)$ is given by

$$p_n(x) = c_n(l)\langle x_n^2 \rangle^{1/2}/c_n \qquad (3.2)$$

It will be observed that the distribution for self-avoiding walks is more flat-topped at the origin, and for larger values of x, it decays more rapidly than the Gaussian distribution for the unrestricted walks. Similar deviations from normality have also been observed for self-avoiding walks on the simple cubic lattice.[1]

To study the shape of the distribution, we consider the reduced moments $m_r^{(n)}$ of the distribution defined by

$$m_r^{(n)} = \langle x_n^r \rangle/\langle x_n^2 \rangle^{r/2} \qquad (3.3)$$

where $\langle x_n^r \rangle$ is the mean rth power of the x component of walks of n steps. The values of $m_4^{(n)}$, $m_6^{(n)}$, and $m_8^{(n)}$ for self-avoiding walks on the diamond lattice are presented in Table IV. In Figures 3–5, the values of these moments are plotted against $1/n$. We have plotted on the same graphs the corresponding values of the moments for self-avoiding walks on the simple cubic lattice given in [1]. From these data, it seems reason-
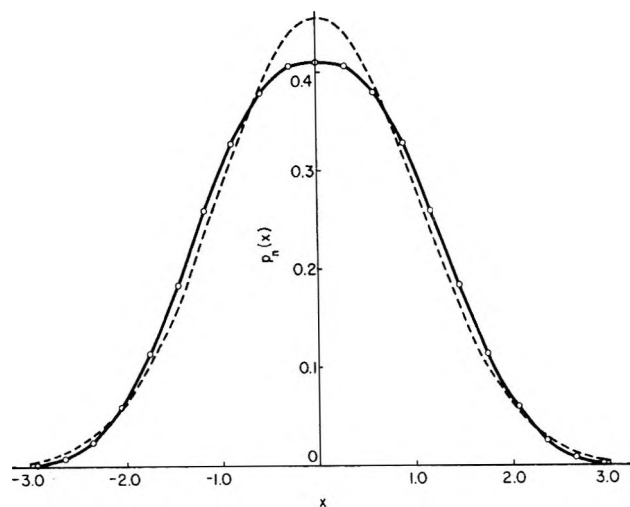

Figure 2. The distribution plots of self-avoiding walks (solid lines) and normal unrestricted walks (broken lines) of 20 steps on the diamond lattice.

(11) J. L. Martin, *Proc. Cambridge Phil. Soc.*, **58**, 92 (1962).

Table II: Distribution on a Coordinate $C_n(l)$ of Self-Avoiding Walks on the Diamond Lattice for Even Number of Steps n. (l Is Given in Units of $1/\sqrt{3}$)

| n	0	2	4	6	8	10	12	14	16	18	20	C_n
0	1											1
2	4	4										12
4	28	24	16									108
6	188	188	128	64								948
8	1428	1368	1120	640	256							8196
10	10708	10572	8864	6208	3072	1024						70188
12	82948	81376	71572	53376	32768	14336	4096					597996
14	644788	637148	570512	453424	304640	166912	65536	16384				5073900
16	5067404	5007560	4572076	3762672	2728256	1669120	827392	294912	65536			42922452
18	40016460	39638728	36618472	31049132	23620736	15756032	8855552	4014080	1310720	262144		362267652
20	317727164	314980912	294030340	254611216	201340944	142390528	88003584	45776896	19136512	5767168	1048576	3051900516
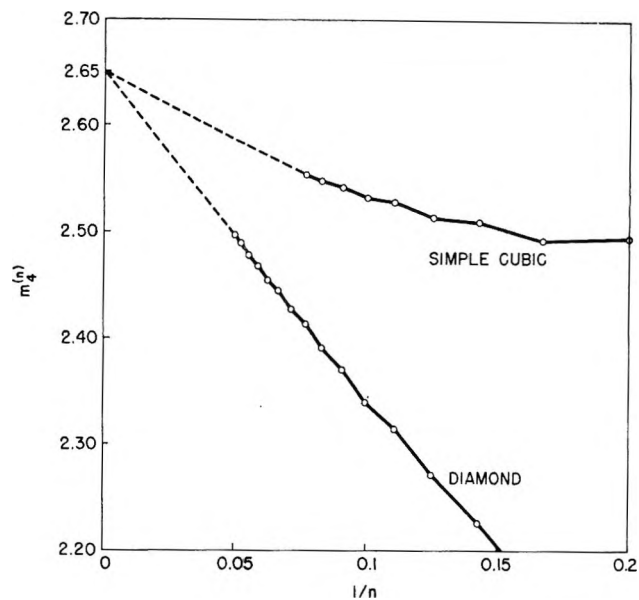
Figure 3. $m_4{}^{(n)}$ vs. $1/n$ for self-avoiding walks on the diamond and simple cubic lattices.
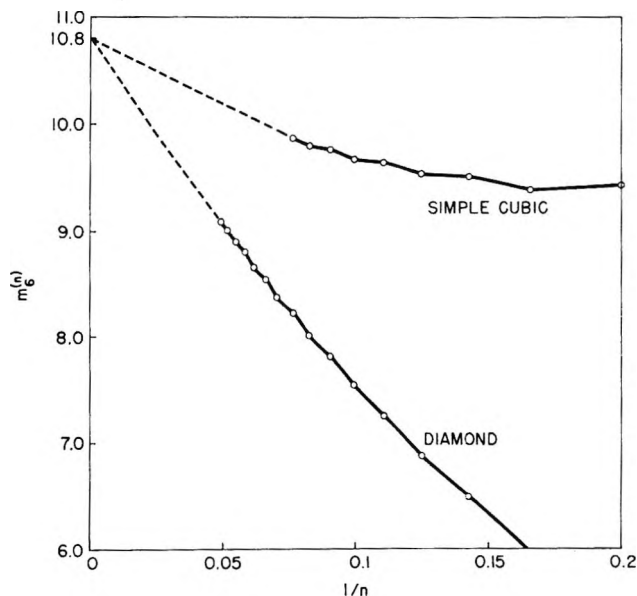

Figure 4. $m_6{}^{(n)}$ vs. $1/n$ for self-avoiding walks on the diamond and simple cubic lattices.

able to conclude that the corresponding moments for the diamond lattice and the simple cubic lattice approach the same limiting values as $n \rightarrow \infty$. These results show that the major feature of the distribution is independent of the detailed structure of the lattice for a given dimensionality. The limiting values of these moments are estimated to be

$$m_4 = 2.65 \pm 0.02$$
$$m_6 = 10.8 \pm 0.2 \qquad (3.4)$$
$$m_8 = 58.0 \pm 2.0$$

Table III: Distribution on a Coordinate $C_n(l)$ of Self-Avoiding Walks on the Diamond Lattice for Odd Number of Steps n. (l Is Given in Units of $1/\sqrt{3}$)

n	1	3	5	7	9	11	13	15	17	19	C_n
1	2										4
3	10	8									36
5	74	56	32								324
7	518	464	288	128							2796
9	3934	3520	2656	1408	512						24060
11	29914	27768	21920	14336	6656	2048					205284
13	232094	217316	181456	128256	74240	30720	8192				1744548
15	1812890	1719616	1475172	1118592	716288	372736	139264	32768			14774652
17	14277886	13633972	11989800	9480048	6586624	3858432	1826816	622592	131072		124814484
19	113016230	108620060	97122184	79485104	58262336	37378048	20193280	8781824	2752512	524288	1052271732

Table IV: Reduced Moments for Self-Avoiding Walks on the Diamond Lattice

n	$m_4{}^{(n)} = \langle x_n{}^4 \rangle/\langle x_n{}^2 \rangle^2$	$m_6{}^{(n)} = \langle x_n{}^6 \rangle/\langle x_n{}^2 \rangle^3$	$m_8{}^{(n)} = \langle x_n{}^8 \rangle/\langle x_n{}^2 \rangle^4$
1	1.00000	1.00000	1.00000
2	1.50000	2.25000	3.37500
3	1.76145	3.43293	6.77181
4	1.95248	4.48436	10.81802
5	2.09956	5.42498	15.17197
6	2.16014	5.95184	18.19266
7	2.22589	6.48698	21.41199
8	2.27094	6.88674	24.06172
9	2.31527	7.26896	26.66473
10	2.34104	7.52601	28.59812
11	2.37136	7.80238	30.63886
12	2.39081	8.00065	32.21175
13	2.41318	8.21068	33.85232
14	2.42750	8.36175	35.11488
15	2.44463	8.52731	36.45617
16	2.45589	8.64825	37.50064
17	2.46955	8.78273	38.62182
18	2.47858	8.88148	39.49756
19	2.48969	8.99257	40.44573
20	2.49715	9.07515	41.19304

Figure 5. $m_8{}^{(n)}$ vs. $1/n$ for self-avoiding walks on the diamond and simple cubic lattices.

If we assume that this distribution can be represented by a function of the form

$$F(x) = \frac{A}{\sigma} \exp -(|x|/\sigma)^\nu \qquad (3.5)$$

then the moments given by (3.4) are best fitted for $\nu = {}^5/_2$, for which the reduced moments of (3.5) are given by

$$\mu_4 = 2.631$$
$$\mu_6 = 10.66 \qquad (3.6)$$
$$\mu_8 = 57.08$$

The principal feature of the distribution function in this form is clearly the index $\nu = {}^5/_2$ which characterizes the shape, and our results, as well as the results for the simple cubic lattice given in [1], clearly suggest that ν depends on the dimensionality but not on the detailed structure of the lattice.
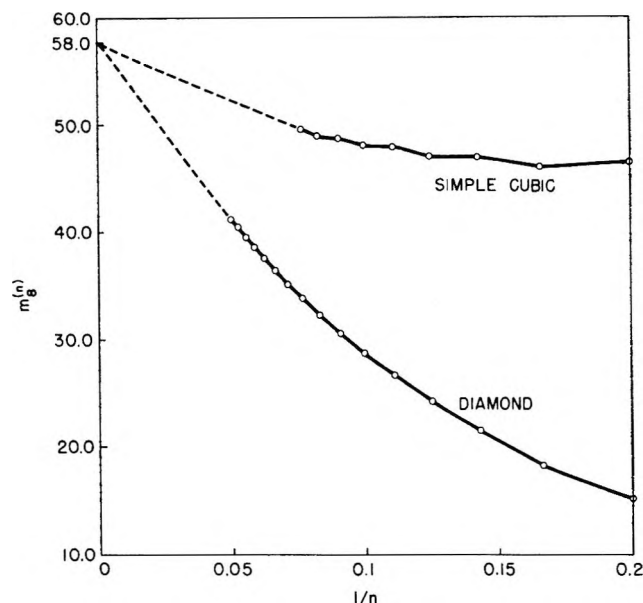
For a finite n, we write the distribution function as $F_n(x)$ and write eq 3.5 as

$$F_n(x) = \frac{A_n}{\sigma_n} \exp -(|x|/\sigma_n)^\nu \qquad (3.7)$$

We now relate the mean $(2r)$th power of the x component, $\langle x_n{}^{2r} \rangle$, of an n-step walk to the quantity denoted by σ_n in eq 3.7 by

$$\langle x_n{}^{2r} \rangle = \int_{-\infty}^{\infty} x^{2r} \exp -(|x|/\sigma_n)^\nu \mathrm{d}x \Big/$$
$$\int_{-\infty}^{\infty} \exp -(|x|/\sigma_n)^\nu \mathrm{d}x =$$
$$\sigma_n{}^{2r} \Gamma[(2r+1)/\nu]/\Gamma(1/\nu) \qquad (3.8)$$

Thus, for $\nu = {}^5/_2$

$$\langle x_n{}^2 \rangle = 0.41394 \sigma_n{}^2 \qquad (3.9)$$

We shall refer to the quantity $p_n(0)$ given by

$$p_n(0) = c_n(0)\langle x_n^2 \rangle^{1/2}/c_n = A_n/0.64338 \quad (3.10)$$

as the amplitude of the distribution. It represents the height at $x = 0$ of the function $p_n(x)$ shown in Figure 2. If we denote the limiting values of $p_n(0)$ and A_n by p and A, respectively, then

$$p = A/0.64338 \quad (3.11)$$

In this way, the constant A is not regarded as a normalization constant but is a constant associated with the amplitude of the distribution.

4. The Amplitude of the Distribution

Although the principal characteristic of the distributions for lattices in a given dimension is insensitive to the detailed structure of the lattice, the amplitude $p_n(0)$ of the distribution can be expected to depend on the lattice structure. The values of $p_n(0)$ for the diamond lattice are given in Table V. By plotting these values against $1/n$ and examining the successive extrapolations, we estimate that the limiting value p of $p_n(0)$ is

Table V: Values of the Amplitudes for Self-Avoiding Walks on the Diamond Lattice

n	$P_n(0)$
8	0.393835
10	0.395237
12	0.401433
14	0.403778
16	0.406656
18	0.408509
20	0.410250

approximately equal to 0.425 in contrast to $p \simeq 0.363$ for the simple cubic lattice. Inserting the value of this amplitude into eq 3.5, we conclude that the x coordinate distribution of self-avoiding walks on the diamond lattice is approximately given by

$$F(x) = \frac{1.465}{\sigma\Gamma(0.4)} \exp\left\{-\left(\frac{|x|}{\sigma}\right)^{5/2}\right\} = $$
$$\frac{0.425}{\langle x^2 \rangle^{1/2}} \exp\left\{\frac{-0.332|x|^{5/2}}{\langle x^2 \rangle^{5/4}}\right\} \quad (4.1)$$

Using the relation given by eq 2.1, the radial distribution of self-avoiding walks on the diamond lattice can therefore be represented by

$$\rho(R) = \frac{7.325}{\sigma\Gamma(0.4)}\left(\frac{R}{\sigma}\right)^{5/2} \exp\left\{-\left(\frac{R}{\sigma}\right)^{5/2}\right\} \quad (4.2)$$

5. Conclusion

Using certain counting theorems proved earlier,[7] we have established exact distributions of the end-to-end separations of self-avoiding random walks of contour lengths up to 20 steps on a diamond lattice. It has also been shown that a high degree of spherical symmetry has been attained by the time the number of steps has reached 20. Various moments have also been determined and the values extrapolated to infinite chains. It appears that the results obtained in this way can be used with some confidence through extrapolation to longer walks.

Mean-Square Intrachain Separations for Self-Avoiding Random

Walks and Ring Closures on the Diamond Lattice

by F. T. Wall* and F. T. Hioe

Department of Chemistry, University of California, San Diego, La Jolla, California 92037 (*Received May 11, 1970*)

This article is concerned with some second-order moments characterizing the mean dimensions of self-avoiding random walks on the diamond lattice. Using a set of counting theorems previously derived by one of the authors, extensive data have been obtained on the mean-square end-to-end distance, $\langle R_n^2 \rangle$, the mean-square distance of walk points from an end point of the walk, $\langle Q_n^2 \rangle$, and the mean-square distance of walk points from the center of mass of the walk, $\langle S_n^2 \rangle$, for self-avoiding walks of n steps on the diamond lattice. The asymptotic behavior of $\langle R_n^2 \rangle$ and the limiting values of the ratios $\langle Q_n^2 \rangle / \langle R_n^2 \rangle$ and $\langle S_n^2 \rangle / \langle R_n^2 \rangle$ are determined within closer limits than heretofore reported. An estimate is also made for the limiting value of the ratio $\langle S_n^2 \rangle_u / \langle S_n^2 \rangle$, where $\langle S_n^2 \rangle_u$ is the mean-square distance from the center of mass of points along self-avoiding ring closures of n steps.

1. Introduction

In the preceding paper,[1] we described the distribution of end-to-end lengths of self-avoiding random walks on the diamond lattice. It was suggested that, in the limit as the number of steps becomes infinite, the distribution can be well represented by a function $\rho(R)$ given by

$$\rho(R) = \frac{7.325}{\sigma \Gamma(0.4)} \left(\frac{R}{\sigma} \right)^{5/2} \exp\left\{ -\left(\frac{R}{\sigma} \right)^{5/2} \right\} \quad (1.1)$$

where $\rho(R)dR$ denotes the probability distribution of walks arriving at a total distance R from the origin, and the quantity σ is related to the moments of $\rho(R)$ by the relationship

$$\langle R^{2r} \rangle = \int_0^\infty R^{2r} \rho(R) dR \Big/ \int_0^\infty \rho(R) dR =$$

$$\sigma^{2r}(2r + 1) \Gamma \left[\frac{2(2r + 1)}{5} \right] \Big/ \Gamma(0.4) \quad (1.2)$$

In the application of self-avoiding walks to the problem of polymer dimensions, an important consideration concerns the overall dimensions of such walks as a function of the number of steps, n, as that number becomes very large. It is the purpose of this paper to consider such aspects of the general problem.

The most useful and convenient parameter characterizing the dimensions of random walks is the mean-square end-to-end separation, $\langle R_n^2 \rangle$. This quantity has been studied extensively for many years and has occupied a central role in the earlier investigations of the effect of excluded volume.[2,3] It has been established from Monte Carlo calculations[4] and exact enumeration methods[5] that

$$\langle R_n^2 \rangle \sim A n^\gamma \quad (1.3)$$

where A is a constant depending on the lattice and γ is

approximately equal to $3/2$ for two-dimensional lattices and approximately equal to $6/5$ for three-dimensional lattices. An extensive study of the behavior of $\langle R_n^2 \rangle$ for various lattices in two and three dimensions was undertaken by Domb[5] using an exact enumeration method. Domb obtained estimates of A and γ by analyzing exact data for short walks obtained through direct counts carried out on an electronic computer. As pointed out in the preceding paper, such direct enumerations cannot be carried very far because of the enormous number of walks involved. The enumeration problem is, however, considerably simplified by the use of a set of counting theorems put forward recently by Hioe.[6] With the aid of these theorems, exact data on $\langle R_n^2 \rangle$ for the diamond lattice have been derived up to $n = 20$ compared to $n = 14$ as derived and analyzed by Domb. In this paper, we make use of the extended data for the more accurate determination of the values of A and γ for the diamond lattice. Accurate estimates of the values A and γ are of particular importance because $\langle R_n^2 \rangle$ is an important quantity in its own right and one with which many other important quantities can be conveniently compared. Two such other quantities will also be examined in this paper; one is the mean-square distance of walk elements from an end point of the walk, denoted by $\langle Q_n^2 \rangle$, and the

(1) F. T. Wall and F. T. Hioe, *J. Phys. Chem.*, **74**, 4410 (1970).

(2) P. J. Flory, "Principles of Polymer Chemistry," Cornell University Press, Ithaca, N. Y., 1953.

(3) F. T. Wall and L. A. Hiller, *Ann. Rev. Phys. Chem.*, **5**, 267 (1954); F. T. Wall, L. A. Hiller, and W. F. Atchison, *J. Chem. Phys.*, **26**, 1742 (1957).

(4) F. T. Wall and J. J. Erpenbeck, *ibid.*, **30**, 634, 637 (1959).

(5) C. Domb, *ibid.*, **38**, 2957 (1963).

(6) F. T. Hioe, *J. Phys. Chem.*, **74**, 4401 (1970).

other is the mean-square distance of walk elements from the center of mass of the walk, denoted by $\langle S_n^2 \rangle$. These quantities provide useful information about the distribution of the intrachain elements of the walk[7,8] and, like $\langle R_n^2 \rangle$, represent moments of the second order associated with the distribution. In the light of eq 1.3, it can reasonably be assumed that, asymptotically at least

$$\langle Q_n^2 \rangle \sim Bn^\gamma \qquad (1.4)$$

and

$$\langle S_n^2 \rangle \sim Cn^\gamma \qquad (1.5)$$

where γ has the same value as for the mean-square end-to-end length, $\langle R_n^2 \rangle$. Estimates of B and C can be derived by analyzing the ratios $\langle Q_n^2 \rangle / \langle R_n^2 \rangle$ and $\langle S_n^2 \rangle / \langle R_n^2 \rangle$ which are indeed of more significance than $\langle Q_n^2 \rangle$ and $\langle S_n^2 \rangle$ by themselves. For unrestricted walks, it can be readily shown[8] that $\langle Q_n^2 \rangle / \langle R_n^2 \rangle = {}^1/_2$ and $\langle S_n^2 \rangle / \langle R_n^2 \rangle \rightarrow {}^1/_6$ as $n \rightarrow \infty$. Estimates of $\langle S_n^2 \rangle / \langle R_n^2 \rangle$ for self-avoiding walks were first given by Wall and Erpenbeck,[4] using Monte Carlo results; the ratio was found to be approximately equal to 0.145 and 0.157, respectively, for the square lattice in two dimensions and the diamond lattice in three dimensions.

More recently, Domb and Hioe[7] used a method of exact enumeration for the square and triangular lattices in two dimensions and for the simple cubic, body-centered cubic, and face-centered cubic lattices in three dimensions to analyze these ratios, and they arrived at a value of 0.140 for the two-dimensional lattices and a value of 0.155 for the three-dimensional lattices. The exact enumeration method has also been applied to the study of the diamond lattice by Hioe[9] and by Kumbar and Windwer.[10] In these studies, the exact data for short walks, on which the asymptotic estimates were based, were derived by counts carried out on a computer. Consequently, the enumeration is very much restricted. With the introduction of the counting theorems by Hioe,[6] it is possible to carry the enumerations a great deal further. In fact, we have made use of these theorems to derive exact data on $\langle Q_n^2 \rangle$ and $\langle S_n^2 \rangle$ up to $n = 18$ for the diamond lattice. An important by-product of this new approach is a set of data on $\langle S_n^2 \rangle_u$, the mean-square distance of walk elements from the center of mass of self-avoiding ring closures or returns of n steps. In this paper, we shall also analyze the ratio $\langle S_n^2 \rangle_u / \langle S_n^2 \rangle$ and give an estimate of its limiting value with a greater degree of accuracy than previously given.[10]

2. The Mean-Square End-to-End Distance, $\langle R_n^2 \rangle$

For physical reasons, substantiated empirically, it is reasonable to assume that the mean-square end-to-end distance of a self-avoiding walk tends to an asymptotic relationship

$$\langle R_n^2 \rangle \sim An^\gamma \qquad (2.1)$$

where $1 < \gamma < 2$, since $\langle R_n^2 \rangle$ must lie between n and n^2. We shall now obtain successive approximations to γ by fitting the numerical data for short walks to the asymptotic form given above. Following Domb,[5] these approximations are obtained by considering successive values of

$$\gamma_n = n \left\{ \frac{\langle R_{n+1}^2 \rangle}{\langle R_n^2 \rangle} - 1 \right\} \qquad (2.2)$$

It would be equally suitable if we consider the successive values of

$$\gamma_n{}^* = n \left\{ \frac{\langle R_n^2 \rangle}{\langle R_{n-1}^2 \rangle} - 1 \right\} \qquad (2.3)$$

which, in the limit as $n \rightarrow \infty$, would clearly approach the same limiting value as γ_n. The transformation from (2.2) to (2.3) is frequently used in the exact enumeration approach and simultaneous examination of both γ_n and $\gamma_n{}^*$ as functions of n is clearly useful. For loose-packed lattices, such as the diamond lattice, the mean values of two successive γ_n and $\gamma_n{}^*$, i.e., $\bar{\gamma}_n = {}^1/_2(\gamma_n + \gamma_{n+1})$ and $\bar{\gamma}_n{}^* = {}^1/_2(\gamma_{n-1}{}^* + \gamma_n{}^*)$, are most useful.

The values of γ_n, $\gamma_n{}^*$, $\bar{\gamma}_n$, and $\bar{\gamma}_n{}^*$, together with the values of $\langle R_n^2 \rangle$ for self-avoiding walks on the diamond lattice are given in Table I, and $\bar{\gamma}_n$ and $\bar{\gamma}_n{}^*$ are plotted

Table I: Values of $\langle R_n^2 \rangle$ and Estimates of γ_n and $\gamma_n{}^*$

| n	$\langle R_n^2 \rangle$	γ_n	$\bar{\gamma}_n$	$\gamma_n{}^*$	$\bar{\gamma}_n{}^*$
1	1.000000	1.66667	1.54167		
2	2.666667	1.41667	1.35467	3.33333	2.72917
3	4.555556	1.29268	1.25619	2.12500	1.92429
4	6.518519	1.21970	1.27459	1.72358	1.62410
5	8.506173	1.32948	1.28501	1.52462	1.56000
6	10.767932	1.24054	1.24898	1.59538	1.52134
7	12.994278	1.25742	1.23774	1.44730	1.44218
8	15.328453	1.21807	1.23894	1.43705	1.40369
9	17.662344	1.25982	1.23611	1.37033	1.38507
10	20.134724	1.21241	1.22759	1.39980	1.36673
11	22.575885	1.24277	1.22549	1.33365	1.34470
12	25.126482	1.20821	1.22239	1.35575	1.33232
13	27.656321	1.23657	1.22113	1.30889	1.32030
14	30.287020	1.20568	1.21806	1.33170	1.31176
15	32.895332	1.23043	1.21677	1.29180	1.30213
16	35.593700	1.20310	1.21462	1.31246	1.29538
17	38.270121	1.22613	1.21391	1.27829	1.28828
18	41.030369	1.20168	1.21201	1.29826	1.28338
19	43.769556	1.22234		1.26849	1.27758
20	46.585407			1.28667	

against $1/n$ in Figure 1. It will be observed that, in the limit as $n \rightarrow \infty$, both sequences move toward a

(7) C. Domb and F. T. Hioe, *J. Chem. Phys.*, **51**, 1915 (1969).

(8) C. Domb and F. T. Hioe, *ibid.*, **51**, 1920 (1969).

(9) F. T. Hioe, Ph.D. Thesis, University of London, 1967.

(10) M. Kumbar and S. Windwer, *J. Chem. Phys.*, **50**, 5257 (1969).
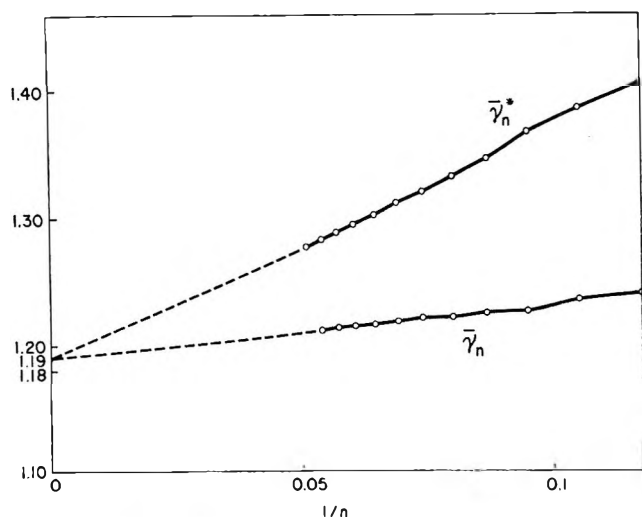
Figure 1. $\bar{\gamma}_n$ and $\bar{\gamma}_n^*$ vs. $1/n$.

Figure 2. A_n and A_n^* vs. $1/n$.

limit close to 1.19. Allowing for some uncertainties in the extrapolation, it seems reasonable to conclude that

$$1.18 \leq \gamma \leq 1.20 \qquad (2.4)$$

It is known that the configurational problems associated with self-avoiding walks on lattices are very similar to those arising in connection with the Ising model[11] and that several physical properties of the Ising model are expressible in terms of exponents involving simple rational fractions.[12] It is therefore tempting to suggest that γ is exactly equal to $^6/_5$, as conjectured by Domb[5] and predicted theoretically by Edwards.[13]

If we accept this conjecture, we can readily obtain estimates of the factor appearing in (2.1) by examining the successive values of A_n and A_n^* given by

$$A_n = \langle R_n^2 \rangle / n^{6/5} \qquad (2.5)$$

and

$$A_n^* = \frac{1}{2}\{nA_n - (n - 2)A_{n-2}\} \qquad (2.6)$$

The values of A_n and A_n^* are presented in Table II and these are plotted against $1/n$ in Figure 2. Assuming that the observed trends continue, we estimate that the limiting value of A_n as $n \to \infty$ for the diamond lattice is approximately given by

$$A \simeq 1.283 \pm 0.001 \qquad (2.7)$$

which we believe to be more accurate than the estimate $A = 1.2875$ given by Domb. We therefore suggest the following asymptotic approximation for the mean-square end-to-end distance of self-avoiding walks on the diamond lattice

$$\langle R_n^2 \rangle \sim 1.283n^{6/5} \qquad (2.8)$$

(It is assumed, of course, that each step length is equal to unity.)
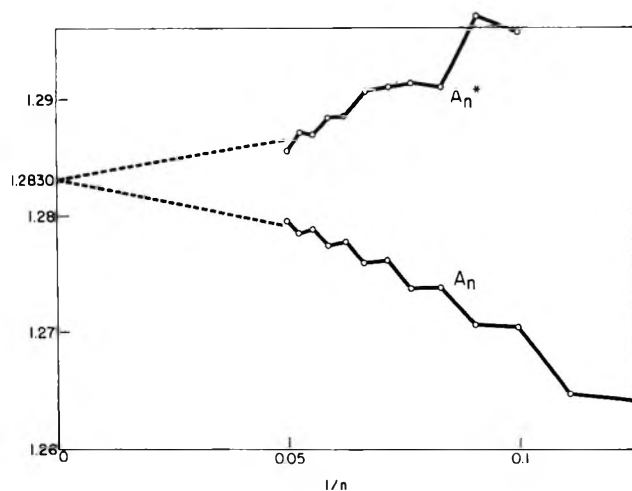
Table II: Estimates of A

n	A_n	A_n^*
1	1.000000	
2	1.160734	1.160734
3	1.218978	1.328467
4	1.235028	1.309322
5	1.233020	1.254083
6	1.254154	1.292406
7	1.257866	1.319981
8	1.264126	1.294042
9	1.264612	1.288223
10	1.270415	1.295571
11	1.270497	1.296980
12	1.273838	1.290953
13	1.273686	1.291226
14	1.276160	1.290092
15	1.275924	1.290471
16	1.277701	1.288488
17	1.277383	1.288326
18	1.278729	1.286953
19	1.278403	1.287073
20	1.279422	1.285659

3. $\langle Q_n^2 \rangle$ and $\langle S_n^2 \rangle$

In this section, we shall examine the mean-square distance of a walk element from an end point of the walk, $\langle Q_n^2 \rangle$, and the mean-square distance of a walk element from the center of mass of the walk, $\langle S_n^2 \rangle$, for self-avoiding walks on the diamond lattice.

If $\langle R_{ij}^2 \rangle_n$ denotes the mean-square distance between elements i,j of the walk, $\langle Q_n^2 \rangle$ and $\langle S_n^2 \rangle$ can be expressed in terms of $\langle R_{ij}^2 \rangle_n$ as follows

$$\langle Q_n^2 \rangle = (n + 1)^{-1} \sum_{j=1}^{n} \langle R_{0j}^2 \rangle_n \qquad (3.1)$$

and

(11) C. Domb, *Advan. Chem. Phys.*, **15**, 229 (1969).

(12) See, *e.g.*, C. Domb, *Advan. Phys.*, **9**, 149 (1960).

(13) S. F. Edwards, *Proc. Phys. Soc.*, **85**, 613 (1965).

$$\langle S_n^2 \rangle = (n + 1)^{-2} \sum_{i=0}^{n-1} \sum_{j>i}^{n} \langle R_{ij}^2 \rangle_n \qquad (3.2)$$

The quantities $\langle Q_n^2 \rangle$, $\langle S_n^2 \rangle$, and $\langle R_{ij}^2 \rangle_n$ can be reasonably assumed to be proportional to n^γ with the same value of γ as for $\langle R_n^2 \rangle$. These quantities representing second-order moments associated with the distribution of the intrachain elements of the walk are closely related to one another, and their relationship is most clearly demonstrated in terms of the correlation function between the steps of the walk.[8]

New values of $\langle Q_n^2 \rangle$ and $\langle S_n^2 \rangle$ have been derived up to $n = 18$ for self-avoiding walks on the diamond lattice, and these are presented, together with the ratios $\mu_n = \langle Q_n^2 \rangle / \langle R_n^2 \rangle$ and $\nu_n = \langle S_n^2 \rangle / \langle R_n^2 \rangle$ in Table III. By plotting μ_n and ν_n against $1/n$ (Figures 3 and
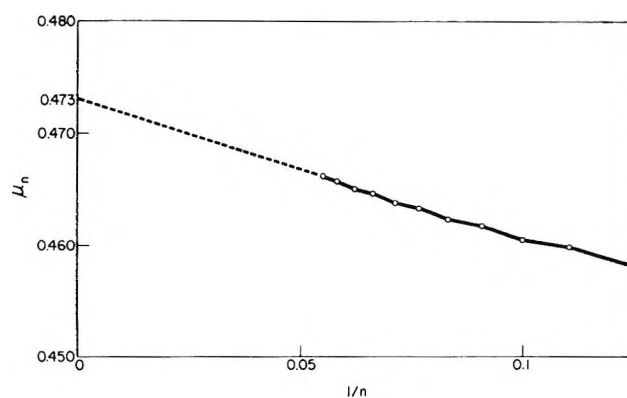
Figure 3. $\mu_n = \langle Q_n^2 \rangle / \langle R_n^2 \rangle$ vs. $1/n$.

Figure 4. $\nu_n = \langle S_n^2 \rangle / \langle R_n^2 \rangle$ vs. $1/n$.

Table III: Values of $\langle Q_n^2 \rangle$, $\langle Q_n^2 \rangle / \langle R_n^2 \rangle$, $\langle S_n^2 \rangle$, and $\langle S_n^2 \rangle / \langle R_n^2 \rangle$

n	$\langle Q_n^2 \rangle$	$\langle Q_n^2 \rangle / \langle R_n^2 \rangle$	$\langle S_n^2 \rangle$	$\langle S_n^2 \rangle / \langle R_n^2 \rangle$
1	0.500000	0.500000	0.250000	0.250000
2	1.222222	0.458333	0.518519	0.194444
3	2.055556	0.451220	0.805556	0.176829
4	2.948148	0.452273	1.105185	0.169545
5	3.874486	0.455491	1.413237	0.166143
6	4.903556	0.455385	1.748041	0.162338
7	5.939199	0.457063	2.088698	0.160740
8	7.023697	0.458213	2.444047	0.159445
9	8.121480	0.459819	2.805292	0.158829
10	9.271634	0.460480	3.180977	0.157985
11	10.422397	0.461661	3.559715	0.157678
12	11.616593	0.462325	3.950772	0.157235
13	12.812722	0.463284	4.344523	0.157090
14	14.047206	0.463803	4.749024	0.156801
15	15.282346	0.464575	5.155783	0.156733
16	16.552005	0.465026	5.572251	0.156552
17	17.821260	0.465670	5.990434	0.156530
18	19.122251	0.466051	6.417514	0.156409

4), we estimate that the limiting value of $\langle Q_n^2 \rangle / \langle R_n^2 \rangle$ to be

$$\mu = \lim_{n \to \infty} \langle Q_n^2 \rangle / \langle R_n^2 \rangle = 0.473 \pm 0.002 \qquad (3.3)$$

and that the limiting value of $\langle S_n^2 \rangle / \langle R_n^2 \rangle$ to be

$$0.155 \le \nu = \lim_{n \to \infty} \langle S_n^2 \rangle / \langle R_n^2 \rangle \le 0.156 \qquad (3.4)$$

These estimates are fully consistent with the estimates, 0.472 ± 0.002 and 0.155 ± 0.001, given by Domb and Hioe[7] for other three-dimensional lattices. However, our new estimate for $\langle S_n^2 \rangle / \langle R_n^2 \rangle$ is now given with increased confidence.

4. $\langle S_n^2 \rangle_u$ for Self-Avoiding Ring Closures or Returns

As mentioned earlier, the quantities $\langle R_n^2 \rangle$, $\langle Q_n^2 \rangle$, and $\langle S_n^2 \rangle$ discussed in the preceding sections were enumerated with the aid of a set of counting theorems which effectively transformed the task of enumerating walks
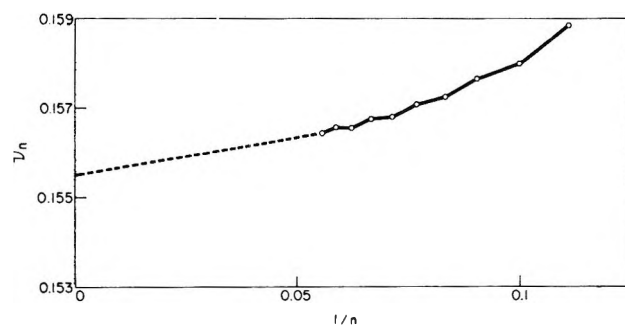
into one of enumerating a class of closed graphs consisting of polygons, θ graphs, and dumbbells.[6] The configurational properties of a simple closed polygon or a self-avoiding return, with particular application to the study of the specific heat of cooperative assemblies and to the study of a ring polymer, are of particular interest in their own right. For a self-avoiding return of n steps, let $\langle R_n^2 \rangle_u$, $\langle Q_n^2 \rangle_u$, and $\langle S_n^2 \rangle_u$ denote quantities corresponding to $\langle R_n^2 \rangle$, $\langle Q_n^2 \rangle$, and $\langle S_n^2 \rangle$. Then of course $\langle R_n^2 \rangle_u = 0$, and it is easy to show that $\langle Q_n^2 \rangle_u = 2\langle S_n^2 \rangle_u$. It can be reasonably assumed that $\langle Q_n^2 \rangle_u$ and $\langle S_n^2 \rangle_u$ are proportional to n^γ with the same value of γ as for $\langle R_n^2 \rangle$, $\langle Q_n^2 \rangle$, or $\langle S_n^2 \rangle$. For a normal unrestricted walk, it is known that[14]

$$\langle S_n^2 \rangle_u / \langle S_n^2 \rangle \longrightarrow {}^1/_2 \qquad (\text{as } n \longrightarrow \infty) \qquad (4.1)$$

In this section, we shall analyze the ratios $\langle S_n^2 \rangle_u / \langle S_n^2 \rangle$ for walks subject to the excluded volume restriction on the diamond lattice.

The values of $\langle S_n^2 \rangle_u$ and of $\langle S_n^2 \rangle_u / \langle S_n^2 \rangle$ for the diamond lattice are presented in Table IV. It will be observed that the values of the ratio $\langle S_n^2 \rangle_u / \langle S_n^2 \rangle$ converge rather slowly. This is not surprising because self-avoiding returns form only a small subset of the walks, and in order to achieve a smoother behavior of $\langle S_n^2 \rangle_u$, the value of n would have to be pushed up correspondingly. However, we think that it is possible

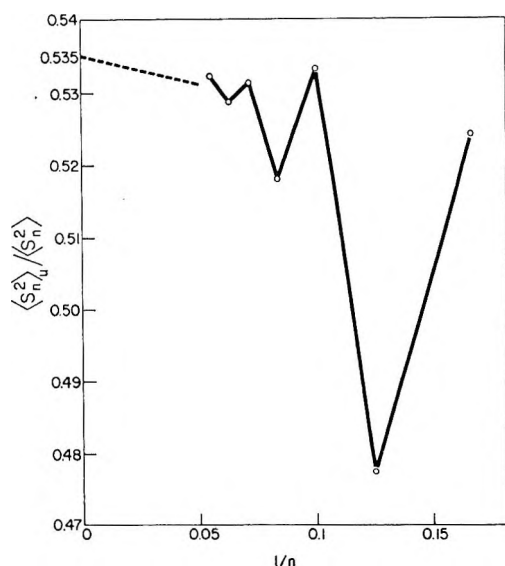(14) B. H. Zimm and W. H. Stockmayer, *J. Chem. Phys.*, **17**, 1301 (1949).

Figure 5. $\langle S_n{}^2 \rangle_u / \langle S_n{}^2 \rangle$ vs. $1/n$.

Table IV: Values of $\langle S_n{}^2 \rangle_u$ and $\langle S_n{}^2 \rangle_n / \langle S_n{}^2 \rangle$

n	$\langle S_n{}^2 \rangle_u$	$\langle S_n{}^2 \rangle_u / \langle S_n{}^2 \rangle$
6	0.916667	0.524397
8	1.166667	0.477350
10	1.696667	0.533379
12	2.045508	0.517749
14	2.523371	0.531345
16	2.946457	0.528773
18	3.415098	0.532153

to make a reasonable estimate of the limiting value of $\langle S_n{}^2 \rangle_u / \langle S_n{}^2 \rangle$ from the data available, and we estimate this limiting value (see plot of $\langle S_n{}^2 \rangle_u / \langle S_n{}^2 \rangle$ against $1/n$ as shown in Figure 5) to be given by

$$\langle S_n{}^2 \rangle_u / \langle S_n{}^2 \rangle \simeq 0.535 \pm 0.005 \qquad (4.2)$$

The limiting value of $\langle S_n{}^2 \rangle_u / \langle S_n{}^2 \rangle$ for a self-avoiding walk therefore differs significantly from the value $1/2$ which is applicable in the absence of the excluded volume effect. Our estimate given by (4.2) is slightly higher than the estimate 0.52 given by Kumbar and Windwer[10] on the basis of their shorter data of up to

$n = 14$. It is not surprising that the ratio is greater than $1/2$. Both $\langle S_n{}^2 \rangle_u$ and $\langle S_n{}^2 \rangle$ will, of course, be larger for non-self-intersecting walks than for random walks. However, $\langle S_n{}^2 \rangle_u$ will be enhanced relatively more because the ring closure will tend to leave the center of mass in a region of low density.

5. Conclusion

On the basis of the exact data more extensive than previously obtained on $\langle R_n{}^2 \rangle$, $\langle Q_n{}^2 \rangle$, and $\langle S_n{}^2 \rangle$ for self-avoiding walks and on $\langle S_n{}^2 \rangle_u$ for self-avoiding returns on the diamond lattice, we put forward the following approximations for the asymptotic behaviors of these quantities in the limit of very large n.

$$\langle R_n{}^2 \rangle \sim 1.483 n^{6/5} \qquad (5.1)$$

$$\langle Q_n{}^2 \rangle / \langle R_n{}^2 \rangle \simeq 0.473 \pm 0.002 \qquad (5.2)$$

$$\langle S_n{}^2 \rangle / \langle R_n{}^2 \rangle = \nu \qquad (0.155 \leq \nu \leq 0.156) \qquad (5.3)$$

and

$$\langle S_n{}^2 \rangle_u / \langle S_n{}^2 \rangle \simeq 0.535 \pm 0.005 \qquad (5.4)$$

A Model for the Binding of Flexible Ligands to the Surfaces of Proteins

and Other Macromolecules. I. Statistical-Mechanical Treatment

by Nora Laiken and George Némethy[1]

The Rockefeller University, New York, New York 10021 (*Received July 7, 1970*)

A theoretical model for the binding of flexible ligands to proteins is presented. The model explicitly accounts for the ability of these chain-like molecules to bind in a large number of configurations, including many in which not all segments are in contact with the protein (configurations with desorbed loops and free ends). The protein surface is represented by a lattice, each site of which binds a single ligand segment. To construct the lattice, a planar lattice with fixed coordination number was folded over a sphere by changing a small number of sites to a lower coordination number. The lattice sites are divided into classes according to their position on the lattice, and a Markov process based on this classification is used to enumerate the configurations of the bound ligands. The same classification may be used to treat surfaces with chemically different sites in various arrangements by assigning different Boltzmann weighting factors to each class of sites. It is assumed that each site on the surface can be occupied by only one segment. Therefore, when the successive binding of several ligands is considered, corrections for occupied sites are applied in the enumeration of configurations. The model allows a calculation of binding isotherms and several parameters characterizing the average configuration of each bound ligand, such as the average fraction of segments adsorbed, average number and length of adsorbed stretches, average length of desorbed loops, and average length of the free chain ends.

I. Introduction

Many proteins can bind a variety of small molecules, or *ligands*. While enzyme–substrate complexes seem to require very specific and well-defined interactions, other molecules bind in a less specific manner and with varying ratios of ligand to protein. Examples of the latter type of binding are the complexes of serum albumin and other proteins with alkanes and their substituted derivatives (*e.g.*, long-chain carboxylic acids, alkyl sulfates, etc.).[2,3] In this study, a theoretical model for the interaction of these chain-like molecules with proteins is presented. Although the model has certain formal similarities to the statistical-mechanical theories of the adsorption of flexible polymers at a surface,[4,5] several features have been included which make the model especially suitable for the description of protein–ligand interactions. This paper describes the general features of the model and the statistical-mechanical derivation of the equations characterizing it. In subsequent parts of this series, the physical properties of various ligand–surface systems will be analyzed,[6] and the results will be compared with experimental observations.[7]

Protein–ligand interactions commonly have been analyzed using the standard formulas governing multiple equilibria,[2,8] in which the bound ligands are grouped into classes according to the strength with which they are bound. In the simplest possible case, all of the ligands bind independently and with equal intrinsic binding constants. If a maximum of M ligands is bound, each with an intrinsic association constant k_{int}, then the average number of ligands bound per protein molecule, $\bar{N}$, bears a simple relationship[8] to the free ligand concentration, c

$$\bar{N} = \frac{M k_{int} c}{1 + k_{int} c} \tag{1}$$

Thus, the binding isotherms, expressed as $\bar{N}$ *vs.* the logarithm of c, have a symmetrical, sigmoidal shape, similar to those obtained in the Langmuir theory of the ideal lattice gas.[9,10] Furthermore, by rearranging eq 1, it can be seen that plots of $\bar{N}/c$ *vs.* $\bar{N}$ and $1/\bar{N}$ *vs.* $1/c$ (the so-called Scatchard and double-reciprocal plots, respectively) will be linear when all ligands are bound as one class.[8] Deviations from linearity commonly are explained by assuming that the bound ligands belong to several classes, so that[2]

$$\bar{N} = \sum_{i=1}^{n_c} \frac{M_i k_{int}^{(i)} c}{1 + k_{int}^{(i)} c} \tag{2}$$

where n_c is the number of classes.

(1) To whom correspondence should be addressed.

(2) J. Steinhardt and J. Reynolds, "Multiple Equilibria in Proteins," Academic Press, New York, N. Y., 1969.

(3) D. S. Goodman, *J. Amer. Chem. Soc.*, **80**, 3892 (1958).

(4) A. Silberberg, *J. Phys. Chem.*, **66**, 1872, 1884 (1962).

(5) R.-J. Roe, *Proc. Nat. Acad. Sci. U. S.*, **53**, 50 (1965); *J. Chem. Phys.*, **43**, 1591 (1965).

(6) N. Laiken and G. Némethy, *J. Phys. Chem.*, **74**, 4431 (1970).

(7) N. Laiken and G. Némethy, *Biochemistry*, in press.

(8) I. M. Klotz in "The Proteins," Vol. IB, H. Neurath and K. Bailey, Ed., Academic Press, New York, N. Y., 1953.

(9) T. Hill, "An Introduction to Statistical Thermodynamics," Addison-Wesley, Reading, Mass., 1960.

(10) C. Tanford, "Physical Chemistry of Macromolecules," Wiley, New York, N. Y., 1961.

However, there are two important reasons why the theory of multiple equilibria is not suitable, in many cases, to describe the interactions of flexible, chain-like molecules with proteins. First of all, the binding site in the theory of multiple equilibria is defined as a functional group on the protein to which a ligand binds in an all-or-none manner. The theory cannot consider situations in which the extent of contact of the bound ligand with the protein is variable. Secondly, the internal degrees of freedom of the bound ligands are ignored, so that all ligands in a given class are assumed to bind in the same, rigidly defined configuration. Although the above two assumptions are reasonable for the binding of small ions or other ligands with a rigid molecular structure (Figure 1a), a chain-like molecule is composed of many functional units, not all of which have to be in contact with the protein simultaneously. Furthermore, the bound ligands can assume many configurations, due to the possibility of internal rotation about single bonds (Figure 1b). Therefore, a new model for multiple equilibria is necessary if the binding of flexible ligands is to be considered. For such a model, it is more realistic to define a binding site as an area on the protein which serves as a point of attachment for a single functional group, or *segment*, of the ligand in question. Thus, when all segments of a ligand are in contact with the protein, several sites will be occupied. The model developed in this paper is based on such a definition of a site and specifically accounts for the flexibility of the bound ligands. In the subsequent papers of this series,[6,7] it will be seen that the configurational entropy contributions arising from ligand flexibility may alter the equilibrium properties of protein–ligand systems considerably, and furthermore, that only when the flexibility of the bound ligand is included can several important features of experimental binding data be reproduced.

II. Description of the Model

Several statistical-mechanical models of polymer adsorption at a surface have been constructed.[4,5] In these theories, the central problem is to enumerate all possible configurations that a flexible polymer might assume in the vicinity of a surface when at least one of its segments is adsorbed to the surface. The enumeration of configurations usually is accomplished with the aid of a lattice model. Neglecting the self-excluded volume of the polymer, there is a one-to-one correspondence between random walk paths on the lattice and polymer chain configurations.

However, these models cannot be applied to the description of protein–ligand interactions since each suffers from one or more of the following limitations. First of all, an infinite, planar surface lattice is utilized. The surface of a protein is neither infinite nor flat, as most proteins have a fairly compact shape. Secondly, the surface sites commonly are regarded as equivalent
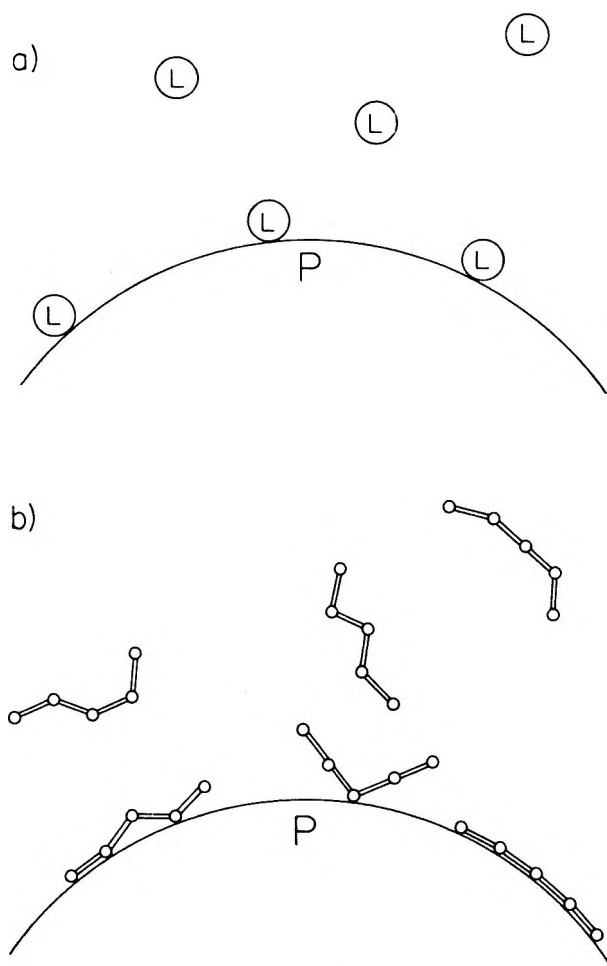

Figure 1. Schematic illustration of the binding of rigid and flexible ligands to a protein. (a) Small ions and other rigid ligands (L) bind to a protein (P) with no changes in configuration. (b) Flexible ligands may assume a large number of configurations in solution and in the bound state.

in their ability to adsorb polymer segments, and the polymer chain is composed of identical segments. In contrast, a protein surface has many different types of binding sites due to the chemical diversity of its constituent amino acids, and many flexible ligands contain segments which differ chemically (*e.g.*, the substituted alkanes). A third limitation of most lattice treatments is that they are formulated only for the limiting case of infinite or very long chains, while most ligands employed in protein binding studies are relatively short (fewer than 20 carbon atoms for the alkanes and their derivatives). Finally, most models emphasize the properties of a single polymer chain at a surface, and the binding of additional molecules, if treated at all, is assumed to occur in the absence of competition for surface sites among adjacent molecules. Experimentally, protein–ligand interactions are studied over a range of concentrations, throughout much of which several ligands are bound to each protein. Due to the finite size of the protein surface, the independence of

Figure 2. Placement of a planar, triangular lattice on a sphere[11] by introducing a small number of penta-coordinated sites at regular intervals (reproduced from Vol. XXVII; Cold Spring Harbor Symposia, 1962, by permission).
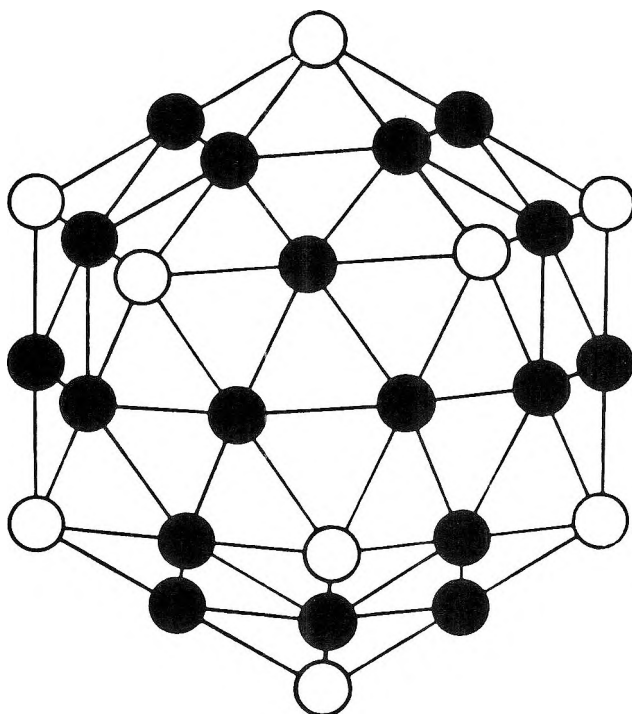

Figure 3. An icosahedron, the regular polyhedron with 20 equilateral triangular faces and 12 vertices (marked in white). Each triangular face of this icosahedron has been subdivided into four equilateral triangles ($D^2 = 4$), thereby creating additional sites on the lattice (marked in black). The sites at the 12 vertices are penta-coordinated (z_2 sites), while all other sites are hexa-coordinated (z_1 sites).

successively bound ligands cannot be assumed automatically.

A finite, planar lattice may be placed upon a closed surface by introducing a small number of irregularities in the lattice pattern. If a sphere is chosen as a model for globular proteins, a triangular (hexa-coordinated) lattice may be placed upon its surface if a small number of penta-coordinated sites are introduced at regular intervals[11] (Figure 2), so that the lattice is characterized by two coordination numbers: $z_1 = 6$ for the hexa-coordinated sites and $z_2 = 5$ for the penta-coordinated sites. This surface lattice actually represents the outward projection of the sites on an icosahedron,[12] the regular polyhedron with 20 equilateral triangular faces and 12 vertices (Figure 3). If each face is subdivided into D^2 equilateral triangles (producing a division of each edge into D segments), a lattice is formed which contains $10(D^2 - 1)$ hexa-coordinated sites and 12 penta-coordinated sites, the latter located at the vertices. To treat the case in which only a restricted area of the protein (*i.e.*, a patch) is capable of binding the ligand, a single triangular face of the icosahedron, or part of it, may be used. Such a single face can be placed upon a surface of any shape, so that the model no longer is restricted to spherical proteins when just a single patch of sites is used.[13]

In addition to their role in adjusting the triangular lattice to a spherical surface, the z_2 sites serve as reference points on the surface. Within each triangular face, each z_1 site may be classified according to its positional relationship to the z_2 sites, providing a convenient labeling system which allows each type of chemical grouping found on a protein to be represented by a different class of sites. The actual classifications used for various lattices will be described below.

The lattice used to describe the solution in the immediate vicinity of the protein surface is constructed of concentric layers of lattice points with patterns identical with the pattern of sites found on the surface, so that the classification established for the surface sites is retained in each layer. This choice of solution lattice requires a slight increase in the spacing between adjacent lattice points as additional layers are added. However, this change in spacing may be neglected for short ligands, such as those used in protein binding studies, whose desorbed segments rarely will extend more than a few layers above the surface. When a ligand segment is on a site in a given layer above the surface, it is assumed that the subsequent segment can be placed on one of the z_1 (or z_2) adjacent sites in that layer or on any of the z_1 (or z_2) sites in the layers above and below, giving coordination numbers $3z_1$ and $3z_2$ for the solution sites in the vicinity of the surface. Since it is assumed that steps to sites directly above or below a given site are not possible, the horizontal and vertical placement of the ligand segments is completely independent.

It is assumed that the lattice is invariant upon bind-

(11) D. L. D. Caspar and A. Klug, *Cold Spring Harbor Symp. Quant. Biol.*, **27**, 1 (1962).

(12) R. W. Marks, "The Dymaxion World of Buckminster Fuller," Reinhold, New York, N. Y., 1960.

(13) The model also could be applied without major modifications to a protein having several patches available for binding if the patches are nonadjacent to each other, and it is assumed that the ligands bind independently to each patch.

ing to their distance in lattice steps, r, from the nearest z_2 site. Although such a classification is perhaps the simplest one possible, rigorously it cannot provide the basis for defining the states of a Markov process. For example, consider the class 3 and class 4 sites of the lattice $D = 6$. Although both are at $r = 2$, the class 3 sites have three neighbors at $r = 3$ while the class 4 sites have only two neighbors at $r = 3$. Thus, if the sites were classified according to their values of r, w_{23} would have to be some sort of average of the values three and two. This averaging, or *lumping process*, is not allowed because it would destroy the Markovian character of the ligand random walk. Furthermore, the more refined classifications illustrated in Figure 4 have the additional advantage that they provide a larger number of classes for a given lattice size, thereby increasing the number of ways in which different kinds of sites may be arranged. In addition, no reclassification of sites is necessary when the single face analog of a given lattice is considered.

$t(0,x,0)$ may be calculated using the above enumeration procedure if each configuration is weighted with Boltzmann factors for the site-segment contacts formed. Thus, the elements $a_j^{(1)}$ and w_{ij} must be multiplied by

$$f_j^{(n)} = e^{-\epsilon_j^{(n)}/kT} \tag{19}$$

where $\epsilon_j^{(n)}$ is the energy of adsorption for the nth segment of the ligand on a class j site.[19] For the case in which all segments of the ligand are identical and only one type of lattice site is included, the same Boltzmann factor is used for all elements

$$f = e^{-\epsilon/kT} \tag{20}$$

Furthermore, in the absence of a detailed correction for self-excluded volume,[16] each w_{ij} in matrices describing segments following the second must be multiplied by a correction factor to exclude immediate reversals of the ligand

$$\frac{z_i - 1}{z_i} \tag{21}$$

where z_i represents the coordination number of a class i site.[20]

For notational clarity, $\mathbf{a}^{(1)}$ and $\mathbf{W}$ will refer to the initial configuration vector and stochastic matrix, respectively, when only an enumeration of configurations is desired (*e.g.*, eq 18). When Boltzmann factors and/or immediate reversal corrections are used, as in the following calculation of the weight $t(0,x,0)$, $\mathbf{a}_s^{(1)}$ and $\mathbf{W}_s$ will be used. Thus

$$t(0,x,0) = \mathbf{a}_s^{(1)}\mathbf{W}_s^{x-1}\mathbf{e} \tag{22}$$

General Equations for $t(S)$. Based on the principles discussed above, it is possible to write expressions for the weights $t(S)$ for states of adsorption containing desorbed loops and free ends. The total number of configurations of a loop or free end may be equated to

the product of its vertical and horizontal configurations, since the vertical and horizontal placement of desorbed segments can be treated independently.[21,22]

If $H(d)$ and $H_0(d_0)$ represent the number of vertical configurations of a loop of d segments and a free end of d_0 segments, respectively, then

$$t(S) = \mathbf{a}_d^{(1)}\mathbf{W}_d^{d_0-1}H_0(d_0) \prod_{\rho=1}^{l-1} \left(\mathbf{W}_s^{s\rho}\mathbf{W}_d^{d\rho}H(d_\rho)\right) \times$$
$$\mathbf{W}_s^{s_l}\mathbf{W}_d^{d_0'}H_0(d_0')\mathbf{e} \tag{23}$$

for the chain with free ends and

$$t(S) = \mathbf{a}_s^{(1)}\mathbf{W}_s^{-1} \prod_{\rho=1}^{l-1} \left(\mathbf{W}_s^{s\rho}\mathbf{W}_d^{d\rho}H(d_{d\rho})\right)\mathbf{W}_s^{s_l}\mathbf{e} \tag{24}$$

when $d_0 = d_0' = 0$. $\mathbf{a}_s^{(1)}$ and $\mathbf{W}_s$ are the vector and matrix described above for adsorbed segments, while $\mathbf{a}_d^{(1)}$ and $\mathbf{W}_d$ are the vector and matrix for the desorbed segments. To form the latter from the elements of $\mathbf{a}^{(1)}$ and $\mathbf{W}$, the only modifications required are new immediate reversal correction factors for the elements of matrices representing segments following the second segment of a desorbed loop or free end

$$\frac{3z_i - 1}{3z_i} \tag{25}$$

Expressions for H and H_0. The parameters $H(d)$ and $H_0(d_0)$ may be calculated in two ways. The first method is of interest primarily because it uses a Markov process to count the vertical configurations of the ligand and thus is related more closely to the methods encountered in the enumeration of the horizontal configurations of the ligand. The second method, however, gives closed expressions for $H(d)$ and $H_0(d_0)$. The vertical configurations of a loop of d segments are those in which the first and dth segments are fixed in the layer $h = 1$, while the intermediate $d - 2$ segments may be placed in any vertical layer $h \geq 1$. One possible vertical configuration of a loop of ten segments is illustrated in Figure 5. For a free end of d_0 segments, only the most proximal segment is constrained to the layer $h = 1$.

Markov Method. The vertical configurations of the ligand may be treated as a Markov process in which the ith state is defined as the placement of a ligand segment in the vertical layer $h = i$. Thus, the elements y_{ij} of

(18) When just a single face is considered, the elements of $\mathbf{a}^{(1)}$ must be altered due to the reduction in the number of lattice sites. Furthermore, the smaller coordination number of the edge sites necessitates a decrease in the matrix elements w_{ij} for values of i corresponding to sites on the edge of the patch (eq 15).

(19) The factors $f_j^{(n)}$ also could include vibrational contributions corresponding to vibrations of the bound segments. The zero of energy corresponds to an infinite separation of the segment and site in question, when both are surrounded by solvent molecules.

(20) Any rigorous correction would depend on j as well as i. Equation 21 represents an average over all j.

(21) On more typical lattices, the assumption of independence is a good one only for small extensions of a long chain.[22]

(22) P. J. Flory, "Principles of Polymer Chemistry," Cornell University Press, Ithaca, N. Y., 1953.

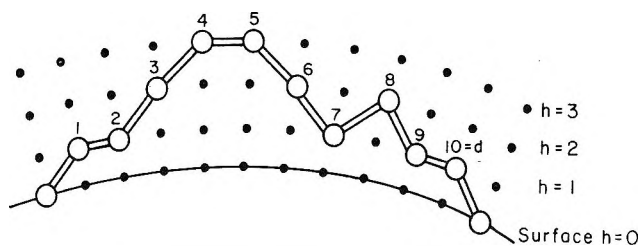Figure 5.   A possible vertical configuration of a loop of 10 (= d) segments.   The first and dth segments are constrained to the first layer of lattice points above the surface (h = 1), while the intermediate segments may be placed in any layer above the surface.

the stochastic matrix $\mathbf{Y}$ represent the number of ways of placing a segment in layer j given that the preceding segment is in layer i.   Since steps to adjacent layers or within the same layer are the only ones possible, $\mathbf{Y}$ is a tridiagonal matrix of the form

$$\mathbf{Y} = \begin{bmatrix} 1 & 1 & 0 & 0 & 0 & 0 & \cdots \\ 1 & 1 & 1 & 0 & 0 & 0 & \cdots \\ 0 & 1 & 1 & 1 & 0 & 0 & \cdots \\ 0 & 0 & 1 & 1 & 1 & 0 & \cdots \\ & & \cdots\cdots\cdots & & \\ & & \cdots\cdots\cdots & & \end{bmatrix} \quad (26)$$

The first segment of a loop or free end always is in the layer $h = i$.   Hence, the initial configuration vector $\mathbf{b}^{(1)}$ is

$$\mathbf{b}^{(1)} = (1 \quad 0 \quad 0 \quad 0 \quad \cdots) \quad (27)$$

Theoretically, the vector and matrix have infinite dimensions, although for a loop or free end of d segments a d-element vector and a matrix of order d are sufficient since h cannot exceed d.   The number of vertical configurations of a loop or free end which result in the placement of the dth segment on a site in layer i is given by the ith element of the vector

$$\mathbf{b}^{(d)} = \mathbf{b}^{(1)}\mathbf{Y}^{d-1} \quad (28)$$

Since the last segment of a loop must lie in the layer $h = 1$, the total number of vertical configurations of a loop of d segments, $H(d)$, may be equated to $b_1{}^{(d)}$

$$H(d) = b_1{}^{(d)} = \mathbf{b}^{(d)}\mathbf{e}' = \mathbf{b}^{(1)}\mathbf{Y}^{d-1}\mathbf{e}' \quad (29)$$

where $\mathbf{e}'$ is a column vector whose first element is unity and all other elements are zero.   On the other hand, the final segment of a free end may lie in any vertical layer above the surface.   Hence, the total number of vertical configurations of a free end of d_0 segments, $H_0(d_0)$, may be equated to the sum of all elements of $\mathbf{b}^{(d_0)}$

$$H_0(d_0) = \mathbf{b}^{(d_0)}\mathbf{e} = \mathbf{b}^{(1)}\mathbf{Y}^{d_0-1}\mathbf{e} \quad (30)$$

Combinatorial Method.   Closed expressions for $H(d)$ and $H_0(d_0)$ may be obtained by modifying some combinatorial theorems for one-dimensional random walks[23] in which the outcome of each step is in one of *two* possi-

ble directions (from level h to level $h + 1$ or $h - 1$).   In the present model, *three* possible outcomes exist for each step, as discussed above.   Therefore, any vertical configuration of a loop can be visualized as a one-dimensional random walk interrupted by steps which retain a constant value of h.   Thus, for the loop illustrated in Figure 5, steps 2 and 3 (the placement of segments 3 and 4) and 5 through 8 (the placement of segments 6 through 9) perform a one-dimensional walk, while steps 1, 4, and 9 remain at positions of constant h.   For a loop of d segments ($d - 1$ steps), any number of steps $2j$ may be involved in the one-dimensional walk, subject to the restriction

$$0 \le j \le [(d - 1)/2] \quad (31)$$

which ensures that segment d of the loop can return to the layer $h = 1$.   In addition, all segments of the loop must remain in layers above the surface.   The total number of configurations for such a one-dimensional walk is[23]

$$\frac{1}{j + 1}\frac{(2j)!}{j!j!} \quad (32)$$

Because the remaining $(d - 1 - 2j)$ steps at constant h can be placed anywhere along the loop, the total number of vertical configurations of the entire loop for a given j is

$$\frac{(d - 1)!}{(2j)!(d - 1 - 2j)!}\frac{1}{j + 1}\frac{(2j)!}{j!j!} =$$
$$\frac{1}{j + 1}\frac{(d - 1)!}{j!j!(d - 1 - 2j)!} \quad (33)$$

Hence

$$H(d) = \sum_{j=0}^{[(d-1)/2]}\frac{1}{j + 1}\frac{(d - 1)!}{j!j!(d - 1 - 2j)!} \quad (34)$$

Similarly, a free end of d_0 segments ($d_0 - 1$ steps) may be visualized as an interrupted one-dimensional walk.   Any number of steps m between 0 and $d_0 - 1$ may be involved in the one-dimensional walk as long as all segments remain above the surface.   The number of configurations for such a one-dimensional walk of m steps is[23]

$$\frac{m!}{\left[\dfrac{m}{2}\right]!\left[\dfrac{m + 1}{2}\right]!} \quad (35)$$

These m steps may be distributed in any manner among the remaining $(d_0 - 1 - m)$ constant h steps of the free end.   Hence, for a fixed m, the total number of vertical configurations for the free end is

(23) W. Feller, "An Introduction to Probability Theory and Its Applications," Vol. I, Wiley, New York, N. Y., 1957.

$$\frac{(d_0 - 1)!}{(d_0 - 1 - m)! \, m!} \frac{m!}{\left[\dfrac{m}{2}\right]! \left[\dfrac{m+1}{2}\right]!} =$$

$$\frac{(d_0 - 1)!}{(d_0 - 1 - m)! \left[\dfrac{m}{2}\right]! \left[\dfrac{m+1}{2}\right]!} \quad (36)$$

Therefore

$$H_0(d_0) = \sum_{m=0}^{d_0-1} \frac{(d_0 - 1)!}{(d_0 - 1 - m)! \left[\dfrac{m}{2}\right]! \left[\dfrac{m+1}{2}\right]!} \quad (37)$$

Evaluation of $q_x(1,n_0,T)$. Equations 23 and 24 may be combined into a single, more general one with the aid of the Kronecker delta

$$t(S) =$$
$$\left(\mathbf{a}_s^{(1)} \mathbf{W}_s^{-1} \delta_{d_0 0} + (1 - \delta_{d_0 0}) \mathbf{a}_d^{(1)} \mathbf{W}_d^{d_0 - 1} H_0(d_0)\right) \times$$
$$\prod_{\rho=1}^{l-1} \left(\mathbf{W}_s^{s_\rho} \mathbf{W}_d^{d_\rho} H(d_\rho)\right) \mathbf{W}_s^{s_l} \left(\delta_{d_0' 0} + \right.$$
$$\left. (1 - \delta_{d_0' 0}) \mathbf{W}_d^{d_0'} H_0(d_0')\right) \mathbf{e} \quad (38)$$

so that eq 12 becomes

$$q_x(1,n_0,T) =$$
$$\sum_{l=1}^{[(x+1)/2]} \sum_{\{S\}} \mathbf{u}_0(d_0) \prod_{\rho=1}^{l-1} \left(\mathbf{V}(s_\rho) \mathbf{U}(d_\rho)\right) \mathbf{V}(s_l) \mathbf{u}_0'(d_0') \quad (39)$$

where

$$\mathbf{u}_0(d_0) = \left(\mathbf{a}_s^{(1)} \mathbf{W}_s^{-1} \delta_{d_0 0} + \right.$$
$$\left. (1 - \delta_{d_0 0}) \mathbf{a}_d^{(1)} \mathbf{W}_d^{d_0 - 1} H_0(d_0)\right) \quad (40)$$

$$\mathbf{V}(s_\rho) = \mathbf{W}_s^{s_\rho} \quad (41)$$

$$\mathbf{U}(d_\rho) = \mathbf{W}_d^{d_\rho} H(d_\rho) \quad (42)$$

$$\mathbf{u}_0'(d_0') = \left(\delta_{d_0' 0} + (1 - \delta_{d_0' 0}) \mathbf{W}_d^{d_0'} H_0(d_0')\right) \mathbf{e} \quad (43)$$

Equation 39 cannot be written in closed form. However, an exact evaluation is possible for relatively small values of x, such as those of the ligands commonly encountered in protein binding studies. As a first step in this evaluation, it is necessary to form the generating function of $q_x(1,n_0,T)$

$$\Gamma(\zeta) = \sum_{x=1}^{\infty} q_x(1,n_0,T) \zeta^x =$$
$$\sum_{x=1}^{\infty} \zeta^x \sum_{l=1}^{[(x+1)/2]} \sum_{\{S\}} \mathbf{u}_0(d_0) \prod_{\rho=1}^{l-1} \left(\mathbf{V}(s_\rho) \mathbf{U}(d_\rho)\right) \mathbf{V}(s_l) \mathbf{u}_0'(d_0') \quad (44)$$

Following the procedure of Lifson,[24] the first two summations are rearranged and the x factors of ζ^x distributed among the terms of $q_x(1,n_0,T)$ to give

$$\Gamma(\zeta) = \sum_{l=1}^{\infty} \sum_{x=2l-1}^{\infty} \sum_{\{S\}} \mathbf{u}_0(d_0) \zeta^{d_0} \prod_{\rho=1}^{l-1} \left(\mathbf{V}(s_\rho) \zeta^{s_\rho} \mathbf{U}(d_\rho) \zeta^{d_\rho}\right) \times$$
$$\mathbf{V}(s_l) \zeta^{s_l} \mathbf{u}_0'(d_0') \zeta^{d_0'} \quad (45)$$

When summing at fixed l over all possible values of $x \geq (2l-1)$, the restriction of eq 11 on $\{S\}$ no longer holds. Thus

$$\Gamma(\zeta) = \sum_{l=1}^{\infty} \sum_{d_0=0}^{\infty} \mathbf{u}_0(d_0) \zeta^{d_0} \prod_{\rho=1}^{l-1} \left(\sum_{s_\rho=1}^{\infty} \mathbf{V}(s_\rho) \zeta^{s_\rho} \times \right.$$
$$\left. \sum_{d_\rho=1}^{\infty} \mathbf{U}(d_\rho) \zeta^{d_\rho}\right) \sum_{s_l=1}^{\infty} \mathbf{V}(s_l) \zeta^{s_l} \sum_{d_0'=0}^{\infty} \mathbf{u}_0'(d_0') \zeta^{d_0'} \quad (46)$$

$q_x(1,n_0,T)$ is the coefficient of ζ^x in this power series (*cf.* eq 44). Using the following convolution formula for the product of two power series

$$\sum_{i=1}^{\infty} a_i \zeta^i \sum_{i=1}^{\infty} b_i \zeta^i = \sum_{i=1}^{\infty} \left(\sum_{j=1}^{i} a_j b_{i+1-j}\right) \zeta^{i+1} \quad (47)$$

it is possible to compute this coefficient for a given x from known functions $\mathbf{u}_0$, $\mathbf{V}$, $\mathbf{U}$, and $\mathbf{u}_0'$.

Average Properties. Any thermodynamic average derivable from $q_x(1,n_0,T)$ may be evaluated in a similar fashion. The averages of interest are those associated with the configuration of the bound ligand, which will be referred to as *configurational parameters*. For example, the average number of ligand segments adsorbed to the surface may be equated to the coefficient of ζ^x in the following power series, divided by $q_x(1,n_0,T)$

$$\sum_{l=1}^{\infty} \sum_{d_0=0}^{\infty} \mathbf{u}_0(d_0) \zeta^{d_0} \left[\sum_{s_1=1}^{\infty} s_1 \mathbf{V}(s_1) \zeta^{s_1} \sum_{d_1=1}^{\infty} \mathbf{U}(d_1) \zeta^{d_1} \times \right.$$
$$\prod_{\rho=2}^{l-1} \left(\sum_{s_\rho=1}^{\infty} \mathbf{V}(s_\rho) \zeta^{s_\rho} \sum_{d_\rho=1}^{\infty} \mathbf{U}(d_\rho) \zeta^{d_\rho}\right) \sum_{s_l=1}^{\infty} \mathbf{V}(s_l) \zeta^{s_l} +$$
$$\sum_{s_1=1}^{\infty} \mathbf{V}(s_1) \zeta^{s_1} \sum_{d_1=1}^{\infty} \mathbf{U}(d_1) \zeta^{d_1} \sum_{s_2=1}^{\infty} s_2 \mathbf{V}(s_2) \zeta^{s_2} \sum_{d_2=1}^{\infty} \mathbf{U}(d_2) \zeta^{d_2} \times$$
$$\prod_{\rho=3}^{l-1} \left(\sum_{s_\rho=1}^{\infty} \mathbf{V}(s_\rho) \zeta^{s_\rho} \sum_{d_\rho=1}^{\infty} \mathbf{U}(d_\rho) \zeta^{d_\rho}\right) \times$$
$$\sum_{s_l=1}^{\infty} \mathbf{V}(s_l) \zeta^{s_l} + \ldots + \prod_{\rho=1}^{l-1} \left(\sum_{s_\rho=1}^{\infty} \mathbf{V}(s_\rho) \zeta^{s_\rho} \times \right.$$
$$\left. \sum_{d_\rho=1}^{\infty} \mathbf{U}(d_\rho) \zeta^{d_\rho}\right) \sum_{s_l=1}^{\infty} s_l \mathbf{V}(s_l) \zeta^{s_l}\right] \sum_{d_0'=0}^{\infty} \mathbf{u}_0'(d_0') \zeta^{d_0'} \quad (48)$$

The average *number* of segments adsorbed commonly is divided by x to give the average *fraction* of segments adsorbed, $\bar{\theta}$.

The coefficient of ζ^x in the power series

$$\sum_{l=1}^{\infty} l \sum_{d_0=0}^{\infty} \mathbf{u}_0(d_0) \zeta^{d_0} \prod_{\rho=1}^{l-1} \left(\sum_{s_\rho=1}^{\infty} \mathbf{V}(s_\rho) \zeta^{s_\rho} \sum_{d_\rho=1}^{\infty} \mathbf{U}(d_\rho) \zeta^{d_\rho}\right) \times$$
$$\sum_{s_l=1}^{\infty} \mathbf{V}(s_l) \zeta^{s_l} \sum_{d_0'=0}^{\infty} \mathbf{u}_0'(d_0') \zeta^{d_0'} \quad (49)$$

when divided by $q_x(1,n_0,T)$, gives the average number of adsorbed stretches, $\bar{l}$. The number-average lengths of the desorbed ends, $\bar{d}_0$ and $\bar{d}_0'$, are calculated from the appropriate coefficients in the following two power series, respectively[25]

(24) S. Lifson, *J. Chem. Phys.*, **40**, 3705 (1964).

$$\sum_{l=1}^{\infty} \sum_{d_0=0}^{\infty} d_0 \mathbf{u}_0(d_0) \zeta^{d_0} \prod_{\rho=1}^{l-1} \left(\sum_{s_\rho=1}^{\infty} \mathbf{V}(s_\rho) \zeta^{s_\rho} \sum_{d_\rho=1}^{\infty} \mathbf{U}(d_\rho) \zeta^{d_\rho} \right) \times$$

$$\sum_{s_l=1}^{\infty} \mathbf{V}(s_l) \zeta^{s_l} \sum_{d_0'=0}^{\infty} \mathbf{u}_0'(d_0') \zeta^{d_0'} \quad (50)$$

$$\sum_{l=1}^{\infty} \sum_{d_0=0}^{\infty} \mathbf{u}_0(d_0) \zeta^{d_0} \prod_{\rho=1}^{l-1} \left(\sum_{s_\rho=1}^{\infty} \mathbf{V}(s_\rho) \zeta^{s_\rho} \sum_{d_\rho=1}^{\infty} \mathbf{U}(d_\rho) \zeta^{d_\rho} \right) \times$$

$$\sum_{s_l=1}^{\infty} \mathbf{V}(s_l) \zeta^{s_l} \sum_{d_0'=0}^{\infty} d_0' \mathbf{u}_0'(d_0') \zeta^{d_0'} \quad (51)$$

Other configurational parameters of the ligand may be calculated directly from the above set. Thus, the number-average length of an adsorbed stretch, $\bar{s}$, and the number-average length of a desorbed loop, $\bar{d}$, are given by

$$\bar{s} = \frac{x\bar{\theta}}{\bar{l}} \quad (52)$$

$$\bar{d} = \frac{x - x\bar{\theta} - \bar{d}_0 - \bar{d}_0'}{\bar{l} - 1} \quad (53)$$

V. The Binding of Additional Ligands

The expressions for $q_x(2,n_0,T)$ through $q_x(M,n_0,T)$ are identical in form with eq 12. However, since fewer lattice sites are available for binding as additional ligands are placed on the surface, the values of the elements of the vector and the matrix describing the adsorbed segments, $\mathbf{a}_s^{(1)}$ and $\mathbf{W}_s$, must be decreased. On the lattice sites above the surface, a smaller fraction of configurations is excluded by previous ligands as a result of the many layers of lattice points available to the segments of loops and free ends. Therefore, no reductions in the elements of $\mathbf{a}_d^{(1)}$ and $\mathbf{W}_d$ are introduced. Thus, for $N > 1$

$$q_x(N,n_0,T) = \sum_{l=1}^{[(x+1)/2]} \sum_{\{S\}} t_{N-1}(S) \quad (54)$$

with

$$t_{N-1}(S) = \left({}_{N-1}\mathbf{a}_s^{(1)} {}_{N-1}\mathbf{W}_s^{-1} \delta_{d_0 0} + \right.$$
$$(1 - \delta_{d_0 0}) \mathbf{a}_d^{(1)} \mathbf{W}_d^{d_0-1} H_0(d_0) \right) \times$$
$$\prod_{\rho=1}^{l-1} \left({}_{N-1}\mathbf{W}_s^{s_\rho} \mathbf{W}_d^{d_\rho} H(d_\rho) \right) {}_{N-1}\mathbf{W}_s^{s_l} \times$$
$$\left(\delta_{d_0' 0} + (1 - \delta_{d_0' 0}) \mathbf{W}_d^{d_0'} H_0(d_0') \right) \mathbf{e} \quad (55)$$

The subscript $N - 1$ signifies that corrections have been made for the $N - 1$ ligands previously bound to the surface.

The correction factors for the elements of $\mathbf{a}_s^{(1)}$ and $\mathbf{W}_s$ may be calculated once the number of occupied sites of each class has been determined. If $\bar{n}_i(N - 1)$ is the average number of occupied sites of class i when $N - 1$ ligands have been bound (eq 62), then

$$_{N-1}a_i^{(1)} = a_i^{(1)} - \bar{n}_i(N - 1) \quad (56)$$

The corrections applied to the elements of $\mathbf{W}_s$ must

account for the fact that each ligand already bound to the surface occupies contiguous lattice sites.[22] Therefore, if any of the z_j sites adjacent to a class j site previously has been established as vacant, the probability that the class j site is vacant is somewhat greater than the average fraction of vacant j sites, $\bar{\xi}_j(N - 1)$, which may be equated to the ratio of the average number of vacant j sites to the total number of j sites

$$\bar{\xi}_j(N - 1) = \frac{a_j^{(1)} - \bar{n}_j(N - 1)}{a_j^{(1)}} \quad (57)$$

The desired correction factor is the probability $\xi_j(N - 1)$ that a class j site is vacant when the vacancy of an adjacent site already has been established. Thus, $\xi_j(N - 1)$ is the ratio of the number of vacant j sites to the total number of j sites which are compatible with the previously confirmed vacancy of a given adjacent site. If ϕ_j is the fraction of the $\bar{n}_j(N - 1)$ occupied j sites which have a neighboring ligand segment on an adjacent site, then[26]

$$\xi_j(N - 1) = \frac{a_j^{(1)} - \bar{n}_j(N - 1)}{a_j^{(1)} - \phi_j \bar{n}_j(N - 1)} \quad (58)$$

ϕ_j may be equated to the ratio of the average number of neighboring segments, per segment, to the coordination number of the site

$$\phi_j = \frac{\dfrac{2(x - 2) + 2}{x}}{z_j} = \frac{2(x - 1)}{x z_j} \quad (59)$$

Hence

$$\xi_j(N - 1) = \frac{a_j^{(1)} - \bar{n}_j(N - 1)}{a_j^{(1)} - \dfrac{2(x - 1)}{x z_j} \bar{n}_j(N - 1)} \quad (60)$$

and

$$_{N-1}w_{ij} = w_{ij} \xi_j(N - 1) \quad (61)$$

Calculation of $\bar{n}_j(N - 1)$. If, for a given j, the jth element of $_{N-2}\mathbf{a}_s^{(1)}$ and the elements of the jth column of $_{N-2}\mathbf{W}_s$ are multiplied by the dummy variables $\alpha_j = 1$ and $\omega_j = 1$, respectively, then $\bar{n}_j(N - 1)$ may be calculated as follows[27,28]

$$\bar{n}_j(N - 1) = \bar{n}_j(N - 2) +$$
$$\frac{\partial \ln q_x(N - 1, n_0, T)}{\partial \omega_j} + \frac{\partial \ln q_x(N - 1, n_0, T)}{\partial \alpha_j} =$$

(25) For ligands composed of identical segments or symmetrical about their midpoints (*e.g.*, α,ω-dicarboxylic acids), the Markov process is reversible,[23] so that $\bar{d}_0 = \bar{d}_0'$.

(26) E. A. Guggenheim, *Proc. Roy. Soc., Ser. A*, **183**, 203 (1944).

(27) The use of the augmented matrix for differentiation of a matrix product is a technique adopted from Flory.[28]

(28) P. J. Flory and W. G. Miller, *J. Mol. Biol.*, **15**, 284 (1966).

$$\bar{n}_j(N-2) + \frac{1}{q_x(N-1,n_0,T)} \sum_{l=1}^{[(x+1)/2]} \sum_{\{S\}} \times$$

$$\left(\delta_{d_0 0 N-2} \mathbf{a}_s^{(1)}[\mathbf{E}_C \mathbf{O}_C]_{N-2}\hat{\mathbf{W}}_s^{-1} + (1 - \delta_{d_0 0})\mathbf{a}_d^{(1)} \times \right.$$

$$[\mathbf{E}_C \mathbf{O}_C]\hat{\mathbf{W}}_d^{d_0-1}H_0(d_0)\Big) \prod_{\rho=1}^{l-1} \left(_{N-2}\hat{\mathbf{W}}_s^{s\rho}\hat{\mathbf{W}}_d^{d\rho}H(d_\rho)\right) \times$$

$$_{N-2}\hat{\mathbf{W}}_s^{sl}\Big(\delta_{d_0'0} + (1 - \delta_{d_0'0})\hat{\mathbf{W}}_d^{d_0'}H_0(d_0')\Big) \times$$

$$\begin{bmatrix}\mathbf{O}_C \\ \mathbf{E}_C\end{bmatrix}\mathbf{e} + \frac{1}{q_x(N-1,n_0,T)} \sum_{l=1}^{[(x+1)/2]} \sum_{\{S\}} {}_{N-2}\hat{\mathbf{a}}_s^{(1)} {}_{N-2}\mathbf{W}_s^{-1} \times$$

$$\prod_{\rho=1}^{l-1} \left(_{N-2}\mathbf{W}_s^{s\rho}\mathbf{W}_d^{d\rho}H(d_\rho)\right)_{N-2}\mathbf{W}_s^{sl} \times$$

$$\Big(\delta_{d_0'0} + (1 - \delta_{d_0'0})\mathbf{W}_d^{d_0'}H_0(d_0')\Big)\mathbf{e} \quad (62)$$

where $\mathbf{E}_C$ and $\mathbf{O}_C$ are, respectively, the identity and null matrices of order C and

$$_{N-2}\hat{\mathbf{W}}_s = \begin{bmatrix} _{N-2}\mathbf{W}_s & _{N-2}\mathbf{W}_s' \\ \mathbf{O}_C & _{N-2}\mathbf{W}_s \end{bmatrix} \quad (63)$$

$$\hat{\mathbf{W}}_d = \begin{bmatrix} \mathbf{W}_d & \mathbf{O}_C \\ \mathbf{O}_C & \mathbf{W}_d \end{bmatrix} \quad (64)$$

$$_{N-2}\hat{\mathbf{a}}_s^{(1)} = \frac{\partial(_{N-2}\mathbf{a}_s^{(1)})}{\partial \alpha_j} \quad (65)$$

with

$$_{N-2}\mathbf{W}_s' = \frac{\partial(_{N-2}\mathbf{W}_s)}{\partial \omega_j} \quad (66)$$

Equation 62 may be evaluated by forming the appropriate generating function and using a procedure analogous to that described above for the evaluation of $q_x(1,n_0,T)$.

Appendix A

The Unbound Ligand. To calculate the equilibrium properties of protein–ligand systems (eq 7 and 8), a value of $q_{x,u}(V)$, the partition function for the unbound ligand, must be specified. The latter may be equated to the number of configurations of a ligand free in solution. In the calculations described in the subsequent papers of this series,[6,7] an approximate enumeration was obtained by counting ligand configurations on a lattice constructed by stacking planar, triangular lattices, so that each site in the bulk solution is characterized by coordination number $3z_1$. This lattice was selected because of its relationship to the lattice on which the configurations of the desorbed loops and free ends of bound ligands were counted. Hence

$$q_{x,u}(V) = \frac{V}{v_s} 3z_1(3z_1 - 1)^{x-2} \quad (67)$$

where V is the volume of the solution and v_s is the volume of a ligand segment. Although this choice of enumeration procedure is somewhat arbitrary, the use of a different counting method simply would require

the multiplication of all equilibrium constants by a constant factor and the shift of all binding isotherms along the log c axis by a constant increment. Thus, the general conclusions drawn from the present model are not affected by the value of $q_{x,u}(V)$.

The chemical potential of the ligand, μ, is

$$\mu = \mu_0 + kT \ln c \quad (68)$$

where c is the concentration of free ligand and μ_0 is the standard chemical potential. The latter may be equated to the chemical potential of a solution in which $c = 1$. Neglecting ligand–ligand interactions, the partition function for such a solution, $Q^0_{x,u}(N_u,V)$, is

$$Q^0_{x,u}(N_u,V) = \frac{(q_{x,u}(V))^{N_u}}{N_u!} \quad (69)$$

where N_u is the number of unbound ligands in a volume V of solution when $c = 1$. Thus

$$\mu_0 = -kT\frac{\partial \ln Q^0_{x,u}(N_u,V)}{\partial N_u} = -kT \ln \frac{q_{x,u}(V)}{N_u} \quad (70)$$

Appendix B

A Model for Rigid Binding. To better evaluate the importance of the flexibility of the bound ligands in quantitative discussions of protein–ligand interactions, a model in which segmented ligands are flexible in solution but bind in a single, rigid configuration also has been constructed. This model for rigid binding is essentially a statistical-mechanical formulation of the theory of multiple equilibria[8] and is entirely equivalent to the latter. However, a statistical-mechanical treatment allows a more direct comparison of the results of this commonly used theory with those of the present model.

The basic statistical-mechanical formulas are identical with those of the model for flexible binding (eq 3 to 8).[29] However, the expressions for the canonical partition functions for the individual ligands (*cf.* eq 12) may be simplified considerably, since the internal degrees of freedom of the bound ligands are neglected and the ligands bind with a unique orientation to nonoverlapping regions of the protein surface. For the case in which the M ligands are assumed to bind as one class (eq 1), the canonical partition function for the binding of the Nth ligand to the protein is

$$q_x(N,n_0,T) = (M - N + 1)e^{-\varepsilon/kT} \quad (71)$$

where $(M - N + 1)$ is a combinatorial factor giving the number of ways of placing the Nth ligand on the protein. ε is the energy of interaction when the *entire ligand* binds to the surface and therefore is a *sum* of site-segment interaction energies for all segments.

If the bound ligands belong to more than one class (eq 2), the grand canonical partition function for the system (*cf.* eq 3) is written as the product of the grand canonical partition functions for the individual classes. The latter are formulated in the manner just described for single-class binding.

A Model for the Binding of Flexible Ligands to the Surfaces of

Proteins and Other Macromolecules.   II.   The Properties

of Ligand–Macromolecule Systems

by Nora Laiken and George Némethy[1]

The Rockefeller University, New York, New York   10021   (Received July 7, 1970)

A statistical-mechanical model for the binding of flexible ligands to proteins, developed in the previous paper of this series, is applied to various ligand–surface systems.   Parameters which characterize the average configuration of each bound ligand (average fraction of segments adsorbed, average number and length of adsorbed stretches, average length of desorbed loops, and average length of the free chain ends) and binding isotherms are calculated.   The dependence of these quantities on parameters such as the ligand–surface interaction energies, ligand chain length, and number and arrangement of lattice sites is discussed.   The interactions between ligands with nonidentical segments (*e.g.*, substituted alkanes) and surfaces containing chemically different sites (*e.g.*, sites with ionic, polar, and nonpolar character), termed "heterogeneous systems," also are studied.   Configurations of the bound ligands with a larger fraction of desorbed segments are preferred as successive ligands are bound, due to the reduced availability of vacant binding sites on the surface.   This variation in the average configuration of the bound ligands produces a change in the intrinsic affinity of the macromolecule for the ligand with increasing saturation, even when all of the binding sites are chemically identical.   For this reason, the binding isotherms calculated with this model are broader than those predicted by the theory of multiple equilibria which commonly is used to analyze protein–ligand interactions.   According to the latter theory, all sites of a given type have the same intrinsic affinity for all ligands, since the ligands are assumed to bind in an identical, rigidly defined configuration.   The model presented here predicts an increase in the strength of binding with increasing chain length, as observed experimentally for several substituted alkanes, while the theory of multiple equilibria predicts the opposite chain length dependence.   In heterogeneous systems, the configuration of the bound ligands may change sharply with ligand concentration, depending on the relative extent of saturation of various types of sites.   In this case, the resulting isotherms are biphasic.   The appearance of an intermediate plateau in the isotherm is determined by the nature and number of various sites.

I.   Introduction

Protein–ligand interactions commonly have been analyzed using the standard formulas which govern multiple binding equilibria.[2]   In the previous paper of this series,[3] it was pointed out that the theory of multiple equilibria, because of its neglect of the internal degrees of freedom of the bound ligands, is not sufficiently general to treat the interactions between proteins and flexible, chain-like molecules.   The latter can bind in a large number of configurations, including many in which not all segments of the ligand are in contact with the protein.   Therefore, a statistical-mechanical model for the binding of flexible ligands to protein surfaces was developed.[3]   This paper presents an analysis of the

properties predicted by this model for various ligand–surface systems.   A comparison of the calculated results with actual experimental observations is presented elsewhere.[4]

The model allows the calculations of two different types of thermodynamic averages.   First of all, from the canonical partition functions for the bound ligands,

parameters which characterize the average configuration of each bound molecule (*e.g.*, average fraction of segments adsorbed, average number and length of loops, etc.) may be obtained (eq I-48 to I-53). Secondly, the grand canonical partition function for the system, Ξ (eq I-3), may be used to study the equilibrium between bound and free ligands. In particular, $\bar{N}$, the average number of ligands bound per protein molecule, may be calculated as a function of c, the concentration of free ligand (corresponding to the experimental binding isotherm), using the relation

$$\bar{N} = kT \frac{\partial \ln \Xi}{\partial \mu} \qquad (1)$$

In this paper, the dependence of these quantities on the specific characteristics of the ligand and the protein surface is described. The systems discussed may be divided into two broad categories: *homogeneous systems*, in which ligands with identical segments bind to surfaces with only one type of site, and *heterogeneous systems*, in which ligands with nonidentical segments and surfaces composed of many types of sites are considered. Each site, as defined in this work,[3] represents a point of attachment for a single segment of the ligand in question. The binding sites may cover the entire protein surface or just a small part of it, referred to here as a *patch*.

II. Configurational Parameters for Homogeneous Systems

The average configuration of the bound ligands is not determined solely by ϵ, the energy of the site–segment interaction, or x, the number of segments in the ligand, since the configurational parameters also vary with N, the number of ligands bound to the surface. This is illustrated in Figures 1–5, in which the configurational parameters for the ligands $x = 8$ and $x = 4$ binding to a lattice with 162 sites, covering a complete surface, are plotted as a function of xN, the number of segments belonging to bound chains.[5] As N increases, the reduction in the number of vacant surface sites results in larger contributions to the partition function from configurations with fewer segments adsorbed to the surface. Thus, the average fraction of segments adsorbed, $\bar{\theta}$, and the average length of an adsorbed stretch, $\bar{s}$, decrease as additional ligands are bound. Comparing these variations at different values of ϵ, the smallest decrease in $\bar{\theta}$ is observed for $\epsilon = -4kT$, since the energy of the site–segment interaction dominates the free-energy change per segment upon binding, overriding the entropy gain due to the formation of loops and free ends. The resulting reduction in the number of vacant surface sites is so large that a very sharp drop in $\bar{\theta}$ occurs as xN approaches n_0, the number of sites on the surface. The drop is somewhat larger for the ligand $x = 4$ than for $x = 8$, since a larger relative change in $\bar{\theta}$ results from the desorption of a single segment for the shorter ligand.
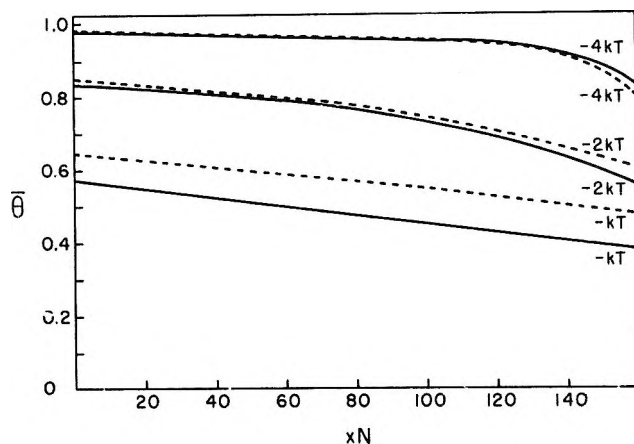
Figure 1. The variation in $\bar{\theta}$, the average fraction of ligand segments adsorbed, with xN, the number of segments belonging to bound chains, for the ligands $x = 8$ (———) and $x = 4$ (– – –). All curves were obtained with a lattice of 162 sites, covering a complete surface. The value of ϵ is indicated by each curve.
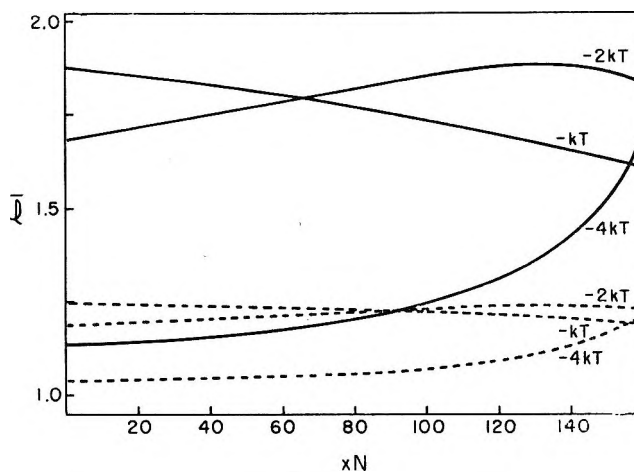

Figure 2. The variation in $\bar{l}$, the average number of adsorbed stretches, with xN, the number of segments belonging to bound chains, for the ligands $x = 8$ (———) and $x = 4$ (– – –). All curves were obtained with a lattice of 162 sites, covering a complete surface. The value of ϵ is indicated by each curve.

As $|\epsilon|$ decreases, $\bar{\theta}$ drops with increasing xN at a more constant rate, since energy and entropy effects are balanced more closely. At these lower values of $|\epsilon|$, the drop is somewhat smaller for the shorter ligand, since it is easier to find smaller clusters of contiguous vacant sites. $\bar{\theta}$ is larger for $x = 4$ than for $x = 8$ at the smaller values of $|\epsilon|$ since the shorter ligand can gain less entropy by forming loops (there are fewer ways of placing a loop along a shorter ligand).

The additional desorbed segments which appear as xN increases can be included in either loops or free ends. For $x = 8$, the average length of a single de-

(5) It should be emphasized that the configurational parameters discussed here characterize the Nth ligand being bound and are not averages of ligands 1 through N.
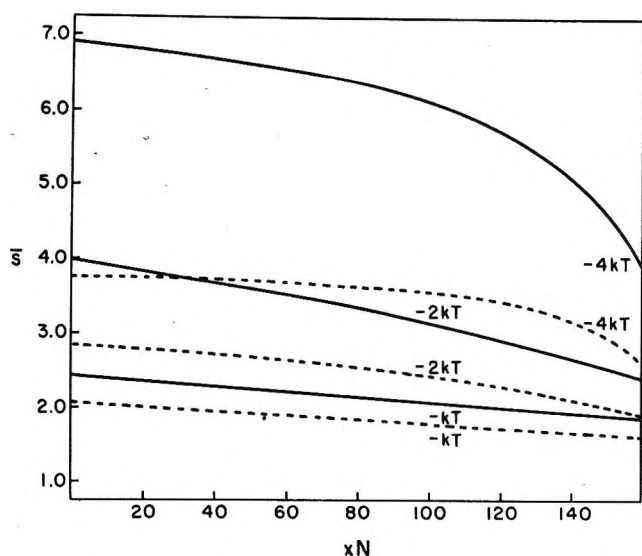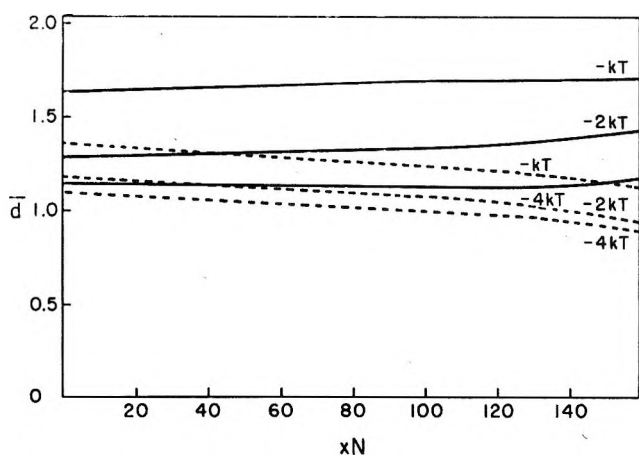
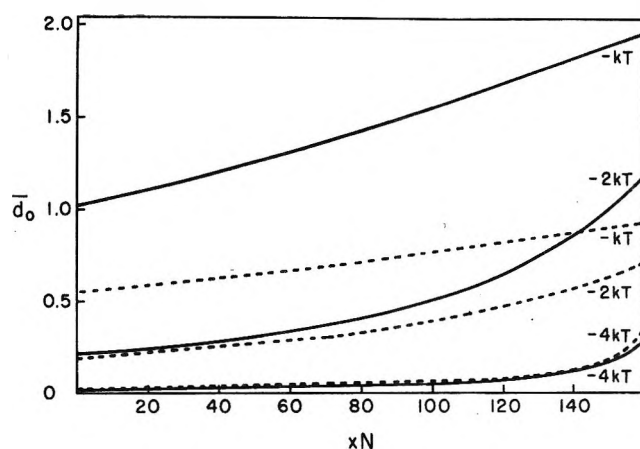Figure 3. The variation in $\bar{s}$, the average length of an adsorbed stretch, with xN, the number of segments belonging to bound chains, for the ligands $x = 8$ (———) and $x = 4$ (– – –). All curves were obtained with a lattice of 162 sites, covering a complete surface. The value of ϵ is indicated by each curve.

Figure 4. The variation in $\bar{d}$, the average length of a desorbed loop, with xN, the number of segments belonging to bound chains, for the ligands $x = 8$ (———) and $x = 4$ (– – –). All curves were obtained with a lattice of 162 sites, covering a complete surface. The value of ϵ is indicated by each curve.

sorbed end, $\bar{d}_0$, increases markedly with xN, while the average length of a loop, $\bar{d}$, remains almost constant (Figures 4 and 5). However, at $\epsilon = -4kT$, the total number of segments in loops does increase, since the average number of loops, $\bar{l} - 1$, increases (Figure 2). Increases in the number of loops rather than in $\bar{d}$ are favored because a larger number of configurations is gained by increases in l than in d. At $\epsilon = -kT$, configurations with $d_0 > 1$ predominate. Therefore, the additional desorbed segments appear almost exclusively in free ends, since desorbed segments in free ends exceeding one segment in length have a larger number of configurations than loops of an equivalent length. In addition, some of the ends lengthen at the expense of

Figure 5. The variation in $\bar{d}_0$, the average length of a single desorbed end, with xN, the number of segments belonging to bound chains, for the ligands $x = 8$ (———) and $x = 4$ (– – –). All curves were obtained with a lattice of 162 sites, covering a complete surface. The value of ϵ is indicated by each curve.

loops, causing $\bar{l}$ to decrease as xN approaches n_0. The graph of $\bar{l}$ vs. xN for $\epsilon = -2kT$ exhibits a maximum, since $\bar{l}$ increases until $\bar{d}_0$ becomes sufficiently large to favor free end formation instead of additional loops.

For $x = 4$, where the maximum number of loops is one and the number of configurations with a single loop is limited by the small value of x, the increase in desorbed segments with xN occurs almost totally in the free ends. The increases in $\bar{l}$ at $\epsilon = -4kT$ and $\epsilon = -2kT$ (low xN) are less marked than those for $x = 8$, since such rises are possible only with a decrease in $\bar{d}$ due to the short length of the chain. At $\epsilon = -kT$ and $\epsilon = -2kT$ (high xN), decreases in $\bar{l}$ also are observed for $x = 4$, but are not as sharp as those for $x = 8$ since the $\bar{d}_0$ values are smaller.

The effect of energy on the configurational parameters for the ligand $x = 8$ is summarized in Table I, which shows these parameters for $N = 1$.

Table I: Dependence of Configurational Parameters on ϵ^a

ϵ	$\bar{\theta}$	$\bar{l}$	$\bar{s}$	$\bar{d}$	$\bar{d}_0$
$-kT$	0.561	1.87	2.41	1.64	1.05
$-2kT$	0.831	1.70	3.91	1.28	0.23
$-4kT$	0.975	1.14	6.86	1.15	0.02

^{a} The values listed are for the ligand $x = 8$ binding to a lattice of 162 sites when $N = 1$.

Binding to a Patch of Sites. Figure 6 illustrates the configurational parameters for the ligand $x = 6$ binding to a patch and a complete surface with an identical number of sites ($n_0 = 42$) for $\epsilon = -2kT$. At low xN, the average properties are nearly indistinguishable for the two cases. However, the presence of boundaries on the patch (Figure 7) becomes evident as additional
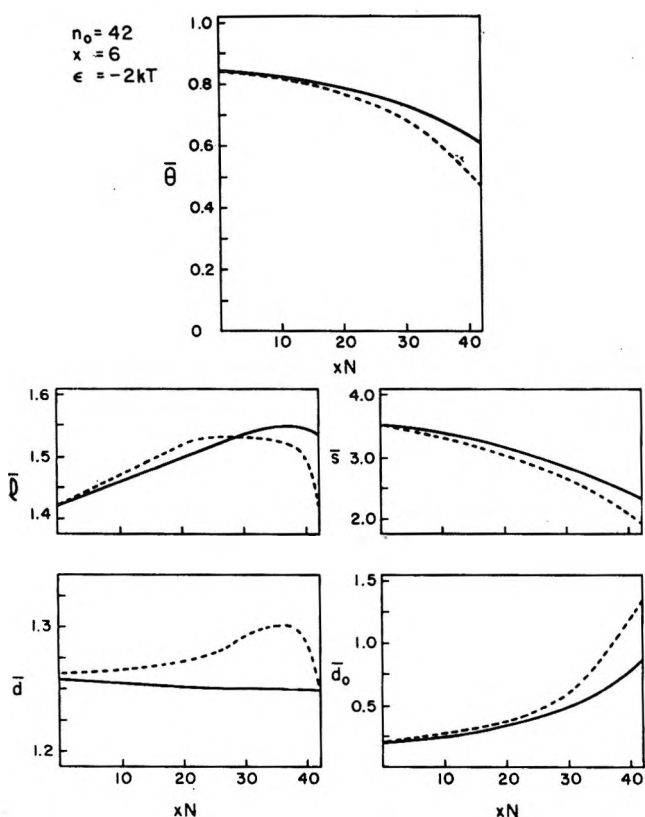
Figure 6. Configurational parameters (as defined in the text and in Figures 1 to 5) for the ligand $x = 6$ binding to a complete surface (——) and a patch (- - -) of identical size (42 sites). All curves were calculated with $\epsilon = -2kT$.
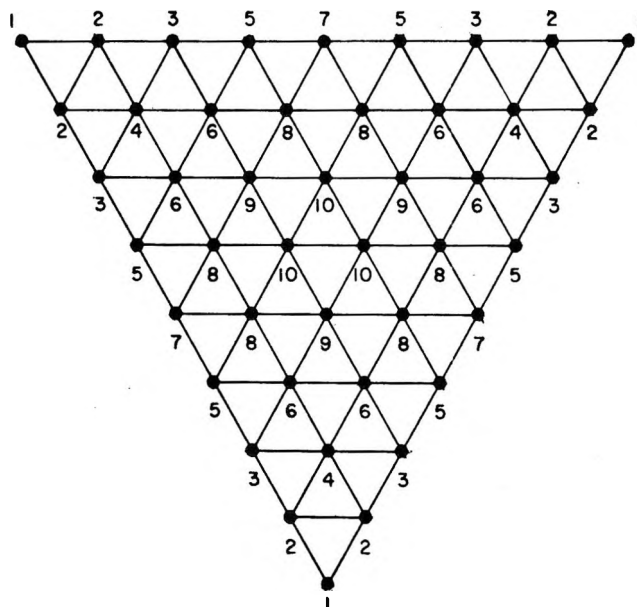

Figure 7. A patch of binding sites. The interior sites (classes 4, 6, 8, 9, and 10) are hexa-coordinated, while the boundary sites (classes 1, 2, 3, 5, and 7) have a lower coordination number. A patch of 42 sites (cf. Figures 6, 10, 13, and 15) can be derived from this patch by omitting the class 1 (corner) sites.
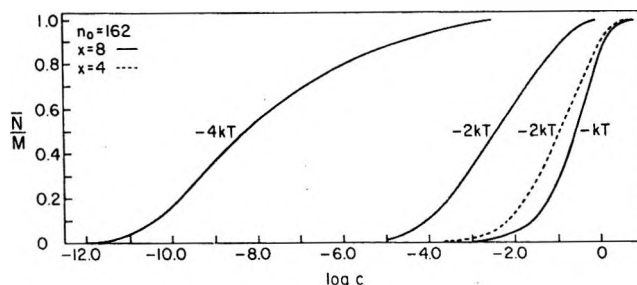

Figure 8. Isotherms for the ligands $x = 8$ (——) and $x = 4$ (- - -) binding to a lattice of 162 sites (cf. Figures 1 to 5), with values of ϵ as indicated.

ligands are bound. Thus, larger decreases in $\bar{\theta}$, $\bar{s}$, and $\bar{l}$ and a sharper increase in $\bar{d}_0$ are observed for the patch. An interesting feature is the presence of a maximum in the $\bar{d}$ vs. xN curve for the patch. Because of the reduced coordination number of the boundary sites, the first ligands bind preferentially in configurations which occupy the interior sites. The ligands $N = 5$ and $N = 6$ bind by forming a large loop over the most interior sites, causing an increase in $\bar{d}$, but due to increased site occupancy, such a loop no longer is possible for the ligand $N = 7$. Thus, $\bar{d}$ drops rapidly after $N = 6$ and the desorbed segments appear as free ends.

III. Equilibrium Behavior of Homogeneous Systems

Figure 8 illustrates binding isotherms [expressed as $\bar{N}/M$ vs. log c, where M is the maximum number of ligands which can bind to the lattice (eq I-4)][6] for the ligands $x = 8$ and $x = 4$ binding to the lattice $n_0 = 162$ (cf. Figures 1–5). As ϵ is varied, both the position and the shape of the curves change. The position of the curve shifts to lower c values as ϵ becomes more negative since the energy gained upon binding is better able to compensate for the accompanying loss of translational and configurational entropy. Such a correlation between binding energy and curve position, in which the more negative energy values are associated with binding at lower values of c, also applies to the ideal lattice gas.[7]

In contrast to the latter, however, the isotherms are not symmetrical about their midpoints, and their shape changes as the energy is varied. The isotherms broaden as saturation is approached, since the decrease in the number of vacant surface sites reduces the number of configurations available to additional ligands, making their binding more difficult. This flattening is most marked for $\epsilon = -4kT$, because the high θ values result in a more rapid depletion of the vacant surface sites by the first ligands bound.

(6) An advantage of such a plot for the representation of binding data is that the conclusions drawn from it are unaffected by the method of calculating the standard chemical potential of the ligand, μ_0, from the partition function for the unbound ligand (paper I, Appendix A), since a change in μ_0 simply would shift the positions of all isotherms along the log c axis by a constant amount. In anticipation of applications of the model,[4] the volume of the ligand segment, v_s, used to calculate μ_0 is that appropriate for hydrocarbon segments (section IV).

(7) T. L. Hill, "An Introduction to Statistical Thermodynamics," Addison-Wesley, Reading, Mass., 1960.

Deviations of binding curves from symmetry also have been noted in studies of enzyme–substrate complexes.[8] In these latter cases, steepening of binding curves is described as *cooperativity*, which is said to occur when the first substrate molecules bound facilitate the binding of additional substrate molecules. The converse case, in which the binding of additional substrate molecules is made more difficult, has been called *negative cooperativity*[9] and is associated with the broadening of enzyme–substrate binding curves. Both generally are attributed to conformational changes in the protein.[8,9] Phenomenologically, a similar flattening of binding curves is observed with the present model. However, it has a totally *different* origin and might be characterized as a type of indirect ligand–ligand interaction, arising not only from the competition of ligands for a limited number of sites (as in the theory of multiple equilibria[2]) but from the effect of ligands on the configurational entropy of other bound ligands as well. It also differs from a direct energetic interaction (such as the electrostatic effects arising in multiple ionization[2]).

The isotherm for the ligand $x = 4$ is somewhat steeper than that for $x = 8$, since it is easier to find smaller clusters of contiguous vacant sites. Thus, less broadening occurs for the shorter ligand. The shift in position of the isotherm with chain length will be discussed below (section VII).

As a further illustration of isotherm broadening in the present model, isotherms have been obtained for the case in which all segments of the bound ligands are adsorbed to surface sites, no loops or free ends being permitted. As illustrated in Figure 9, the resulting isotherms are equally broad at all values of ϵ since $\bar{\theta} = 1$ in each case, resulting in a maximum amount of flattening.

Binding to a Patch of Sites. When ligand binding to a patch of sites is studied as a function of ϵ, the variations in curve position and shape are identical with those described for a lattice which covers a complete surface. Isotherms for a patch and a complete surface with an identical number of sites are compared in Figure 10. As a result of the edge effects mentioned in the study of configurational parameters (Figure 6), binding to the patch is somewhat more difficult.

Isotherms for Rigid Binding. As discussed in paper I, when the commonly used theory of multiple equilibria[2] forms the theoretical framework for analyzing protein–ligand interactions, flexible ligands are assumed to bind in a rigid configuration. Using the model for rigid binding discussed in paper I (Appendix B), a comparison of the isotherms for single-class binding in the theory of multiple equilibria with those for homogeneous systems in the present model is possible. For example, the isotherms in Figure 11 are obtained when systems analogous to those in Figure 8 are studied under the conditions of rigid binding. The resulting
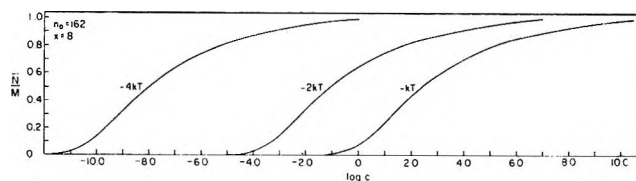

Figure 9. Isotherms for totally adsorbed ligands. The curves were obtained for the ligand $x = 8$ binding to a lattice of 162 sites, as in Figure 8. However, the ligands were constrained to bind with all segments adsorbed to the surface (no loops or free ends being permitted). The value of ϵ is indicated by each curve.
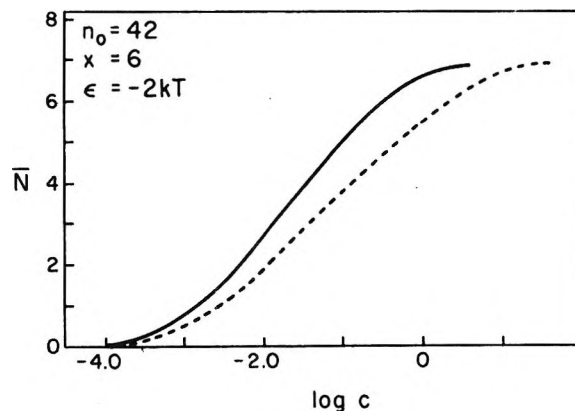

Figure 10. Isotherms for the ligand $x = 6$ binding to a complete surface (———) and a patch (– – –) of identical size (42 sites; cf. Figure 6). Both curves were calculated with $\epsilon = -2kT$.
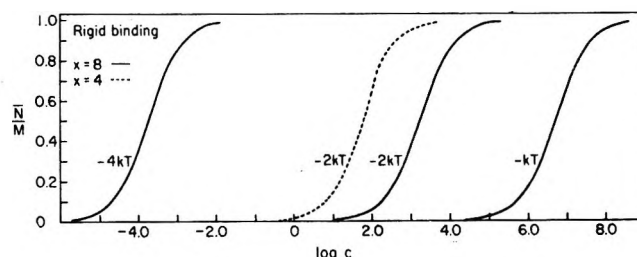

Figure 11. Isotherms for rigid binding. The curves for the ligand $x = 8$ (———) were obtained when 20 ligands bind with an energy 8ϵ, while those for the ligand $x = 4$ were obtained when 40 ligands bind with an energy 4ϵ, allowing a comparison with the isotherms of Figure 8.

curves are symmetrical about their midpoints, as expected for single-class binding, and there is no change in curve shape with variations in ϵ or x. As discussed in detail below (section VII), the variation in curve position with x differs from that obtained with the flexible binding model.

In the rigid binding model, as in the theory of multiple equilibria, when all ligands bind as one class the

(8) D. E. Koshland, Jr., G. Némethy, and D. Filmer, *Biochemistry*, 5, 365 (1966).

(9) A. Levitzki and D. E. Koshland, Jr., *Proc. Nat. Acad. Sci. U. S.*, 62, 1121 (1969).

equilibrium constants for the formation of successive protein–ligand complexes differ only by a statistical factor which accounts for the different ways of placing the ligand on the protein. Thus, each constant can be written as the product of a statistical factor and an intrinsic association constant, the same for all N. For such systems, plots of $\bar{N}/c$ vs. $\bar{N}$ and $1/\bar{N}$ vs. $1/c$ (the so-called Scatchard and double-reciprocal plots, respectively) will be linear.[2] A very significant feature of the model for flexible binding is that these commonly used plots fail to be linear, even for homogeneous systems. Owing to the neglect of the internal degrees of freedom of the bound ligands in the rigid binding model, single-class binding not only implies that the surface is chemically homogeneous, but that all ligands bind in an identical configuration as well. In the present model, in which the flexibility of the bound ligands is included, any given ligand can bind in many different configurations. As additional ligands are bound, the number of possible configurations decreases, so that the ligands do not bind in an identical fashion, even though all of the binding sites are chemically the same. Each ligand binds with a characteristic equilibrium constant which reflects its unique manner of binding as well as simple statistical considerations. The asymmetry of the isotherms (Figures 8 to 10) also results from this failure of the ligands to bind in an identical configuration.

IV. Physical Parameters for Heterogeneous Systems

The model developed in paper I can be used to treat systems which include chemically different surface sites and ligands having nonidentical segments. This feature allows its application to a wide variety of physical systems. The present paper will consider interactions between substituted alkanes and proteins only, in anticipation of applications of the model.[4]

The ligand configurations are counted on a triangular (hexa-coordinated) lattice, with successive ligand segments placed on adjacent sites. This lattice would not be suitable for substituted alkanes if the *statistical segment*, as used in such calculations, were equated to the methylene group (–CH₂–) of the alkyl chains, due to the bond angle restrictions between successive carbon–carbon bonds. If the statistical segment is equated to a –CH₂–CH₂– group, the resulting statistical chain has enough flexibility to be accommodated on the triangular lattice used in this model. By analogy, the (noncarbon) atoms of the ionic or polar head group of the ligand also are counted as a single segment.

In the partition function for the unbound ligand (eq I-67), a numerical value is needed for the volume of a statistical segment, v_s. From the bond angles, bond lengths, and van der Waals radii of the atoms of the ligand,[10] an average v_s of 48 Å³ has been estimated.

The precise chemical groupings on a protein to which the term *site* is to be applied must correspond in size to the statistical segment. Thus, most polar and ionic

groups on amino acid side chains (–NH₃⁺, –COO⁻, –CH₂OH, etc.) constitute a single site, a nonpolar (hydrocarbon) site is defined as two methylene groups (–CH₂–CH₂–), and the polar peptide backbone of each residue, when on the surface, is divided into two sites (>C=O and –NHCᵅH–).

In sections V and VI, the binding of carboxylic acids to protein surfaces containing ionic (–NH₃⁺), nonpolar (–CH₂–CH₂–), and polar (>C=O and –NHCᵅH–) sites is discussed. The appropriate site–segment interaction energies, to be derived in Appendix B, are listed in Table II. All calculations have been performed at $T = 298°K$.

Table II: Site–Segment Interaction Energies

| | ϵ, cal/mol[a] | |
Site	Carboxyl segment	Hydrocarbon segment
–NH₃⁺	−5000	∞
>C=O	−2700	−150
–NHCᵅH–	−1500	−450
–CH₂–CH₂–	∞	−1300

[a] Interactions between nonpolar groups and ionic groups are so unfavorable that the energies have been assigned the value ∞, giving a Boltzmann factor of zero for these contacts.

V. Configurational Parameters for Heterogeneous Systems

When the binding of carboxylic acids to surfaces with chemically different sites is considered, the variations in the average fraction of ligand segments adsorbed, $\bar{\theta}$, and the average length of the free carboxyl end, $\bar{d}_0$, differ markedly from the analogous parameters for homogeneous systems (Figures 1 and 5), as illustrated in Figure 12. In the latter, the carboxylic acids $x = 9$ and $x = 5$ bind to a lattice containing 12 cationic sites (–NH₃⁺) and 150 nonpolar sites. The energy of the carboxyl segment–amino site interaction is so favorable (Table II) that the first 12 ligands bind almost exclusively in configurations with their carboxyl segments adsorbed to ionic sites. Thus, a sharp increase in $\bar{d}_0$ and a resulting drop in $\bar{\theta}$ occur at $N = 12$, since configurations with $d_0 \geqslant 1$ are the only one available thereafter. The more gradual changes in $\bar{\theta}$ and $\bar{d}_0$ elsewhere along the curves reflect the reduced availability of vacant surface sites, as observed for homogeneous systems.

Positioning of Ionic Sites. The specific position of the ionic sites is relatively unimportant in determining the variations in the parameters $\bar{\theta}$ and $\bar{d}_0$, as shown in Figure 13. With a patch of three cationic sites and 39 nonpolar sites, the results with the ionic sites located near the center of the patch (class 9 sites in Figure 7)

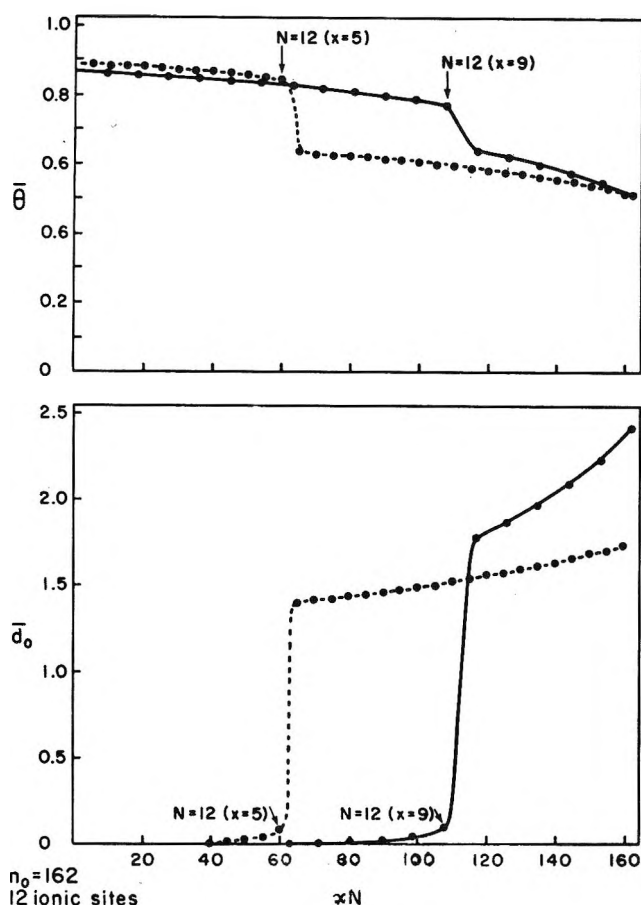(10) H. A. Scheraga, *Advan. Phys. Org. Chem.*, **6**, 103 (1968).

Figure 12. Variations in $\bar{\theta}$, the average fraction of ligand segments adsorbed, and $\bar{d}_0$, the average length of the free carboxyl end, with xN, the number of segments belonging to bound chains, for the carboxylic acids $x = 9$ (●—●) and $x = 5$ (●- -●). The curves were calculated for a lattice with 12 cationic sites ($-NH_3^+$) and 150 nonpolar sites.

are almost identical with those obtained when the ionic sites are located near its corners (class 4 sites).[11]

Polar Sites. Figure 13 also includes configurational parameters for a surface with uncharged polar sites. Thus, in the central arrangement of ionic sites, $-NHC^\alpha H-$ groups have been placed on the class 8 sites and $>C=O$ groups on the sites of classes 7 and 10, while $-NHC^\alpha H-$ groups and $>C=O$ groups have been placed on class 3 and 2 sites, respectively, in the corner arrangement, for a total of 12 polar sites in each case. With such additional heterogeneity, the changes in the configurational parameters are not as sharp as those for the surfaces with just two types of sites, since the polar sites remain as possible binding sites for the carboxylate segment after the ionic sites are filled.

Positioning of Polar Sites. The rise in $\bar{d}_0$ and drop in $\bar{\theta}$ are largest for the corner arrangement of ionic and polar sites, since the configurations containing carboxyl segment–polar site interactions make a smaller contribution to the partition function due to the reduced coordination number of the polar sites in this arrangement. A calculation of the occupancies of the various
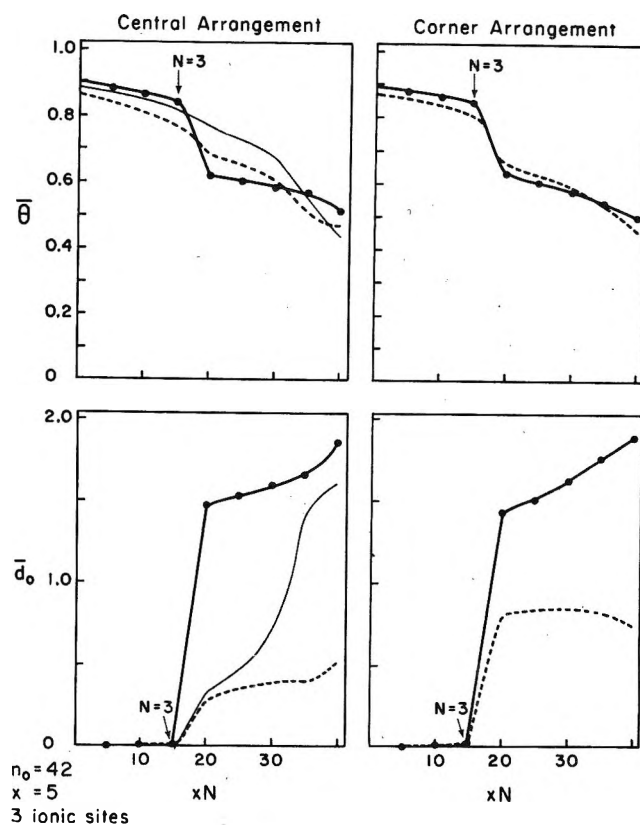

Figure 13. Variations in $\bar{\theta}$, the average fraction of ligand segments adsorbed, and $\bar{d}_0$, the average length of the free carboxyl end, with xN, the number of segments belonging to bound chains, for the carboxylic acid $x = 5$ binding to a patch of three cationic sites and 39 nonpolar sites (●—●). The results obtained with the ionic sites located near the center of the patch (central arrangement—class 9 sites of Figure 7) may be compared with those obtained with the ionic sites located near the corners (corner arrangement—class 4 sites of Figure 7). The effects of introducing 12 polar sites in the vicinity of the ionic sites in each arrangement (as described in the text) are indicated (- - -). In the central arrangement, a patch with six polar sites in the vicinity of the ionic sites also has been studied (——).

types of sites (eq I-62) indicates that those carboxyl segments which are adsorbed after $N = 3$ for the corner arrangement bind preferentially to $-NHC^\alpha H-$ sites, since the greater inaccessibility of the $>C=O$ sites (in this particular arrangement) overrides their energetic advantage (Table II). But after $N = 6$, the availability of surface sites has been curtailed considerably and the possible energy gain for binding a carboxyl segment to the thus far relatively vacant $>C=O$ sites becomes more important, so that further chains bind with their carboxyl segments on the surface and $\bar{d}_0$ decreases at high values of N.

For the central arrangement, the ligands after $N = 3$ bind with their carboxyl segments attached primarily to the $>C=O$ sites, since the latter not only are favored

(11) When referring to these two arrangements of ionic sites, the terms *central arrangement* and *corner arrangement* will be used.

energetically over the $-NHC^{\alpha}H-$ sites, but are occupied to a lesser extent by previously bound hydrocarbon segments as well (for the latter, the $-NHC^{\alpha}H-$ sites are favored energetically over the $>C=O$ sites; see Table II). The accelerated rise in $\bar{d}_0$ after $N = 6$ results from the reduced accessibility of the $>C=O$ sites.

Figure 13 also illustrates configurational parameters for the case in which the central arrangement includes only *six* polar sites ($-NHC^{\alpha}H-$ groups on the class 10 sites and $>C=O$ groups on the class 7 sites). On this lattice, as with the central arrangement with 12 polar sites, the carboxyl segments bind preferentially to the $>C=O$ sites after $N = 3$. The rather marked change in the parameters at $N = 6$ reflects the saturation of the three $>C=O$ sites; binding of the carboxyl segment to $-NHC^{\alpha}H-$ groups does not occur significantly thereafter due to the reduced accessibility of these sites.

VI. Equilibrium Behavior of Heterogeneous Systems

Biphasic isotherms are obtained when the carboxylic acids $x = 9$ and $x = 5$ bind to a lattice with 12 ionic sites and 150 nonpolar sites, as illustrated in Figure 14 (*cf.* Figure 12). An intermediate plateau occurs at $\bar{N} = 12$, corresponding to the saturation of the ionic sites, followed by another rise to the final plateau at $\bar{N} = M$. This second phase represents the binding of ligands with free carboxyl ends, and therefore it occurs at higher ligand concentrations.

The first phase of the isotherm is steeper for the ligand $x = 5$, since fewer segments are bound to the surface when the 12 ionic sites become saturated (when $N = 12$, $xN = 60$ for the ligand $x = 5$, as compared with $xN = 108$ for the ligand $x = 9$) so that less broadening due to negative cooperativity results. A similar correlation between chain length and isotherm broadness is found in the second phase of the curves. For the ligand $x = 5$, the second phase is even steeper than the curve expected for the binding of four hydrocarbon segments to the available number of nonpolar sites. Due to the entropy gain possible when $d_0 > 1$, the necessity for the carboxyl segment to be located in a free end favors the lengthening of that end. As a result, the ligands for which $N > 12$ have lower $\bar{\theta}$ values than would be anticipated, given the hydrocarbon segment-nonpolar site interaction energy used here ($\approx -2kT$ at 298°K; see Figure 8). This steepens the isotherm. No such effect is possible for $x = 9$, because the nonpolar sites are occupied to a much greater extent when $N = 12$, and therefore hydrocarbon segments would form a loose end even if the free carboxyl segment were not present.

Positioning of Ionic Sites and Introduction of Polar Sites. Isotherms for the carboxylic acid $x = 5$ binding to a patch of 39 nonpolar and three ionic sites are presented in Figure 15 (*cf.* Figure 13). Again, the curves are biphasic with an intermediate plateau at a value of $\bar{N}$ corresponding to the saturation of the ionic sites.
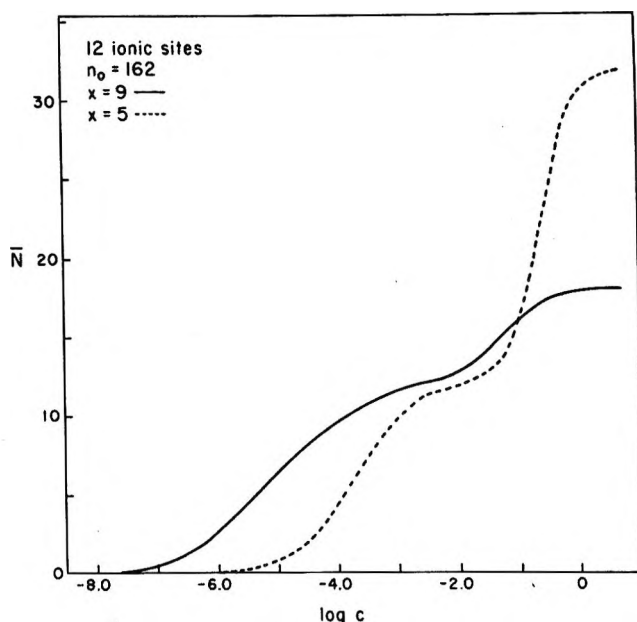
Figure 14. Isotherms for the carboxylic acids $x = 9$ (———) and $x = 5$ (– – –) binding to a lattice with 12 ionic sites and 150 nonpolar sites (*cf.* Figure 12).
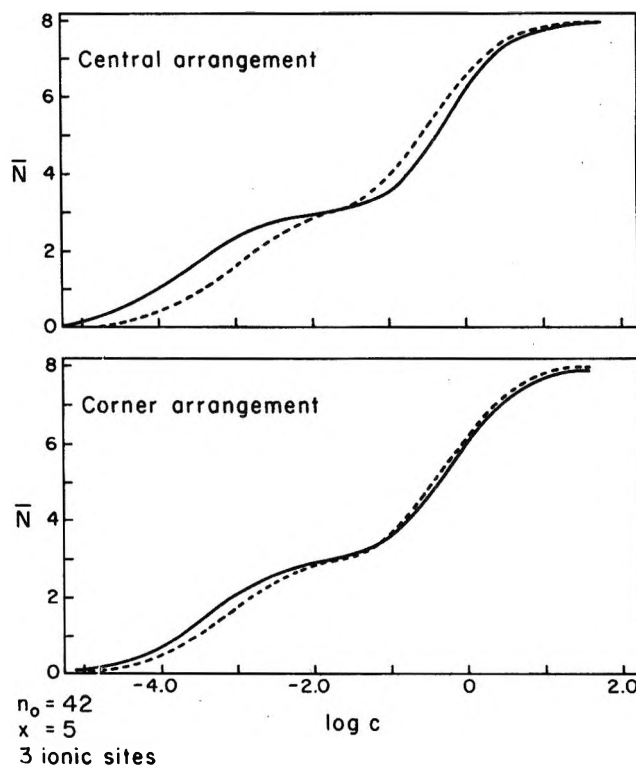

Figure 15. Isotherms for the carboxylic acid $x = 5$ binding to a patch of three ionic sites and 39 nonpolar sites (———) (*cf.* Figure 13). In the upper figure, the ionic sites are located near the center of the patch (central arrangement—class 9 sites of Figure 7), while in the lower figure they are located near the corners (corner arrangement—class 4 sites of Figure 7). The effects of introducing 12 polar sites in the vicinity of the ionic sites (as described in the text) also are indicated (– – –).

The location of the latter hardly affects either the position or the shape of the isotherms. The introduction

of 12 polar sites in each arrangement shifts the first phase of the curves to higher values of c, since a smaller amount of energy is gained when ligands bind in configurations with some hydrocarbon segments attached to polar sites (such configurations will occur since the polar sites are adjacent to the ionic sites). On the other hand, the presence of polar sites shifts the second phase of the isotherms to lower values of c, because of the energy gained from carboxyl segment–polar site interactions (without the polar sites, the carboxyl segment would not be adsorbed). In both phases, the shifts are larger for the central arrangement, in which most of the polar sites are hexa-coordinated, so that configurations which include them make larger contributions to the partition function. As might be expected, the isotherm for the central arrangement with only six polar sites (*cf.* Figure 13) would fall between the two illustrated for the central arrangement.

Thus, the general effect of introducing polar sites is to decrease the difference in position between the two phases of the isotherm, shortening the intermediate plateau region. Further studies have shown that when a sufficiently large number of polar sites is introduced (for example, if less than one-half of the lattice sites are nonpolar sites), the intermediate plateau disappears almost *entirely*, and the isotherm appears to be a monophasic sigmoidal curve, similar to those observed for homogeneous systems. Thus, if a sigmoidal binding isotherm is observed in an experiment, this in itself does not establish that the binding region is chemically homogeneous. Conversely, the presence of a marked intermediate plateau may be taken as evidence that a fairly large number of nonpolar sites is present in the vicinity of the ionic sites, or more generally, that there are so many low-energy sites that they are only partially saturated when the high-energy sites are occupied completely.

VII. Chain Length Dependence

A very important difference between the model discussed in paper I and the theory of multiple equilibria (or its statistical-mechanical equivalent, the rigid binding model of paper I) emerges when the dependence of the strength of binding on the chain length of the ligand is studied. In experimental studies of the interactions between proteins and substituted alkanes, it is found that the strength of binding increases with the chain length of the ligand,[12] implying a negative value for $\partial \Delta F^\circ / \partial x$, the per-segment increment in the change of free energy upon binding. The latter can be separated into energy and entropy contributions

$$\frac{\partial \Delta F^\circ}{\partial x} = \frac{\partial \Delta E^\circ}{\partial x} - T \frac{\partial \Delta S^\circ}{\partial x} \qquad (2)$$

In both models, $\partial \Delta E^\circ / \partial x$ is negative, since it corresponds to the site–segment interaction energy, ϵ, but $\partial \Delta S^\circ / \partial x$ also is negative due to the loss of translational

and configurational entropy upon binding. However, whereas the bound ligands retain some configurational entropy in the model for flexible binding, *all* configurational entropy is lost in the rigid binding model. Therefore

$$\frac{\partial \Delta S^\circ}{\partial x} \text{ (rigid binding model)} <$$

$$\frac{\partial \Delta S^\circ}{\partial x} \text{ (flexible binding model)} \qquad (3)$$

In the model for flexible binding, $\epsilon = -2kT$ (which corresponds approximately to the strength of the hydrocarbon segment–nonpolar site interaction) is sufficiently negative to give an increase in the strength of binding with increasing chain length (shifting the isotherm to lower c values) (Figure 8), while the rigid binding model predicts a decrease in the strength of binding with increasing chain length at $\epsilon = -2kT$ (Figure 11), contrary to experimental results.

In the rigid binding model, much larger values of $|\epsilon|$ would have to be assumed to result in $\partial \Delta F^\circ / \partial x < 0$. The simplicity of that model allows a determination of the value of ϵ required to balance the loss of entropy upon binding, corresponding to the condition

$$\frac{\partial \Delta F^\circ}{\partial x} = 0 \qquad (4)$$

Using the appropriate partition functions (eq I-67 and I-71) to calculate the equilibrium constant for binding (eq I-8), it is found that

$$\frac{\partial \Delta F^\circ}{\partial x} = \epsilon + kT \ln (3z_1 - 1) \qquad (5)$$

where $3z_1$ is the coordination number of the lattice sites in bulk solution (*cf.* paper I). For $z_1 = 6$ as used here, eq 4 is satisfied when

$$\epsilon = -2.83kT \qquad (6)$$

but ϵ would have to be considerably more negative (approximately $-4kT$) to cause $\partial \Delta F^\circ / \partial x$ to approach the experimentally observed values[12] for the alkyl sulfates and carboxylic acids. Although no such explicit condition may be calculated for the flexible binding model, it has been estimated from computed values of ΔF° that $\epsilon \approx -0.5kT$ will satisfy eq 4.

Thus, both models can give an increase in the strength of binding with increasing chain length, as observed experimentally. However, as shown above, at a value of $\partial \Delta E^\circ / \partial x$ appropriate for the binding of substituted

(12) F. Karush and M. Sonenberg, *J. Amer. Chem. Soc.*, **71**, 1369 (1949); J. D. Teresi and J. M. Luck, *J. Biol. Chem.*, **194**, 823 (1952); D. S. Goodman, *J. Amer. Chem. Soc.*, **80**, 3892 (1958); A. Ray, J. Reynolds, H. Polet, and J. Steinhardt, *Biochemistry*, **5**, 2606 (1966); J. Reynolds, S. Herbert, H. Polet, and J. Steinhardt, *ibid.*, **6**, 937 (1967); J. Reynolds, S. Herbert, and J. Steinhardt, *ibid.*, **7**, 1357 (1968); A. Spector, K. John, and J. Fletcher, *J. Lipid Res.*, **10**, 56 (1969).

alkanes to proteins (corresponding to the strength of the hydrocarbon segment–nonpolar site interaction), only the model for flexible binding gives a negative $\partial \Delta F°/\partial x$. This observation confirms that the flexible binding model is the appropriate theoretical model for analyzing the interactions between substituted alkanes and proteins.

VIII. Discussion

Several assumptions are implicit in the model as it is presented here. Most importantly, it is assumed that the protein or other macromolecular surface to which the ligands bind does not change structure during the binding process. Thus, conformational changes, which are known to occur in many experimental situations (e.g., protein–detergent interactions), cannot be treated with the model in its present form. If conformational changes occur, a different surface lattice would have to be used for each conformation. If there is an equilibrium between two well-defined conformations and the equilibrium is shifted by ligand binding, an extension of the model would be possible, in principle, by combining two partition functions of the form of eq I-12. However, the increase in the number of the parameters probably would render verification of the model difficult, if not impossible.

It is assumed that a lattice site covered by a ligand segment no longer is available for the binding of further ligands; i.e., the possibility of multilayer binding is not considered here. This assumption may not always be realistic. For example, when a hydrocarbon segment is bound to a nonpolar site, hydrocarbon segments of other ligands might bind on top of the first segment. A crude correction could be made by omitting the corrections for occupied sites (eq I-56 and I-61). However, the possibility of multilayer adsorption on loops near the surface also would have to be considered, and no simple extension of the model is feasible in this case.

Cooperative binding, i.e., the strengthening of the affinity of the macromolecule for further ligands after some ligands are bound, may occur, although this possibility was not considered here. If cooperativity occurs as a result of favorable ligand–ligand interaction energies, this might be treated by making the Boltzmann factors describing the site–segment interactions (eq I-19) a function of the extent of saturation. However, if such changes in the Boltzmann factors were applied to only a few sites of a given class, the use of a Markov process for the enumeration of configurations (eq I-18) no longer would be practical.

Applications of the Model. While most of the discussion presented in this paper was centered on protein–ligand interactions and the latter are used for comparisons of the theory with experiment,[4] the model is not restricted to proteins. It can be applied to any compact macromolecular surface interacting with flexible ligands and could be used to analyze binding to any

small particle. The chemical nature of the ligand segments and the surface sites can be varied as needed, by introducing the appropriate interaction energies (cf. Table II and Appendix B).

Using a patch of binding sites, the interaction of flexible ligands with any rigid molecule representing a more or less flat surface (and not necessarily of macromolecular nature, e.g., condensed aromatic derivatives) could be treated with the model.

Appendix A

The Enumeration of Ligand Configurations on Different Lattices. As discussed in paper I, the lattice on which the present model is based differs from those used in theories of polymer adsorption.[13] In particular, to allow the placement of a planar lattice (with coordination number z_1) on a closed surface, the lattice of the present model includes a small number of sites of a lower coordination number (z_2) at regular intervals. Therefore, it is important to compare the configurational entropy of a ligand on this lattice with that calculated on a uniform planar lattice without such irregularities, i.e., with all sites having coordination number z_1. A totally adsorbed ligand of x segments may assume $\nu(x)$ configurations on the lattice of the present model (eq I-18). According to the Flory–Huggins theory of polymer configurations, the number of configurations on the corresponding uniform lattice is[14,15]

$$\nu_F(x) = n_0 z_1^{x-1} \tag{7}$$

where the subscript F denotes the Flory model.[16] If a small number, $(1 - p)n_0$, of sites with coordination number z_2 are *randomly* distributed among the n_0 sites of the Flory lattice, eq 7 becomes

$$\nu_R(x) = n_0(z_1 p + z_2(1 - p))^{x-1} \tag{8}$$

where p is the fraction of z_1 sites on the lattice and the subscript R denotes the random placement of the z_2 sites.

Entropies, $S = k \ln \nu$, calculated for the three examples mentioned, are compared in Table III for var-

(13) A. Silberberg, *J. Phys. Chem.*, **66**, 1872, 1884 (1962); R.-J. Roe, *Proc. Nat. Acad. Sci. U. S.*, **53**, 50 (1965); R.-J. Roe, *J. Chem. Phys.*, **43**, 1591 (1965).

(14) P. J. Flory, "Principles of Polymer Chemistry," Cornell University Press, Ithaca, N. Y., 1953.

(15) The original form of eq 7 is $n_0 z_1(z_1 - 1)^{x-2}$ to correct for immediate reversals.[14] Although the complete calculations of paper I and this paper also contain a correction to exclude immediate reversals, the correction is not made in eq I-18 and hence is not included here.

(16) Equation 7 strictly is suitable only for very large lattices on which edge effects can be neglected.[14]

Table III: Configurational Entropies[a] on Various Types of Lattices

n_0	p	x	$S(x) \times 10^{16}$	$S_F(x) \times 10^{16}$	$S_R(x) \times 10^{16}$
92	0.869	10	28.2	28.4	28.1
		20	52.5	53.0	52.4
		30	76.9	77.5	76.6
162	0.926	10	29.1	29.2	29.0
		20	53.5	53.7	53.4
		30	78.0	78.3	77.8
252	0.952	10	29.7	29.8	29.7
		20	54.2	54.3	54.1
		30	78.8	79.0	78.7

[a] The entropies are given in units of erg/(deg molecule).

ious values of x and n_0. They were calculated for $z_1 = 6$, $z_2 = 5$, and 12 z_2 sites. $S_F(x)$ is larger than both $S(x)$ and $S_R(x)$, since $\nu_F(x)$ is increased by a factor of $z_1 = 6$ with the placement of each segment. The randomly placed z_2 sites on the modified Flory lattice reduce the rate of increase of $\nu_R(x)$ to $5 + p$, while the lattice of the present model represents an intermediate case, since $\nu(x)$ is increased by a factor of $z_1 = 6 \left(= \sum_{j=1}^{C} w_{ij} \text{ for } i = 2, 3, \ldots C; \text{ see eq I-15} \right)$ for the placement of all segments except those which follow a z_2 site. The differences between $S(x)$, $S_F(x)$, and $S_R(x)$ are magnified as x increases since these quantities increase linearly with x. As n_0 increases and p approaches unity, the presence of the z_2 sites is less evident, and a decrease in the differences between these three quantities is seen.

Appendix B

Site–Segment Interaction Energies. No precise values for the energies of interaction between various ligand segments and surface sites are available, either from theoretical or empirical considerations. However, estimates for these energies can be obtained with the aid of methods currently being developed for calculating protein conformations from known amino acid sequences.[10] The segment and site are assumed to contact each other such that their constituent atoms are separated by a distance equal to the sum of their van der Waals radii, at which the potential energy of interaction between the atoms is a minimum.[10] Furthermore, it is assumed that standard bond length and bond angle values[10] apply, and that no energy contributions from torsion about single bonds result when forming a given contact. The interaction energy (eq I-19) is equated to a sum of contributions from nonbonded (van der Waals) interactions, electrostatic interactions, and desolvation

$$\epsilon_j^{(n)} = {}_{NB}\epsilon_j^{(n)} + {}_{E}\epsilon_j^{(n)} + {}_{S}\epsilon_j^{(n)} \quad (9)$$

where the subscripts NB, E, and S refer to the contributions from nonbonded interactions, electrostatic interactions, and desolvation, respectively.

To calculate the nonbonded contribution, ${}_{NB}\epsilon_j^{(n)}$, the Lennard-Jones "6-12" potential is used[10]

$$_{NB}\epsilon_j^{(n)} = \sum_{i,k} \frac{\alpha_{ik}}{r^{12}} - \frac{\beta_{ik}}{r^6} \quad (10)$$

where the summation is over all extended atoms[17,18] of the jth site and the nth segment. α_{ik} and β_{ik} are the coefficients for repulsion and attraction, respectively, and r is the distance between the centers of extended atoms i and k and is equated to r_{ik}, the sum of their van der Waals radii. Values for the coefficients α and β are obtained as described by Scheraga.[10]

The electrostatic contribution, ${}_{E}\epsilon_j^{(n)}$, is a sum of Coulomb interactions between all pairs of extended atoms of the site and segment. These are calculated by the standard formulas[19] for charge–charge, charge–dipole, and dipole–dipole interactions, averaged over all orientations of the atoms. The local dielectric constant is taken as 3.5 in the vicinity of the protein surface in aqueous solution.[20]

The desolvation contribution, ${}_{S}\epsilon_j^{(n)}$, is equated to the sum of the energies of desolvating the extended atoms involved in the interaction. The contribution from a given atom consists of a desolvation energy per water molecule removed multiplied by the number of water molecules displaced when the contact is established. Estimates for the latter may be obtained by dividing the volumes of the approaching extended atoms[21] by 30 Å³, the volume of a water molecule.[18] The desolvation energies for charged and polar groups may be calculated as charge–dipole and dipole–dipole interactions, respectively. Breaking water–hydrocarbon contacts involves changes in water structure[22] and therefore results in both entropy and energy changes. The ϵ values listed in Table II include both contributions and therefore should be considered properly as free energies. Their values have been obtained from the analysis of thermodynamic properties of aqueous solutions of the hydrocarbons.[18,22]

(17) For simplicity, hydrogen atoms are not considered individually. Instead, they are regarded as part of an *extended atom*, such as $-CH_2-$ or $-NH-$.[18]

(18) K. D. Gibson and H. A. Scheraga, *Proc. Nat. Acad. Sci. U. S.*, **58**, 420 (1967).

(19) J. O. Hirschfelder, C. F. Curtiss, and R. B. Bird, "Molecular Theory of Gases and Liquids," Wiley, New York, N. Y., 1954.

(20) D. A. Brant and P. J. Flory, *J. Amer. Chem. Soc.*, **87**, 2791 (1965).

(21) A. Bondi, *J. Phys. Chem.*, **68**, 441 (1964).

(22) G. Némethy and H. A. Scheraga, *J. Chem. Phys.*, **36**, 3401 (1962).

Intermolecular Hydrogen Bond of β-Naphthol with Azaaromatics

and Aromatic Hydrocarbons

by Benoy B. Bhowmik

Physical Chemistry Laboratory, Jadavpur University, Calcutta-32, India   (Received February 12, 1970)

The spectrophotometric and thermodynamic properties of hydrogen-bonded complexes of β-naphthol as proton donor and azaaromatics and aromatic hydrocarbons as proton acceptors have been determined from the longest wavelength $\pi \rightarrow \pi^*$ absorption band of β-naphthol in cyclohexane solution. The equilibrium constants have been found to increase linearly with the basicity of the proton acceptors. The heats of formation $(-\Delta H^\circ)$ of these complexes are linearly related to spectral shifts $(\Delta\nu, \text{cm}^{-1})$ and to oscillator strengths (f) due to hydrogen bonding. These are also related to ionization potentials of azaaromatics and aromatic hydrocarbons.

Introduction

It has long been noticed that n electrons of azaaromatics and π electrons of olefins and aromatic compounds act as the proton acceptors in hydrogen bonding.[1] Hydrogen-bonded complexes in which phenols serve as proton donors have been studied extensively. When a phenolic hydroxyl group enters into hydrogen bond formation with a suitable proton acceptor, the longest wavelength $\pi \rightarrow \pi^*$ absorption band of the phenol shows a forward or low-frequency shift.[2] The π electron of aromatic hydrocarbon or the n electron of azaaromatic can act as a proton acceptor, so the longest wavelength $\pi \rightarrow \pi^*$ absorption band of a phenol dissolved in benzene or in pyridine should appear at a longer wavelength as compared to that in cyclohexane solution. The association constants of hydrogen-bonded complexes of α- and β-naphthol with azaaromatics and aromatic hydrocarbons have been determined,[3,4] but no values have been reported for the thermodynamic and spectrophotometric properties of these complexes.

Mulliken[5] showed that the intensity of the absorption band of the molecular complexes, especially charge-transfer complexes, should vary directly with $-\Delta H^\circ$ in a series of related complexes. The experimental results show that Mulliken's theory holds good for strong complexes but experiments on weak complexes disagree with Mulliken's prediction. It is interesting to see whether there is any relation between the intensity of the absorption band of hydrogen-bonded complexes and their stabilities. Thus quantitative spectrophotometric and thermodynamic studies of both strong OH...n-electron and weak OH...π-electron hydrogen-bonded complexes seem important. In this paper hydrogen-bonded complexes of β-naphthol (proton donor) with azaaromatics and aromatic hydrocarbons (proton acceptors) are studied spectrophotometrically in cyclohexane at different temperatures.

Experimental Section

β-Naphthol was supplied by Matheson Coleman and Bell which was recrystallized from ethanol–water, mp 122.5–123.5°. All azaaromatics and aromatic hydrocarbons listed in Table I were supplied by Aldrich Chemical Co. and Eastman Organic Chemicals and were fractionally distilled just before use. Matheson Coleman and Bell spectroquality cyclohexane was used as solvent without further purification.

Absorption spectra were recorded on a Cary Model 15 spectrophotometer with fused silica cells of 1.0-cm optical path.

Results

Figures 1 and 2 show the near-ultraviolet absorption band of β-naphthol in cyclohexane and the $\pi \rightarrow \pi^*$ shift due to hydrogen bond formation with pyridine and benzene. The absorption spectra of β-naphthol in cyclohexane show maximum at 328 mμ (ϵ 2360). The shapes of the near-ultraviolet bands of other hydrogen-bonded complexes (not shown) are similar in each series. The equilibrium constants of these complexes were determined by measuring the optical density at the complex absorption maximum for a series of solutions of varying concentrations of the proton acceptors with a fixed concentration of β-naphthol. For a 1:1 complex it has been shown[3] that ϵ_c, the molar extinction coefficient of hydrogen-bonded complex, and K, the equilibrium constant, can be obtained from

$$\frac{[A]}{(\epsilon - \epsilon_0)} = \frac{[A]}{(\epsilon_c - \epsilon_0)} + \frac{1}{(\epsilon_c - \epsilon_0)K} \qquad (1)$$

(1) G. C. Pimental and A. L. McClellan, "The Hydrogen Bond," Freeman and Co., San Francisco, Calif., 1960.

(2) B. B. Bhowmik and S. Basu, *Trans. Faraday Soc.*, **59**, 813 (1963).

(3) B. B. Bhowmik, *Indian J. Chem.*, **7**, 788 (1969).

(4) B. Ghosh and S. Basu, *Trans. Faraday Soc.*, **61**, 2097 (1965).

(5) R. S. Mulliken, *J. Amer. Chem. Soc.*, **74**, 811 (1952).

Table I:[a]   Thermodynamic and Spectrophotometric Data of Hydrogen-Bonded Complexes of β-Naphthol with Azaaromatics and Aromatic Hydrocarbons in Cyclohexane

Proton acceptor	Concn range of proton acceptor, mol/l. $\times 10^2$ [b]	Equilibrium constant, K,[c] l./mol			$-\Delta G°$, kcal	$-\Delta H°$, kcal	$-\Delta S°$, eu	Hydrogen-bonded band[d] ν_{max}, cm^{-1}	ϵ_0	$f \times 10^2$
		14°	24°	40°						
Pyridine	1.24–3.72	94.50	66.50	40.90	2.49	5.80 ± 0.17	11.15 ± 0.55	29940	2670	3.20
2-Picoline	1.01–3.04	131.50	86.90	48.50	2.65	6.90 ± 0.15	14.30 ± 0.50	29886	2760	3.47
3-Picoline	1.03–3.09	114.50	79.30	45.60	2.60	6.35 ± 0.07	12.62 ± 0.27	29895	2710	3.31
4-Picoline	1.03–3.08	138.00	91.20	49.00	2.68	7.14 ± 0.08	15.03 ± 0.29	29869	2840	3.55
Benzene	112.5–562.5	0.175	0.159	0.140	−1.09	1.57 ± 0.10	3.96 ± 0.33	30294	2990	2.74
Toluene	94.0–470.0	0.264	0.238	0.198	−0.85	1.96 ± 0.19	9.47 ± 0.64	30285	2950	2.62
o-Xylene	82.9–414.5	0.587	0.502	0.403	−0.41	2.61 ± 0.06	10.15 ± 0.22	30280	2860	2.53
m-Xylene	81.4–407.0	0.620	0.527	0.424	−0.38	2.65 ± 0.12	10.20 ± 0.40	30280	2820	2.45
p-Xylene	81.1–405.5	0.549	0.476	0.380	−0.44	2.52 ± 0.10	9.97 ± 0.30	30280	2920	2.56
Mesitylene	71.9–359.5	1.190	0.975	0.742	−0.02	3.28 ± 0.11	11.10 ± 0.38	30271	2480	2.23

[a] No comparison of the data between the azaaromatic–β-naphthol and aromatic hydrocarbon–β-naphthol series is attempted; each series is treated separately.   [b] Concentration of β-naphthol is 2.79×10^{-4} mol/l. in all cases.   [c] These are average of five such measurements at near band maximum of the complex with an average deviation of only 1%.   [d] The data for free β-naphthol band are $\nu_{max} = 30{,}488$ cm^{-1}, ϵ_{max} 2360, $f = 2.01 \times 10^{-2}$.
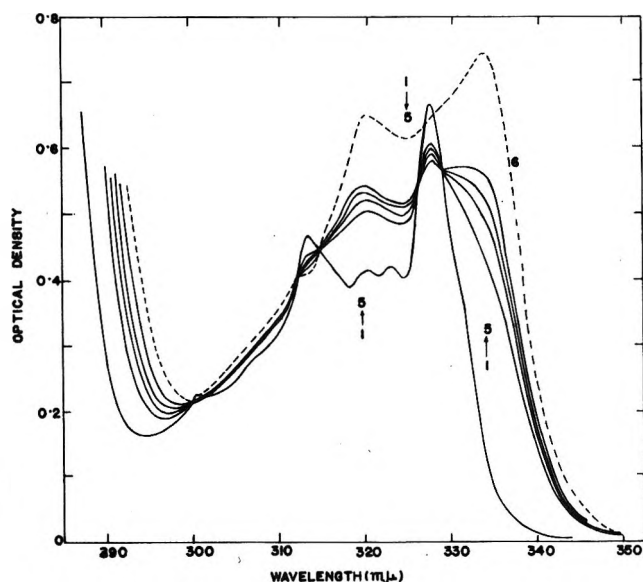

Figure 1. The near-ultraviolet absorption spectra of β-naphthol–pyridine in cyclohexane (temperature, 24°; cell, 1 cm). Concentration of β-naphthol: 2.79×10^{-4} M, concentration of pyridine (M): (1) 0, (2) 1.24×10^{-2}, (3) 1.86×10^{-2}, (4) 2.48×10^{-2}, and (5) 3.10×10^{-2}. Curve 6, for the absorption due solely to hydrogen-bonded β-naphthol, was recorded as described in the text.

Figure 2. The near-ultraviolet absorption spectra of β-naphthol–benzene in cyclohexane (temperature, 24°; cell, 1 cm). Concentration of β-naphthol: 2.79×10^{-4} M, concentration of benzene (M): (1) 0, (2) 1.125, (3) 2.250, (4) 4.375, and (5) 4.500. Curve 6, for the absorption due solely to hydrogen-bonded β-naphthol, was recorded as described in the text.

where [A] is the initial molar concentration of the proton acceptor and ϵ and ϵ_0 refer to the molar extinction coefficient of β-naphthol at the complex absorption maximum with and without the proton acceptor. Equation 1 is applicable when the proton acceptor has no appreciable absorption at the complex absorption maximum and its concentration is many times larger than that of β-naphthol. The plots of [A]/($\epsilon - \epsilon_0$) against [A] were found to be linear in all cases and are shown in Figures 3 and 4. With the aid of the equilibrium constant value, the absorption spectra due solely to hydro-
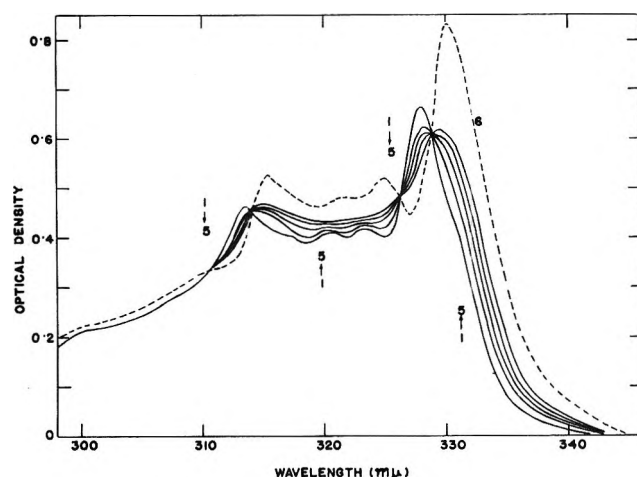
gen-bonded complex (curve 6 of Figures 1 and 2) are obtained by balancing the solution of the complex against the equilibrium concentrations of free β-naphthol and free proton acceptor present in the solution of the complex.[6] The thermodynamic quantities ($\Delta H°$, $\Delta S°$) were obtained from the equilibrium constants at three different temperatures (40, 24, 14°) by the usual method.[7] The measurements at 40 and 14° were made by preheating and precooling the cells with the solutions in a constant temperature bath. The thermodynamic properties determined by eq 1 are listed in Table I.

(6) V. G. Krishna and B. B. Bhowmik, J. Amer. Chem. Soc., 90, 1700 (1968).

(7) L. J. Andrews and R. M. Keefer, "Molecular Complexes in Organic Chemistry," Holden-Day, San Francisco, Calif., 1964, p 104.
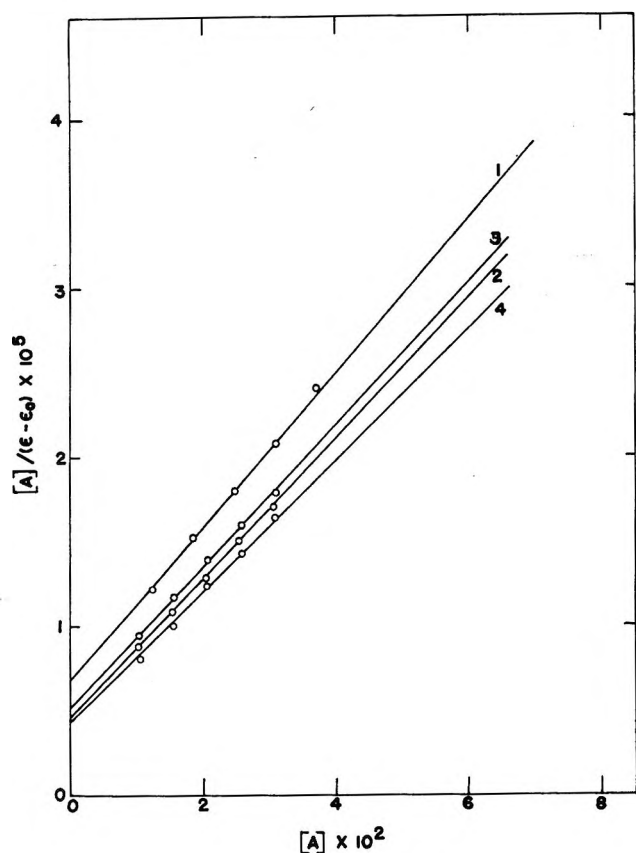
Figure 3. Spectral determination of equilibrium constant for β-naphthol–azaaromatic systems at 24°: (1) pyridine, (2) 2-picoline, (3) 3-picoline, and (4) 4-picoline.

Figure 4. Spectral determination of equilibrium constant for β-naphthol–aromatic hydrocarbon systems at 24°: (1) benzene, (2) toluene, (3) o-xylene, (4) m-xylene, (5) p-xylene, and (6) mesitylene.

Experimental oscillator strengths (f) are generally calculated using the approximate formula,[8] $f = 4.319 \times 10^{-9} \times \epsilon_{max}\nu_{1/2}$, where $\nu_{1/2}$ is the band width for half-intensity in cm^{-1}. But in this case, the oscillator strengths of hydrogen-bonded complexes and free β-naphthol were determined as done by Kubota.[9] The absorption bands of β-naphthol and its hydrogen-bonded complexes were plotted on graph paper separately on a large scale, and the oscillator strengths were calculated from these curves with a planimeter. These results were verified by counting the squares inside the whole area covered by the absorption band. The area of the absorption band corresponding to single electron transition was considered over the wave number range, 29,200 to 34,075 cm^{-1} for free β-naphthol and 28,570 to 33,900 cm^{-1} for complexed β-naphthol. The values of oscillator strengths are reported in Table I with other spectrophotometric data such as molar extinction coefficients, ϵ_c, and the band positions, ν_{max} (cm^{-1}) of hydrogen-bonded complexes.

Discussion

As is apparent from Tables I and II, the equilibrium constants and the thermodynamic quantities due to hydrogen bond formation between azaaromatics and β-naphthol increase in the order of increasing basicity
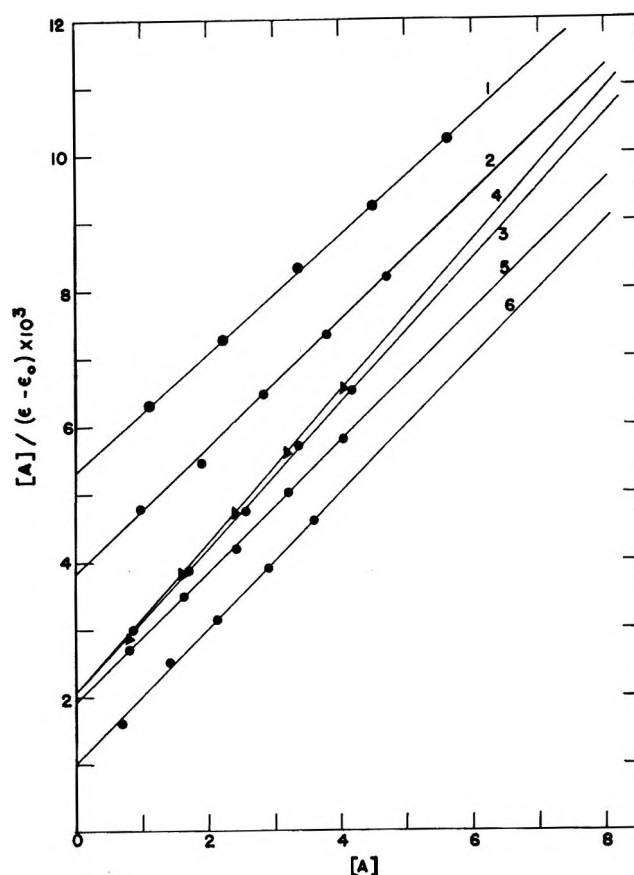
of azaaromatics. The linear relationship between the logarithms of the equilibrium constant for hydrogen bond formation of azaaromatics with β-naphthol and their pK values was shown before.[3] In the case of aromatic hydrocarbon complexes with β-naphthol, all the thermodynamic quantities and the equilibrium constants increase in the order mesitylene > xylene (m-, o-, p-) > toluene > benzene. The small equilibrium constants and relatively large heats of formation of the π complexes were explained before.[10] Aromatic hydrocarbons are weak Brønsted bases[11] and are capable of accepting a proton from proton donors. Thus the equilibrium constants of hydrogen-bonded complexes of aromatic hydrocarbons with β-naphthol should increase with increasing basicity of aromatic hydrocarbons like β-naphthol–azaaromatics complexes. The relation between logarithms of the equilibrium constants of aromatic hydrocarbons with β-naphthol and their pK values is shown in Table II. Table II also shows that

(8) H. Tsubomura and R. P. Lang, J. Amer. Chem. Soc., 83, 2085 (1961).

(9) T. Kubota, ibid., 88, 211 (1966).

(10) K. B. Whetsel and J. H. Lady, J. Phys. Chem., 69, 1596 (1965).

(11) M. G. Kuz'min, B. M. Uzhinov, and L. V. Berezin, Russ. J. Phys. Chem., 41, 222 (1967).

Table II: Equilibrium Constant and Wave Number Shift Due to Hydrogen-Bonded Complexes, Base Strength, and Ionization Potential of Azaaromatics and Aromatic Hydrocarbons

Proton acceptors	log K	pK	Δν, cm^{-1}	I.P., eV
Pyridine	1.823	5.17[a]	548	9.76[c]
2-Picoline	1.939	5.97[a]	602	9.66[c]
3-Picoline	1.899	5.68[a]	593	9.71[c]
4 Picoline	1.960	6.02[a]	619	9.56[c]
Benzene	−0.798	9.40[b]	194	9.24[d]
Toluene	−0.623	6.30[b]	203	8.82[d]
o-Xylene	−0.300	5.00[b]	208	8.58[d]
m-Xylene	−0.278	3.20[b]	208	8.58[d]
p-Xylene	−0.322	5.70[b]	208	8.48[d]
Mesitylene	−0.011	0.50[b]	217	8.39[d]

[a] E. A. Braude and F. C. Nachod, "Determination of Organic Structures by Physical Methods," Vol. 1, Academic Press, New York, N. Y., 1955, p 594. The pK values of azaaromatics refer to the base strength expressed as the dissociation of the conjugate acid in aqueous solution. [b] See ref 11. The pK values of aromatic hydrocarbons were determined in solution in liquid hydrogen fluoride. [c] H. Baba, I. Omura, and K. Higasi, *Bull. Chem. Soc. Jap.*, **29**, 521 (1956). These values are considered as n-ionization potential. Recent value reported for pyridine is 10.54 eV [R. S. Mulliken, *J. Amer. Chem. Soc.*, **91**, 1237 (1969)]. [d] K. Watanabe, *J. Chem. Phys.*, **26**, 542 (1957).

Δν, the spectral shift of β-naphthol due to hydrogen bonding, increases with −ΔH° of hydrogen-bonded complexes. On the other hand, the magnitude of the perturbation of β-naphthol produced by hydrogen bonding corresponds to the energy of formation of hydrogen bond. That is to say, the proton acceptors, 4-picoline and mesitylene, which form strongest hydrogen bond in each series, exert the largest effect on the absorption spectrum of the proton donor, β-naphthol. These two above correlations support the electrostatic attraction between proton donor and acceptor in hydrogen bonding.

According to charge-transfer mechanisms of hydrogen bonding,[12] proton donor and proton acceptor can be regarded as electron acceptor and electron donor, respectively, and the bonding energy may be interpreted as the stabilization energy mainly caused by the resonance of nonpolar and dative structures. It is expected that azaaromatic and aromatic hydrocarbon are, respectively, n- and π-electron donors to β-naphthol and the electron-donating power of azaaromatic or aromatic hydrocarbon depends on its respective ionization potential and the lower it is, the stronger is hydrogen bonding. The values of ionization potentials of azaaromatics and aromatic hydrocarbons are given in Table II. The relation between these ionization potentials and the stabilities (−ΔH°) of hydrogen-bonded complexes is in the right sequence. Further, the experimental results (Table I) of hydrogen-bonded complexes of β-naphthol with azaaromatics show that the stability of the com-

plex (−ΔH°) increases with the increase of the intensity, i.e., the oscillator strength of hydrogen-bonded band (f). This relation has also been found true; i.e., the intensity (f) of the absorption band of hydrogen-bonded complexes varies directly with the enthalpy change (−ΔH°) of trimethyl N-oxide complexes with phenol, β-naphthol, and α-naphthol,[9] but in the case of β-naphthol–aromatic hydrocarbons complexes, the experimental results show that the stability increases with the decrease of the intensity, and this disagrees with Mulliken's prediction. For strong charge-transfer complexes of iodine with azaaromatics, it has been shown experimentally that Mulliken's theory is correct,[6] but experimental results on weak charge-transfer complexes of iodine with aromatic hydrocarbons lead to a contrary opinion of that theory. Modifications to Mulliken's theory have been suggested to account for the observed discrepancy in such cases. The first modification involves the contribution from the nonbonded contact pairs to the charge-transfer intensity.[13] The second takes into account the possibility of interaction between the locally excited states of the donor and the charge-transfer states as a source of charge-transfer intensity.[14,15] Recently, this observed discrepancy in weak charge-transfer complexes has been discussed[16] considering second equilibrium between iodine and the solvent in addition to the normal iodine–aromatic hydrocarbon interaction. This iodine–solvent interaction does not allow one to estimate the exact stability and intensity of the normal complex, and it always decreases the stability and increases the apparent intensity of the normal complex. The influence of iodine–solvent interaction in the case of strong iodine azaaromatic complexes can be neglected owing to high equilibrium constants for the latter. In the case of weak hydrogen-bonded complexes, β-naphthol–solvent interaction or any other factor[17] may play an important role by decreasing the intensity of the absorption band of hydrogen-bonded complex of β-naphthol with aromatic hydrocarbon with increasing stability of the complex. This effect is negligible in strong hydrogen-bonded complex of β-naphthol with azaaromatic. Thus,

(12) K. Szczepaniak and A. Tramer, *J. Phys. Chem.*, **71**, 3035 (1967); earlier references are cited in this paper.

(13) L. E. Orgel and R. S. Mulliken, *J. Amer. Chem. Soc.*, **79**, 4839 (1957).

(14) J. N. Murrell, *ibid.*, **81**, 5037 (1959).

(15) M. Chowdhury and L. Goodman, *ibid.*, **86**, 2777 (1964).

(16) B. B. Bhowmik, *Spectrochim. Acta.*, in press.

(17) One referee has raised a point concerning the activity coefficients of aromatic hydrocarbons in cyclohexane solution due to their high concentration. Experimentally determined values of activity coefficients of aromatic hydrocarbons are not available. Using evaluated values for benzene in cyclohexane [S. K. Suri and V. Ramakrishna, *J. Phys. Chem.*, **72**, 1555 (1968)] and assuming that other aromatic hydrocarbons should have the same activity coefficients at same concentrations, the equilibrium constants and molar extinction coefficients of weak hydrogen-bonded complexes have been calculated. These values are different from Table I, but the relationship remains the same; i.e., the equilibrium constant increases with decreasing molar extinction coefficient.

Dielectric Behavior of Helical Polyamino Acids in Shear Gradients

by Shiro Takashima

Electromedical Division, Moore School of Electrical Engineering, University of Pennsylvania,
Philadelphia, Pennsylvania 19104   (Received January 26, 1970)

The dielectric constant of α-helical polybenzyl-L-glutamate (PBLG) and polymethyl-L-glutamate (PMLG) is measured in a rotating dielectric cell in the presence of a velocity gradient as well as an electric field. In the present experimental arrangement, the electric field and the mechanical force vector are perpendicular to each other. The dielectric cell is built in a birefringence measuring apparatus, and it enables us to determine the extinction angle as well as the dielectric constant. It was found that the dielectric constant of PBLG solutions decreased substantially when velocity gradients are applied. This result is interpreted as the indication that PBLG has a large longitudinal moment as has been postulated. The results obtained in this work also indicate that a small transverse moment is present. The transverse moment is tentatively attributed to molecular aggregates of PBLG of unknown size, dimers, trimers, and most probably a mixture of various sizes. Contrary to PBLG, the dielectric behavior of PMLG is only slightly affected by the velocity gradient. The dielectric behavior of these polymers in the presence of a mechanical force is analyzed on the basis of the simultaneously measured orientation parameters.

Introduction

Measurement of dielectric constants of biological polymers in the presence of a mechanical force was first carried out by Jacobsen,[1] Jacobsen and Wenner,[2] and subsequently by Jerrard and Simmons.[3] Jacobsen and Wenner found that the dielectric increment of the DNA solution decreased when a mechanical force was applied perpendicular to the electric field while that of a protein, hemocyanin, was unaffected. They concluded from these observations that the electric polarization of DNA is due to the molecular orientation in its entirety and that the polarization of the protein is not due to a molecular orientation but due only to the bound water. These observations, however, can be better explained if they are assumed to be due to the large anisotropic polarizability of the DNA molecule.[4]

Recently, Takashima[5] reported that the dielectric constant of a helical polyamino acid, polybenzyl-L-glutamate (PBLG), decreased considerably when these molecules are aligned perpendicularly to the electric field by applying a velocity gradient. Takashima interpreted this result as the indication that PBLG has an anisotropic electric polarizability along the longitudinal axis. The results obtained by this author, however, indicate that there is a minor dipole moment in the transverse direction. This conclusion, however, cannot easily be accepted on the basis that α-helical polyamino acids have a spiral symmetry, and the possible transverse moment should be vanishingly small because of the mutual cancellation. Further experiments are, therefore, carried out with a larger PBLG sample. The experimental data, in particular with high velocity gradients, are carefully analyzed.

The dielectric behavior of polymethyl-L-glutamate (PMLG) is also investigated with and without the velocity gradient. Contrary to PBLG, the dielectric constant of PMLG solutions is decreased by the velocity gradient only slightly.

The interpretation of these observations is greatly facilitated by the exact knowledge of the orientational

(1) B. Jacobsen, *Rev. Sci. Instrum.,* **24,** 949 (1953).

(2) B. Jacobsen and M. Wenner, *Biochim. Biophys. Acta,* **13,** 3604 (1956).

(3) H. G. Jerrard and B. A. W. Simmons, *Nature,* **184,** 1715 (1959).

(4) S. Takashima, "Advances in Chemistry Series," No. 63, American Chemical Society, Washington, D. C., 1963, p 203.

(5) S. Takashima, Symposium on Ordered Fluids and Liquid Crystals, New York, N. Y., 1969.

behavior of these polymers in the velocity gradients. In the previous experiments by Jacobsen and Wenner[2] and by Jerrard and Simmons,[3] the rotating dielectric cell arrangements were such that the actual molecular orientation of polymers in the velocity gradient could not be measured. In the present experiment, the rotating dielectric cell is built in a flow birefringence apparatus so that dielectric constant as well as extinction angle can be measured simultaneously. Therefore, we can analyze the change in the dielectric constant of polymers due to the velocity gradient in terms of an exact knowledge of the average orientation of polymer molecules. Without this additional information, quantitative analyses do not seem meaningful.

Experimental Section

The impedance bridge used for these measurements was designed by Schwan,[6] and the details are described elsewhere. The bridge operates between 100 Hz and 200 KHz with a resolution of ± 0.1 $\mu\mu$F in the capacity reading and ± 0.001 μmho in the conductance reading. The resolution decreases somewhat below 100 Hz but is still sufficiently accurate to warrant a dielectric constant to the second decimal point. The lowest frequency used with a reasonable accuracy is 50 Hz.

The electrodes consist of two concentric stainless steel cylinders whose diameters are 39 and 40 mm, respectively. The annular gap between the inner and outer cylinders is, therefore, 0.5 mm. The outer cylinder is rotated to produce a velocity gradient. The velocity gradient used in these measurements ranges from 0 to 4400 sec^{-1}. The inner cylinder is static and connected to the high potential side of the bridge. The rotating outer cylinder is connected to the ground of the bridge using a silver-plated brush. The electrical noise due to friction is usually small except at very low rotation. At higher rotations and, in particular, at low frequencies, the disturbance of the bridge reading due to the friction is negligible. The temperature in the annular gap was not measured during the rotation. However, at high rotations, a slight temperature rise is noted although the cell is rigorously cooled, by the slow increase of the conductivity of the solution. The dielectric constant is, however, unaffected by the small temperature rise.

The dielectric cell was fitted into the flow birefringence apparatus Rao B-22 and was placed between a polarizer and an analyzer. The static inner cylinder was carefully insulated by replacing the metal parts, which were originally used by the manufacturer, by plastic parts. The measurements of the extinction angle and birefringence was described in detail by Edsall[7] and will not be repeated. The dielectric constant of a solution using the coaxial cell is calculated by

$$\epsilon = \frac{C_s - C_0}{C_{sol} - C_0}\epsilon_{sol} \qquad (1)$$

where C_s, C_{sol}, and C_0 are the capacities of the cell with the sample, with the solvent, and with air, respectively. ϵ_{sol} is the dielectric constant of solvents. The dipole moment is calculated by[8]

$$\mu = 2.36\sqrt{M\Delta\delta}D \qquad (2)$$

where M is the molecular weight and $\Delta\delta$ is the dielectric increment per gram per liter.

An electric field is applied across the annular gap, and the gap is simultaneously illuminated through the strain free glass bottom. The dielectric constant as well as the extinction angle is measured at different frequencies with various velocity gradients. The direction of the electric field is perpendicular to the mechanical force in these experiments. The application of a mechanical force parallel to the electric field is not attempted in the present experiment.

Two polyamino acids are investigated in this research, i.e., polybenzyl-L-glutamate and polymethyl-L-glutamate. The molecular weights of PBLG samples are 200,000 and 335,000, respectively. PBLG was dissolved in helix-forming solvents such as dioxane, ethylene dichloride, ethylene dibromide, and m-cresol. Dioxane was found to be, by far, the best solvent for this investigation because of the low dielectric constant and low conductivity. The molecular weight of PMLG is 300,000. PMLG was dissolved in chloroform, and the dielectric properties were investigated. Since the dielectric behavior of PMLG has not been studied, efforts were made to establish the dielectric relaxation of this polymer before the effect of the velocity gradient was investigated.

The rotary diffusion constants of these samples at various velocity gradients were studied before the dielectric measurements. The effective length of these samples was calculated from the rotary diffusion constant using the approximate Perrin equation[13]

$$\theta_b = \frac{3KT}{16\pi\eta a^3}\left(2\ln\frac{2a}{b} - 1\right) \qquad (3)$$

(where θ_b is the rotary diffusion constant along the major axis, a and b are the major and minor axes, respectively, and η is the viscosity of the solvent). The results of these measurements are summarized in Table I. It should be noted that the effective length of PBLD is strongly dependent on the concentration. These data will be discussed later in conjunction with their dielectric behavior in the velocity gradient.

Results

A. Polybenzyl-L-glutamate. The frequency profile of the dielectric constant of PBLG at two concentrations

(6) H. P. Schwan, "Physical Technology in Biological Research," Vol. 6, Academic Press, New York, N. Y., 1963, Chapter 6.

(7) J. T. Edsall, *Advan. Colloid Sci.*, 1, 269 (1942).

(8) J. L. Oncley, "Protein Amino Acids and Peptides," Cohn and Edsall, Ed., Reinhold, New York, N. Y., 1943.

Table I: Orientation Parameters and the Length of PBLG and PMLG (Velocity Gradient: 3620 sec^{-1})

Concentration, g/l.	Extinction angle, deg	Rotary diff. constant, sec^{-1}	Length, Å
PBLG (molecular weight: 335,000)			
4.0	16.8	260	4400
11.0	12.8	148	5400
PBLG (molecular weight: 200,000)			
4.0	28.0	813	2840
16.8	21.4	435	3760
PMLG (molecular weight: 300,000)			
2.5	28.3	804	2960

Figure 2. Concentration dependence of the dielectric increment per gram per liter: curve 1, PBLG, and curve 2, PMLG.

Figure 1. Frequency profile of the dielectric constant of PBLG with and without the velocity gradient. Curve 1, without the velocity gradient, and curve 2, with the velocity gradient 3620 sec^{-1}; concentration 16.8 g/l.; molecular weight: 200,000. Curves 3 and 4 (concentration 4 g/l.) are the same sample with and without the velocity gradient.

Figure 3. Effect of the velocity gradient on the dielectric constant of PBLG at various frequencies. The ordinate is the dielectric constant and the abscissa is the velocity gradient. Curve 1, extrapolated zero frequency dielectric constant ϵ_0; curve 2, at 50 Hz; curve 3, 70 Hz; curve 4, 100 Hz; and curve 5, 200 Hz.

without the velocity gradient is shown in Figure 1 (curves 1 and 3). The curves are obtained with a PBLG sample with a molecular weight 200,000. The result obtained with a sample with a molecular weight 335,000 is shown in Figure 4 (curve 1). The dielectric increment per gram per liter is obtained at the infinite dilution (see Figure 2) and found to be 1.05 for the molecular weight 335,000. From this value, the dipole moment is calculated to be 1400 D. The relaxation time for the same sample is 1.6×10^{-3} sec. These values are slightly different from those reported by Wada.[9,10] However, considering the uncertainty of the molecular weight determination and the strong dependence of the dielectric properties on the molecular weight, the difference between Wada's observation and the present results is not substantial.

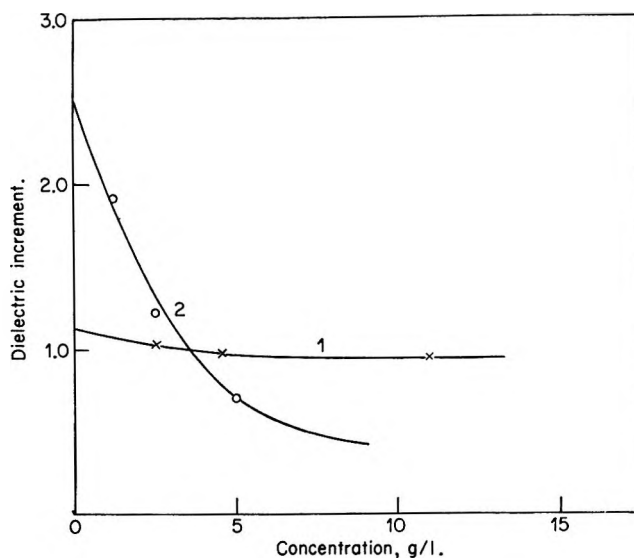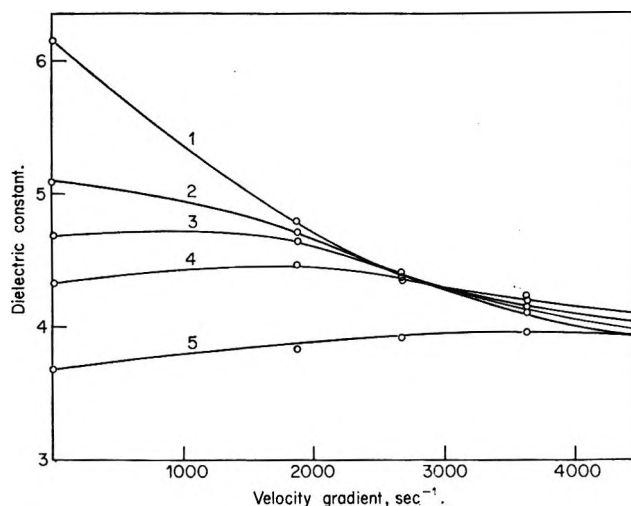Having confirmed that the present system produces

reasonable results which are in agreement with the previous results, the effect of velocity gradient on the dielectric properties was investigated. The dielectric constant of the PBLG solution was measured with various velocity gradients at different frequencies. The results at a few frequencies are illustrated in Figure 3 where the change in the dielectric constant is plotted against the velocity gradient. As is obvious from this figure, the velocity gradient decreases the dielectric

(9) A. Wada, *J. Chem. Phys.*, **31**, 495 (1959).

(10) A. Wada, "Polyamino Acids, Polyelectrolytes, and Proteins," M. A. Stahman, Ed., University of Wisconsin Press, Madison, Wis., 1962.

constant of the PBLG solution considerably if the frequency is sufficiently low.

The decrease, however, levels off at high velocity gradients and curves seem to approach certain values asymptotically which are still higher than that of the solvent. It must be noted that these curves do not seem to approach the dielectric constant of the solvent (2 in this case). However, as will be discussed later, we cannot extrapolate these curves with certainty unless we can measure the dielectric constant with even higher velocity gradients. If the frequency is increased, the effect of the velocity gradient is reversed, and the dielectric constant of the solution increases instead of a decrease. Although the increase observed at these frequencies is not large, the measurements are sufficiently accurate to detect the small change. As the frequency is further increased, the effect of the velocity gradient becomes vanishingly small. This seemingly complex effect of the velocity gradient can better be understood when the dielectric constant of the solution in the presence of the velocity gradient is replotted against the frequency (Figure 1, curve 2). Curve 1 is obtained without the velocity gradient, and curve 2 is obtained with a velocity gradient 3620 sec^{-1}. Similar curves can be drawn for velocity gradients between 0 and 3620 sec^{-1}. Extending these dispersion curves, we obtain the zero frequency dielectric constant ϵ_0 for each velocity gradient, and these values are plotted in Figure 3 (curve 1). This curve represents the true effect of velocity gradient on the total dielectric increment of PBLG. It must be noted in Figure 1 that as frequency increases, two curves cross over and the dielectric constant without the velocity gradient becomes lower than that with velocity gradient. This behavior can best be understood if we assume that PBLG has two dipolar components, one of which decreases with increasing velocity gradient and the other, a component which increases with the velocity gradient.

The effect of the velocity gradient diminishes considerably when the concentration is lowered (curves 3 and 4). It is shown in Table I that the effective length PBLG decreases on dilution. Obviously we need a greater velocity gradient to cause a substantial orientation for dilute solution.

The effect of the velocity gradient becomes more pronounced even at low concentrations when the larger PBLG sample is used. Figure 4 shows the result of these measurements. The dielectric relaxation of this sample is found in a very low frequency region and the low-frequency plateau is not reached even at 50 Hz. When the velocity gradient is applied, the dispersion curve is profoundly affected. The dispersion curve shifts toward a higher frequency region and the low-frequency plateau is clearly observed. Not only the change in the dielectric constant and relaxation frequency, the shape of the dispersion curve
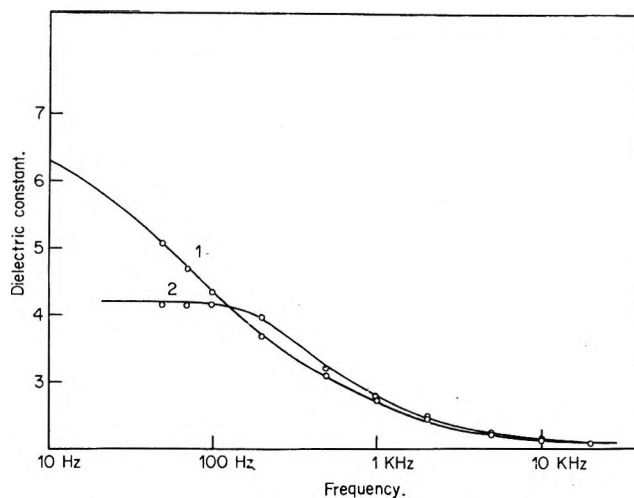

Figure 4. Frequency profile of the dielectric constant of PBLG with and without the velocity gradient. Curve 1, without the velocity gradient, and curve 2, with the velocity gradient. Molecular weight of the sample is 335,000.
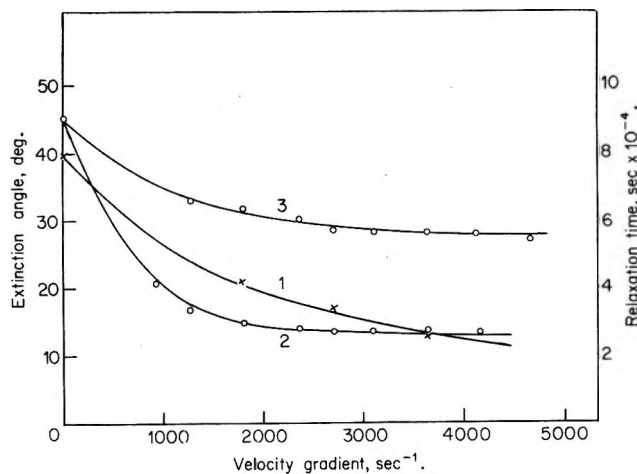

Figure 5. Dependence of the relaxation time of PBLG (curve 1) and the extinction angle of PBLG (curve 2) and PMLG (curve 3) on the velocity gradient. The left ordinate is the extinction angle and the right scale is the relaxation time.

is also altered considerably. These, again, indicate the presence of a second, although it is small, relaxation process which is normally swamped into the larger low-frequency relaxation process. The low-frequency relaxation can be interpreted as due to the longitudinal moment and the latter due to the small transverse moment. If the transverse component does not exist, the dielectric constant should decrease monotonically without changing the relaxation frequency. In the limiting case where a very high velocity gradient is applied, the dielectric constant of the solution should converge to a value which is slightly smaller than that of the solvent. On the contrary, we observe that the velocity gradient changes the relaxation frequency, which, in the end, approaches a certain limiting value. The relaxation time ($=2\pi f_c$, where f_c is the
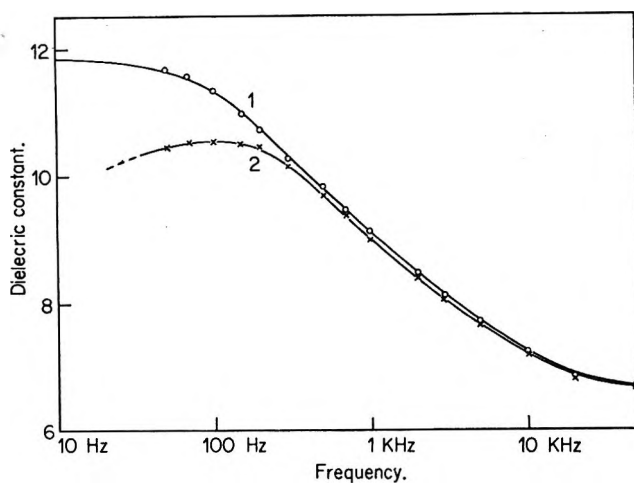
Figure 6. Frequency dependence of the dielectric constant of PMLG in chloroform. Curve 1, without the velocity gradient, and curve 2, with the velocity gradient 3620 sec^{-1}; molecular weight, 300,000.

relaxation frequency) is plotted against the applied velocity gradient (see Figure 5). This curve should be compared with the variation of the extinction angle measured with the same sample. The parallelism between these curves indicates a close correlation between the change of the relaxation time and the molecular orientation in the velocity gradient.

B. Polymethyl-L-glutamate. Since the dielectric relaxation of PMLG has not hitherto been investigated, it seems necessary to establish the relaxation curve before we study the effect of a velocity gradient. The molecular weight of PMLG used is 300,000 and is comparable to one of the PBLG samples. It is noted in Table I that the rotary diffusion constant of PMLG is higher than that of PBLG, and the effective length is considerably shorter than PBLG. These results will be discussed later again in conjunction with the dielectric properties.

The frequency profile of the dielectric constant of PMLG in chloroform is shown in Figure 6. The following remarks are made as to the dielectric dispersion curve of PMLG.

(1) The dielectric increment of PMLG is plotted as a function of the concentration as shown in Figure 2. The increment per gram strongly depends on the concentration, and the true increment value must be obtained by the extrapolation from which we obtain a value 2.4 g^{-1} l.$^{-1}$. This gives rise to a dipole moment 2020 D. This value is larger than that of PBLG with the same molecular weight.

(2) The relaxation frequency of PMLG in chloroform is found to be 1.5 kHz, which gives rise to a relaxation time 1.04 × 10^{-4} sec. This value is much lower than that of PBLG although the molecular weights of both samples are comparable.

Having obtained the dielectric dispersion curve for PMLG, the effect of the velocity gradient on the

dielectric behavior of PMLG was then investigated. The dispersion curves of PMLG with and without the velocity gradient are shown in Figure 6. Clearly, the velocity gradient has only a small effect in this case. The change in the zero frequency dielectric constant ϵ_0 is only from 11.65 to 10.43 This behavior is drastically different from that of PBLG in dioxane.

At this point, it is indeed appropriate to discuss the orientational behavior of PMLG in chloroform as shown in Table I and Figure 5. The extinction angle of PMLG is actually much larger than that of PBLG, indicating that the average inclination of PMLG with respect to the stream line is still very little even at high velocity gradients. This in turn means that PMLG is in nearly a randomly oriented state. Clearly the observed little effect of velocity gradient on PMLG is due to the fact that the velocity gradient used is not simply sufficient to orient PMLG molecules, and the above results should not be interpreted as the indication of the presence of a large transverse moment. This situation is similar to the dilute PBLG solution (curves 3 and 4, Figure 1). Measurements at higher concentrations of PMLG turned out to be very difficult because of the very high viscosity.

Discussion

The experimental observations described above unequivocally prove that helical polyamino acids have a major dipole moment along the longitudinal axis as has been postulated.[9,10] These results, however, indicate the presence of a small transverse moment. Since this result is somewhat intriguing, more discussion seems necessary.

The dielectric behavior of flexible polymers in a laminar flow is treated theoretically by Saito, *et al.*,[11] for the case of the longitudinal dipole moment and by Peterlin, *et al.*,[12] for the case of the transverse moment. In the present research α helix is a rigid rod, and we can safely assume that the velocity gradient does not unfold the polymer chain. In this case, the theoretical treatment is much simpler.

Figure 7 illustrates the behavior of a polar molecule in an electric field. The measured mean moment of a group of polar molecules with a dipole moment μ is given by $\mu \cos \theta$, where $\overline{\cos \theta}$ is the mean direction cosine.[13] When the field intensity is strong enough and all the molecules are aligned along the vector of the electric field, the mean direction cosine is unity and the mean moment is exactly equal to the dipole moment μ. On the other hand, if the field intensity is very small, the direction cosine becomes nearly zero and the mean moment reduces to zero. If a mechanical force is applied in perpendicular to that

(11) N. Saito and T. Kato, *J. Phys. Soc. Jap.*, **12**, 1383 (1957).

(12) A. Peterlin and C. Reinhold, *Kolloid-Z.*, **5**, 23 (1965).

(13) P. Debye, "Polar Molecules," Dover Publications, New York, N. Y., 1929.
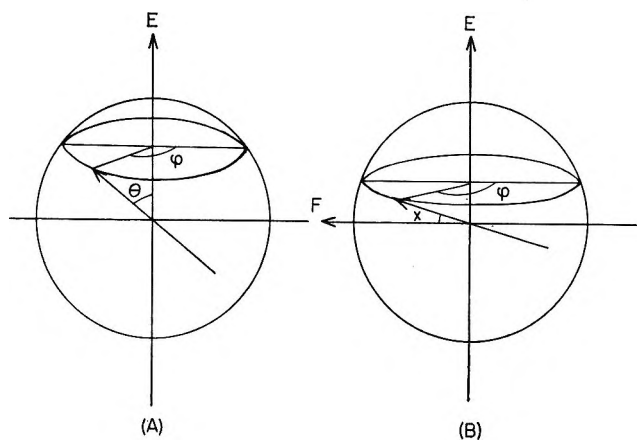
Figure 7. (a) Behavior of a polar molecule in an electric field without the velocity gradient. E represents the electric field. (b) Behavior of a polar molecule in an electric field with a perpendicularly applied mechanical force. The arrows E and F represent the electrical and mechanical forces.

Figure 8. The dielectric increment per gram per liter of PBLG and PMLG vs. the reciprocal of the velocity gradient (1/G). Curves 1 and 2 represent PBLG with a molecular weight 200,000 and 335,000. Curve 3 is PMLG with a molecular weight 300,000.

of the electric field (Figure 7b) and if the mechanical force is much greater than that of the electric field, the direction cosine will be substantially altered. In extreme cases, the mechanical force orients the molecules perpendicularly to the electric field, thus making the average direction cosine $\overline{\cos\theta}$ zero. In those cases, the dipole moment along the major axis ceases to contribute to the mean moment. If the polar molecule has only a longitudinal moment, the measured mean moment will reduce to zero if the mechanical force is infinitely large. Of course, we cannot create a sufficiently large shearing force to produce a complete orientation. However, we can obtain experimental points at finite velocity gradients and extrapolate these points to the infinite velocity gradient choosing an appropriate coordinate system.

Figure 8 illustrates the decrease of the dielectric constant as a function of the reciprocal of the velocity gradient. The extrapolations are made through the experimental points to $1/G = 0$. Unfortunately, the plot of the dielectric increment vs. $1/G$ is not linear, and there is certain uncertainty in the extrapolated value. However, the extrapolated increment value seems to be nonzero though it is small. Although measurements at higher velocity gradients are desirable in order to make the extrapolation more accurate, it seems reasonable to conclude that there is a small transverse moment in addition to the large longitudinal moment.

We now have to discuss the origin of the transverse moment. From Table I, we find that the effective length of PBLG in dioxane is about 3500–4000 Å. Since the PBLG used in this experiment has a molecular weight 335,000, the length of a PBLG molecule should be less than 2500 Å if we assume that PBLG is 100% helix. That is, the measured effective length of PBLG is considerably longer than the possible theoretical
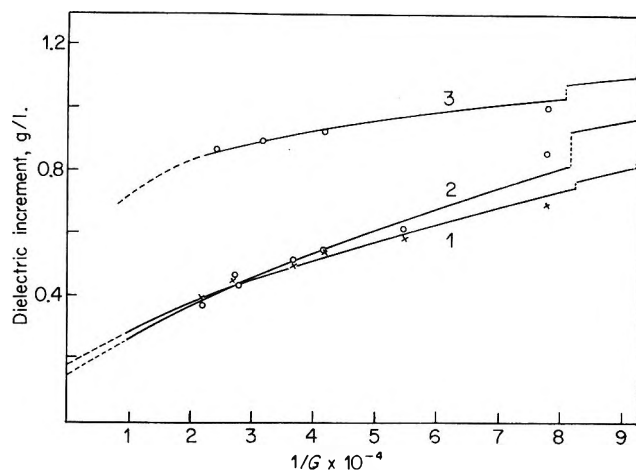
length. This is a strong indication that PBLG molecules, or some fraction of it, form aggregates of various sizes. This discussion is further supported by the fact that the effective length of PBLG decreases as the concentration is lowered. The same discussion holds for the smaller PBLG sample with the molecular weight 200,000 (see Table I). As Doty, et al.,[14] stated, PBLG forms an end-to-end dimer with small angle between them. In reality, however, it is more likely that PBLG forms aggregates of various sizes.[15] It is then readily understood that the aggregate formation will create a transverse moment even if the individual PBLG molecule has no transverse moment.

If PBLG has a longitudinal and a transverse moment, we can treat the relaxation of PBLG with two time constants. Consequently, the dielectric relaxation of PBLG can be expressed by

$$\epsilon = \epsilon_\infty + \frac{\Delta\epsilon_1}{1 + (f/f_1)^2} + \frac{\Delta\epsilon_2}{1 + (f/f_2)^2} \qquad (4)$$

where $\Delta\epsilon_1$ and $\Delta\epsilon_2$ are the dielectric increments along the longitudinal and the transverse axes; f_1 and f_2 are the relaxation frequencies along these axes. Since the relaxation time is controlled by the rotary diffusion of the molecule, we can calculate the relaxation times $\tau_1(1/2\pi f_1)$ and $\tau_2(1/2\pi f_2)$ approximately by use of Perrin's equation.[16] The relaxation time along the longitudinal axis can be calculated using eq 3. The relaxation time along the transverse axis can be calculated by using eq 5

(14) P. Doty, J. H. Bradbury, and A. M. Holtzer. J. Amer. Chem. Soc., 76, 947 (1956).

(15) S. Takashima, Biopolymers, 2, 287 (1964).

(16) F. Perrin, J. Phys. Radium, 7, 5, 497 (1934).

$$\frac{\tau_b}{\tau_0} = \frac{4}{3[1 - (b/a)^2 \ln (2a/b)]} \quad (5)$$

where τ_0 is the relaxation time of an equivalent sphere and is calculated by

$$\tau_0 = kT/8\pi ab^2\eta \quad (6)$$

where η is the viscosity of the solvent in poises. The following values are calculated assuming that the major axis of PBLG is 4000 Å and varying b from 20 to 200 Å.

Experimentally, we find, from Figure 5, that the relaxation time of PBLG approaches a value 2.0×10^{-4} sec in the presence of a large velocity gradient. Unfortunately, the plot τ vs. $1/G$ is very nonlinear, and we cannot obtain the relaxation time along the transverse axis by extrapolation. However, if we assume the value 2.0×10^{-4} sec is close enough to the transverse relaxation time, we find, from Table II,

Table II: Calculated Transverse Relaxation Time (τ_b) of Cylindrical Polymers. Major Axis a Assumed To Be 4000 Å

a, Å	4000				
b, Å	20	50	100	150	200
$\tau_b \times 10^{-4}$	0.037	0.227	0.9	2.03	3.6

that this time constant corresponds to an effective axis 150 Å. This value is certainly much larger than the radius of a single α helix even with large side chains. Therefore, the observed small transverse moment is most likely not due to the transverse moment of an individual α helix but to molecular aggregates of various sizes.

Now we turn to PMLG. From Table I, we find that the effective length of PMLG in chloroform is approximately 3000 Å. Theoretically, a PMLG molecule with a molecular weight 300,000 should have a length about 2800 Å assuming that they are 100% helix. Therefore, PMLG in chloroform behaves as if it is a single unit rather than an aggregate. Apparently, a very large velocity gradient is required to produce a substantial orientation of PMLG molecule along the stream line. The velocity gradient produced by the present system is simply inadequate for the purpose of this measurement. Nevertheless, curve 3 in Figure 7 shows that the velocity gradient, although it is not sufficiently large, decreases the dielectric increment of PMLG solution.

COMMUNICATIONS TO THE EDITOR

Comparison of Ion-Exchange Plate Heights Calculated from Countercurrent Extraction and Rate Theory[1a]

Sir: Recently, Hagiwara developed equations for calculating the theoretical plate height in ion-exchange displacement development processes.[1b] With these equations, derived from fundamental rate theory, Hagiwara studied the elution behavior of several pairs of adjacent rare earths with common chelating agents and was able to determine the rate-controlling mechanism (film or particle diffusion).[1-3]

Hagiwara also noted that the plate height calculated from rate theory agreed with that calculated from the countercurrent extraction theory of Powell and Spedding.[4] We wish to point out that the plate height values agree because the equations of Hagiwara and Powell and Spedding are similar, becoming identical in the limit of identical metal chelate stability constants for the ions being separated.

For the separation of two rare earth ions (A and B) by displacement development with a chelating agent (Y), assume that A elutes from the column first, followed by the A–B overlap region, and then by pure B. A forms a stronger complex with Y than does B ($K_{AY} > K_{BY}$). At a given plane in the A–B overlap region, assuming particle diffusion is the rate-determining step in the ion exchange process, Hagiwara derived the equation

$$Z = \frac{H_p}{\alpha - 1}[-\ln x + \alpha \ln (1 - x) + (\alpha - 1)C_1] \quad (1)$$

(1) (a) The information contained in this article was developed during the course of work under Contract AT(07-2)-1 with the U. S. Atomic Energy Commission. (b) Z. Hagiwara, *J. Inorg. Nucl. Chem.*, **31,** 2933 (1969).

(2) Z. Hagiwara, *J. Phys. Chem.*, **73,** 3102 (1969).

(3) Z. Hagiwara, A. Banno, and A. Kamei, *J. Inorg. Nucl. Chem.*, **31,** 3295 (1969).

(4) J. E. Powell and F. H. Spedding, *Chem. Eng. Progr., Symp. Ser.*, **55,** 101 (1959).

where Z = distance of the plane from an arbitrary reference plane, H_p = plate height for particle diffusion control, $\alpha = K_{AY}/K_{BY}$, x = mole fraction of B, and C_1 = constant of integration.

By requiring $\int_0^1 Z dx = 0$, Hagiwara calculated $C_1 = 1$. With the slightly different, but more useful experimentally, boundary condition that $Z = 0$ at $x = 0.5$, we obtain $C_1 = \ln 2$ and

$$H_p = \frac{(\alpha - 1)(Z)}{\ln [(1 - x)^\alpha/x] + (\ln 2)(\alpha - 1)} \quad (2)$$

Z is negative when $x > 0.5$.

Similarly, Hagiwara's plate height for film diffusion control can be written as

$$H_f = \frac{(\alpha - 1)(Z)}{\ln [(1 - x)/x^\alpha] - (\ln 2)(\alpha - 1)} \quad (3)$$

The equation derived by Powell and Spedding from countercurrent extraction theory is

$$\ln \frac{R_1}{R_2} = \frac{(Z_1 - Z_2) \ln \alpha}{h} \quad (4)$$

where R_1 = ratio of A to B at a plane with coordinate Z_1, R_2 = ratio of A to B at a plane with coordinate Z_2, and h = theoretical plate-height from countercurrent extraction theory.

Replacing R with $(1 - x)/x$ and using the same boundary condition as before

$$h = \frac{Z \ln \alpha}{\ln [(1 - x)/x]} \quad (5)$$

Dividing eq 2 and 3 by eq 5 gives

$$\frac{H_p}{h} = \left(\frac{\alpha - 1}{\ln \alpha}\right) \frac{\ln [(1 - x)/x]}{\ln [(1 - x)^\alpha/x] + (\ln 2)(\alpha - 1)} \quad (6)$$

$$\frac{H_f}{h} = \left(\frac{\alpha - 1}{\ln \alpha}\right) \frac{\ln [(1 - x)/x]}{\ln [(1 - x)/x^\alpha] - (\ln 2)(\alpha - 1)} \quad (7)$$

Because $(\alpha - 1)$ is the first term in the power series expansion of $\ln \alpha$, H_p/h and H_f/h approach 1 as α approaches 1.

If points 1 and 2 are any two points in the A–B overlap region, more general equations for H_p/h and H_f/h can be written as follows

$$\frac{H_p}{h} = \frac{\alpha - 1}{\ln \alpha} \frac{\ln \left[\left(\frac{x_2}{x_1}\right)\left(\frac{1 - x_1}{1 - x_2}\right)\right]}{\ln \left[\left(\frac{x_2}{x_1}\right)\left(\frac{1 - x_1}{1 - x_2}\right)^\alpha\right]} \quad (8)$$

$$\frac{H_f}{h} = \frac{\alpha - 1}{\ln \alpha} \frac{\ln \left[\left(\frac{x_1}{x_2}\right)\left(\frac{1 - x_1}{1 - x_2}\right)\right]}{\ln \left[\left(\frac{x_2}{x_1}\right)^\alpha \left(\frac{1 - x_1}{1 - x_2}\right)\right]} \quad (9)$$

With the boundary condition, $x_2 = 0.5$ at $Z_2 = 0$,

Table I

x	$\alpha = 1.10$		$\alpha = 1.50$		$\alpha = 2.00$	
	H_p/h	H_f/h	H_p/h	H_f/h	H_p/h	H_f/h
0.01	1.034	0.967	1.148	0.865	1.256	0.779
0.10	1.022	0.978	1.088	0.903	1.138	0.833
0.30	1.009	0.990	1.029	0.948	1.033	0.900
0.49	1.000	0.999	0.988	0.985	0.965	0.959
0.51	0.999	1.000	0.985	0.988	0.959	0.965
0.70	0.990	1.009	0.948	1.029	0.900	1.033
0.90	0.978	1.022	0.903	1.088	0.833	1.138
0.99	0.967	1.034	0.865	1.148	0.779	1.256

values of H_p/h and H_f/h as a function of x have been calculated for several values of α as shown below in Table I.

The h in Powell and Spedding's work is usually determined from the slope of a log R vs. Z plot. The values of h can be either higher (data weighted toward values of $x > 0.5$) or lower ($x < 0.5$) than H_p values obtained by curve fitting. In any case, plate heights calculated from countercurrent extraction and rate theories must be in close agreement because the mathematical forms are similar, not necessarily because "the elution system had arrived at a state of dynamic equilibrum."[2]

Savannah River Laboratory   William H. Hale, Jr.
E. I. du Pont de Nemours and Co.
Aiken, South Carolina 29801

## Semiideal Behavior of Solutions of Solvated Nonelectrolytes

Sir: Garrod and Herrington[1] have claimed that the water activities and activity coefficients of sucrose solutions are inconsistent with eq 40 of their paper so that sucrose solutions cannot be described as "semi-ideal dilute." Since we have demonstrated[2] that an essentially similar semiideal model unrestricted to dilute solutions does adequately describe the behavior of sucrose solutions, it is necessary to discuss their argument. They find for the case where a solute s interacts with water to form various hydrates, denoting the actual mole fractions of each species at equilibrium by η_w, η_s, η_{sw}, etc. (N_w, N_0, N_1, etc., in the notation of our previous paper[2]), that $\eta_s + \eta_w < 1$, which is indeed obvious from the definition of mole fractions, as long as at least one other species such as sw is present at all. In terms of their "semi-ideal dilute" solution model they

(1) J. E. Garrod and T. M. Herrington, *J. Phys. Chem.*, **74**, 363 (1970).

(2) R. H. Stokes and R. A. Robinson, *ibid.*, **70**, 2126 (1966).

then correctly put in their eq 37 $\eta_w = a_w$, where a_w is the conventional water activity, and incorrectly, $\eta_s = \gamma_{x,s} \cdot X_s$, where X_s is the stoichiometric mole-fraction of solute, and $\gamma_{x,s}$ is "the activity coefficient of the solute on the Henry's law mole fraction scale". It is apparent from their eq 39 that their $\gamma_{x,s}$ is to be identified with the conventional mole fraction scale activity coefficient.[3]

Irrespective of what activity scales are used, the total Gibbs energy of a fixed quantity of a given solution is invariant. For simplicity let us consider the case of a solute s in equilibrium with a *single* hydrate sw
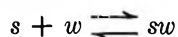
$$s + w \rightleftharpoons sw$$

Taking 1 kg of water containing m mol of total solute, we let m_s denote the number of moles of the anhydrous species s present at equilibrium. Then the total free energy of the solution can be written

$$G = (0.001M_1 + m_s - m)\mu_w + m_s\mu_s + (m - m_s)\mu_{sw}$$

which, since $\mu_{sw} = \mu_s + \mu_w$ at equilibrium, reduces to

$$G = (0.001M_1)\mu_w + m\mu_s$$

But the free energy G can also be written in terms of the conventional chemical potential of the solute, μ_B

$$G = (0.001M_1)\mu_w + m\mu_B$$

so that

$$\mu_B = \mu_s \tag{1}$$

In terms of activities, this becomes

$$\mu_B{}^0 + RT \ln m + RT \ln \gamma =$$
$$\mu_s{}^0 + RT \ln \eta_s + RT \ln f_s \tag{2}$$

where γ is the conventional stoichiometric molal activity coefficient, and superscript zeros denote the *appropriate* standard states.

It should be noted that (1) does not imply $\mu_B{}^0 = \mu_s{}^0$ in the standard states; the standard state for B is a *hypothetical* solution of total solute molality m unity and molal scale activity coefficient unity, containing both the anhydrous solute and the solvate, while the standard state for s is a hypothetical solution of mole-fraction $X_s = 1$, containing the anhydrous solute s only. Likewise, that for sw is a hypothetical solution with $X_{sw} = 1$, containing no anhydrous solute.

At infinite dilution, $a_w = 1$, the solute consists of s and sw in the ratio $\lim (m - m_s)/m_s = K$, $\lim m_s/m = 1/(1 + K)$, and all activity coefficients are unity, $K = \eta_{sw}/(\eta_s a_w)$ being the mole fraction scale equilibrium constant for the hydration process. On Garrod and Herrington's "semiideal dilute" model, $f_s = 1$ at all concentrations so that (2) becomes

$$\eta_s = Am\gamma \tag{3}$$

where A is a constant involving the differences of

chemical potentials in the standard states for B and s. We evaluate this constant in the usual way by finding the limit of (η_s/m) as all solute concentrations tend to zero and $\gamma \rightarrow 1$. In this limit, $\eta_s \rightarrow (0.001 M_1) \cdot m_s$ and hence

$$A = \lim (\eta_s/m) = \lim (0.001M_1)(m_s/m) =$$
$$(0.001M_1)/(1 + K)$$

Using (3) with this value of A, the Garrod-Herrington inequality becomes

$$a_w + 0.001M_1 \cdot \frac{m\gamma}{1 + K} < 1 \tag{4}$$

instead of their eq 40

$$a_w + 0.001M_1m\gamma < 1$$

The correct inequality (4) is easily satisfied with an appropriate value of K, whereas their eq 40 is not.

Our earlier treatment[2] of semiideal solutions was based on the equations

$$a_w = \frac{1 - 0.001M_1hm}{1 + 0.001M_1(1 - h)m}$$

or

$$1 - a_w = \frac{0.001M_1m}{1 + 0.001M_1(1 - h)m} \tag{5}$$

where $h = \sigma/\Sigma$ and, if there is only one stage of hydration, $\Sigma = \eta_s(1 + Ka_w)$ $\sigma = \eta_s Ka_w$, and

$$a_w + \eta_s + \eta_{sw} = a_w + \eta_s(1 + Ka_w) = 1 \tag{6}$$

These equations, together with eq 3 and our value of A, give

$$\gamma = \frac{1 + K}{1 + Ka_w} \times \frac{1}{1 + 0.001M_1(1 - h)m} =$$
$$\frac{1 + K}{1 + Ka_w} \times \frac{1 - a_w}{0.001M_1m} \tag{7}$$

By similar methods it can be shown that if there are several stages of hydration

$$\gamma = \frac{\Sigma^0}{\Sigma} \frac{1}{1 + 0.001M_1(1 - h)m} = \frac{\Sigma^0}{\Sigma} \frac{1 - a_w}{0.001M_1m} \tag{8}$$

where $h = \sigma/\Sigma$, $\Sigma = \eta_s(1 + Ka_w + K^2a_w{}^2 + ---)$, $\Sigma^0 = \eta_s(1 + K + K^2 + ---)$, $\sigma = \eta_s(Ka_w + 2K^2a_w{}^2 + ---)$. Corresponding with eq 4, we have for the case of multiple hydration

$$a_w + \frac{0.001M_1m\gamma}{\Sigma^0} < 1 \tag{9}$$

For aqueous solutions of sucrose,[2] with 11 sites available for hydration, $K = 0.994$ and $\Sigma^0 = 11.61$.

(3) R. A. Robinson and R. H. Stokes, "Electrolyte Solutions," revised ed, Butterworth and Co. Ltd., London, 1968, p 27.

Table I

m	a_w	γ	$\dfrac{a_w + 0.001}{M_1 m \gamma / \Sigma^0}$
0.1	0.99819	1.015	0.99835
0.4	0.99260	1.062	0.99325
1.0	0.98065	1.177	0.98254
6.0	0.8496	2.845	0.8761

Using values of a_w and γ already determined,[4] the following values of $a_w + 0.001 \, M_1 m \gamma / \Sigma^0$ are calculated in Table I. There is, therefore, no inconsistency between the semiideal behavior of sucrose solutions and the experimental data.

(4) R. A. Robinson and R. H. Stokes, *J. Phys. Chem.*, **65**, 1954 (1961)·

* To whom correspondence should be addressed at State University of New York at Binghamton, Binghamton, N. Y.

UNIVERSITY OF NEW ENGLAND   R. H. STOKES
ARMIDALE, N. S. W. AUSTRALIA
STATE UNIVERSITY OF NEW YORK   R. A. ROBINSON*
AT BINGHAMTON
BINGHAMTON, NEW YORK

Allyl Radicals in the Vacuum Ultraviolet Photolysis of Propane

Sir: The previously unreported products, 4-methyl-1-pentene, 1-hexene, and 1,5-hexadiene have been identified in the product mixture resulting from the photolysis of propane.[1] The photolysis was carried to less than 0.1% conversion in the gas phase using a microwave powered krypton resonance lamp. The only other six-carbon products are 2,3-dimethylbutane, 2-methylpentane, and n-hexane. It is noteworthy that only unsaturated products containing terminal double bonds are observed. This strongly suggests that the precursor of the unsaturated product is an unsaturated radical. If a hexane formed with excess energy *via* the recombination of propyl radicals were to decompose by hydrogen elimination, instead of the more favorable carbon–carbon bond scission, it would certainly decompose to give some of the thermodynamically favored products with interior double bonds. Moreover, the production of olefins from saturated six-carbon precursors would easily be pressure quenched at one atmosphere of total sample pressure.[2] The most important six-carbon olefin, 4-methyl-1-pentene, is still present in significant quantities at pressures greater than 5 atm. It seems most reasonable to conclude that the observed unsaturated products result from the combination of allyl radicals with isopropyl, n-propyl, and allyl radicals, respectively. The product distribution in Table I is consistent with this conclusion.
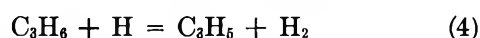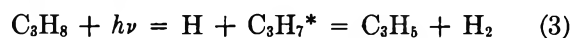
In addition to the possibility that allyl radicals are produced in a primary process such as reaction 1, one must also consider the possibility that they result from the decomposition of excited species formed in the primary photolytic process such as 2 and 3, and finally radical–olefin bimolecular reactions such as 4 and 5 must be considered as possible sources.

Table I: Relative Yields of Six Carbon Products from the Photolysis of Propane at 123.6 nm[a]

Methane	1000
4-Methyl-1-pentene	106
2,3-Dimethylbutane	260
2-Methylpentane	93
1,5-Hexadiene	2
1-Hexene	15
n-Hexane	9

[a] Pressure of propane = 50 Torr.

$$C_3H_8 + h\nu = C_3H_5 + H_2 + H \qquad (1)$$

$$C_3H_8 + h\nu = H_2 + C_3H_6{}^* = C_3H_5 + H \qquad (2)$$

$$C_3H_8 + h\nu = H + C_3H_7{}^* = C_3H_5 + H_2 \qquad (3)$$

$$C_3H_6 + H = C_3H_5 + H_2 \qquad (4)$$

$$CH_3 + C_2H_2 = C_3H_5 \qquad (5)$$

Previously determined rate constants for reactions 4 and 5 suggest that they, in fact, will not be important relative to other reactions of H and CH_3. At 0.1% conversion, abstraction from propane and addition to propylene by hydrogen atoms will effectively use 97% of the available H relative to reaction 4.[3] The remaining small fraction of H can account for less than 1% of the observed allyl radical yield. To be certain that some unusual reaction involving propylene was not occurring, *e.g.*, with energetic H atoms, excess propylene was added to the reactant propane. Up to 1% propylene by volume did not appreciably affect the yield of hexenes relative to hexanes. Similar considerations for the methyl radical show that it is a thousand times as likely to recombine with other radicals in the photolytic system as to add to acetylene

(1) (a) A. L. Lane, Ph.D. Thesis, University of Illinois, 1968; *Nucl. Sci. Abstr.*, **23** (14), 28652 (1969); (b) R. E. Rebbert and P. Ausloos, *J. Chem. Phys.*, **46**, 4333 (1967); (c) D. W. L. Griffith and R. A. Back, *ibid.*, **46**, 3913 (1967); (d) A. H. Laufer and J. R. McNesby, *ibid.*, **70**, 4094 (1966); (e) P. Ausloos and S. G. Lias, *ibid.*, **44**, 521 (1966); (f) J. R. McNesby and H. Okabe, *Advan. Photochem.*, **3**, 157 (1964); (g) P. Ausloos, S. G. Lias, and I. B. Sandoval, *Discuss. Faraday Soc.*, **36**, 66 (1963); (h) H. Okabe and J. R. McNesby, *J. Chem. Phys.*, **37**, 1340 (1962).

(2) B. S. Rabinovitch and D. W. Setser, *Advan. Photochem.*, **3**, 1 (1964).

(3) K. R. Jennings and J. R. Cvetanovic, *J. Chem. Phys.*, **35**, 1233 (1961).
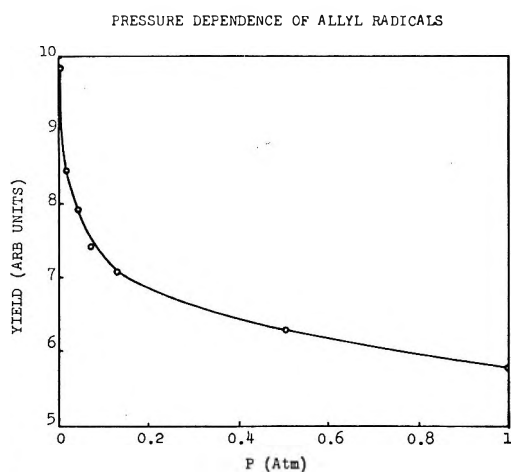
PRESSURE DEPENDENCE OF ALLYL RADICALS

Figure 1.

at the concentrations of acetylene available at low conversion (0.1%).[4] Any other bimolecular mechanism that one can conceive involving the fragments available from the photolysis of propane can be discounted in a manner similar to that used for the examples of reactions 4 and 5. The essential difference between reaction 1 and reactions 2 and 3 is whether all three bonds are broken simultaneously or in a stepwise fashion. The contributions of decompositions such as 2 and 3 cannot be easily determined. Increasing pressure will tend to stabilize such excited species. However, as these species may decompose by more than one path, a direct relationship is difficult to establish.

Allyl radicals are apparently produced via unimolecular decompositions. However, whether it is the unimolecular decomposition of C_3H_8,* C_3H_7*, or C_3H_6* or some combination has not been established. The shape of the curve in Figure 1 suggests that more than one precursor (or one precursor decomposing via different modes) are important. Using the simplest case of multiple precursors, two, we have determined two lifetimes (reciprocal of the unimolecular rate constant). The lifetime of the short-lived precursor was determined from the linear high-pressure region of the curve. This contribution was subtracted from the low-pressure region and a lifetime for the long-lived precursor was calculated. These calculations give lifetimes of 2×10^{-11} sec and 9×10^{-9} sec for the short- and long-lived precursors, respectively.

Since it is not apparently known how energy partitions among fragments in the photolysis of propane, the lifetimes determined cannot be associated with specific fragments or states as precursors on the basis of presently available data. Since most other fragments arising from the photolysis of propane show a much less striking dependence on pressure than allyl radicals, it is reasonable to conclude that primary photodecomposition in propane occurs in $\leq 2 \times 10^{-11}$ sec.

(4) L. Mandelcorn and E. W. R. Steacie, Can. J. Chem., 32, 474 (1954).

* To whom correspondence should be addressed.

DEPARTMENT OF CHEMISTRY   J. H. VORACHEK
NORTH DAKOTA STATE UNIVERSITY   R. D. KOOB*
FARGO, NORTH DAKOTA 58102